SINGULAR FINITE ELEMENTS FOR NEWTONIAN FLOW PROBLEMS WITH STRESS SINGULARITIES

by
Georgios C. Georgiou

A dissertation submitted in partial fulfillment
of the requirements for the degree of
Doctor of Philosophy
(Chemical Engineering)
in The University of Michigan
1989

Doctoral Committee:

- Professor Erdogan Gulari, Co-Chairperson
- Assistant Professor William W. Schultz, Co-Chairperson
- Professor Brice Carnahan
- Professor Robert H. Kadlec
- Assistant Professor Lorraine G. Olson

"If the truth is beyond our grasp, the errors of to-morrow are still to be preferred to the errors of yesterday; for error in the sciences is only another name for the progressive approximation to truth."

E. R. Dodds, *The Greeks and the Irrational.*

To my parents

ACKNOWLEDGEMENTS

I would like to express my gratitude to my thesis co-chairpersons Profs. Erdogan Gulari and William Schultz for their constant encouragement, inspiration and support, and to the other committee members Profs. Brice Carnahan, Robert Kadlec and Lorraine Olson for their advice and guidance.

To Prof. Gulari I owe a special expression of appreciation. As a teacher in academia and as such a personality in the 'real world', he has helped me set new personal standards.

Prof. Schultz has provided critical momentum for this thesis with his patient and priceless discussions.

I should like to express my indebtedness to Prof. Lorraine Olson who was *de facto* a third co-chairperson in my committee. With her valuable criticism and her encouragement, she has critically contributed to the completion of my thesis.

Particular thanks are extended to Prof. Skip Scriven for helping me to enhance and broaden my technical context, and to Prof. James Wilkes for his excellent instruction in the finite element course.

My sincere thanks are due to my friends and colleagues who directly contributed to my thesis: Daniel Kathios who read the first two chapters and whose criticisms and suggestions have been useful; Jeff Dupuie who made valuable suggestions in the modelling of the CVD reactor in appendix A; Dimitris Fotiadis (with the University of Minnesota) who provided useful material on the same matter and was extremely helpful in initiating the CVD project; Kevin Ellwood and John Gyenese who were particularly helpful in resolving graphics difficulties on the Apollos.

I would like also to take the opportunity to thank my friends and colleagues Nikos Antoniadis, Krishnan Balakrishnan, Dr. Zhao Chen, Christos and Filio Christodoulou, Alex Couzis, Dimitrios Hatzinikolaou, Dr. George Kastanas, Dr. Greg Keoleian, Dr. Ellen Kock, Prof. Robert Lee, Dr. Themis Matsoukas, Sotiris Mouskos, Dr. Russel Moy, Sadettin Ozturk, Dimitris Padelis, Dr. Nick Papadakis, Prof. Photis Papoulias, Prof. Balasubramaniam Ramaswami, Dr. Amit Sachdev, Chien Sze, Ioannis Trakakis, Dennis Vigil, Dr. Rosemary Wesson, and Ronggang Zhang, whose friendship has indirectly, yet significantly, influenced this work.

This thesis is dedicated to my parents Christos and Eleni for their support throughout the years of my studies.

TABLE OF CONTENTS

CHAPTER

LIST OF FIGURES

Figure

LIST OF TABLES

Table

LIST OF APPENDICES

Appendix

ABSTRACT

SINGULAR FINITE ELEMENTS FOR NEWTONIAN FLOW PROBLEMS WITH STRESS SINGULARITIES

by
Georgios C. Georgiou

Chairpersons: Erdogan Gulari, William W. Schultz

Stress singularities in fluid mechanics problems arise at points where there is an abrupt change in a boundary condition or in the boundary shape. In solving singular problems numerically, special attention is required around the singular point in order to achieve reasonable accuracy and convergence rates. The most common approach is to refine the grid around the singular point. However, this treatment cannot completely eliminate the numerical inaccuracies, e.g., spurious stress oscillations, which may contaminate the global solution. Some investigators modify the mathematical problem to alleviate the singularity by smoothing either the boundary or the boundary conditions.

In this work, we acknowledge the singularity – incorporating the asymptotic solution into a finite element scheme to avoid inaccuracies due to the singularity. This idea has been successfully used in fracture mechanics with a variety of numerical methods, and it is extended here to solve Newtonian flow problems with finite elements. Two different approaches are followed for this purpose: (1) the singular element approach in which special elements that embody the radial form of the singularity are constructed around the singular point, and (2) the singular basis function approach in which the known local solution is subtracted from the governing equations.

The stick-slip, the sudden-expansion, and the die-swell problems have been solved with the singular element method, and improved accuracy has been achieved with coarse meshes in the neighborhood of the singular point. In the die-swell problem, the convergence of the free surface is dramatically accelerated. A novel singular basis function method based on the subtraction of the exact asymptotic terms and on a double integration by parts is also proposed. When applied to standard Laplace-equation problems, this method improves the solution accuracy and gives more accurate singular coefficients than those obtained with other singular techniques. It also gives satisfactory results for the stick-slip problem. A comparison of the two methods is also made and their advantages and their limitations are discussed.

CHAPTER I

INTRODUCTION

> "Among the corollaries of the doctrine that there is nothing lacking compensation in something else, there is one whose theoretical importance is very small, but which induced us, toward the end or the beginning of the tenth century, to disperse ourselves over the face of the earth. It can be stated in these words: "There exists a river whose waters grant immortality; in some region there must be another river whose waters remove it." The number of rivers is not infinite; an immortal traveler who traverses the world will finally, some day, have drunk from all of them. We proposed to discover that river."
>
> Jorge Luis Borges, *The Immortal (Labyrinths).*

This thesis concerns the use of finite elements for the solution of Newtonian fluid flow problems with stress singularities. The objective is to improve the accuracy and the convergence rate of the solution in the neighborhood of the singular point.

1.1 Singularities and numerical difficulties

A well-known feature of *elliptic* boundary value problems is the appearance of singularities in the solution. The solution is said to possess singularities at points, lines or surfaces in the domain, when values of it or its partial derivatives approach infinity at these places [25].

Consider the following model problem defined in a bounded region V:

$$\begin{aligned} \nabla \cdot (K\, \nabla u) &= F, && \text{in} \quad V \\ A\,\frac{\partial u}{\partial n} + B\,u &= G, && \text{on} \quad \partial V \end{aligned} \tag{1.1}$$

where n is the outer normal to the boundary ∂V. If the data K, A, B, F, and G are analytic and the boundary ∂V itself is analytic, then the solution is analytic[1]. This means that singular behavior can arise only in cases where either the boundary or part of the data are irregular[2]. This very often is the case in many prototype problems in solid and fluid mechanics.

Geometrically, we can classify singularities for two-dimensional problems into two types [99]:

1. *Line singularities.* One or more of the coefficients are discontinuous across a line within the domain. Such discontinuities typically arise at interfaces.
2. *Point singularities.* The coefficients or the boundary are non-analytic at a point (or points) in the domain.

In this thesis, we are interested in point singularities in *two-dimensional* domains. Asymptotic expansions of the solution of equation (1.1) at corners or boundary points with discontinuous data were obtained by Wasow [161] and later adapted by Lehman [94]. A summary of these results is given in [141]. If plane polar coordinates, (r, θ), centered at the corner or the discontinuity point are used, then the local asymptotic solution is of the form

$$u = \sum_{i=1}^{\infty} \alpha_i\, r^{\lambda_i}\, f_i(\theta), \tag{1.2}$$

---

[1] This is a consequence of Weyl's lemma [141].

[2] This irregularity condition is not necessary for *hyperbolic systems*, in which singular behavior (e.g., shocks) can arise even if all the parameters involved are smooth.

where λ_i are the exponents of the solution determined from the boundary conditions, and α_i are unknown coefficients (depending on the global solution).

In fluid mechanics, stress singularities arise at corners (abrupt change in the geometry) or *contact points* (abrupt change in the boundary conditions). Some well-known examples of singular fluid flow problems are the *sudden-expansion*, the *die-swell*, and the *driven-cavity* problems (see, Figure 1.1). Notice that in the last two problems, neither the boundary nor the boundary conditions are smooth at the singular point.

The structure of the singularity for two-dimensional *Newtonian* flows can be obtained by a local analysis as suggested by Michael [100] and Moffatt [104]. For steady, incompressible flow near a corner, inertia forces are negligible and the stream function $\Psi(r, \theta)$ satisfies the Stokes equation

$$\nabla^4 \Psi = 0 . \tag{1.3}$$

Near the singularity, the streamfunction is expressed as an eigenfunction expansion [32, 100,104]:

$$\Psi = \sum_{i=1}^{\infty} \alpha_i \, r^{(\lambda_i+1)} \, f_{\lambda_i}(\theta) , \tag{1.4}$$

where λ_i are the eigenvalues (or exponents) determined from the boundary conditions (see Figure 1.2). According to equation (1.4), the velocities vary as r^{λ}, and the velocity derivatives and the stresses vary as $r^{(\lambda-1)}$. Thus if the real part of λ is less than unity, the velocity derivatives and the stresses are singular at $r = 0$. In the sudden-expansion problem, for example, two of the exponents are less than 1 (Figure 1.1). The corresponding terms dominate near the singular point, and the stresses vary as $c_1 \, r^{-0.456} + c_2 \, r^{-0.091}$. In the die-swell problem, the stresses vary approximately as $r^{-1/2}$. In the driven-cavity problem, they vary as r^{-1} near the upper corners.

The local analyses for two-dimensional Newtonian flows are well established [100,104].

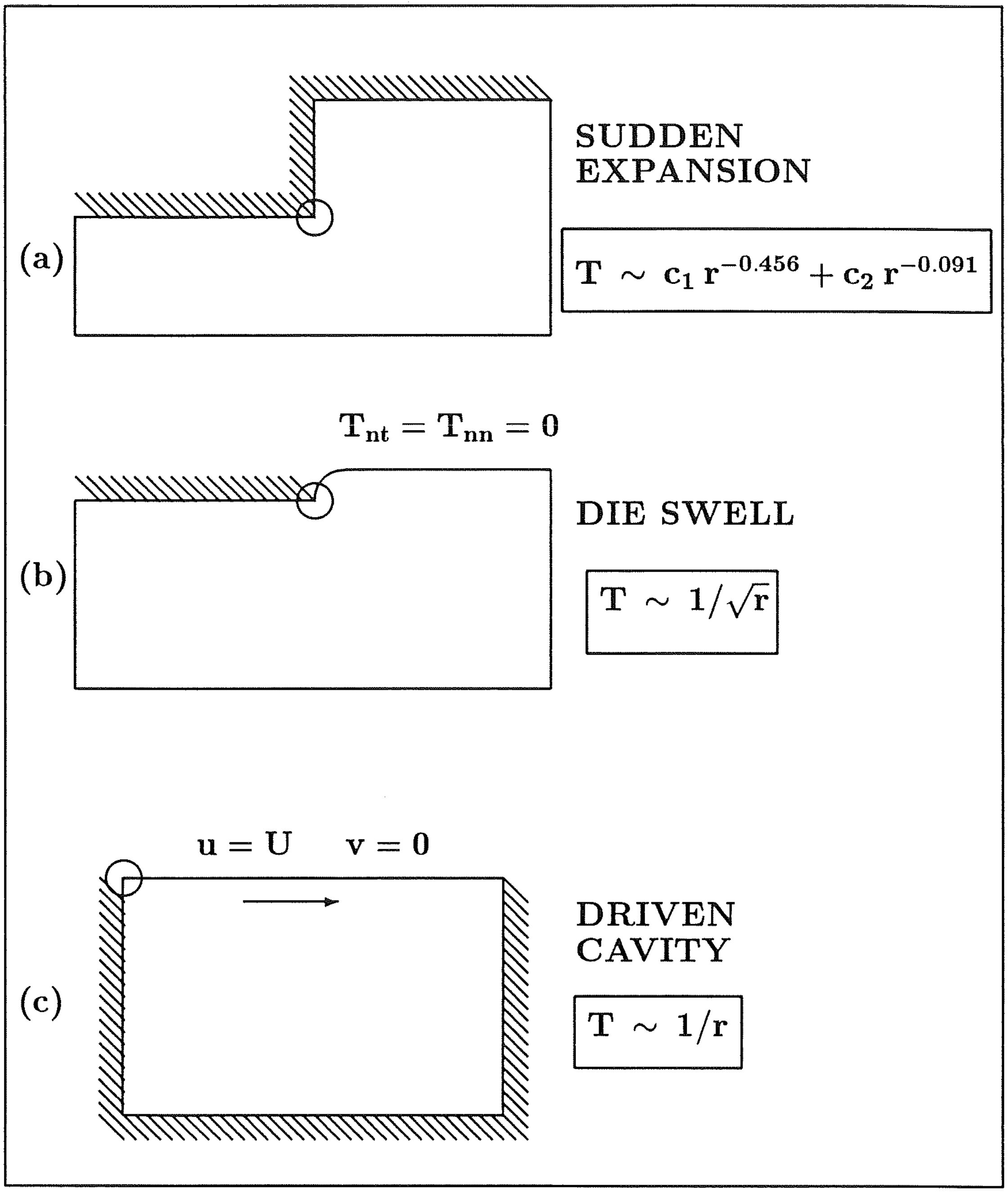

Figure 1.1: Examples of fluid flow problems with singularities. The forms of the singularities correspond to the Newtonian flows.

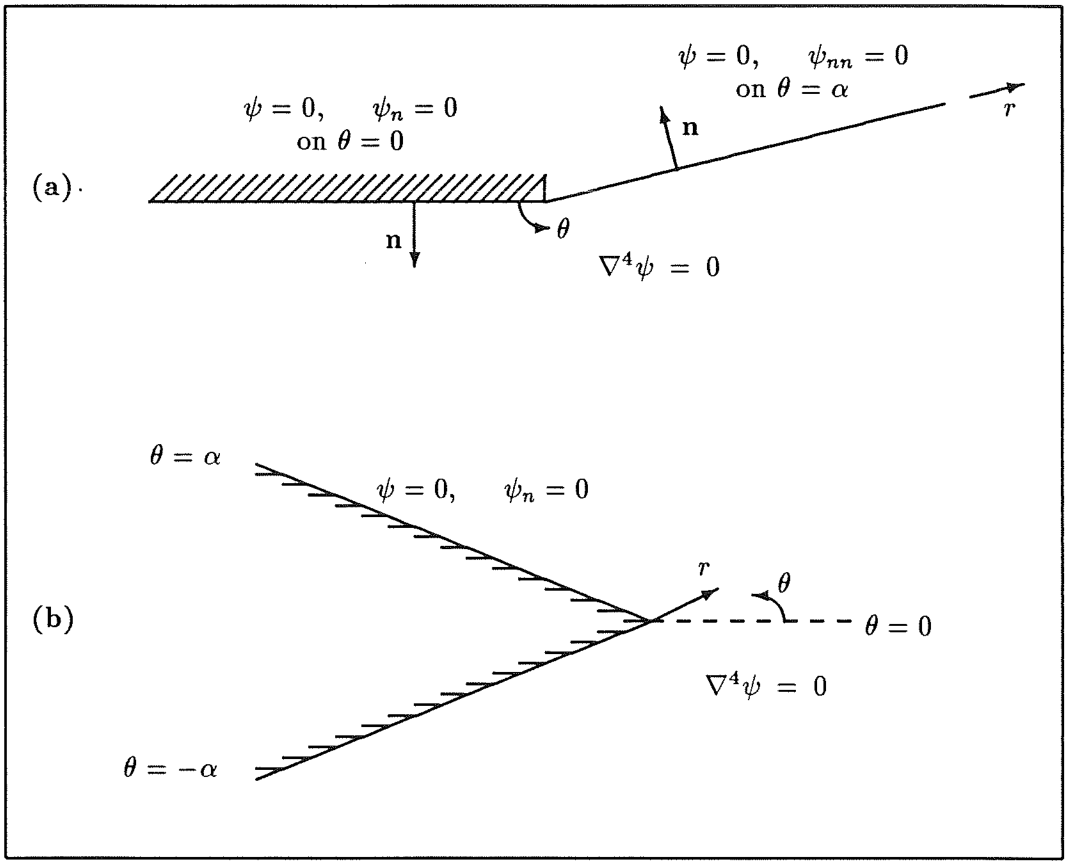

Figure 1.2: Geometry and boundary conditions for (a) Flow near the intersection of a wall and a free surface and (b) Flow near a sharp corner.

Two special cases, illustrated in Figure 1.2, are of interest in this work[3]:

1. The flow near the intersection of a wall and a free surface (e.g, as in the die-swell problem), and
2. The flow near a sharp corner (e.g., as in the sudden-expansion problem).

In non-Newtonian flows, explicit local analyses have been presented only for a few special cases concerning power-law [144,66] and second-order fluids[4] [144]. Stokesian analyses are difficult to extend to viscoelastic flows because of the nonlinearity introduced by the convected derivative. Nevertheless, estimates for the radial form of the local solution can be obtained with some constitutive models [4].

In the vicinity of singular points the solution field is steep, and thus special attention is required when the partial differential equations involved are solved numerically. The most common treatment, in both the finite element and the finite difference methods, is to refine the grid around the singular point. However, even with mesh refinement, the rate of convergence and the accuracy are not always satisfactory [141,6,48]. Another disadvantage is the generation of extremely large stiffness matrices resulting in higher computational costs.

In fluid mechanics, the numerical inaccuracies due to the presence of a singularity are often severe and may not be restricted to the neighborhood of the singular point, propagating to the bulk solution. In general, the continuous representation for the unknown fields used in the standard numerical methods (e.g., finite elements) fails to accurately reproduce the singular behavior of the exact solution. The stresses cannot be infinite in compliance with the asymptotic solution, and thus are tainted by spurious oscillations around the singular point [95,55,57]. In most Newtonian flows, the convergence of the

---

[3] The local solutions for the two paradigms of Figure 1.2 are discussed in Appendix B.

[4] The second-order fluid (SOF) is the lowest-order approximation to viscoelastic flow beyond the Newtonian fluid in Simple Fluid theory.

finite element solution with mesh refinement is observed everywhere in the flow domain except in the region around the singular point [87,55]. But what is more frustrating is the contamination of the global solution in some problems. In the die-swell problem, it is well-known that the position of the free surface and the resulting die-swell ratio depend on the mesh refinement in the region around the singularity, and that a coarser mesh gives more swelling [144,2,57].

The contamination of the global solution is far more serious in non-Newtonian flows than in their Newtonian counterparts. Numerical inaccuracies caused by singularities can lead to numerically stiff iteration schemes, to the formation of fictitious limit points, or to artificial changes of type of the governing equations [22,4,97]. The *high Weissenberg number problem*[5] is partially due to the excessive approximation error caused by the singularity[6], or to the *non-integrability* of the singularities[7] [22,87,97,95].

Non-integrable stresses are physically inadmissible since they lead to infinite forces. In fact, even finite stresses greater than some value corresponding to the "strength" of the continuum (typically of order $10^9 Pa$) are inadmissible [95]. In most Newtonian flows, these inadmissible stresses are encountered over length scales where the continuum hypothesis breaks down and the singularity is not felt by the bulk flow. In contrast to the Newtonian flows, the stresses in viscoelastic flows reach inadmissible values over length scales where the continuum hypothesis is still valid. This ultimately results in the

---

[5] The high Weissenberg number problem is the failure of the numerical schemes to provide solutions beyond some critical value of the Weissenberg number, a dimensionless group which determines the elastic character of the flow [87].

[6] Other possible mechanisms for the numerical failure at high Weissenberg numbers are: (a) Multiplicity or loss of two-dimensional steady solutions or bifurcation to three-dimensional flows, and (b) Change of mathematical type in the coupled momentum/continuity/constitutive equation set (see [22]).

[7] The integrability criterion is satisfied when

$$\left[\int_V (\mathbf{T}:\mathbf{T})\, dV\right]^{1/2} < \infty\,,$$

where $\mathbf{T}$ is the stress tensor. The singularity of the driven-cavity problem, for example, is not integrable.

contamination of the bulk solution and, often, in the failure of the numerical scheme [95].

Some investigators have modified the physical problem to alleviate or to completely remove the singularity by

1. modifying the boundary conditions (e.g., relaxing the *no-slip* condition for a smooth transition from a velocity to a stress boundary condition [135]), or
2. smoothing the boundary (e.g., replacing a re-entrant corner by a circular arc of small radius [22,125]).

As indicated in the literature [90,118], the relaxation of the no-slip condition is very likely consistent with the real physical behavior near regions of high stresses[8]. Lau and Schowalter [90] provide a table with examples of materials reported to exhibit wall slip[9]. The use of a slip boundary condition is imperative for satisfactory continuum models of flows with *dynamic contact lines* [79,80,37,38]. Silliman and Scriven [135]-[137] studied the effect of a slip coefficient on the solution of the die-swell problem (which involves a *static contact line*). Hocking [72,73] showed that taking the irregularities of the solid surface into account is equivalent to introducing an effective slip coefficient (which is proportional to the depth and/or the spacing of the irregularities). However, the slip condition is difficult to apply near corners without avoiding flow through the boundary walls. Brown *et al.* [22] and Rosenberg and Keunings [125] replaced the corners by a circular arc in their calculations for abrupt-contraction flow of a viscoelastic fluid. This changed the character of the spurious stress oscillations but it did not remove them nor resolve the numerical difficulties.

---

[8] Effects of density and viscosity gradients and non-Newtonian behavior may be possible in high stress regions, but they could not alleviate the singularity.

[9] The slip condition is also known as the Navier condition as opposed to the Stokes condition for no slip. For slip at a plane solid wall, the Navier condition is given by

$$T_{xy} = -\frac{u}{\beta},$$

where T_{xy} is the shear stress, u is the velocity in the x direction, and β is the slip coefficient.

An alternate approach, based on the acknowledgement of the singularity rather than on its removal, is the incorporation of the local solution into the numerical scheme. This idea has been extensively used in solving solid mechanics problems with finite elements and gives accurate results for relatively coarse meshes (see reviews in [6,7,42,48,134,141]). More recently, singular methods were used to solve fluid mechanics problems with finite elements [163,55,56], finite differences [74], boundary elements [82,93], and global elements [98,99].

The need for special finite elements in Newtonian and non-Newtonian flow problems with singularities has been indicated by various researchers in recent years (Keunings [87]; André and Clermont [2]; Lipscomb *et al.* [95]; Davies [31]). The use of such special elements in viscoelastic flows is presently inhibited by the lack of local analyses, despite a recent attempt by Davies [31] to develop a method for analyzing the local solutions for some viscoelastic fluids. (As we mentioned before, non-Newtonian local analyses are available only for the power-law and the second-order fluids.)

In this thesis, we devise special finite elements for Newtonian flow problems with stress singularities which take into account the structure of the singularity. The objective is to obtain more accurate solutions and faster convergence rates than those achieved with standard finite element methods. One could choose another numerical technique like finite differences, spectral methods and boundary elements. However, the last two methods are limited to specific types of problems (see, e.g., Brebbia [19], Voigt *et al.* [154] and Crochet [29]). In fact, some of their limitations are related to or caused by singularities [19,154,92,132,117]. Compared to the finite difference method, the finite element method can be more easily implemented in complex geometries [29].

1.2 Singular finite element approaches

In the standard finite element method, the domain V is subdivided into small elements, and the solution u is approximated by a piecewise analytic function (typically a low-order polynomial) over each element. For the two-dimensional case of equation (1.1) one may use 9-node rectangular elements with bi-quadratic basis functions, Φ^i:

$$u = \sum_{i=1}^{N} u_i \, \Phi^i, \tag{1.5}$$

where u_i are the nodal values, and N is the total number of nodes.

In the *Galerkin method*, which is used throughout this thesis, the governing equation is weighted by the same functions used to expand the unknown variable:

$$\int_V \nabla^2 u \, \Phi^i \, dV = 0, \qquad i = 1, 2, \cdots, N, \tag{1.6}$$

or after using Green's theorem

$$\int_{\partial V} \frac{\partial u}{\partial n} \Phi^i \, dV - \int_V \nabla u \cdot \nabla \Phi^i \, dV = 0, \qquad i = 1, 2, \cdots, N. \tag{1.7}$$

Equations (1.7) form a linear system of equations with the nodal values u_i as unknowns.

Let us assume that the meshsize is h and the basis functions are complete polynomials of order k, and that the solution is in the Sobolev space[10] $H^m(V)$ and the finite element approximation is denoted by u_h. Then the error satisfies an estimate of the type[11] [25,

---

[10] A function u is in the class $H^m(V)$, if u and all of its derivatives of order less than or equal to m (m being a nonnegative number) are ***square-integrable*** over V [25].
A function f is square-integrable over V if

$$\int_V f^2 \, dx < \infty \, .$$

[11] The energy error is considered here, i.e., the H^1-norm. For $V = (0,1)$

$$\|u - u_h\|_1 = \left\{ \int_0^1 \left[\left(\frac{du}{dx} - \frac{du_h}{dx} \right)^2 + (u - u_h)^2 \right] dx \right\}^{1/2} .$$

141,9]:

$$\|u - u_h\|_1 \leq C\, h^{\mu}\, \|u\|_m \tag{1.8}$$

with

$$\mu \,=\, \min\{k,\, m-1\}\,. \tag{1.9}$$

where C is a generic constant (independent of h). If the solution u is regular (smooth), then m is very large and $\mu = k$. The error is of order h^k in this case. We can increase the rate of convergence by increasing the order of the basis functions, k. However, if the solution is irregular, then m is small and $m - 1 \leq k$. Therefore, no matter how large k is, the error will be of order h^{m-1} and the rate of convergence will be very small [12].

The different approaches used to incorporate the structure of the singularity into a finite element scheme can be classified into two categories [25]:

1. *Singular basis function approach*, and
2. *Singular element approach.*

The two approaches are explained and discussed below.

Singular basis function approach

Quoting Carey and Oden [25], this approach is very likely "the most logical approach for removing the singularity". A set of supplementary basis functions, W^i, chosen to reproduce the leading terms[13] of the local solution is added to the standard finite element solution expansion [141,106]:

$$u \,=\, \sum_{i=1}^{N} u_i\, \Phi^i \,+\, \sum_{i=1}^{N_{SBF}} \alpha_i\, W^i\,. \tag{1.10}$$

---

[12] Notice that m is not necessarily an integer. Generalized Sobolev spaces (or fractional Sobolev spaces) are considered [138]. In this case, $1/m$ provides a quantitative measure of the strength of the singularity.

[13] The leading terms of the local solution dominate as we approach the singular point.

Here N_{SBF} is the number of the singular functions and α_i the unknown singular coefficients. The singular functions are usually defined over several elements and can span the entire domain. They approximate the exact asymptotic terms close to the singular point:

$$\lim_{r\to 0} W^i = \lim_{r\to 0} \left\{ r^{\lambda_i} f_i(\theta) \right\} . \tag{1.11}$$

Therefore, knowledge of both the radial and the angular forms of the local solution is required. The singularity expansion coefficients, α_i, are directly calculated using the singular basis function approach.

It can be shown [25,141,8] that the full rate of convergence (the same as that for the regular problem) is theoretically obtained with this treatment. In other words, if

$$u_h^* = \sum_{i=1}^{N} u_i \, \Phi^i \tag{1.12}$$

is the regular element contribution to the solution and u^* is the 'exact' contribution, then the error satisfies an estimate of the form

$$\|u - u_h\|_1 \leq C \, h^k \, \|u^*\|_k . \tag{1.13}$$

However, we should notice that practical difficulties may inhibit such fast convergence. These difficulties include integration inaccuracies when calculating the stiffness matrix and possible ill-conditioning of the stiffness matrix [25,141].

Singular element approach

In the singular element approach, special elements are used in a small region around the singularity, while conventional elements are used in the rest of the domain. These elements take into account the structure of the singularity, and they must be relatively large in size to be effective. This is their major limitation because they do not allow extensive refinement of the domain near the singularity. Nevertheless, if the convergence is rapid, further refinement may not be necessary.

The various elements used by other researchers can be classified in three categories:

(1) Embodied singularity elements.[14]

Special elements are employed around the singular point where the basis functions are constructed to describe the radial form of the singularity [149,150,5]. These elements are *conforming* (compatible with the adjacent ordinary elements). They can also describe singular primary variables, they conform to curved boundaries without significant loss of accuracy, and they can describe different singular behaviors by changing the shape functions. Obviously, they do not require knowledge of the angular form of the solution.

(2) Embedded singularity elements.

The leading terms of the singular expansion are used to describe the full local solution in a small core around the singular point, and conventional elements are used elsewhere [134], with the requirement that the conventional polynomial functions match the local solution at the boundary of the core. This is equivalent to using a multi-node element in the core. The main drawback of the embedded singularity elements is their incompatibility with the ordinary elements, i.e., it is difficult to enforce the boundary matching. In addition, the optimum size of the core is unknown. Knowledge of both the radial and the angular forms of the local solution is required with these elements.

(3) Singular isoparametric elements.[15]

The desired singular behavior is obtained by changing the position and/or the number of 'mid-nodes' in the elements sharing the singular point and by using an *isoparametric transformation* to map the actual elements onto standard elements with equally spaced

---

[14] *Embodied singularity elements* is the expression suggested by Georgiou *et al.* [55]. Carey and Oden [25] recognize two kinds of elements which, according to our definition, fall in the same category:

1. Akin's family of singular elements.
2. Stern's family of singular elements.

What is different in these families is the way the basis functions are constructed [3,140].

[15] Carey and Oden [25] use the expression *degenerate isoparametric elements* instead.

mid-nodes[16]. Celebrated examples of elements in this category are the *quarter-point elements* [70,157,12]. The singular isoparametric elements require a variable number of mid-nodes to describe general power-type singularities. Unlike the embodied and the embedded singularity elements, they become inaccurate with curved boundaries and cannot handle singular primary variables.

Both the singular basis function and the singular element approaches have been successful in solving solid mechanics problems [6,7,42,141,134], and therefore both the approaches are examined in this dissertation. It should be emphasized that fluid flow problems are more complicated than solid mechanics problems because, in addition to the velocity derivatives, the pressure –a primary unknown– is also singular. Another complication arises in free-surface problems in which we have curved boundaries and the form of the singularity is not exactly known.

Among the various kinds of singular elements, the embodied singularity elements are the most suitable for our purposes. Unlike the embedded singularity elements, they are compatible with the ordinary elements and they do not require knowledge of the angular form of the local solution. The embodied singularity elements are superior to the singular isoparametric elements for the following reasons:

1. They can handle singular primary variables (such as pressure) when constructed such that there is no node at the singular point for the corresponding variables.

2. They easily conform to curved boundaries (such as free surfaces) without significant loss of accuracy.

3. They can describe general power-type singularities by using different field shape functions. (With the singular isoparametric elements one has either to vary the

---

[16] The Jacobian of the isoparametric transformation is singular and so are the gradients of the primitive variables.

number of nodes per element or to construct special field shape functions which, in combination with the distortion of the physical element, will yield the desired behavior.)

1.3 Dissertation format and chapter content description

I should warn the reader that there is some material overlap between chapters and/or appendices since most of them were originally independent papers. This, I hope, is mitigated by the fact that one can follow any chapter or appendix without having to refer to the previous material. On the other hand, the reader may notice that the bibliography is common for all chapters and appendices and that introductory remarks are provided in all chapters in order to ensure the continuity of the dissertation. Care was also taken to use consistent nomenclature in all chapters and appendices. I hope that all these have resulted in a unified product.

The only obvious exception is Appendix A which concerns the modeling of a vertical CVD reactor with finite elements. The CVD project was completely parallel and independent, and it does not involve nor require the use of singular finite elements. The fact that this material is relegated to an appendix is by no means indicative of its importance.

Chapter one has been written for a general audience, and it is intended as a basic introduction to singularities, the associated numerical difficulties in fluid flow problems and the singular finite element approaches.

Chapter two concerns the solution of both the planar and the round die-swell problems with standard finite elements and full-Newton iteration. The Galerkin method is outlined in detail and special emphasis is placed on the numerical calculations in order to show the robustness of the method. The calculations are compared with available experimental and theoretical results.

Chapters three and four implement and discuss the singular element approach. Chapter three describes the construction of singular elements for the stick-slip problem[17]. The method is extended to the sudden-expansion and to the die-swell problems in chapter four. It is shown that the singular finite elements give more accurate results than the standard finite elements, and that they accelerate the convergence rate of the free surface in the die-swell problem.

Chapters five and six concern the singular basis function approach. In chapter five, a novel method is developed and applied to two benchmark Laplace-equation problems: the Motz problem and the cracked-beam problem. Very accurate estimates of the leading singular coefficients are directly calculated. The method is extended to fluid flow problems, namely the stick-slip problem, in chapter six.

Finally, chapter seven summarizes this work and suggests future directions.

All the programs developed in this work were written in FORTRAN 77 and run on an IBM 3090-600E/VM[18].

---

[17] The stick-slip and the sudden-contraction problems have been benchmark problems for viscoelastic simulations in the last ten years. In fact, these two problems along with the steady motion of a sphere along the axis of a cylinder filled with fluid, the flow in a tube of sinusoidally varying cross section and the eccentric cylinder flow were defined as the benchmark problems for the 6th International Workshop on Numerical Methods in Non-Newtonian Flow, Lyngby (Denmark), June 1989 [67].

[18] For additional information about the programs developed in this thesis contact Dr. Georgios Georgiou, c/o Prof. Erdogan Gulari, Department of Chemical Engineering, The University of Michigan, Ann Arbor, MI 48109.

CHAPTER II

THE ANALYSIS OF PLANAR AND ROUND NEWTONIAN JETS

> "One no longer loves one's knowledge enough when one has communicated it."
>
> Friedrich Nietzsche, *Beyond Good and Evil.*

In this chapter, we demonstrate the implementation of the *full-Newton iteration* method for the solution of both the planar and round Newtonian *die-swell*[1] problems. Special emphasis is given to the finite element formulation and to the treatment of the free surface which are critical in understanding the remaining chapters of the dissertation. In addition, results are presented in order to illustrate the power of the method and its applicability in wide ranges of the dimensionless parameters involved[2].

2.1 Introduction

The extrusion of a viscous jet from a die into an inviscid medium is of considerable importance in many polymer-processing operations. The behavior and shape of the free surface are of particular interest. A quantitative measure of this behavior is the *die-swell ratio*, defined as the ratio of the final jet dimension to that of the die. It is an

---

[1] The die-swell phenomenon is also known as the *extrudate-swell* phenomenon.

[2] Some of the results presented in this chapter appear also in the author's Preliminary Research Proposal and in [51,41].

important design parameter in polymer processing operations (e.g., extrusion), and it is strongly dependent on the rheological properties of the fluid, the die geometry, and the flow conditions. But before attempting to solve the more complex non-Newtonian die-swell problem it is reasonable to develop first a reliable, fast and relatively inexpensive algorithm for the Newtonian case.

By neglecting gravity and axial tension, the shapes of Newtonian jets emerging from a long die depend only on two dimensionless parameters: the Reynolds and capillary numbers (Re and Ca)[3]. It is known from experimental data that the die-swell ratio for Newtonian creeping flow without surface tension is approximately 1.19 for a plane and 1.13 for an axisymmetric jet [102,58,13,119]. In general, the die-swell ratio decreases as the Reynolds number increases. The jet expands monotonically at low Re and contracts monotonically at high Re. However, at some intermediate critical range of Reynolds numbers, the jet first contracts and then expands to its final dimension [58,119].

The surface-tension effect is also important. In general, surface tension tends to reduce either expansion or contraction of the jet. For infinite surface tension ($Ca = 0$), neither expansion nor contraction is expected over the entire Reynolds number range. However, at high Reynolds numbers the effect of surface tension on the jet profile is weaker than it is at low Reynolds numbers. This indicates that inertia is the major controlling factor at high Reynolds numbers [119]. The *stick-slip* problem[4] defined by Richardson [121,122] is equivalent to the plane Newtonian creeping flow with infinite surface tension in which the boundary conditions suddenly change from no slip at the wall to perfect slip along a planar free surface. The exact solution to this problem obtained by Richardson is often used as a check on the various proposed methods for die-swell computations [108,127]. In fact, Richardson's solution for the very special case

---

[3] The Reynolds and the capillary numbers are defined in the next section.

[4] More details about the stick-slip problem are given in Chapter III.

$Ca = 0$, $Re = 0$ is the only known analytical solution for the die-swell problem. Otherwise, the problem is analytically intractable due mainly to the presence of the free surface, the location of which is unknown, causing difficulties in specifying the boundary conditions. Furthermore, the normal-stress condition depends on the unknown shape of the free surface. A further complication is the presence of the *stress singularity*[5] at the line of separation [100,104,79]. Because of these difficulties, numerical methods provide the only means for solving the die-swell problem.

Finite element methods for the die-swell problem

Due to its superiority in dealing with free surface problems, the finite-element method has been widely used by several investigators to solve the Newtonian-jet problem, with the velocity and the pressure as the primitive unknowns. In most cases, the free-surface boundary shape is computed by means of a *Picard iteration* which follows the general three-step scheme:

1. Assume a free surface profile.
2. Calculate the flow field for the current domain, relaxing one of the three boundary conditions at the free surface (kinematic, normal stress, or shear stress conditions)
3. Compute the new free surface shape for the calculated flow field to satisfy the neglected boundary condition.

This cycle is repeated until the desired degree of convergence is achieved. Depending on which of the three boundary conditions is used as the criterion for relocating the free surface, the Picard iterative schemes can be classified as either: (1) kinematic iteration, (2) normal-stress iteration, or (3) shear-stress iteration schemes [136]. The last scheme has never been reported in the literature.

---

[5] The stress singularity is addressed in detail in Appendix B, and in Chapters III and IV.

Nickell *et al.* used the kinematic iteration scheme to solve the round-jet problem with no surface tension [108]. The normal-stress iteration scheme was used by Orr and Scriven to solve a different free-surface flow problem with surface tension (rimming flow) [115]. The kinematic iteration scheme was used by Reddy and Tanner in an attempt to extend the round-jet computations to higher Reynolds numbers (up to 50) and to include the effect of surface-tension forces (capillary numbers as low as 1) [119]. The convergence for high Re was slow and for $Ca < 1$ convergence could not be achieved. The kinematic iteration scheme was also used by Omodei to solve both the planar and the round jets in two consecutive papers [113,114]. He obtained results for Re up to 500 and Ca down to 0.2; the convergence for high Re was again slow and for $Ca < 1$ the computed free-surface profiles were characterized by severe oscillations. Silliman and Scriven solved the planar jet problem and showed that at low surface tension, $Ca > 1$, the kinematic iteration scheme converged very rapidly compared to the normal-stress iteration scheme [135]. However, for high surface tension, $Ca < 1$, the opposite was true.

Picard iteration schemes are based on successive approximations to the free-surface profile and at best exhibit linear convergence [135]. As a result the computational cost is excessively high. Special strategies must be employed to determine the mean curvature at each node, and, in addition, extrapolation techniques must be used when the free boundaries fall outside the domain in which the approximate velocity field is known. These limitations become even more severe at high surface tension and ultimately result in oscillations of the free-surface profile. For very high surface tensions, $Ca < 0.2$, convergence has never been achieved with Picard iteration schemes.

The alternative to utilizing the Picard iteration schemes is to solve the complete set of equations with the velocities, the pressure, and the free-surface profile as primitive unknowns. In this approach, the free-surface profile is computed simultaneously with the other unknowns, and the grid that covers the flow region under the free surface is updated at every iteration step. This scheme which was initiated by Ruschak [127], is called the *full-Newton iteration* scheme and it was further developed by Scriven and his co-workers [128,89] for non-axisymmetric two-dimensional flows. Ruschak applied this method to analyze the planar Newtonian jet at low Reynolds numbers [127]. But the fact that he used linear basis functions for the velocities and for the elevation of the free surface, and piecewise constant basis functions for the pressure, prevented an accurate and detailed study of the effect of the various parameters involved. Georgiou *et al.* extended the method to round jets [51]. By using biquadratic basis functions for the velocities and bilinear basis functions for the pressure, they obtained results in wide ranges of Re and Ca.

The advantages of the full-Newton iteration method compared to the Picard iteration schemes are:

1. Simultaneous evaluation of all the unknowns and quadratic convergence.
2. Larger convergence radius of Reynolds and capillary numbers, and
3. Direct evaluation of the Jacobian which is required for linear stability analysis [21].

In the remaining sections of this chapter, the full Newton iteration is applied to both the planar and the round die-swell problems with emphasis on the finite element formulation. Gravity in the direction of flow is also included into the analysis. The governing equations and the boundary conditions are discussed in section 2.2. The step-by-step finite-element formulation is given in section 2.3. The numerical results are presented and discussed in section 2.4.

2.2 Governing equations and boundary conditions

The flow configuration and coordinates for the round jet are shown in Figure 2.1 (Figure 2.2 is an analogous illustration for the planar jet). Taking advantage of the axisymmetry makes it possible to solve the problem on only half of the flow field. The flow is governed by the momentum and continuity equations. For steady, incompressible flow, the dimensionless forms of these equations are

$$Re\, \mathbf{u} \cdot \nabla \mathbf{u} = \nabla \cdot \mathbf{T} + St\, \mathbf{g}, \tag{2.1}$$

and

$$\nabla \cdot \mathbf{u} = 0. \tag{2.2}$$

In these equations, lengths are measured in units of the radius h_0 (or the channel half-width for the planar case), $\mathbf{u}$ is the velocity measured in units of the mean velocity U in the die, and $\mathbf{T}$ is the total stress tensor measured in units of $\mu U / h_0$. For a Newtonian liquid the stress tensor is given by

$$\mathbf{T} = -p\,\mathbf{I} + [\nabla \mathbf{u} + (\nabla \mathbf{u})^T], \tag{2.3}$$

where p is the pressure relative to that in the adjacent gas phase and $\mathbf{I}$ is the unit tensor. Also, $\mathbf{g}$ is the unit vector in the direction of the gravitational acceleration (which coincides with the direction of flow),

$$Re \equiv \frac{\rho\, U\, h_o}{\mu} \tag{2.4}$$

is the Reynolds number, and

$$St \equiv \frac{\rho\, g\, h_o^2}{\mu\, U} \tag{2.5}$$

is an inverse Stokes number; g is the gravitational acceleration, ρ is the density and μ is viscosity of the Newtonian liquid.

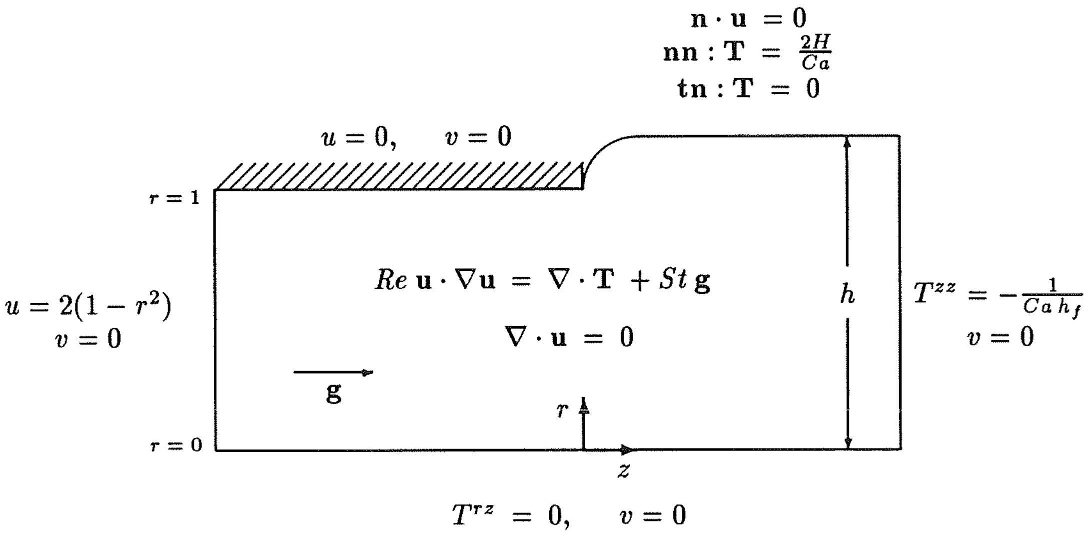

Figure 2.1: Geometry and governing equations for the round jet.

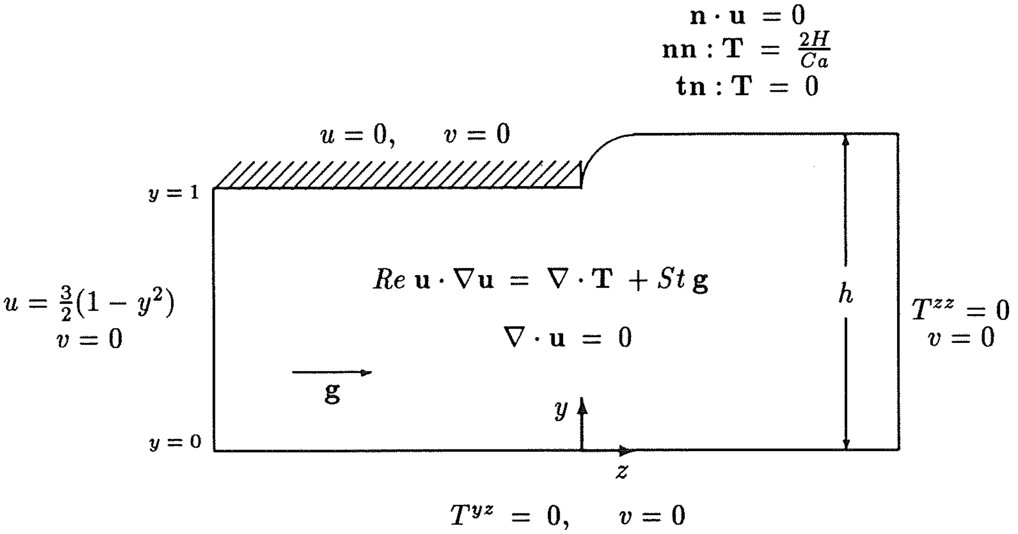

Figure 2.2: Geometry and governing equations for the planar jet.

Apart from the axial and radial velocity components (u and v) and the pressure (p), the location of the free surface (h) is an additional unknown field. The kinematic condition that the free surface remains a material surface provides the additional equation needed,

$$\mathbf{n} \cdot \mathbf{u} = 0\,, \tag{2.6}$$

where $\mathbf{n}$ is the unit normal vector to the free surface given by

$$\mathbf{n} = \frac{-h_z\,\mathbf{e_z} + \mathbf{e_r}}{\sqrt{1+h_z^2}}\,. \tag{2.7}$$

Here h is the distance from the centerline, the subscript z denotes differentiation with respect to z, and $\mathbf{e_z}$, $\mathbf{e_r}$ are the unit vectors in the cylindrical coordinates of Figure 2.1.

The momentum-equation components require two boundary conditions. Five different boundaries must be examined in this problem: the free-surface, the outflow plane, the midplane, the inlet plane, and the solid-wall boundaries. The appropriate boundary conditions are depicted in Figure 2.1 and are explained below.

A momentum balance on the free surface leads to the equation

$$\mathbf{n} \cdot \mathbf{T} = \frac{2H}{Ca}\,\mathbf{n}\,, \tag{2.8}$$

where Ca is the capillary number, defined as

$$Ca \equiv \frac{\mu\,U}{\sigma}\,, \tag{2.9}$$

and σ is the surface tension. Also, $2H$ is the mean curvature of the free surface, given by

$$2H = \frac{h_{zz}}{[\,1+h_z^2\,]^{3/2}} - \frac{1}{h\,\sqrt{1+h_z^2}} \tag{2.10}$$

for the round jet[6], and by

$$2H = \frac{h_{zz}}{[\,1+h_z^2\,]^{3/2}} \tag{2.11}$$

---

[6] Again, the subscripts in (2.10) and (2.11) denote differentiation.

for the planar case. The normal and tangential components of (2.8) are given by

$$T_N = \mathbf{nn} : \mathbf{T} = \frac{2H}{Ca}, \tag{2.12}$$

and

$$T_S = \mathbf{tn} : \mathbf{T} = 0. \tag{2.13}$$

In other words, the momentum principle requires the normal stress in the liquid (T_N) to balance any capillary pressure, and the shear stress (T_S) to vanish. Here, $\mathbf{t}$ is the unit tangent vector to the free surface given by

$$\mathbf{t} = \frac{\mathbf{e_z} + h_z\,\mathbf{e_r}}{\sqrt{1+h_z^2}}. \tag{2.14}$$

At a distance L_2 sufficiently far downstream, the flow is assumed to be fully developed (practically zero radial velocity and uniform axial velocity). At the outflow plane $h_z = h_{zz} = 0$, and, according to equation (2.11), the total normal stress is zero for the planar jet; However, for the round jet we have

$$T_N = -\frac{1}{Ca\,h_f}, \tag{2.15}$$

where h_f is the final jet dimension. As discussed later, the outlet boundary conditions are satisfactory even when gravity is taken into account ($St \neq 0$), provided that the outflow plane is taken to be sufficiently far downstream.

At the symmetry plane there is neither normal velocity nor shear stress. The inflow boundary is taken at distance L_1 sufficiently far upstream so that the flow can be considered as fully-developed Poiseuille flow. At the solid wall there is neither slip nor penetration (both the velocity components are zero).

2.3 Galerkin finite-element formulation

In this section we develop the finite element formulation for the round jet. The formulation for the planar jet is similar and simpler; only the final residual equations are given for this case[7].

The first step in the finite-element formulation is the discretization of the flow domain into finite elements. The axisymmetric nature of the flow allows for any θ-section of the flow domain to be used. A convenient θ-section is the half of the flow field illustrated in Figure 2.3a. The origin of the cylindrical coordinate system is chosen at the exit of the die; θ goes from 0 to π, z is extended at distances L_1 upstream and L_2 downstream, and r goes from 0 to h; $h = R$ in the die and $h = h_f$ at the outflow plane.

The actual elements are axisymmetric semi-rings of curvilinear-rectangle cross section. Because of the axisymmetry, these three-dimensional elements can be projected to their cross section after integrating over θ as illustrated in Figure 2.3b. Thus the elements become two-dimensional and the flow domain is reduced to a tessellation of an (r-z)-plane. The shape of the finite-element mesh is shown in Figure 2.3b. Two opposite sides of the elements are segments of convenient spines at constant z, so that the mesh is finer around the exit where the velocity and pressure gradients are steep. The other two sides are made to intersect those spines at fixed ratios to the position of the free surface or the wall. Thus the elements under the solid wall are of straight sides and fixed, whereas the elements under the free surface have two curved sides the r-coordinates of which are repeatedly updated. In order to accommodate the irregular boundaries, the elements in the (r-z)-plane are considered as mappings of the standard 2x2 square in the (ξ, η) plane:

$$z = \sum_{i=1}^{9} z_i \, \Phi^i(\xi, \eta), \tag{2.16}$$

$$r = \sum_{i=1}^{9} r_i \, \Phi^i(\xi, \eta), \tag{2.17}$$

where $-1 < \xi < 1$, $-1 < \eta < 1$, (z_i, r_i) are the coordinates of ith node, and Φ^i are biquadratic basis functions. These transformations define a global map of the complicated

---

[7] For more details about the finite element formulation for the planar case see [136].

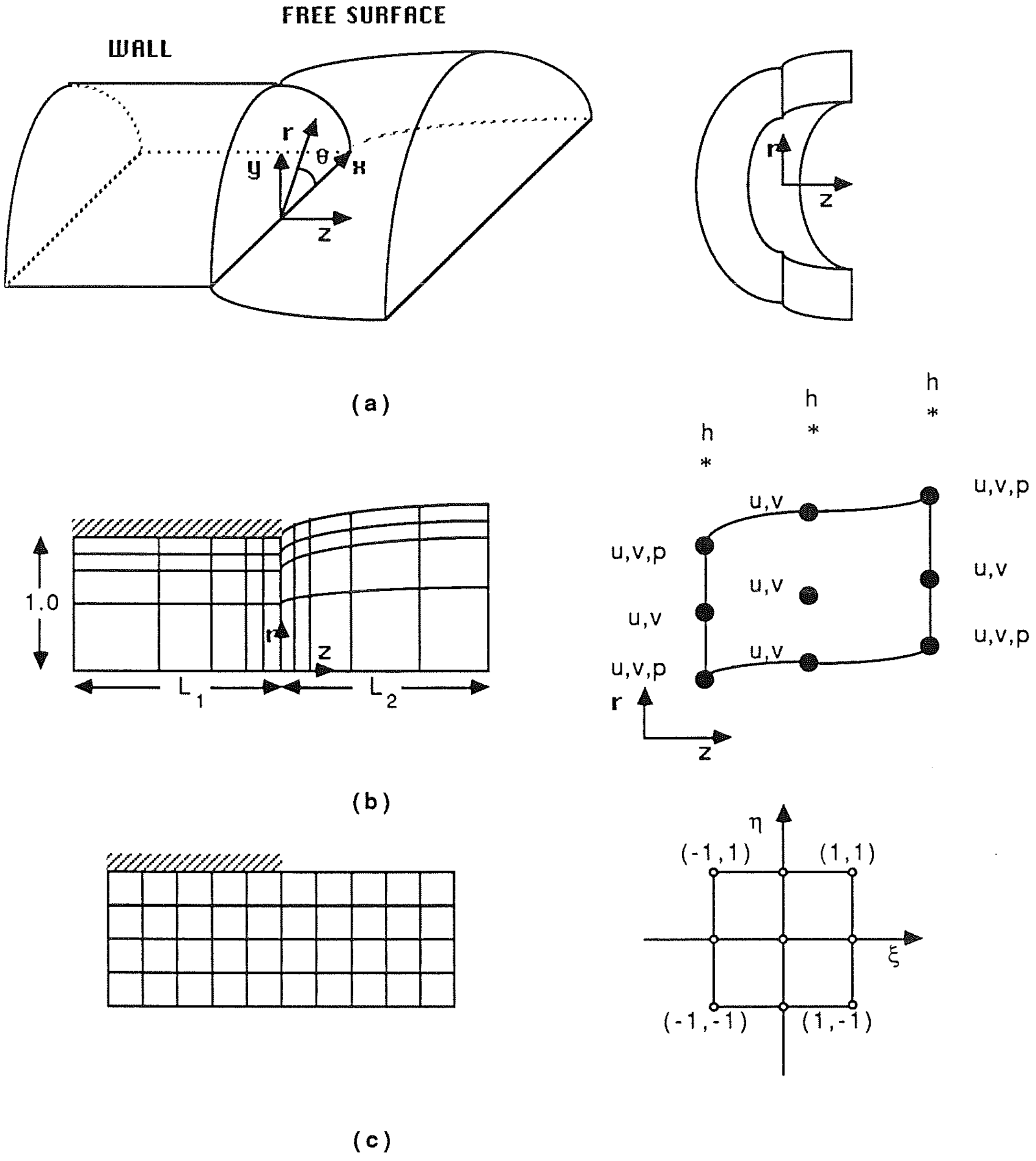

Figure 2.3: Round jet:
(a) Physical domain and 3-D elements.
(b) Projection of physical domain and 2-D elements.
(c) Computational domain and standard 2x2 elements.

curvilinear free-surface flow into a rectilinear domain as shown in Figure 2.3c. This domain is called the *computational domain.* The governing equations are in effect solved on the computational domain, the mapping onto the projected physical domain being part of the problem. The local mappings make the free surface a straight line ($\eta = 1$) on the computational domain and the formulae of the unit tangent and normal vectors become [89]:

$$\mathbf{n} \;=\; \frac{-h_z\,\mathbf{e_z} + \mathbf{e_r}}{\sqrt{1+h_z^2}} = \frac{-h_\xi\,\mathbf{e_z} + z_\xi\,\mathbf{e_r}}{\sqrt{z_\xi^2 + h_\xi^2}}\,, \tag{2.18}$$

$$\mathbf{t} \;=\; \frac{\mathbf{e_z} + h_z\,\mathbf{e_r}}{\sqrt{1+h_z^2}} = \frac{z_\xi\,\mathbf{e_z} + h_\xi\,\mathbf{e_r}}{\sqrt{z_\xi^2 + h_\xi^2}}\,. \tag{2.19}$$

The derivatives with respect to ξ are evaluated directly from equations (2.16) and (2.17).

A typical element with its nodal unknowns is shown in Figure 2.3b. Nine-node biquadratic basis functions are used for the velocity components and four-node bilinear functions are used for the pressure. When an element is under the free surface, three extra notes (denoted by asterisks) are employed to account for the free-surface location unknowns. Thus there are 25 or 22 unknowns (or *degrees of freedom*) in one element depending on whether or not the element is under the free surface. If N_u is the number of the velocity nodes, N_p is the number of the pressure nodes and N_h is the number of the free-surface nodes, then the total number of unknowns is $2N_u + N_p + N_h$ and the total number of nodes is $N_u + N_h$.

The unknowns u, v, p, h are expanded in terms of biquadratic ,Φ^i, bilinear, Ψ^i, and quadratic, M^i, basis functions:

$$u \;=\; \sum_{i=1}^{N_u} u_i\,\Phi^i(\xi,\eta)\,, \tag{2.20}$$

$$v \;=\; \sum_{i=1}^{N_u} v_i\,\Phi^i(\xi,\eta)\,, \tag{2.21}$$

$$p = \sum_{i=1}^{N_p} p_i \, \Psi^i(\xi,\eta)\,, \tag{2.22}$$

$$h = \sum_{i=1}^{N_h} h_i \, M^i(\xi)\,. \tag{2.23}$$

The Galerkin residuals are obtained weighting the continuity equation with Ψ^i, the momentum equation with Φ^i, and the kinematic equation with M^i:

$$R_C^i = \int_V \nabla \cdot \mathbf{u} \, \Psi^i \, dV = 0\,, \qquad i = 1,2,\cdots,N_p \tag{2.24}$$

$$\mathbf{R}_{\mathbf{M}}^{\mathbf{i}} = \int_V [\, \nabla \cdot \mathbf{T} - Re \, \mathbf{u}\cdot\nabla\mathbf{u} \, + \, St \, \mathbf{e_z}] \, \Phi^i \, dV = 0\,, \; i = 1,2,\cdots,N_u \tag{2.25}$$

$$R_K^i = \int_{S_3} \mathbf{n} \cdot \mathbf{u} \, M^i \, dS = 0\,, \qquad i = 1,2,\cdots,N_h \tag{2.26}$$

where R_C^i, $\mathbf{R}_{\mathbf{M}}^{\mathbf{i}}$ and R_K^i are the continuity, momentum, and kinematic residuals respectively, S_3 stands for the free surface, $dV = r \, d\theta dr dz$, and $dS = \sqrt{1 + h_z^2} \, h \, d\theta dz$.

In cylindrical coordinates and after integrating over θ, equation (2.24) becomes

$$R_C^i = \int_{-L_1}^{L_2} \int_0^{h(z)} \left(\frac{\partial u}{\partial z} + \frac{\partial v}{\partial r} + \frac{v}{r} \right) \Psi^i \, r \, drdz = 0\,, \qquad 1,2,\cdots,N_p\,, \tag{2.27}$$

since the integrand is independent of θ.

The momentum residuals are broken into two integrals by applying the divergence theorem:

$$\mathbf{R}_{\mathbf{M}}^{\mathbf{i}} = -\int_V [\mathbf{T}\cdot\nabla\Phi^i + Re\mathbf{u}\cdot\nabla\mathbf{u}\Phi^i - St\Phi^i\mathbf{e_z}]dV + \int_S \mathbf{n}\cdot\mathbf{T}\Phi^i dS, \quad i = 1,2,\cdots,N_u. \tag{2.28}$$

Here, S is the boundary of the domain V and $\mathbf{n}$ is the outward pointing normal unit vector. The boundary S consists of the five following parts:

1. The inflow plane S_1 with $\mathbf{n} = -\mathbf{e_z}$ and $dS = r \, d\theta dr$,

2. The solid wall S_2 with $\mathbf{n} = \mathbf{e_r}$ and $dS = h_o \, d\theta dz$,

3. The free surface S_3 with $\mathbf{n} = \frac{-h_z\,\mathbf{e_z} + \mathbf{e_r}}{\sqrt{1+h_z^2}}$, and $dS = \sqrt{1+h_z^2}\, h\, d\theta dz$,

4. The outflow plane S_4 with $\mathbf{n} = \mathbf{e_z}$ and $dS = r\, d\theta dr$, and

5. The midplane S_5 with $\mathbf{n} = \pm\mathbf{e}_\theta$ and $dS = drdz$.

Thus upon substitution, the following equation is derived

$$
\begin{aligned}
\mathbf{R}_{\mathbf{M}}^{\mathbf{i}} \;=\; & -\int_V [\mathbf{T}\cdot\nabla\Phi^i + Re\,\mathbf{u}\cdot\nabla\mathbf{u}\,\Phi^i - St\,\Phi^i\,\mathbf{e_z}]\, dV - \int_{S_1} \mathbf{e_z}\cdot\mathbf{T}\,\Phi^i\, r\, d\theta dr \\
& + \int_{S_2} \mathbf{e_r}\cdot\mathbf{T}\,\Phi^i\, R\, d\theta dz + \int_{S_3} (-h_z\mathbf{e_z} + \mathbf{e_r})\cdot\mathbf{T}\,\Phi^i\, h\, d\theta dz \\
& + \int_{S_4} \mathbf{e_z}\cdot\mathbf{T}\,\Phi^i\, r\, d\theta dr + \int_{S_5} (-\mathbf{e}_\theta\cdot\mathbf{T}|_{\theta=0} + \mathbf{e}_\theta\cdot\mathbf{T}|_{\theta=\pi})\,\Phi^i\, drdz, \\
& \qquad\qquad\qquad\qquad\qquad\qquad\qquad i = 1, 2, \cdots, N_u. \qquad (2.29)
\end{aligned}
$$

The surface integrals on the inflow plane S_1 and on the solid wall S_2 are set to zero because the corresponding equations are to be replaced by the essential[8] boundary conditions. The two terms in the last integral of equation (2.29) are combined because $\mathbf{e}_\theta|_{\theta=0} = -\mathbf{e}_\theta|_{\theta=\pi}$. Axisymmetry implies for the stress tensor that

$$
\mathbf{T} = \mathbf{e_r}\mathbf{e_r}\, T^{rr} + \mathbf{e_r}\mathbf{e_z}\, T^{rz} + \mathbf{e_z}\mathbf{e_r}\, T^{zr} + \mathbf{e_z}\mathbf{e_z}\, T^{zz} + \mathbf{e}_\theta\mathbf{e}_\theta\, T^{\theta\theta}. \qquad (2.30)
$$

All the other components of the stress tensor are zero[9]. On the free surface, S_3, the tangential stress component is zero, so that

$$
\mathbf{n}\cdot\mathbf{T} \;=\; \mathbf{n}\frac{2H}{Ca} = \frac{\mathbf{n}}{Ca}\left[\frac{h_{zz}}{[1+h_z^2]^{3/2}} - \frac{1}{h\sqrt{1+h_z^2}}\right]. \qquad (2.31)
$$

---

[8] 'Essential condition' is an alternative term for the Dirichlet condition.

[9] The superscripts in equation (2.30) denote the directions of the stress tensor components.

Substituting (2.30) and (2.31) into (2.29) gives

$$\begin{aligned}\mathbf{R}^{\mathbf{i}}_{\mathbf{M}} = & -\int_{-L_1}^{L_2}\int_0^h\int_0^\pi \mathbf{e_z}\left[T^{zz}\frac{\partial\Phi^i}{\partial z}+T^{zr}\frac{\partial\Phi^i}{\partial r}+Re\,\Phi^i\left(u\frac{\partial u}{\partial z}+v\frac{\partial u}{\partial r}\right)-St\,\Phi^i\right] r\,d\theta drdz \\ & -\int_{-L_1}^{L_2}\int_0^h\int_0^\pi \mathbf{e_r}\left[T^{zr}\frac{\partial\Phi^i}{\partial z}+T^{rr}\frac{\partial\Phi^i}{\partial r}+Re\,\Phi^i\left(u\frac{\partial v}{\partial z}+v\frac{\partial v}{\partial r}\right)\right] r\,d\theta drdz \\ & +\frac{1}{Ca}\int_0^{L_2}\int_0^\pi (h_z\mathbf{e_z}+\mathbf{e_r})\left(\frac{h_{zz}}{[1+h_z^2]^{3/2}}-\frac{1}{h\sqrt{1+h_z^2}}\right)\Phi^i\,h\,d\theta dz \\ & +\int_0^{h_f}\int_0^\pi (T^{zr}\mathbf{e_r}+T^{zz}\mathbf{e_z})\,\Phi^i\,r\,d\theta dr - 2\int_{-L_1}^{L_2}\int_0^h \mathbf{e}_\theta\,T^{\theta\theta}|_{\theta=0}\,\Phi^i\,drdz, \\ & \qquad i=1,2,\cdots,N_u. \end{aligned} \tag{2.32}$$

In the outflow-plane surface integral, the radial component is set to zero because of the essential condition for v. The normal stress T^{zz} needed for the axial residual component is given by equation (2.15). The momentum residuals are expressed in a fixed cartesian coordinate system (**i**, **j**, **k**), shown in Figure 2.3c, by invoking the identities:

$$\mathbf{e_r} = \mathbf{j}\sin\theta + \mathbf{i}\cos\theta\,,$$

$$\mathbf{e_z} = \mathbf{k}\,,$$

and

$$\mathbf{e}_\theta|_{\theta=0} = -\mathbf{e}_\theta|_{\theta=\pi} = -\mathbf{j}.$$

After an integration over θ, the **i**-component is identically zero. After combining the mid-plane boundary term with the volume integral in the **j**-direction, the **k**- and **j**- components become:

$$\begin{aligned}R^i_u = & -\int_{-L_1}^{L_2}\int_0^h \left[T^{zz}\frac{\partial\Phi^i}{\partial z}+T^{zr}\frac{\partial\Phi^i}{\partial r}+Re\,\Phi^i\left(u\frac{\partial u}{\partial z}+v\frac{\partial u}{\partial r}\right)-St\,\Phi^i\right] r\,drdz \\ & -\frac{1}{Ca}\int_0^{L_2}\left(\frac{hh_zh_{zz}}{[1+h_z^2]^{3/2}}-\frac{h_z}{\sqrt{1+h_z^2}}\right)\Phi^i\,dz \\ & -\frac{1}{Ca}\int_0^{h_f}\frac{r}{h_f}\,\Phi^i\,dr\,, \qquad i=1,2,\cdots,N_u, \end{aligned} \tag{2.33}$$

and,

$$R_v^i \;=\; -\int_{-L_1}^{L_2}\int_0^h \left[T^{zr}\frac{\partial\Phi^i}{\partial z} + T^{rr}\frac{\partial\Phi^i}{\partial r} + Re\,\Phi^i\left(u\frac{\partial v}{\partial z} + v\frac{\partial v}{\partial r}\right) + \frac{T^{\theta\theta}}{r}\,\Phi^i\right] r\,drdz$$

$$+\frac{1}{Ca}\int_0^{L_2}\left(\frac{hh_{zz}}{[1+h_z^2]^{3/2}} - \frac{1}{\sqrt{1+h_z^2}}\right)\Phi^i\,dz, \qquad i = 1,2,\cdots,N_u. \tag{2.34}$$

The kinematic residuals are obtained from (2.26) by substituting for $\mathbf{n}$ and dS, and integrating over θ:

$$R_K^i = \int_0^{L_2}(-h_z u + v)\,h\,M^i\,dz = 0\,, \qquad i = 1,2,\cdots,N_h. \tag{2.35}$$

Equations (2.27), (2.33), (2.34), and (2.35) are the projections of the initial equations on the two-dimensional domain of Figure 2.3b. All the quantities in the above equations must be further expressed in the (ξ,η) domain. The unknowns u, v, p, h have already been expanded in terms of ξ and η. The velocity derivatives and the stresses are easily calculated using the chain rule. The following identity is also used

$$drdz \;=\; |J|\,d\xi d\eta\,, \tag{2.36}$$

where

$$|J| \;=\; \frac{\partial z}{\partial \xi}\frac{\partial r}{\partial \eta} - \frac{\partial r}{\partial \xi}\frac{\partial z}{\partial \eta}\,, \tag{2.37}$$

is the Jacobian of the mapping [141,170]. After integrating the free surface integrals by parts, the final forms of the residuals are obtained on the computational domain:

$$R_C^i \;=\; -\int_{-L_1}^{L_2}\int_0^h \left[\left(\frac{\partial u}{\partial z} + \frac{\partial v}{\partial r}\right) r^\alpha + \alpha v\right]\Psi^i\,|J|\,d\xi d\eta\,, \qquad i = 1,2,\cdots,N_p, \tag{2.38}$$

$$R_u^i \;=\; -\int_{-L_1}^{L_2}\int_0^h \left[T^{zz}\frac{\partial\Phi^i}{\partial z} + T^{zr}\frac{\partial\Phi^i}{\partial r} + Re\,\Phi^i\left(u\frac{\partial u}{\partial z} + v\frac{\partial u}{\partial r}\right) - St\,\Phi^i\right] r^\alpha\,|J|\,d\xi d\eta$$

$$-\frac{1}{Ca}\int_0^{L_2}\frac{h^\alpha z_\xi}{\sqrt{z_\xi^2 + h_\xi^2}}\frac{\partial\Phi^i}{\partial\xi}\,d\xi + \frac{1}{Ca}\,\frac{h^\alpha z_\xi}{\sqrt{z_\xi^2 + h_\xi^2}}\Big|_{\eta=1,z=L_2}$$

$$-\frac{\alpha}{Ca}\int_0^{h_f}\frac{r}{h_f}\frac{\partial r}{\partial \eta}\,\Phi^i\,d\eta\,, \qquad i=1,2,\cdots,N_u, \tag{2.39}$$

$$\begin{aligned} R_v^i \;=\; & -\int_{-L_1}^{L_2}\int_0^h\left[T^{zr}\frac{\partial\Phi^i}{\partial z}+T^{rr}\frac{\partial\Phi^i}{\partial r}+Re\,\Phi^i\left(u\frac{\partial v}{\partial z}+v\frac{\partial v}{\partial r}\right)+\alpha\,\frac{T^{\theta\theta}}{r}\,\Phi^i\right]r^\alpha\,|J|\,d\xi d\eta \\ & -\frac{1}{Ca}\int_0^{L_2}\left[\alpha\,\Phi^i\sqrt{z_\xi^2+h_\xi^2}+\frac{h^\alpha h_\xi}{\sqrt{z_\xi^2+h_\xi^2}}\,\frac{\partial\Phi^i}{\partial\xi}\right]d\xi\,, \qquad i=1,2,\cdots,N_u, \end{aligned} \tag{2.40}$$

$$R_K^i \;=\; \int_0^{L_2}(-u\,h_\xi+v\,z_\xi)\,M^i\,h^\alpha\,d\xi\,, \qquad i=1,2,\cdots,N_h. \tag{2.41}$$

Here, α is a constant utilized to include the planar case in the final equations. It is equal to 1 for the round jet. For the planar case, α is zero and r is replaced by y. The limits of integration are kept to denote that the integration is carried out over the elements in the specified range[10]. Because of the essential conditions $u=v=0$ at the first, and $v=0$ at the last free-surface node only one of the boundary terms, that result from the integration by parts of the capillary stress along the free surface, survives in the **k**-momentum residual. This term is not zero only at the last free-surface node ($\eta=1, z=L_2$).

The nonlinear system of equations (2.38), (2.39), (2.40) and (2.41) can be written as

$$\mathbf{R}(\mathbf{x})=\mathbf{0}\,, \tag{2.42}$$

where $\mathbf{x}$ is the is the column vector of the nodal unknowns, and $\mathbf{R}$ is the column vector of the Galerkin weighted residuals. This system is solved by using the Newton iteration method:

$$\mathbf{J}(\mathbf{x}^k)\,[\mathbf{x}^{k+1}-\mathbf{x}^k] \;=\; -\mathbf{R}(\mathbf{x}^k)\,, \tag{2.43}$$

where $\mathbf{J}$ is the Jacobian matrix,

$$\mathbf{J}\equiv\frac{\partial\mathbf{R}}{\partial\mathbf{x}}\,, \tag{2.44}$$

---

[10] The integration is actually carried out from -1 to 1 for both ξ and η over each element.

and k is the iteration counter. The set of linear equations in (2.43) is repeatedly solved by a *frontal* technique[11] developed by Hood [75]. The tessellation is updated at every iteration with the newly found free-surface.

The above formulation is not restricted to a Newtonian fluid. Stresses are readily expressed in terms of the unknown velocities u, v, and pressure p by means of any constitutive equation for a non-Newtonian liquid.

2.4 Results and discussion

In this section we present results for both the planar and the round jets at Reynolds numbers ranging from 0 to 2,000, and capillary numbers varying from 10^5 to 10^{-5}. The results reported by Omodei are restricted to $Re \leq 500$ and $Ca > 0.2$ [113,114].

The upstream and downstream lengths of the domain, L_1 and L_2, were chosen to be sufficiently large to ensure the validity of the imposed boundary conditions. $L_1 = 4$ was found adequate for all Re and St, whereas L_2 had to be increased as Re and St increased. For zero St, $L_2 = 25$ was adequate for $Re \leq 20$, $L_2 = 100$ for $Re \leq 200$, and $L_2 = 300$ for $Re \leq 2{,}000$; for nonzero St, L_2 had to be increased further. It must be noted here that the value $L_2 = 2$ used by Dutta and Ryan in solving the creeping flow problem with finite differences was too small to give the correct free-surface profiles [39]. The finite element mesh was more refined in the neighborhood of the exit in order to capture the sudden changes in the flow field. The number of elements ranged from 150 to 222 and the number of unknowns varied from 1,541 to 2,273.

The solution at one set of Re, St, and Ca provided the initial estimate for the Newton iteration at higher Re or St, and lower Ca (*zero-order continuation*). The step in Ca was in general of the same order of magnitude as the new Ca. Convergence was achieved once the largest relative change in the unknowns was less than 10^{-4}, i.e., the criterion for

---

[11] For more information about frontal solvers, see also [83,160,18].

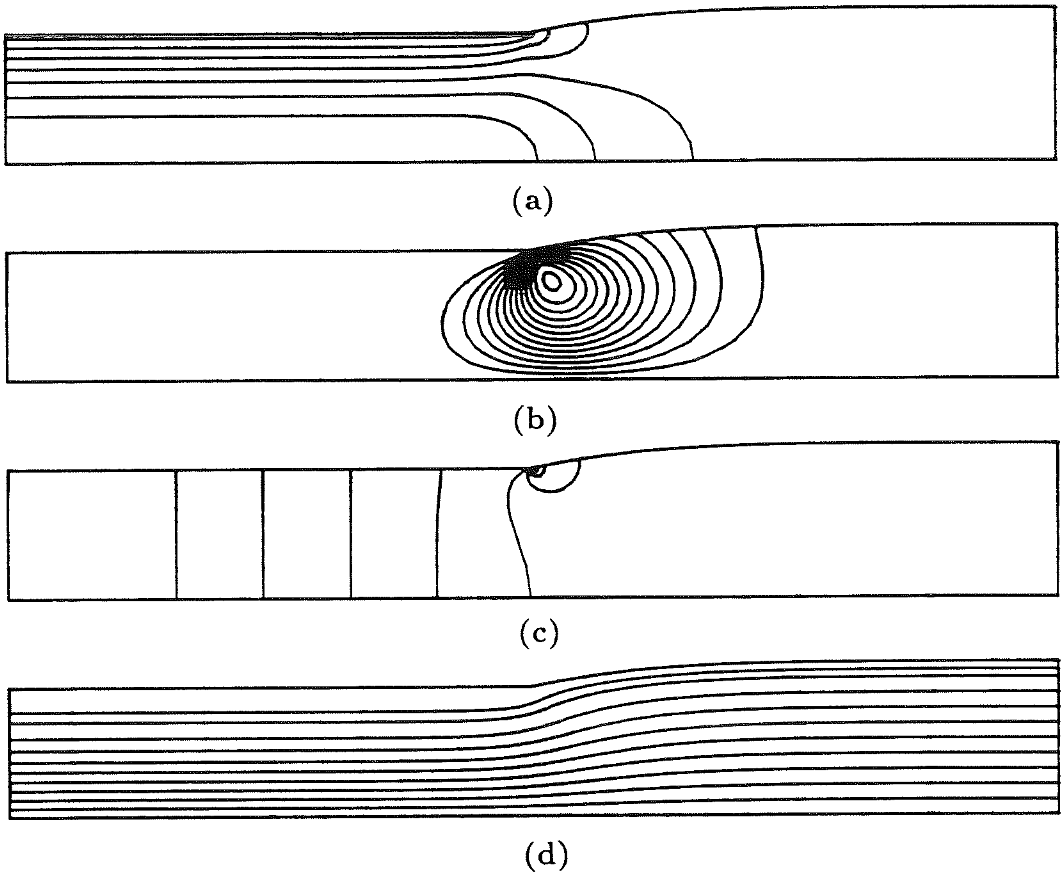

(a)

(b)

(c)

(d)

Figure 2.4: Solution of the planar die-swell problem: (a) z-velocity, (b) y-velocity, (c) pressure and (d) streamlines.

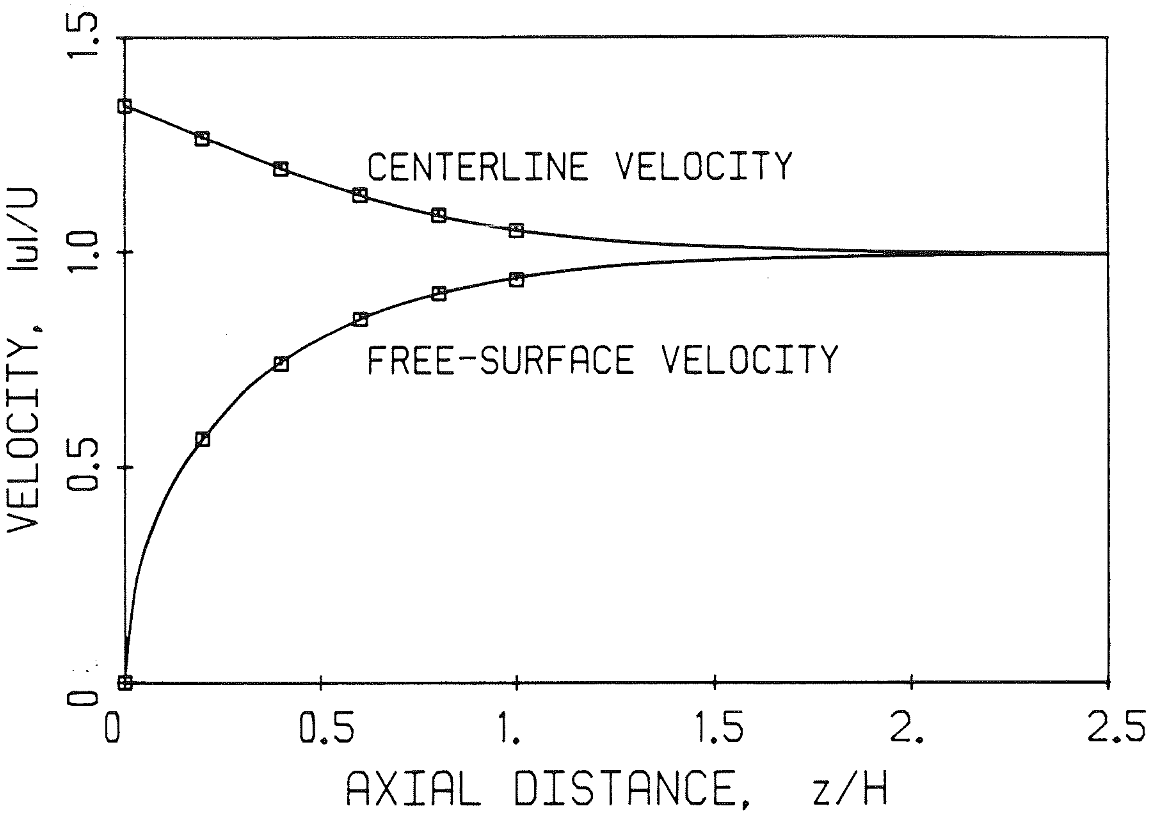

Figure 2.5: Centerline and free-surface velocities for the stick-slip problem.
□ : Analytic solution.
—— : Finite element solution at $Re=0$ and $Ca=10^{-5}$.

convergence was

$$\max_i |\frac{x_i^{k+1} - x_i^k}{x_i^{k+1}}| \leq 10^{-4}\,. \qquad (2.45)$$

The Newton iteration converged quadratically in 3 to 5 iterations. Only at very low Ca (less than 0.01) were more iterations (up to 8) necessary.

The solution of the planar die-swell problem is illustrated in Figure 2.4, where we plot the velocity and pressure contours and the streamlines.

To check the accuracy of the finite-element predictions, the centerline and free-surface velocities of the planar jet at $Re = 0$ and $Ca = 10^{-5}$ are compared with Richardson's analytic solution for the stick-slip problem [121,122]. As shown in Figure 2.5 the predictions agree with the analytic solution to within 0.1%. The finite element solution here was obtained as the limiting case of the general problem at $Re = 0$ and $Ca = 10^{-5}$, i.e., the location of the free surface was not fixed *a priori.* The expected planar interface in this limiting case was predicted to within 0.01%.

The computed surface profiles of a planar jet, without gravity and surface tension at several Re are shown in Figure 2.6. The surface-tension effects at Reynolds numbers 0, 9, 12.5, and 100 are shown in Figure 2.7. Unlike earlier analyses [113], no oscillations are observed as Ca decreases. The surface tension reduces either expansion or contraction of the jet; at very high surface tension ($Ca \rightarrow 0$), there is no swelling at all, as expected. At moderate Reynolds numbers, from 4 to 15, the surface profile is characterized by a necking. In this critical range, as surface tension increases, the die-swell first increases but then starts to decrease, as shown in Figure 2.7b. The results show that the inertia is the major controlling factor for the die-swell ratio at high Re where the surface-tension effect becomes insignificant. The free-surface profiles of the round jet without gravity and surface tension are shown in Figure 2.8 for various Re. The surface tension effects at Reynolds numbers 0, 8, 10, and 100 are shown in Figure 2.9. The critical Reynolds-

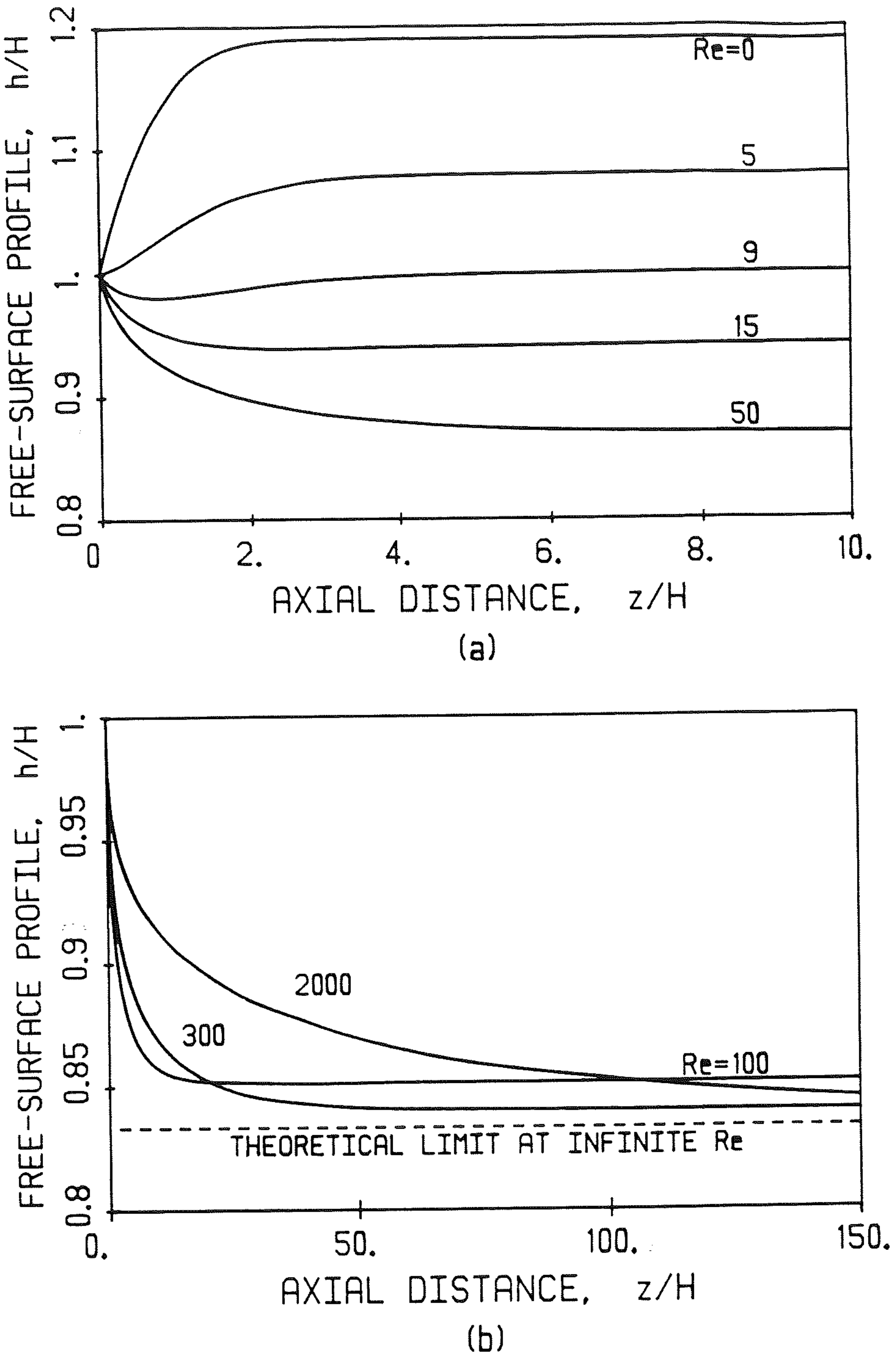

Figure 2.6: Predicted free-surface profiles of the planar jet at various $Re = \frac{\rho U H}{\mu}$ and zero surface tension.

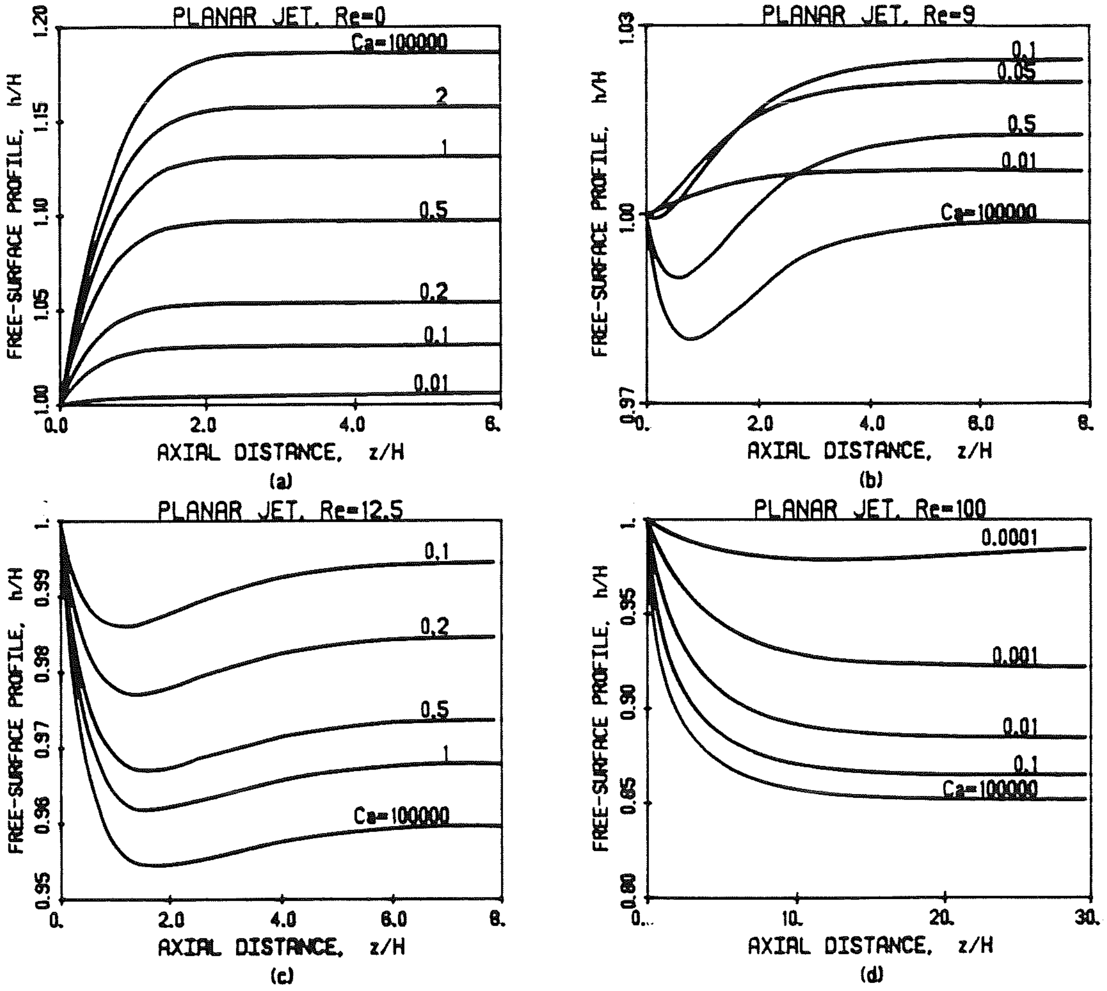

Figure 2.7: Predicted free-surface profiles of the planar jet at various $Re = \frac{\rho U H}{\mu}$ and $Ca = \frac{\mu U}{\sigma}$.

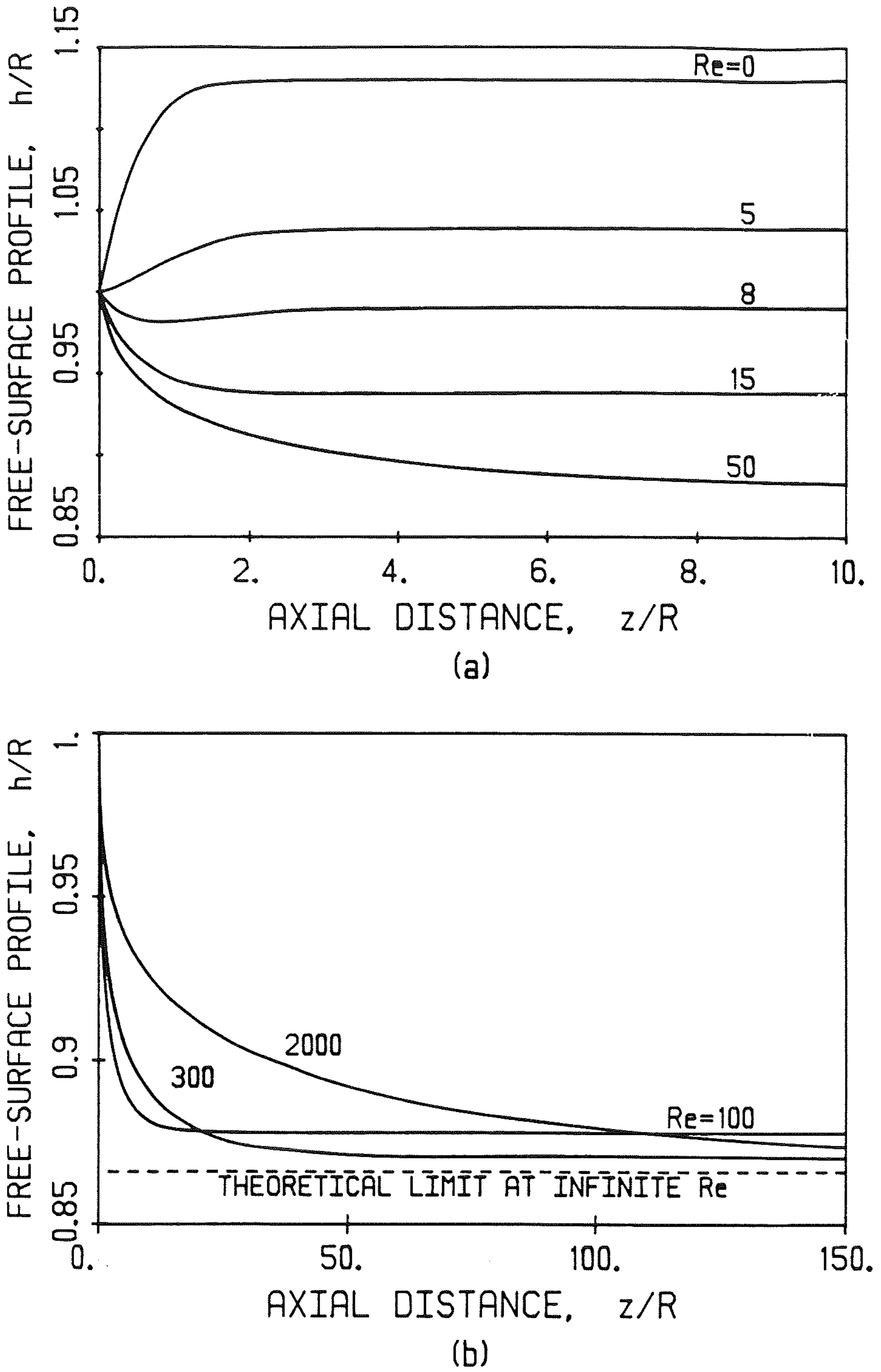

Figure 2.8: Predicted free-surface profiles of the round jet at various $Re=\frac{\rho U R}{\mu}$ and zero surface tension.

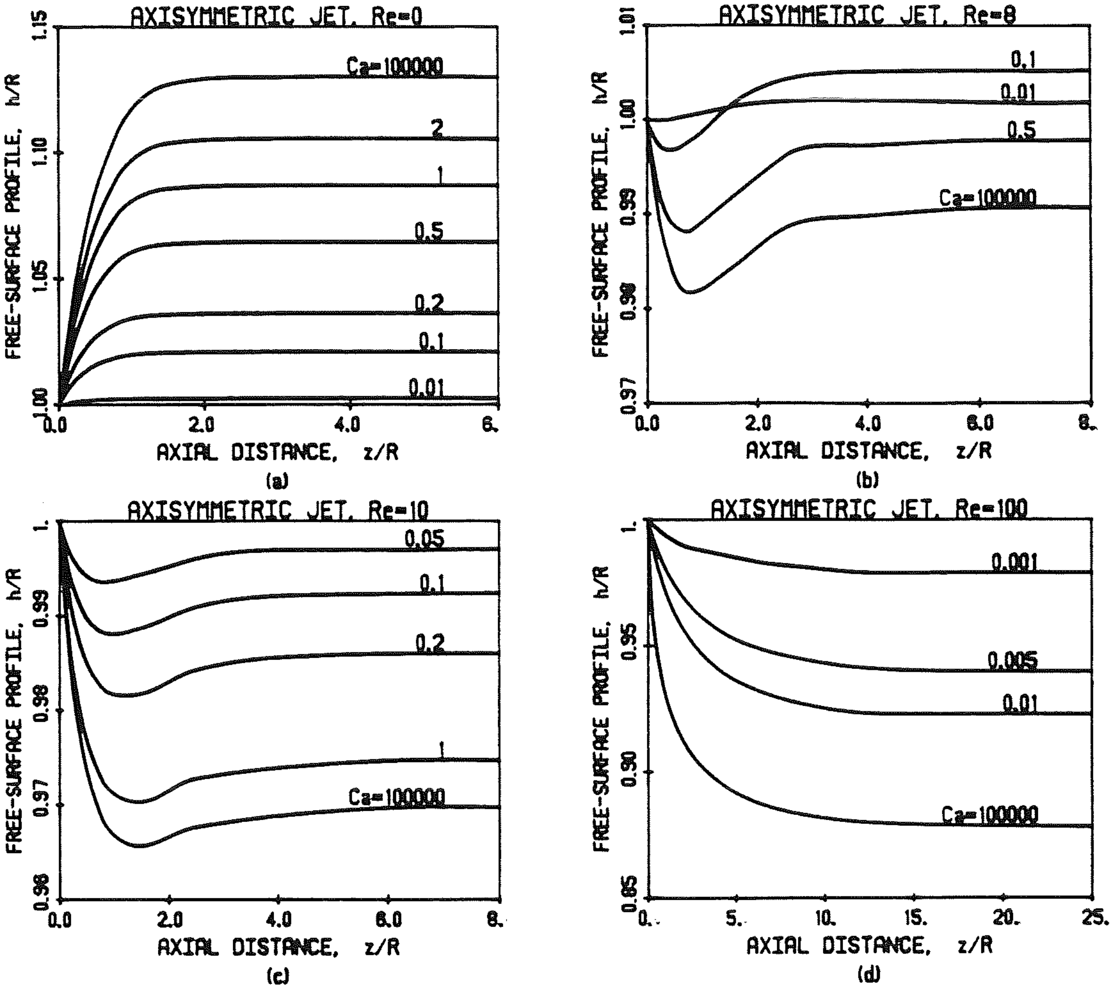

Figure 2.9: Predicted free-surface profiles of the round jet at various $Re = \frac{\rho U R}{\mu}$ and $Ca = \frac{\mu U}{\sigma}$.

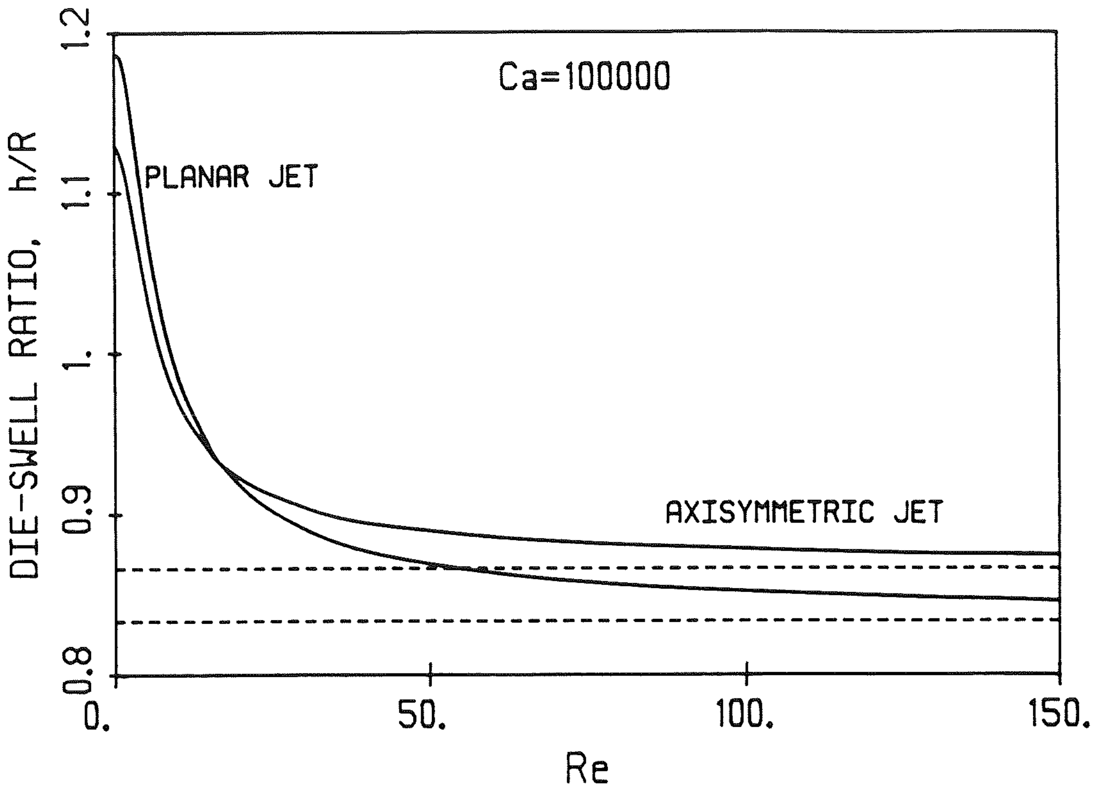

Figure 2.10: Predicted die-swell ratio vs the Reynolds number at zero surface tension, for the planar and the round jets.
- - - -: asymptotic values at infinite Reynolds number.

number range for necking is from 5 to 15. The results for $St = 0$ and $Ca > 0.2$ are identical to those of Omodei [113,114]. But unlike his results, no oscillations are observed at lower capillary numbers. We have obtained results at very low values of Ca close to zero ($Ca < 10^{-5}$).

As illustrated in Figure 2.10, the axisymmetric jet swells less than its planar counterpart at low Reynolds numbers. At high Reynolds numbers the opposite is observed. For the planar jet, the die-swell ratio is 1.186 for $Re = 0$, 1 for $Re \approx 9$, and 0.835 for $Re = 2{,}000$ approaching the theoretical limit 0.8333 at infinite Re[12] [147]; for the axisymmetric jet

---

[12] The limits of the die-swell ratio at infinite Re for Newtonian fluids are obtained in section 2.6

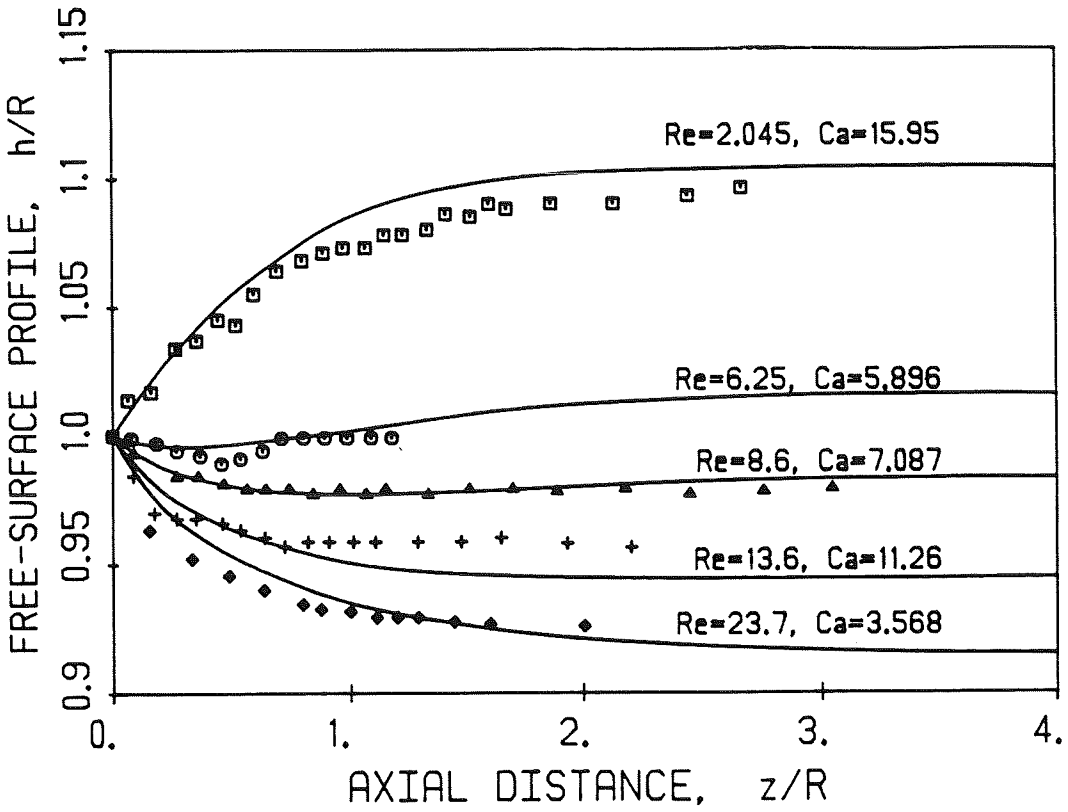

Figure 2.11: Predicted free-surface profiles of the round jet without gravity. Comparison with data from Gear *et al.* (1982).

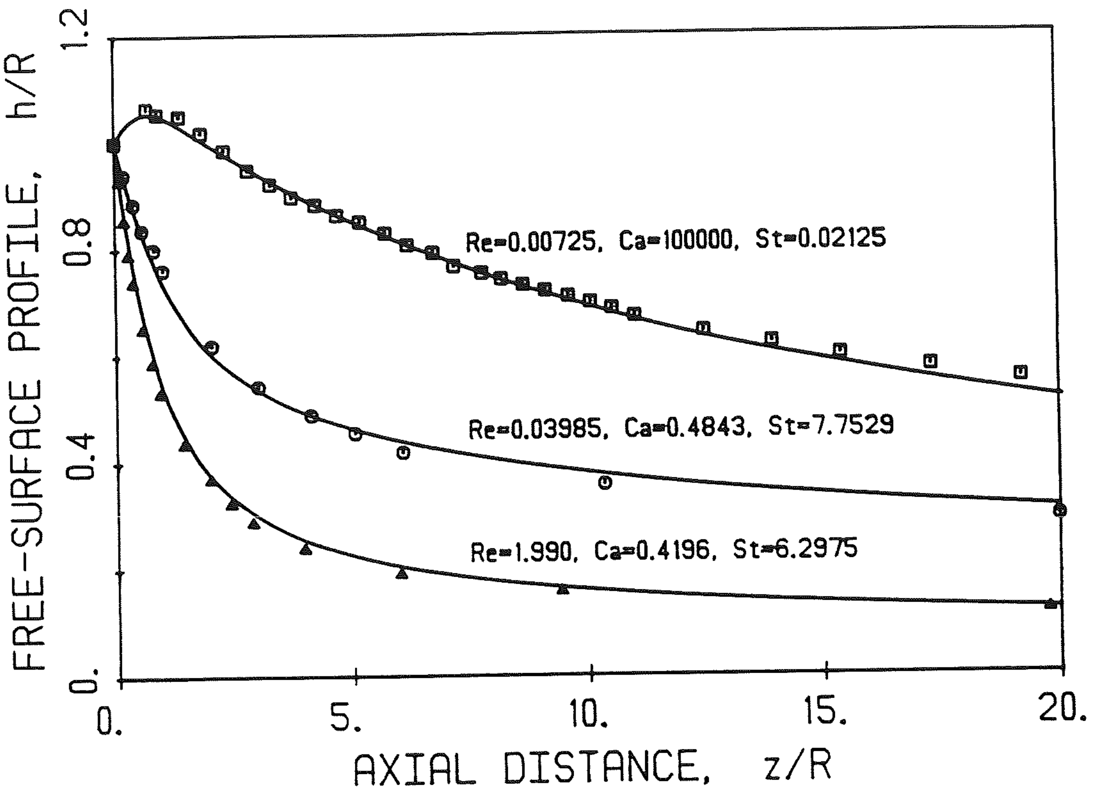

Figure 2.12: Predicted free-surface profiles of the round jet with gravity. Comparison with data from Trang and Yeow (1986; top curve) and Adachi and Yoshioka (1984).

it is 1.130 for $Re = 0$, 1 for $Re \approx 7$, and 0.867 for $Re = 2{,}000$ approaching the theoretical limit 0.8660 for infinite Re [65].

2.4.1 Comparisons with experimental data

The finite element calculations were tested against the data of Gear *et al.* [49] at several Reynolds and capillary numbers. The computed and the experimental final diameters agree to within 1% (Figure 2.11). As noted by Gear *et al.*, the discrepancies in shapes are probably due to factors not taken into account (variation of the surface tension along the jet, rounding of the exit nozzle) and/or experimental errors [49].

An additional feature of this work is the inclusion of the gravity effect. No difficulties

---

as special cases of the Herschel-Bulkley fluid.

were encountered in solving the gravity-drawn jet on a finite two-dimensional domain. The boundary condition $v=0$ at the outflow plane was adequate for nonzero St, inasmuch as the outflow plane was taken far from the domain of interest. In Figure 2.12 we compare our predictions with data taken from Trang and Yeow [151] and Adachi and Yoshioka [1]. Predictions and data agree to within less than 3%.

2.5 Concluding remarks

The full-Newton iteration method was used to solve the planar and the round Newtonian jets. The method is based on Galerkin finite elements, free-surface parameterization, and global Newton iteration. The Newton iteration converges rapidly in practically any range of dimensionless numbers examined: Reynolds numbers from zero to 2,000, capillary numbers from zero to infinity and Stokes numbers from zero to 10. These ranges of parameters are wider than those previously reported with Picard iteration schemes. The calculations agree with the analytic solution of the stick-slip problem at the limiting case of zero Reynolds and infinite surface tension, yield the asymptotic values at infinite Reynolds numbers, and compare well with experimental data at several Reynolds, capillary and Stokes numbers. The finite element formulation has been developed in terms of the stress and therefore any differential constitutive model can be accommodated. In fact, this work has been already extended to power-law and Bingham-plastic fluids (see Georgiou *et al.* [52,53] and [41]).

2.6 Asymptotic die-swell ratios for the Herschel-Bulkley fluid

We consider the Herschel-Bulkley model which describes a power-law fluid with yield stress [20]:

$$\mathbf{D} = \mathbf{0}\,, \qquad \text{for} \quad \frac{1}{2} II_{\mathbf{T}} \leq {\tau_y}^2$$

$$(2.46)$$

$$\tau = 2\,[\,K\,|2\,II_{\mathbf{D}}|^{(n-1)/2} + \frac{\tau_y}{\sqrt{2 II_{\mathbf{D}}}}\,]\,\mathbf{D}\,, \quad \text{for} \quad \frac{1}{2} II_{\mathbf{T}} \geq {\tau_y}^2$$

where τ is the viscous stress tensor, $\mathbf{D}$ and $II_{\mathbf{D}}$ are the rate of strain tensor and its second invariant, K is a 'viscosity' constant, n is the shear-thinning parameter, and τ_y is the yield stress.

The dimensionless velocity for 1-D or round fully developed flow is given by the general form

$$u = \frac{n}{(n+1)\,C}\,(C - T_y)^{(n+1)/n} \qquad \text{for} \qquad 0 \leq r \leq W,$$

$$(2.47)$$

$$u = \frac{n}{(n+1)\,C}\,[(C - T_y)^{(n+1)/n} - (Cr - T_y)^{(n+1)/n}] \quad \text{for} \quad W \leq r \leq 1,$$

where

$$T_y = \frac{\tau_y\, K\, U^n}{h_o^n} \tag{2.48}$$

is a dimensionless yield stress number,

$$W = \frac{T_y}{C} \tag{2.49}$$

is the distance of the yield surface from the centerline, and $C = \frac{\Delta P}{\Delta L}$ is the constant pressure gradient calculated by demanding that the mean dimensionless velocity in the die is equal to 1.

For the round tube, it turns out that C is the bigger root of

$$n\,(C - T_y)^{1/n}\,[(n+1)(2n+1)C^3 - (n+1)\,T_y\,C^2 - 2n\,T_y^2\,C - 2n^2\,T_y^3] - \\ (n+1)(2n+1)(3n+1)\,C^3 \;=\; 0\,. \qquad (2.50)$$

For Bingham-plastic flow (n=1) equation (2.50) becomes:

$$3\,C^4 \;-\; 4\,(3+T_y)\,C^3 \;+\; T_y^4 \;=\; 0\,; \qquad (2.51)$$

for power-law flow (τ_y=0) the solution is

$$C \;=\; \left(\frac{3n+1}{n}\right)^n . \qquad (2.52)$$

For the planar case C is in general the bigger root[13] of

$$n\,(C - T_y)^{1/n}\,[(n+1)^2\,C^2 - T_y\,C - n\,T_y^2] \;-\; (n+1)(2n+1)\,C^2 = 0\,. \qquad (2.53)$$

For Bingham-plastic flow the solution of equation (2.53) is

$$C \;=\; (2+\tau_y)\,\left[\frac{1}{2} \;+\; \cos\left\{\frac{1}{3}\;\cos^{-1}\left(1 - \frac{2\tau_y^3}{(2+\tau_y)^3}\right)\right\}\right]\;; \qquad (2.54)$$

for power-law flow the solution is

$$C \;=\; \left(\frac{2n+1}{n}\right)^n . \qquad (2.55)$$

Notice that at the limits of $T_y \to \infty$ or $n \to 0$ the inlet velocity profile is plug and the flow reduces to pure solid translation.

Asymptotic values of the die-swell ratio

The theoretical limits of the die-swell ratio at infinite Reynolds number, $h_{f\infty}$, are obtained by taking mass and momentum balances between the exit of the die, where the flow is assumed to be fully developed, and at a plane very far downstream where the flow

---

[13] In solving equations (2.50) and (2.53) with Newton-Raphson iteration, it is preferable to start with a very large estimate for C.

is taken as plug. The Newtonian limits are $\sqrt{3}/2$ for the round jet [Harmon, 1955] and 5/6 for the planar jet [Tillet, 1968].

By using the equation of continuity[14] for the round case, one obtains

$$u_{f\infty}\,(\pi h_{f\infty}^2) \;=\; \pi$$

or

$$u_{f\infty}\, h_{f\infty}^2 \;=\; 1\,, \tag{2.56}$$

where the subscript f_∞ denotes the outflow quantities at the asymptotic limit.

Now, from the conservation of momentum we may write

$$u_{f\infty}^2\,(\pi h_{f\infty}^2) \;=\; \int_0^1 u^2\, 2\, \pi\, r\, dr$$

or

$$u_{f\infty}^2\, h_{f\infty}^2 \;=\; 2 \int_0^1 u^2\, r\, dr\,. \tag{2.57}$$

By combining equations (2.56) and (2.57) we have for the asymptotic die-swell ratio

$$h_{f\infty} \;=\; \frac{1}{\sqrt{2\,\int_0^1 \; u^2\, r\, dr}}\,. \tag{2.58}$$

The analogous expression for the planar case is

$$h_{f\infty} \;=\; \frac{1}{\int_0^1 \; u^2\, dy}\,. \tag{2.59}$$

By substituting equation (2.47) into (2.58) and by integrating one obtains for the round Herschel-Bulkley jet

$$h_{f\infty} \;=\; \left[\frac{(2n+1)(3n+1)(3n+2)}{(3n+2)(n+1)^2C^2 + \,6n(n+1)^2T_yC + \,(9n+7)n^2T_y^2}\right]^{1/2} \frac{(n+1)\,C^2}{n\,(C-T_y)^{(n+1)/n}}\,. \tag{2.60}$$

For the round Bingham-plastic jet, equation (2.60) becomes

$$h_{f\infty} \;=\; \left[\frac{60}{5C^2 + 6\tau_yC + 4{\tau_y}^2}\right]^{1/2} \frac{C^2}{(C-\tau_y)^2}\;; \tag{2.61}$$

---

[14] Notice that we use the dimensionless forms of the equations.

for the power-law fluid we obtain

$$h_{f\infty} = \left(\frac{2n+1}{3n+1}\right)^{1/2} . \tag{2.62}$$

For the planar Herschel-Bulkley jet we substitute equation (2.47) into (2.59) and integrate. The asymptotic die-swell ratio is given by

$$h_{f\infty} = \frac{(2n+1)(3n+2)(n+1)^2\, C^3}{n^2\, (C-T_y)^{2(n+1)/n}\, [2(n+1)^2 C + n(4n+3)T_y]} \tag{2.63}$$

which reduces to

$$h_{f\infty} = \frac{60\, C^3}{(8C+7\tau_y)\,(C-\tau_y)^4} \tag{2.64}$$

for a Bingham-plastic planar jet and to

$$h_{f\infty} = \frac{3n+2}{2(2n+1)} \tag{2.65}$$

for a power-law jet. C is the constant pressure gradient obtained from equations (2.50) and (2.53). The above expressions yield the Newtonian limits for zero yield stress T_y and $n = 1$. As expected $h_{f\infty}$ goes to 1 as T_y goes to infinity or as n goes to zero. The limits for $n \rightarrow \infty$ are $\sqrt{2/3}$ for the round jet and $3/4$ for the planar jet.

The asymptotic values of the die-swell ratio at infinite Reynolds number provide a useful theoretical check to the finite element calculations at high Reynolds numbers [52,53,41].

CHAPTER III

SINGULAR FINITE ELEMENTS FOR STOKES FLOW: THE STICK-SLIP PROBLEM

> "Science may set limits to knowledge, but should not set limits to imagination."
>
> Bertrand Russell, *A History of Western Philosophy.*

In this chapter we develop *singular finite elements* for the solution of the stick-slip problem[1]. The solution of more complicated fluid mechanics problems, such as the die-swell and the sudden-expansion problems, is the subject of Chapter IV.

3.1 Introduction

The extrusion of a viscous jet from a die into an inviscid medium has been the focus of a plethora of theoretical, experimental and computational works due to its importance in polymer-processing operations and other industrial applications. Two characteristics of the die-swell problem are the expansion of the jet at low Reynolds numbers and the presence of a *stress singularity* at the die's exit. The problem is analytically intractable because of the nonlinear boundary conditions on the free surface. Numerical methods,

---

[1] The material of this chapter will appear in the *Int. j. numer. methods fluids* [55].

especially finite elements, have been used extensively to overcome this difficulty [108,127, 113,51].

The stress singularity, which is the focus of this work, arises from the abrupt change in the boundary condition at the exit of the die; its analysis is very important for a good comprehension of the die-swell phenomenon [2]. Generally speaking, singularities require special treatment in the numerical solution of singular problems. In finite element analysis, local refinement around the singular point is often employed in order to improve the accuracy. However, the accuracy and the rate of convergence are not in general satisfactory. Standard finite elements predict inaccurate stresses around the lip of the die; the stresses cannot be infinite at the singular point as the local asymptotic solution demands. Furthermore, the stiffness matrix becomes large as the mesh is refined and therefore the computational cost increases. Silliman and Scriven [135] applied a slip boundary condition in the upstream vicinity of the contact line to alleviate the stress singularity, since the no-slip boundary condition may be not valid in this region. They do not adequately resolve the singularity as the slip coefficient goes to zero, but they determine that a wide range of slip coefficients gives the same global behavior.

Incorporating the nature of the singularity, obtained by an asymptotic analysis, in the numerical solution proves to be a very effective way to improve the accuracy in the neighborhood of the singularity and speed up the rate of convergence. This idea has been successfully adopted in solving mainly fracture mechanics problems by a variety of methods: finite differences [163], finite elements [141,149], boundary and global elements [82,86], and spectral methods [91]. Two singular finite element approaches appear in the literature [86]:

1. *Singular basis function approach.* A set of supplementary basis functions chosen to reproduce the leading terms of the singularity solution is added to the standard

finite element solution expansion [141,106]. The singular functions are usually defined over several elements and can span the entire domain.

2. *Singular element approach.* Special elements are used in a small region around the singularity, while conventional elements are used in the rest of the domain. The various proposed elements can be classified in three categories:

    (a) *Embodied singularity elements* – Special elements are employed around the singular point, and the corresponding field shape functions embody the form of the singularity [149,150,5].

    (b) *Embedded singularity elements* – The leading terms of the singularity expansion are used to describe the full solution over a multi-node element surrounding the singular point and conventional elements are used elsewhere [134].

    (c) *Singular isoparametric elements* – Singular geometric transformations, defined on the elements surrounding the singular point, can provide finite element approximations with the desired singular behavior. The transformation becomes singular by properly changing the position of the midnodes, e.g., quarter-point elements [70,157,12].

There is a wealth of published work on singular finite element approaches due to their success in fracture mechanics. A review is given by Gallagher [48] in which the various approaches are critically examined and their relative advantages and disadvantages are discussed[2].

The main objective of the present work was to use the ideas developed in solid mechanics to solve singular problems in fluid mechanics, which are more complicated because, in addition to the velocity derivatives, the pressure –a primary unknown– is also singular.

---

[2] For other reviews of singular finite elements, see [6,7,42,141,153].

Another complication arises in free-surface problems in which we have curved boundaries and the form of the singularity is not exactly known.

We have chosen to solve the stick-slip problem in this chapter, using embodied singularity elements. The stick-slip problem is a limiting case of the die-swell problem, equivalent to the creeping Newtonian planar jet at infinite surface tension; no expansion occurs in this case and the free surface is flat. The boundary conditions suddenly change from no-slip along the wall to perfect-slip along the planar 'free' surface. For this particular case, the nonlinearity due to the free surface is eliminated, and the stick-slip problem is amenable to analytical solution. The planar problem was solved analytically by Richardson [121] using the Wiener-Hopf method, and by Sturges [142] using the eigenfunction method[3]. Trogdon and Joseph [152] solved the round stick-slip problem using both methods. Nevertheless, the local solution near the lip is just a special case of the general flow of a viscous fluid near a corner formed by a solid wall and a flat free surface; the local analysis is described by Michael [100] and Moffatt [104]. The velocity components vary as the square root of the radial distance from the singular point resulting in an inverse square root singularity for the stresses.

The singular elements developed here are similar to those introduced by Tracey [149] for the crack-tip problem, which also exhibits an inverse square root singularity for the stresses. Compared to the singular basis function approach or to the embedded singularity elements, the embodied singularity elements can be more easily included in a general finite element code and do not require knowledge of the angular dependence of the solution. Furthermore, they are compatible with the adjoining ordinary elements and can be extended to free surface flow problems, e.g., the die-swell problem.

Even though the singular isoparametric elements have been successful in dealing with

---

[3] Another solution of the plane stick-slip problem with the eigenfunction method was reported by Dutta [40].

crack problems in fracture mechanics [70,12] and are equivalent to the embodied singularity elements in some cases, the latter are more appropriate for fluid flow problems for the following reasons:

(a) Singular isoparametric elements can not handle singular primary variables. The proposed elements can be constructed with no node at the singular point for the singular primary variables.

(b) Singular isoparametric elements with curved sides are difficult to use without loss of accuracy. Consequently, they are not as effective as the embodied singularity elements for free-surface problems.

(c) In order to describe general power-type singularities with isoparametric elements, one has either to increase the number of nodes per element or to construct special field shape functions which in combination with the distortion of the physical element will yield the desired behavior. With the embodied singularity elements one has to modify only the field shape functions.

Singular elements can be applied to a general class of singular fluid mechanics problems, provided that the radial form of the local solution is known or can be obtained by an asymptotic analysis. Thus, singular finite elements can be used to solve nonzero Reynolds number or non-Newtonian flows. For a nonzero Reynolds number, the analysis is valid near the singularity, where the viscous effect is dominant, and the form of the local solution remains the same. Schultz and Gervasio [131] showed that the resulting local eigenproblem can be solved if the slip surface is flat or the curvature of the free surface is integrable. An asymptotic analysis to obtain the radial form of the singularity is also possible for various viscoelastic flows such as the stick-slip flow of an Oldroyd-B or a second-order fluid [81,4]. Apelian *et al* [4], in solving the stick-slip problem with a modified upper-convected Maxwell model, showed that the elastic contribution to the stress varies as $r^{-1/5}$. The developed elements can easily embody both the Newtonian and the elastic contributions by appropriately modifying the field shape functions [78]. Therefore, the method can be used in viscoelastic flows, provided that the encountered stresses are integrable.

As we will see in the following sections, the embodied singularity elements give results that are more accurate than those from conventional finite elements even if coarser meshes are used. The governing equations and the asymptotic solution are given in section 3.2. The finite element formulation, the construction of the field shape functions, and the numerical integration over the singular elements are discussed in section 3.3. Finally, the results are presented and discussed in section 3.4.

3.2 Governing Equations and Local Solution

The geometry, governing equations, and boundary conditions for the stick-slip problem are depicted in Figure 3.1. The flow is governed by Stokes' equation and continuity:

$$\nabla \cdot \mathbf{T} = 0 , \tag{3.1}$$

and

$$\nabla \cdot \mathbf{u} = 0 . \tag{3.2}$$

Here $\mathbf{T}$ is the stress tensor for a Newtonian liquid, measured in units of $\mu U/H$, μ is the viscosity, U is the mean velocity in the channel, and H is the channel half-width. The velocity $\mathbf{u}$ is scaled by U.

The form of the singularity is known as a special case of the steady plane flow near a corner of angle α formed by a rigid boundary and a flat free surface, as shown in Figure 3.1b. This general flow was analysed in plane polar coordinates (r,θ) by Michael [100] and Moffatt [104]. For the stick-slip case, $\alpha = \pi$ and there are two possible sets of

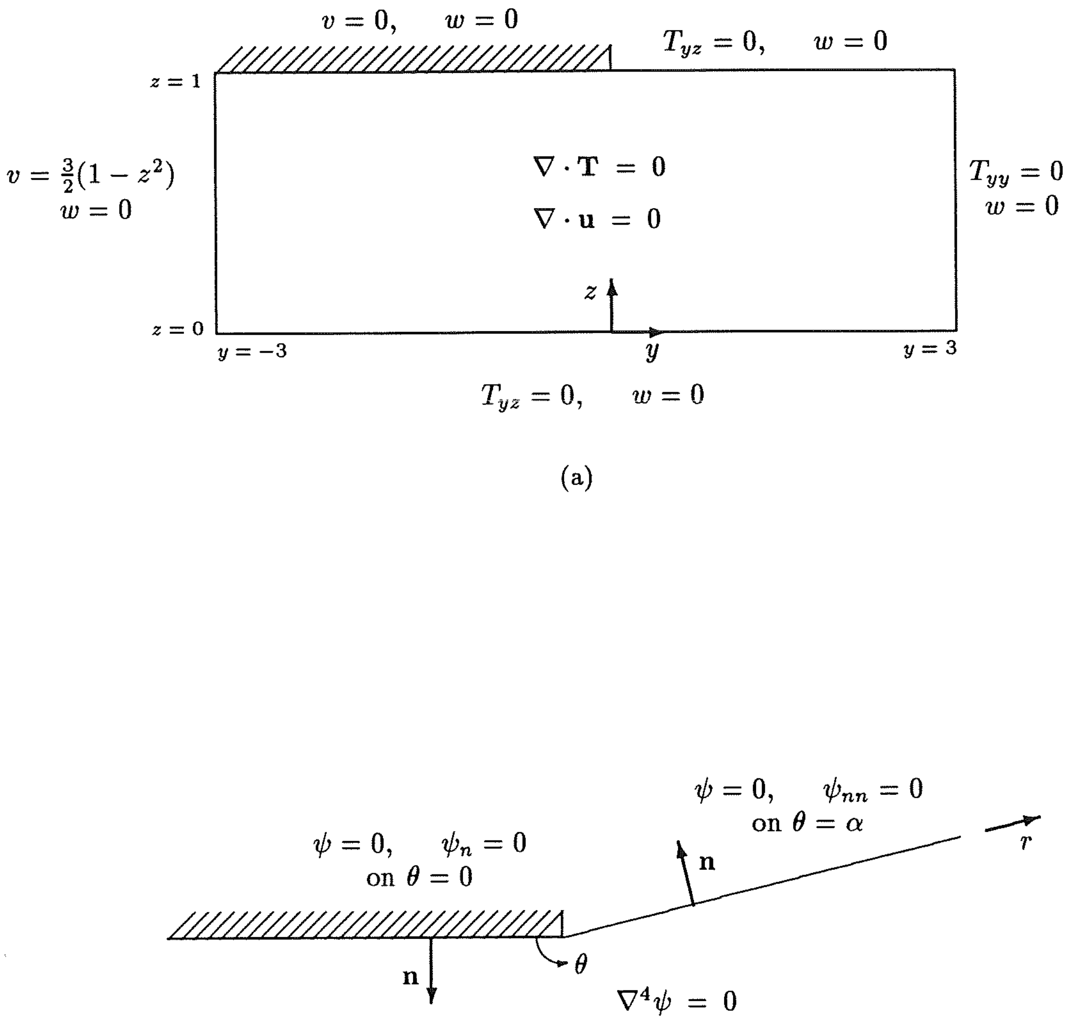

(a)

(b)

Figure 3.1: (a) The stick-slip problem.(b) Local analysis of the singularity.

solutions for the streamfunction ψ:

$$\psi = r^{\lambda+1}\,\alpha_\lambda\,[\,\cos(\lambda+1)\theta - \cos(\lambda-1)\theta\,]\,, \qquad \text{for } \lambda = \frac{1}{2}, \frac{3}{2}, \frac{5}{2}\cdots\,, \tag{3.3}$$

and

$$\psi = r^{\lambda+1}\,\beta_\lambda\,[\,(\lambda-1)\sin(\lambda+1)\theta - (\lambda+1)\sin(\lambda-1)\theta\,]\,, \text{ for } \lambda = 2,3,4,\cdots\,, \tag{3.4}$$

where α_λ and β_λ are arbitrary constants. The velocity components are proportional to r^λ. For $\theta=\pi$ the contributions of equation (3.4) become zero and the y component of velocity is given by

$$v = 2\alpha_{1/2}\,y^{1/2} - 2\alpha_{3/2}\,y^{3/2} + 2\alpha_{5/2}\,y^{5/2} + O(y^{7/2})\,. \tag{3.5}$$

From the analytical solution the first constant is $\alpha_{1/2} = \sqrt{3/2\pi} = 0.690988$. As indicated by Ingham and Kelmanson [82], the value $\alpha_{1/2} = 0.581$ given by Richardson [121] is wrong. Pressure and stresses are proportional to $r^{\lambda-1}$ and the inverse square root singularity is due to the first term of equation (3.3). The normal stress, T_N, on the slip surface is nonsingular and represents a very severe test for the numerical calculations. It turns out that only the pressure contributions from the integer-power solutions are nonzero and the normal stress on the slip surface is of the form

$$T_N = c - 24\beta_2\,y + 48\beta_3\,y^2 + 80\beta_4\,y^3 + O(y^4)\,, \tag{3.6}$$

where c is a constant.

3.3 Finite Element Formulation

The finite element method is well established ([14], [11]) and therefore we emphasize only the aspects related to singular finite elements: the construction of field shape functions and the numerical integration over the singular elements.

The physical domain of the stick-slip problem, shown in Figure 3.1, extends three channel half-widths upstream and downstream, a distance sufficiently large to ensure the validity of the imposed boundary conditions. Taking the outflow and inflow planes farther from the lip causes negligible changes in the calculated flow field.

3.3.1 Construction of the singular elements

In the finite element discretization, we use singular triangular-shaped elements in a small core around the singularity and ordinary rectangular elements in the rest of the domain, as illustrated in Figures 3.2 and 3.4. In the ordinary elements, the basis functions are biquadratic for the velocities and bilinear for the pressure. These elements are mapped on a 2x2 master element in (ξ, η) coordinates with biquadratic shape functions.

The construction of field shape functions, describing derivative singularities of the general form r^{n-1} $(0 < n < 1)$, has been the central subject of various works [78,110]. Hughes and Akin [78] presented an algorithm for generating shape functions from an arbitrary starting set of independent functions. The generated functions are capable of representing different singular behaviors within the element. For the present problem, a simple Lagrange interpolation in terms of $\sqrt{r}$ is adequate for deriving the field shape functions[4]. Figure 3.2 shows the rectangular master element with the (ξ,η) coordinates mapped approximately to the physical radial and circumferential coordinates respectively [149]. The mapping of the singular elements is discussed more in section 3.6. The field shape functions must embody the singularity and be compatible with the adjacent ordinary elements. Hence the shape functions for the velocities, Φ^i, are of the general form:

$$\Phi^i = N^i(\xi)\, P^i(\eta)\,, \tag{3.7}$$

---

[4] For a detailed discussion about the construction of basis functions and the various families of isoparametric elements, see [88].

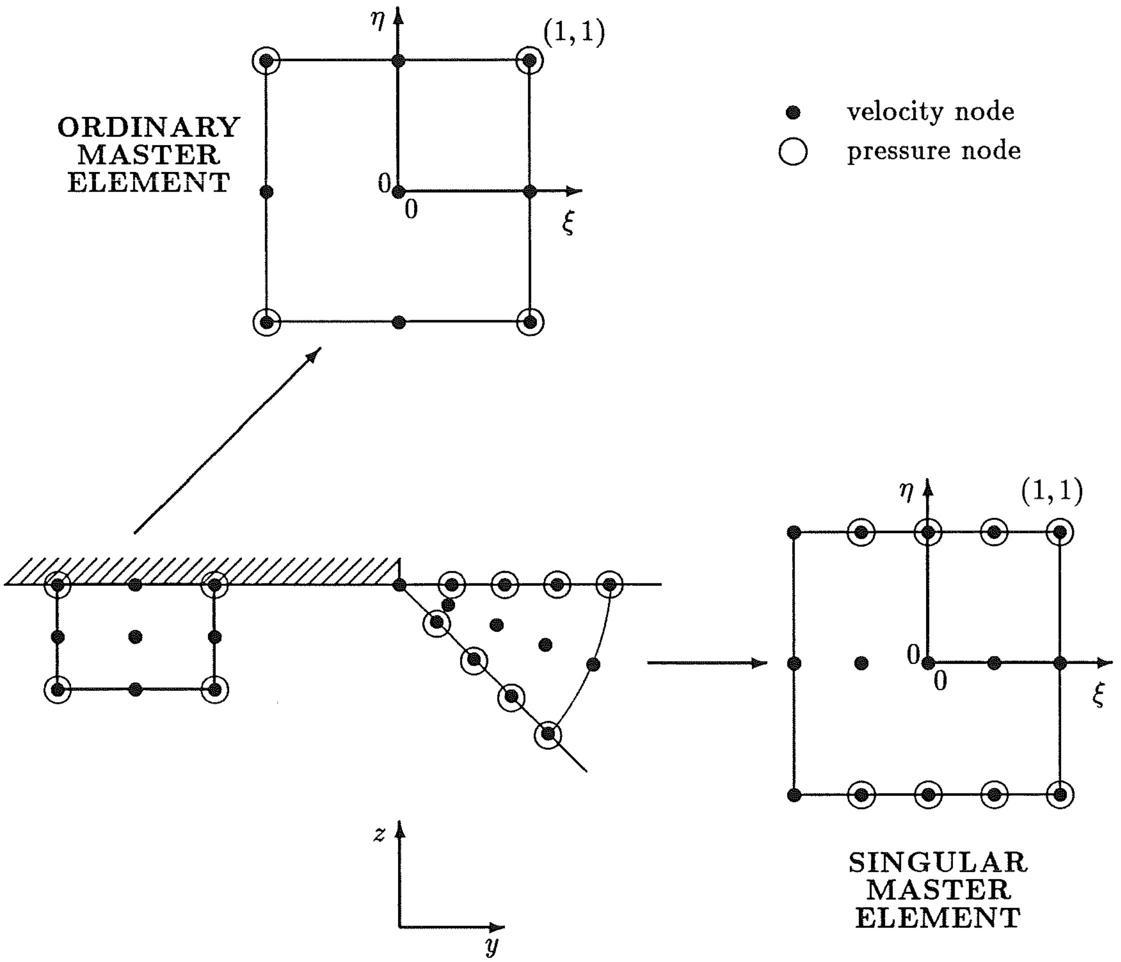

Figure 3.2: Ordinary and singular elements.

with P varying quadratically with η to maintain compatibility with the adjoining elements. Three velocity nodes are thus needed in the η direction. At $\xi = -1$, $P = 1$ and the three velocity nodes collapse to one node with only two degrees of freedom for the two velocity components. To include the first two contributions from both the equations (3.3) and (3.4), five velocity nodes are needed in the ξ direction and N^i takes the form:

$$N^i(\xi) \;=\; a + b\,(1+\xi)^{\frac{1}{2}} + c\,(1+\xi) + d\,(1+\xi)^{\frac{3}{2}} + e\,(1+\xi)^2\,. \tag{3.8}$$

Requiring that $N^i(\xi_j) = \delta_{ij}$ and using Lagrange interpolation with respect to the square root of the radial coordinate give:

$$N^1 \;=\; (\,1 - \sqrt{x}\,)(\,1 - \sqrt{\tfrac{4}{3}x}\,)(\,1 - \sqrt{2\,x}\,)(\,1 - \sqrt{4\,x}\,)$$

$$N^2 \;=\; \frac{4\sqrt{6}}{(\,\sqrt{2} - 1\,)(\,\sqrt{3} - 1\,)}\,\sqrt{x}\,(\,1 - \sqrt{x}\,)(\,1 - \sqrt{\tfrac{4}{3}x}\,)(\,1 - \sqrt{2\,x}\,)$$

$$N^3 \;=\; -\frac{2\sqrt{3}}{(\,\sqrt{3} - \sqrt{2}\,)(\,3 - 2\sqrt{2}\,)}\,\sqrt{x}\,(\,1 - \sqrt{x}\,)(\,1 - \sqrt{\tfrac{4}{3}x}\,)(\,1 - \sqrt{4\,x}\,)$$

$$N^4 \;=\; \frac{4\sqrt{2}}{\sqrt{3}(\,2 - \sqrt{3}\,)(\,\sqrt{3} - \sqrt{2}\,)(\,\sqrt{3} - 1\,)}\,\sqrt{x}\,(\,1 - \sqrt{x}\,)(\,1 - \sqrt{2\,x}\,)(\,1 - \sqrt{4\,x}\,)$$

$$N^5 \;=\; -\frac{\sqrt{3}}{(\,2 - \sqrt{3}\,)(\,\sqrt{2} - 1\,)}\,\sqrt{x}\,(\,1 - \sqrt{\tfrac{4}{3}x}\,)(\,1 - \sqrt{2\,x}\,)(\,1 - \sqrt{4\,x}\,)$$

where $x = (1+\xi)/2$ and the nodes are numbered sequentially in the ξ direction.

For the pressure shape functions, Ψ^i, we use a lower order representation:

$$\Psi^i \;=\; M^i(\xi)\,Q^i(\eta)\,, \tag{3.9}$$

with Q varying linearly with η (two pressure nodes in η direction) and M^i having the same form as $dN^i/d\xi$:

$$M^i(\xi) \;=\; a'\,(1+\xi)^{-\frac{1}{2}} + b' + c'\,(1+\xi)^{\frac{1}{2}} + d'\,(1+\xi)\,. \tag{3.10}$$

Four pressure nodes are needed in the ξ direction and because pressure is singular no node is placed at $\xi = -1$ (Figure 3.2). Using Lagrange interpolation gives:

$$
\begin{aligned}
M^1 &= \frac{\sqrt{6}}{(\sqrt{3}-1)(\sqrt{2}-1)} \frac{1}{\sqrt{x}} (1-\sqrt{x})(1-\sqrt{\tfrac{4}{3}x})(1-\sqrt{2x}) \\
M^2 &= -\frac{\sqrt{3}}{(3-2\sqrt{2})(\sqrt{3}-\sqrt{2})} \frac{1}{\sqrt{x}} (1-\sqrt{x})(1-\sqrt{\tfrac{4}{3}x})(1-\sqrt{4x}) \\
M^3 &= \frac{\sqrt{6}}{(2-\sqrt{3})(\sqrt{3}-\sqrt{2})(\sqrt{3}-1)} \frac{1}{\sqrt{x}} (1-\sqrt{x})(1-\sqrt{2x})(1-\sqrt{4x}) \\
M^4 &= -\frac{\sqrt{3}}{(2-\sqrt{3})(\sqrt{2}-1)} \frac{1}{\sqrt{x}} (1-\sqrt{\tfrac{4}{3}x})(1-\sqrt{2x})(1-\sqrt{4x})
\end{aligned}
$$

with the nodes numbered sequentially in the ξ direction. Note that the constructed shape functions satisfy the conditions $\sum \Phi^i = 1$, $\sum \Psi^i = 1$ and are linearly independent. The master element is mapped to the triangular physical element by means of ordinary polynomial shape functions of the fourth order in the ξ direction and second order in the η direction.

3.3.2 Galerkin method

Applying the Galerkin principle, we weight the momentum and continuity equations by the velocity and pressure basis functions. After applying Green's theorem we have

$$
\int_S \mathbf{n} \cdot \mathbf{T} \, \Phi^i \, dS - \int_V \mathbf{T} \cdot \nabla \Phi^i \, dV = 0, \qquad i = 1, 2, \cdots, N_u, \tag{3.11}
$$

and

$$
\int_V \nabla \cdot \mathbf{u} \, \Psi^i \, dV = 0, \qquad i = 1, 2, \cdots, N_p, \tag{3.12}
$$

where V and S are the domain and its boundary, $\mathbf{n}$ is the unit normal vector pointing outward to the boundary, and N_u and N_p are the numbers of velocity and pressure nodes, respectively. The total number of unknowns is $2N_u + N_p$. Equations (3.11) and (3.12) constitute a system of linear equations efficiently solved by standard subroutines, e.g., frontal methods [75,160].

3.3.3 Numerical integration

Standard 3x3 Gaussian quadrature is used for the integration over the ordinary elements [24]. As noted by various investigators [150,139,140], a standard quadrature rule of low order is inappropriate for the integration over the singular elements. Special quadrature rules for singular elements with an r^n behavior, with the quadrature points and weights varying with the exponent n, are described by Solecki and Swedlow [139]. However, for the square root behavior examined here, the substitution

$$\sqrt{1+\xi} = \frac{s+1}{\sqrt{2}} \tag{3.13}$$

transforms the encountered integrands into simple polynomials in the s domain, and therefore standard Gauss-Legendre quadrature suffices for an exact integration. This treatment is equivalent to modifying the standard Gauss weights w_k^G and points γ_i^G as follows:

$$\gamma_i = \frac{(\gamma_i^G + 1)^2}{2} - 1\,, \tag{3.14}$$

and

$$w_i = w_i^G(\gamma_i^G + 1)\,, \tag{3.15}$$

for the integration along the radial direction. We use a 5x3 modified Gaussian quadrature for integration over the singular elements.

3.4 Results and Discussion

The stick-slip problem was solved using both ordinary and singular finite elements. Five ordinary meshes and three singular meshes, shown in Figures 3.3 and 3.4, were

Mesh I, 24 elements

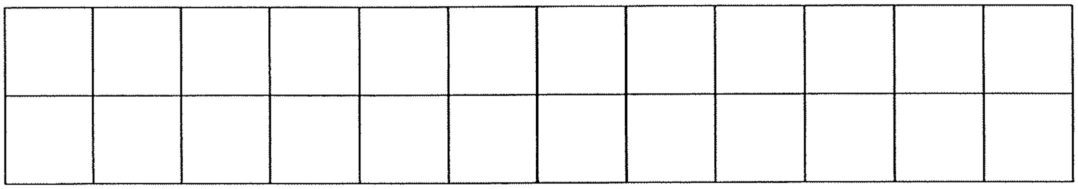

Mesh II, 96 elements

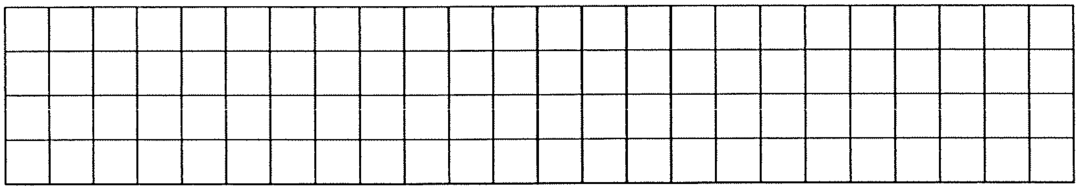

Mesh III, 384 elements

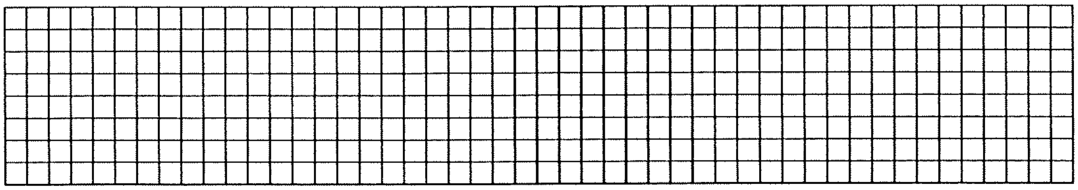

Mesh IV, 450 elements

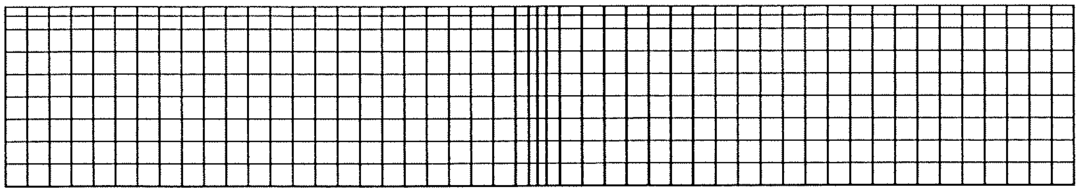

Mesh V, 520 elements

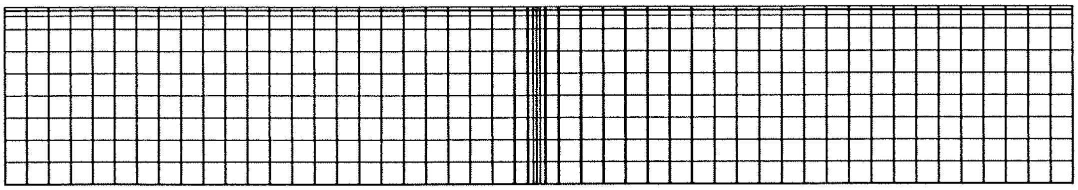

Figure 3.3: Ordinary element meshes.

Mesh I, 32 elements

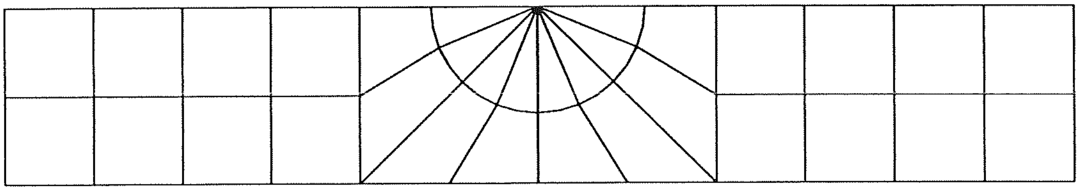

Mesh II, 104 elements

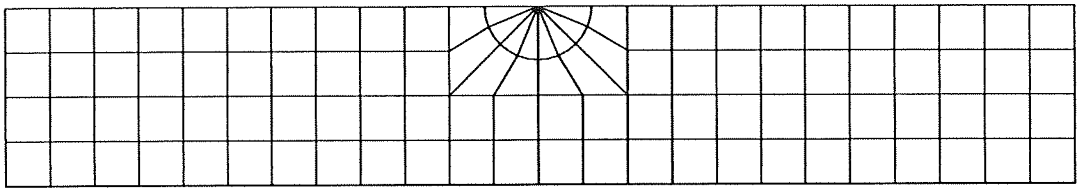

Mesh III, 392 elements

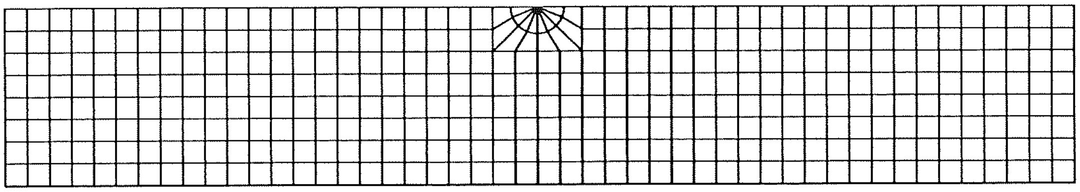

Figure 3.4: Singular element meshes.

(a) y-velocity

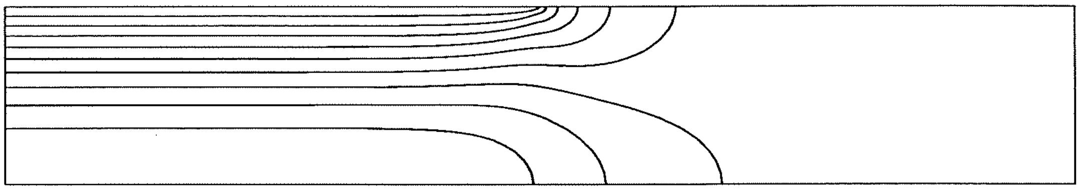

(b) z-velocity

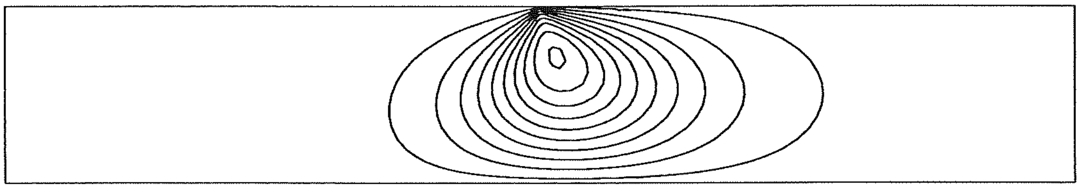

(c) Pressure

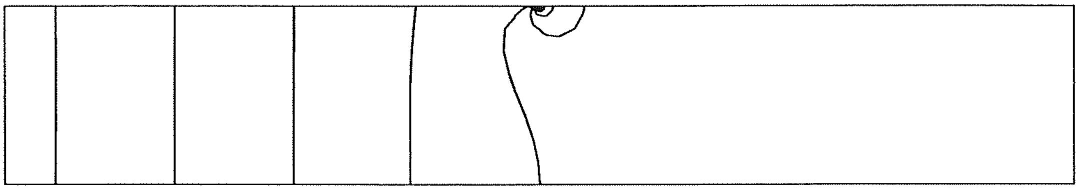

(d) Streamfunction

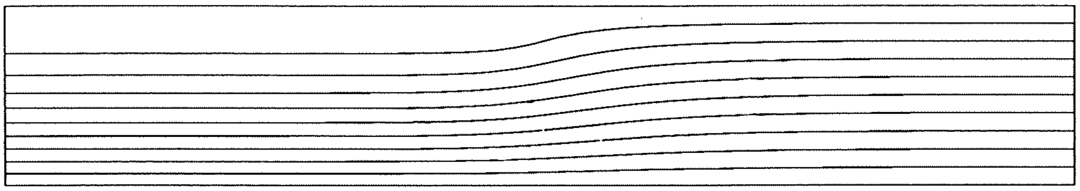

Figure 3.5: Solution of the stick-slip problem: (a) y-velocity, (b) z-velocity, (c) pressure and (d) streamlines.

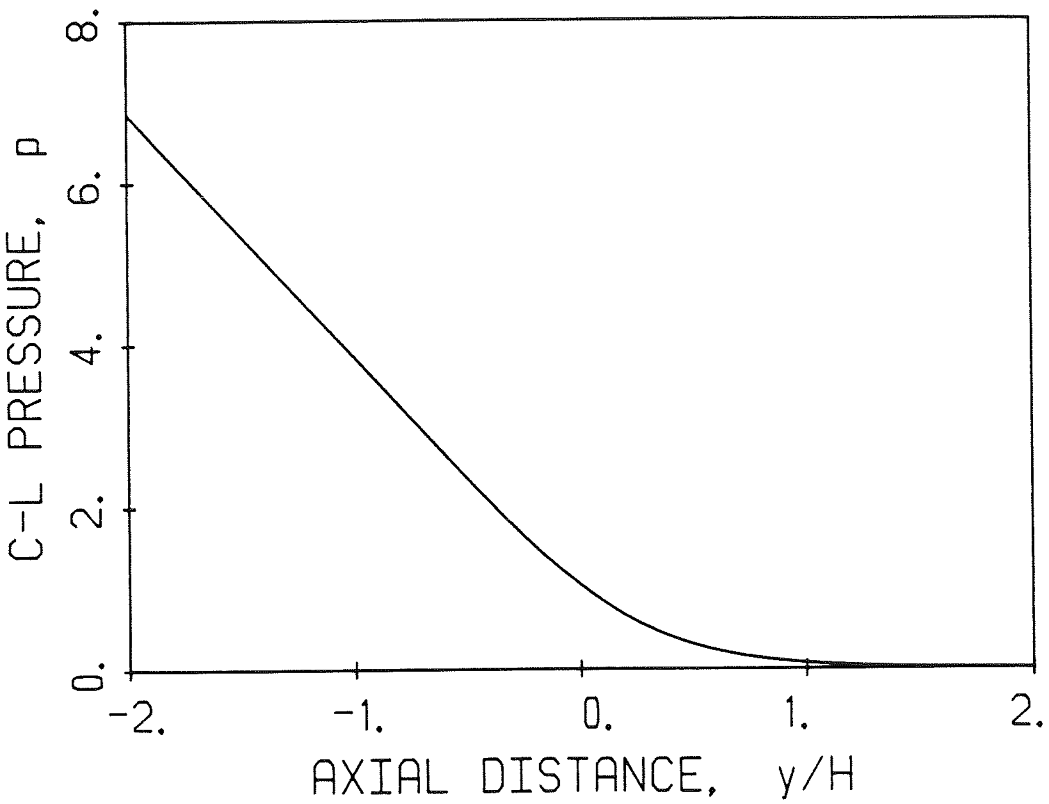

Figure 3.6: Predicted centerline pressure with singular and ordinary elements.

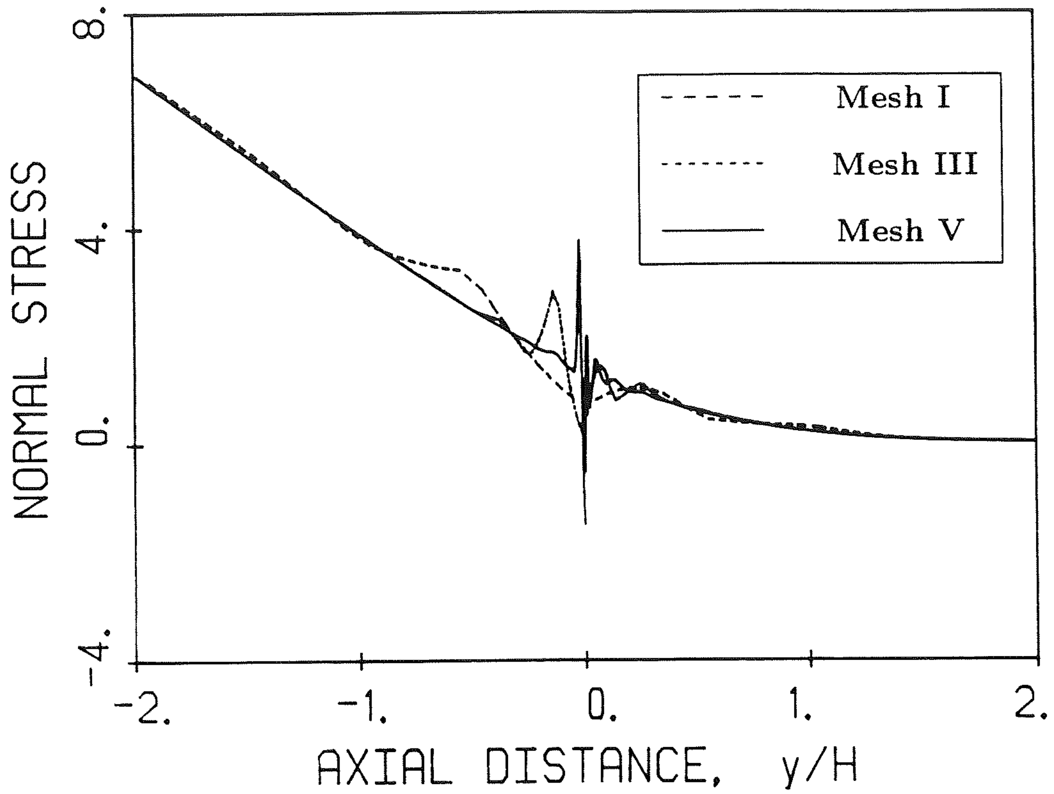

Figure 3.7: Predicted normal stresses at $z = 1$ with ordinary elements for the planar stick-slip problem (– – –: mesh I, - - - -: mesh III, ——: mesh V).

constructed for this purpose. The first three ordinary meshes (I,II and III) were uniform and consisted of 24, 96, and 384 square elements. The last two meshes (IV and V) were obtained by refining only the row and columns around the tip; they consisted of 450 and 520 elements. To generate the singular meshes, we modified the uniform ordinary meshes: eight ordinary square elements were replaced by eight singular triangular-shaped elements and eight ordinary transition elements in the circular pattern shown in Figure 3.4. Of course, uniform meshes are by no means optimum for the stick-slip problem, but in this work they appear to be more appropriate for comparisons between singular and ordinary finite elements.

The solution of the stick-slip problem obtained with the finest singular mesh is illustrated in Figure 3.5, where we plot the velocity and pressure contours and the stream-

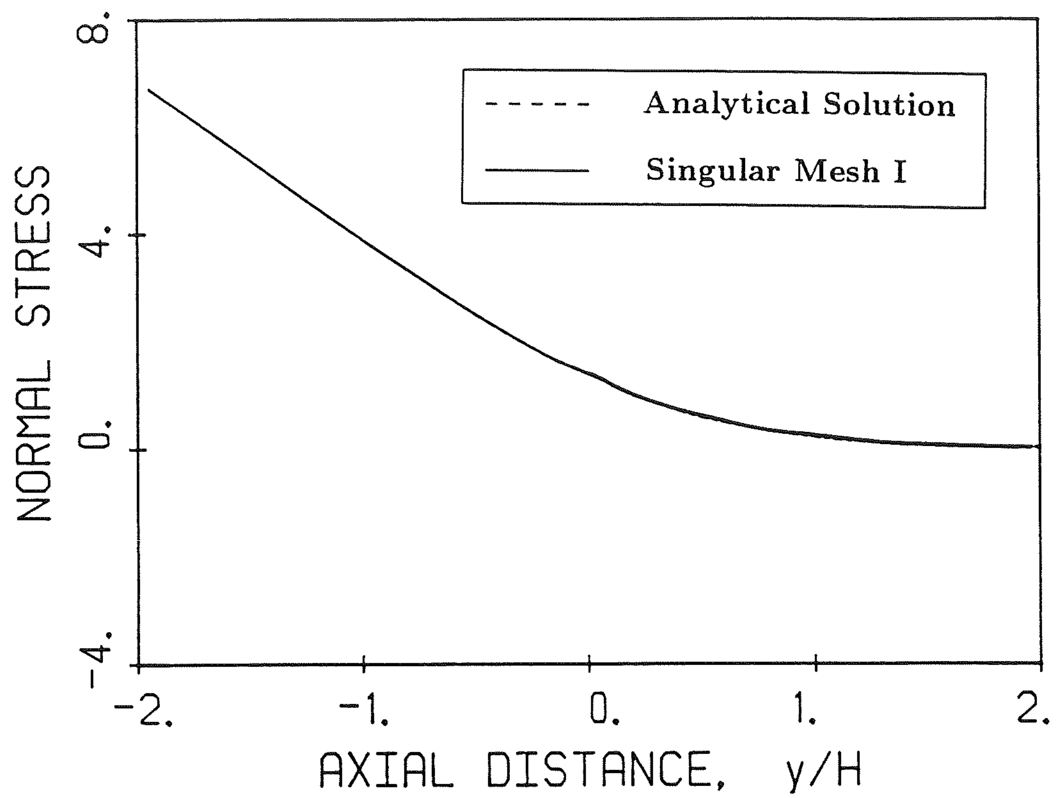

Figure 3.8: Normal stresses at $z = 1$ (——: singular elements, mesh I, - - -: theory).

lines. The results clearly depict the rearrangement of the flow from a Poiseuille-flow to a uniform-flow regime.

The singular and ordinary finite element results far from the singular point are in good agreement. Both methods predict essentially the same centerline pressure (Figure 3.6); it varies linearly with the axial distance inside the die and goes smoothly to zero in the jet. However, the results around the singularity differ dramatically. We focus on two important quantities, the normal stress along the wall and the slip surface and the velocity along the slip surface.

The normal stresses predicted with the ordinary finite elements meshes I, III and V are plotted in Figure 3.7. We observe that the normal stress oscillates spuriously around the singularity; the oscillations on the wall are of smaller frequency and greater amplitude than those on slip surface. As we refine the mesh, the oscillations move towards the singular point and their amplitude increases.

By using singular finite elements, we practically eliminate these oscillations. The normal stress obtained with the coarsest singular mesh is smooth and agrees well with the analytical solution (Figure 3.8). Note that the coarsest mesh gives virtually the same normal stress results as the finest mesh, indicating that relatively coarse meshes may be used with singular finite elements. However, some oscillations of very small amplitude still occur very close to the singularity with the finer meshes. These oscillations are not restricted to the singular elements but also appear in the surrounding ordinary elements; this may be due to the fact that the pressure and viscous stress grow large with opposite signs which gives rise to a numerical error.

No matter what the cause of the oscillations is, the main disadvantage of the embodied singularity elements is apparent: by refining the mesh, we reduce the size of the singular elements over which the singularity is given special attention. Nevertheless, this problem may be partially resolved by restructuring the mesh so that the size of the singular elements is fixed and independent of mesh refinement (e.g., by using more ordinary transition elements or by using triangular instead of rectangular ordinary elements).

The normal stress results were used to choose the order and the number of the singular elements and to check whether ordinary transition elements are necessary around the singular elements. In addition to the aforementioned pattern with eight 13-node singular elements and eight transition elements, three alternative mesh patterns were also examined: (i) eight 7-node singular elements with eight ordinary transition elements, (ii) four 13-node singular elements with four ordinary transition elements, and (iii) eight 13-node singular elements with no ordinary transition elements. All the examined mesh patterns are shown in Figure 3.9. The predicted normal stresses were better than those

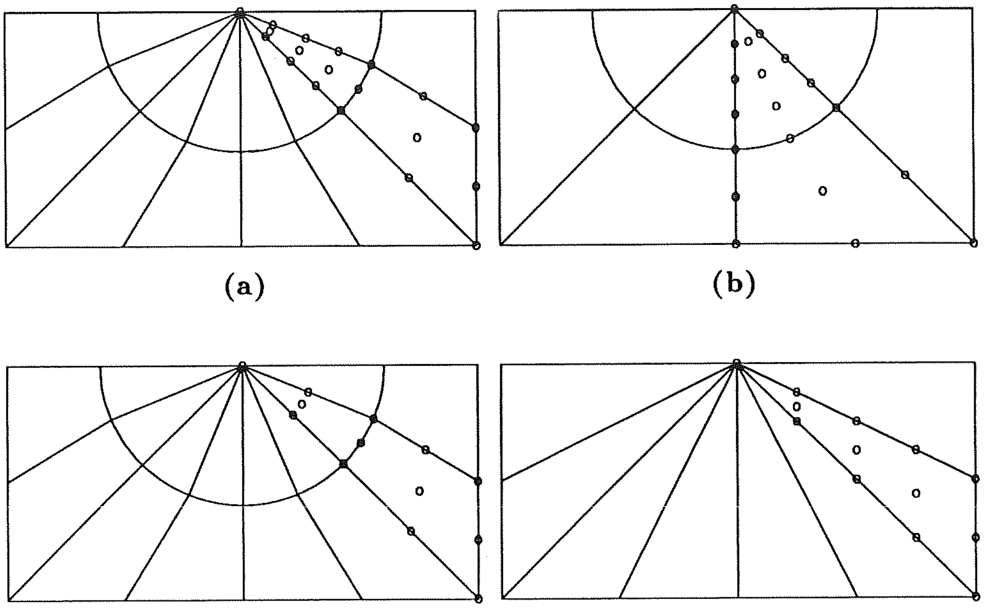

(a) (b)

(c) (d)

Figure 3.9: Examined mesh patterns around the singular point.

obtained with ordinary elements in all cases. However, the results with the alternative mesh patterns examined were characterized by some oscillations, which disappear with mesh refinement. The most severe oscillations occur with the 7-node singular elements (Figure 3.10). This is due not only to the lower order of the element but also to the fact that some terms of the basis functions become zero in accordance with the analytical solution. Consequently, only one term survives to express the radial dependence of the normal stress. The 13-node elements overcome this difficulty. The mesh pattern with eight 13-node singular elements and eight ordinary transition elements appeared to give satisfactory results and adequately captured the θ dependence of the local solution. After some preliminary tests, the radius of the singular elements was taken to be 1.2 times the size of the original ordinary square.

To assure that the improved solution is due to the singular basis functions and not to the different shapes and mesh patterns used with the singular elements, we solved

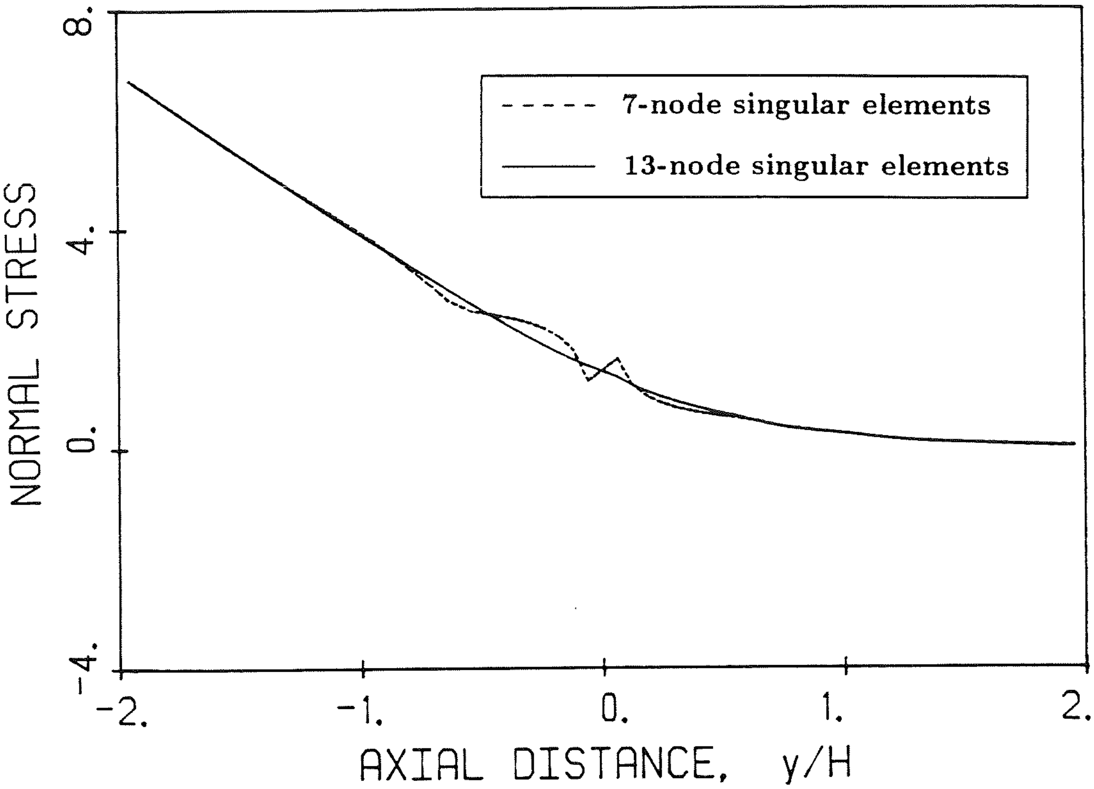

Figure 3.10: Computed normal stresses with 7-node (- - -) and 13-node (——) singular elements (mesh I).

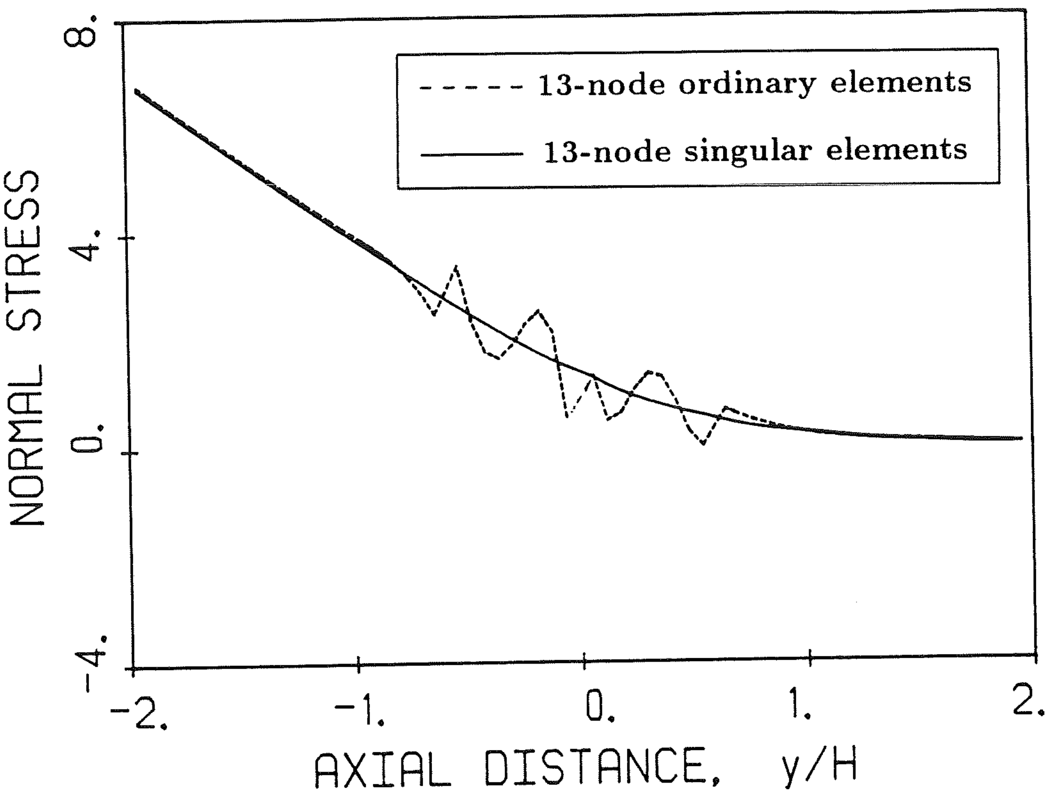

Figure 3.11: Computed normal stresses with 13-node ordinary (- - -) and singular (—) elements (mesh *I*).

Table 3.1: Inverse condition number of the stiffness matrix for various elements and meshes.

Mesh	Elements	1/cond(A)
I	Ordinary 9-node	$3.234\ 10^{-4}$
II	Ordinary 9-node	$1.015\ 10^{-4}$
III	Ordinary 9-node	$4.009\ 10^{-5}$
I	Singular 7-node	$2.394\ 10^{-5}$
II	Singular 7-node	$7.236\ 10^{-6}$
I	Singular 13-node	$2.456\ 10^{-7}$
II	Singular 13-node	$7.505\ 10^{-8}$

the problem by replacing the 13-node singular elements with 13-node ordinary elements. Comparison of the computed normal stresses, in Figure 3.11, indicates that the singular basis functions are important for an improved solution.

As with the use of singular basis functions [141], the condition number of the stiffness matrix becomes larger if singular elements are used. Table 3.1 summarizes how the condition number changes with the mesh and type of element. The condition number, computed using the LINPACK subroutine DGBCO, was sufficiently small for all our double precision computations.

The second quantity we examined was the velocity on the slip surface. The computed nodal slip surface velocities from ordinary mesh IV and singular mesh II are shown in Figure 3.12, along with the asymptotic solution. The singular finite element values agree well with the analytical solution; the ordinary element results differ slightly and converge to the analytical solution with mesh refinement. Again, the coarse singular element meshes give more accurate results than refined ordinary meshes.

For another comparison with the analytical solution, we estimated the first expansion coefficients using a least-squares fit of equation (3.5) to the eight nodal slip-surface velocities closest to the singularity. Estimates of the first three expansion coefficients are given by Ingham and Kelmanson [82] who used a singular boundary integral method to

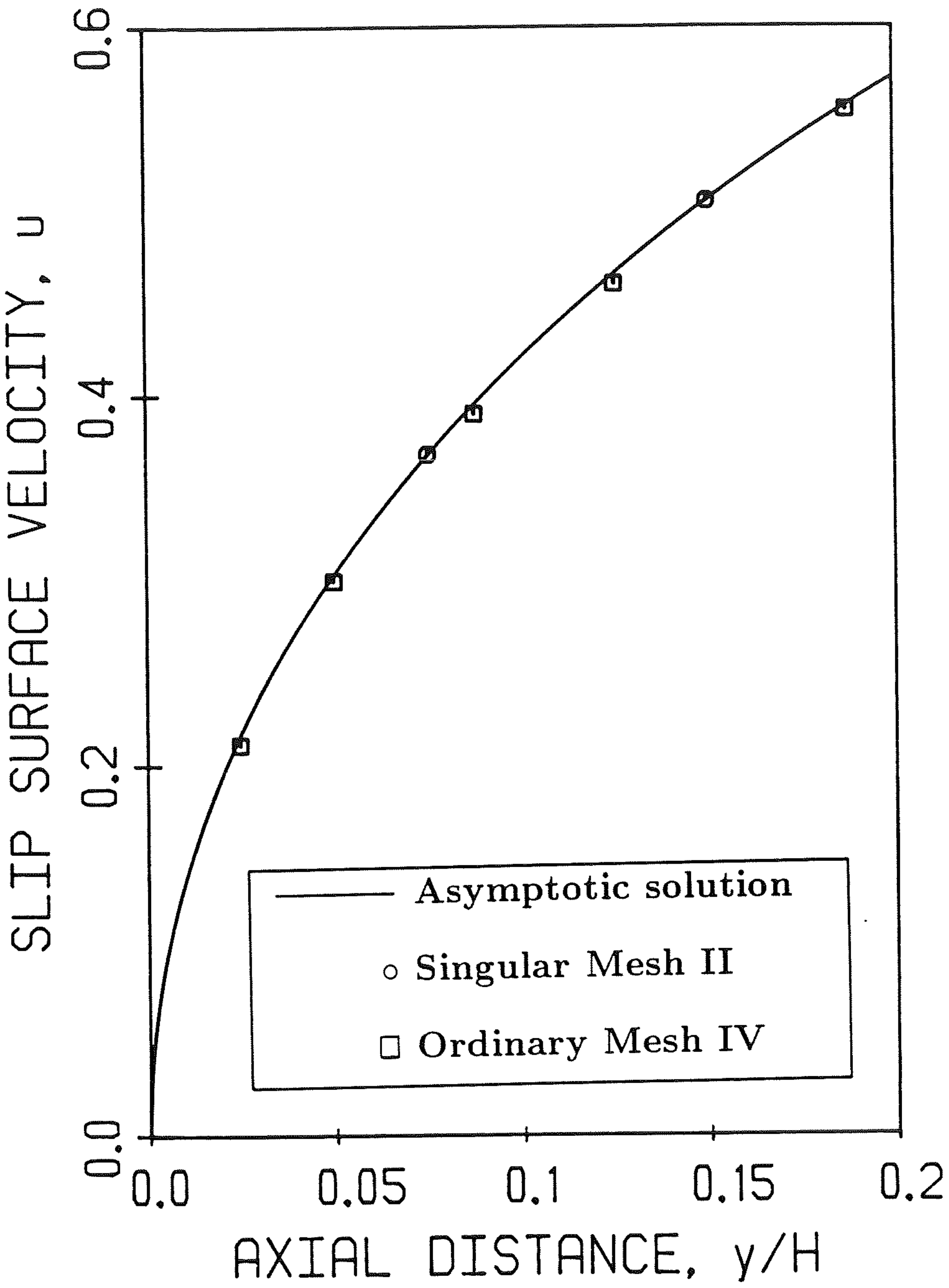

Figure 3.12: Comparison of predicted slip surface velocities near the singularity (——: asymptotic solution, o: singular mesh *II*, ☐: ordinary mesh *IV*).

Table 3.2: Computed singularity expansion coefficients.

Method	$\alpha_{1/2}$	$\alpha_{3/2}$	$\alpha_{5/2}$
Ordinary elements	0.67170	0.19812	−0.02297
Singular elements	0.69173	0.27168	0.05013
Ingham & Kelmanson	0.69108	0.26435	0.04962
Analytical solution	0.69099	– – – – –	– – – – –

solve the planar stick-slip problem. The estimated parameters for meshes *III* are listed in Table 3.2 along with the extrapolated values given in [82]. The agreement with the analytical solution is satisfactory despite the fact that the least-squares fit was not rigorous with regard to the number and the weight of the nodal points.

3.5 Concluding remarks

Singular finite elements have been developed for the stick-slip problem in order to improve the solution in the neighborhood of the singularity. These elements are similar in principle to the crack-tip elements used in fracture mechanics; however, in fluid flow problems the pressure, a primary unknown, is singular. Compared to ordinary finite elements, the singular elements give more accurate results for relatively coarse meshes. Good approximations to the leading singular coefficients have also been obtained. The method can be readily applied to other problems in fluid mechanics for which the radial form of the singularity can be obtained by a local analysis. As mentioned in the introduction, the method is not restricted to creeping and Newtonian flows, but is also applicable to nonzero Reynolds number and non-Newtonian flows, provided that the encountered stresses are integrable.

From some preliminary results [54], it appears that the removal of the pressure node from the singular point plays a crucial role to the improvement of the solution. Singular finite elements, with an approximate singularity exponent independent of the free-surface shape and location, can be used to study singular free-surface problems. They can also be used for problems with non-integrable singularities by approximating the singular quantities by $r^{-1+\epsilon}$ where $0 < \epsilon \ll 1$. In the next chapter, we present the solution of the sudden expansion and the die-swell problems.

3.6 Appendix: Mapping for singular elements

As in Tracey [149], we demonstrate that the ξ coordinate for the element shown in Figure 3.2 is approximately mapped to the radial direction, and the η coordinate is mapped to the circumferential angle. Suppose that the global radius of the element is given by R and the total global angle subtended by the element is β. By directly applying the standard polynomial shape functions for an element, we find that

$$y = \frac{R}{2}(1+\xi)\left[\frac{\eta}{2}(1+\eta) + \cos\frac{\beta}{2}(1-\eta^2) - \cos\beta\frac{\eta}{2}(1-\eta)\right] \sim \frac{R}{2}(1+\xi) \qquad (3.16)$$

and

$$z = \frac{R}{2}(1+\xi)\left[-\sin\frac{\beta}{2}(1-\eta^2) + \sin\beta\frac{\eta}{2}(1-\eta)\right] \sim -\frac{R\beta}{4}(1+\xi)(1-\eta)\,, \qquad (3.17)$$

where the simplifications use small angle approximations. Then the determinant of the Jacobian matrix is

$$|\mathbf{J}| = \frac{R^2}{8}\beta\,(1+\xi)\,,$$

i.e., the differential area of the singular element is $r\;drd\theta = |\mathbf{J}|\;d\xi d\eta$.

CHAPTER IV

SINGULAR FINITE ELEMENTS FOR THE SUDDEN-EXPANSION AND THE DIE-SWELL PROBLEMS

> "In the critics' vocabulary, the word "precursor" is indispensable, but it should be cleansed of all connotation of polemics or rivalry. The fact is that every writer *creates* his own precursors. His work modifies our conception of the past, as it will modify the future. In this correlation the identity or plurality of the men involved is unimportant."
>
> Jorge Luis Borges, *Kafka and His Precursors (Labyrinths).*

The singular elements constructed in Chapter III for the stick-slip problem are further developed in this chapter to solve two standard fluid mechanics problems:

1. The sudden-expansion problem with a singularity of different nature from that present in the stick-slip geometry, and
2. The die-swell problem, extensively discussed in Chapter II, which requires the singular elements to have curved sides due to the presence of the free surface[1].

---

[1] The material of this chapter will appear in the *Int. j. numer. methods fluids* [57].

4.1 Introduction

Stress singularities in fluid mechanics arise whenever there is an abrupt change in a boundary condition or in the boundary itself. Some well-known examples of singular problems are the sudden-expansion, the die-swell, the stick-slip, and the driven-cavity problems, which are often used as model problems for the various numerical methods proposed for Newtonian or non-Newtonian flows.

Singularities require special attention, no matter what numerical method is used. The most common treatment is to refine the grid around the singular point in order to capture the abrupt changes in the flow field. However, the rate of convergence and the accuracy are generally unsatisfactory. The stresses cannot be infinite (in compliance with the asymptotic solution), and they are tainted by spurious oscillations. This contamination is far more serious in non-Newtonian flows than in the corresponding Newtonian flows. Numerical inaccuracies caused by singularities can lead to numerically stiff iteration schemes, to the formation of fictitious limit points, or to artificial changes of type of the governing equations [22,97]. Another inherent disadvantage in local refinement is the generation of extremely large matrices, resulting in higher computational costs.

Some investigators have modified the mathematical problem to alleviate the singularity (a) by modifying the boundary conditions (e.g., relaxing the no-slip condition for a smooth transition from a velocity to a stress boundary condition [135]) or (b) by smoothing the boundary (e.g., replacing a re-entrant corner by a circular arc of small radius [22,125]).

An alternate approach, based on the acknowledgement of the singularity rather than on its alleviation, is the incorporation of the local asymptotic solution (if known) into the numerical scheme (finite differences, finite elements, boundary elements, etc). This idea has been extensively used in fracture mechanics and gives accurate results for relatively coarse meshes [48,42]. More recently, singular methods were used to solve singular fluid mechanics problems with finite differences [74], boundary elements [82], and finite elements [55,56]. In the singular finite element method (SFEM), special elements that take into account the nature of the singularity are used in a small core around the singular region and ordinary elements are used in the rest of the domain. The basis functions for the primitive variables over the singular elements embody the radial form of the singularity, which can be obtained by an asymptotic analysis.

A feature of the singular fluid flow problems that does not appear in fracture mechanics is that, in addition to the velocity derivatives, the pressure, a primitive variable, is singular [55]. An additional complication arises in free-surface problems since the angle of separation is unknown and the boundaries are curved; hence, the exact form of the singularity is unknown.

The SFEM has been used in Chapter III to solve the Newtonian stick-slip problem (see also [55]). The results indicate that the SFEM improves the stress representation and gives more accurate results than those from more refined ordinary finite element meshes. It was also noted that the method can be applied to other singular fluid flow problems for which the radial form of the singularity can be obtained by a local analysis. Such analyses are possible with various geometries for both Newtonian ([100,104,143]) and non-Newtonian ([4,95,69,31]) flows; in some non-Newtonian flows the local solution is identical to that of the Newtonian case. Thus, the SFEM is applicable to some non-Newtonian flows provided the encountered stresses are integrable. The SFEM is also suited to nonzero Reynolds number flows, because the local solution remains unchanged near the singularity where the viscous effect dominates. This implies that the singular elements constructed for creeping flows can be used to solve the nonzero Reynolds number problems as well.

With this background in mind, the main objective of this chapter is to generalize the SFEM for flows with different singularity powers, nonzero Reynolds number flows and flows with free surfaces. We chose to solve two singular problems: (a) the planar 2:1 sudden-expansion problem and (b) the planar die-swell problem. These problems are important in polymer processing and in other industrial applications and have been the subject of a considerable amount of experimental and numerical work (e.g., [162,113]). Even though our work aims towards solving viscoelastic flows, which are more challenging than their Newtonian counterparts, here we restrict ourselves to the Newtonian cases. Despite the simplification introduced by the Newtonian assumption, the two problems are analytically intractable due to the singularities and the nonlinearity of the convective terms. In the case of the die-swell problem, the boundary conditions on the free surface (the location of which is unknown) are also nonlinear. Numerical methods, especially finite elements, have been used extensively to overcome all these difficulties. The free surface location is computed by either Picard iteration [135,108,113] or full-Newton iteration schemes [127,51][2].

The sudden expansion problem was solved for different Reynolds numbers, up to 100, using the singular elements constructed for creeping flow. The SFEM performs well for nonzero Reynolds numbers and yields more accurate predictions for the stresses than the ordinary finite element method. The solution also appears to be rather insensitive to substantial variations of the powers used in the construction of the basis functions. It seems that the elimination of the pressure node from the singular point plays a crucial role in the improvement of the solution.

The planar die-swell problem was solved by singular finite elements, free-surface parameterization, and full-Newton iteration. The singular elements developed for the stick-

---

[2] The Picard and full-Newton iteration schemes have been extensively discussed in Chapter II.

slip problem were used for the die-swell problem over the full range of Reynolds and capillary numbers examined. As we will see in the following sections, the SFEM speeds up the convergence of the free surface dramatically.

The governing equations and the local solutions around the singularities are presented in section 4.2, the construction of the singular basis functions and the finite element formulation are presented in section 4.3, and the results are discussed in section 4.4.

4.2 Governing Equations

The flow geometry, the governing equations and the boundary conditions for the sudden-expansion and the die-swell problems are depicted in Figures 4.1a and 4.2a, respectively. The flows are governed by the two-dimensional momentum equation and continuity; for incompressible flow and neglecting gravity,

$$Re\, \mathbf{u} \cdot \nabla \mathbf{u} = \nabla \cdot \mathbf{T} \,, \tag{4.1}$$

and

$$\nabla \cdot \mathbf{u} = 0 \,, \tag{4.2}$$

where length is measured in units of the entrance half-width H, the velocity $\mathbf{u}$ is scaled by the mean velocity in the entrance channel U, the Newtonian stress tensor,

$$\mathbf{T} = -p\,\mathbf{I} + [\nabla \mathbf{u} + (\nabla \mathbf{u})^T] \,,$$

is scaled by $\mu U/H$, and μ is the viscosity. The Reynolds number is defined as

$$Re \equiv \frac{\rho U H}{\mu} \,, \tag{4.3}$$

where ρ is the density.

In addition to the two velocity components, u and v, and the pressure, p, the free surface location, h, is an additional unknown in the die-swell problem. The kinematic

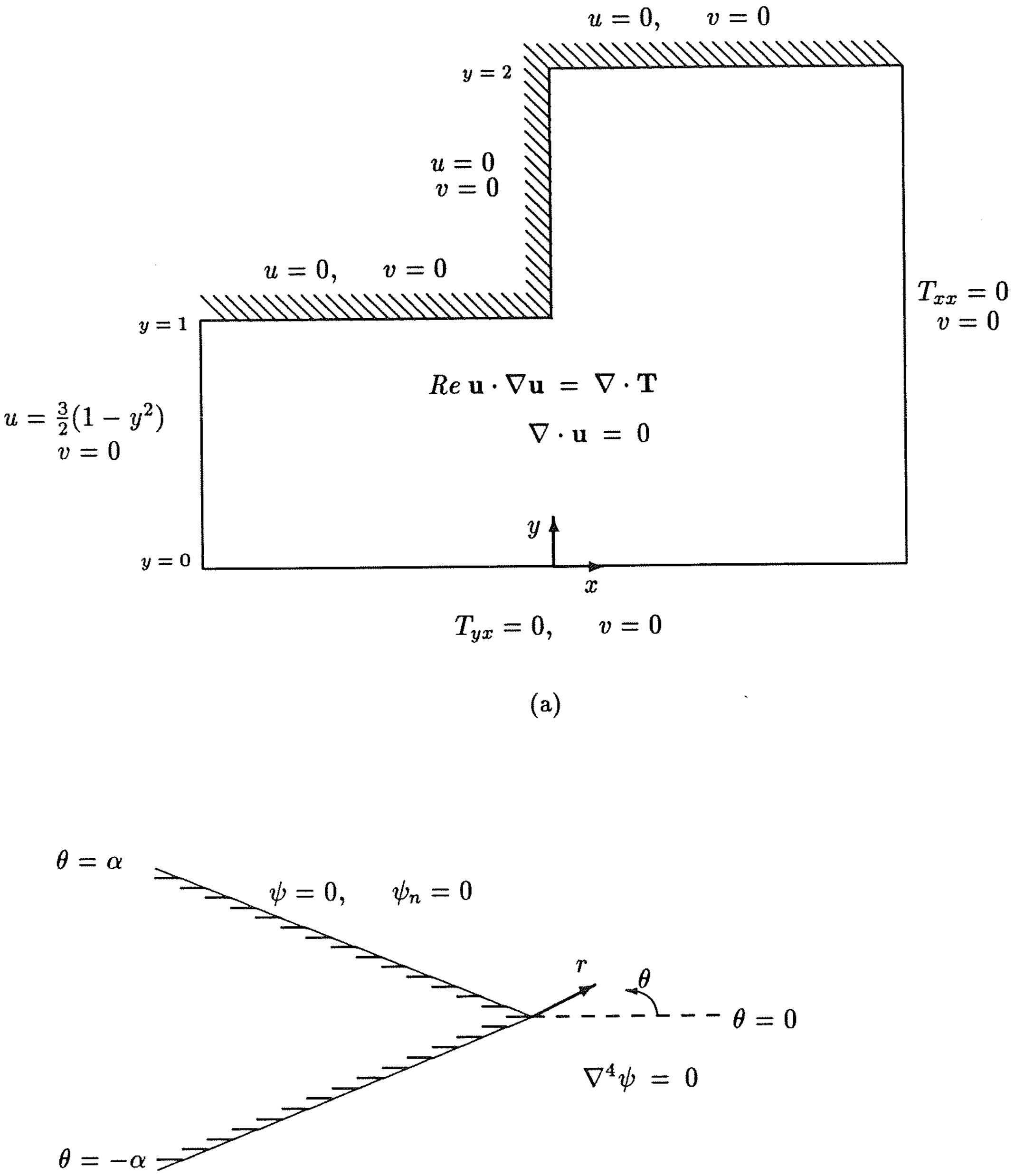

(a)

(b)

Figure 4.1: (a) Sudden-expansion problem. (b) Local analysis of the singularity.

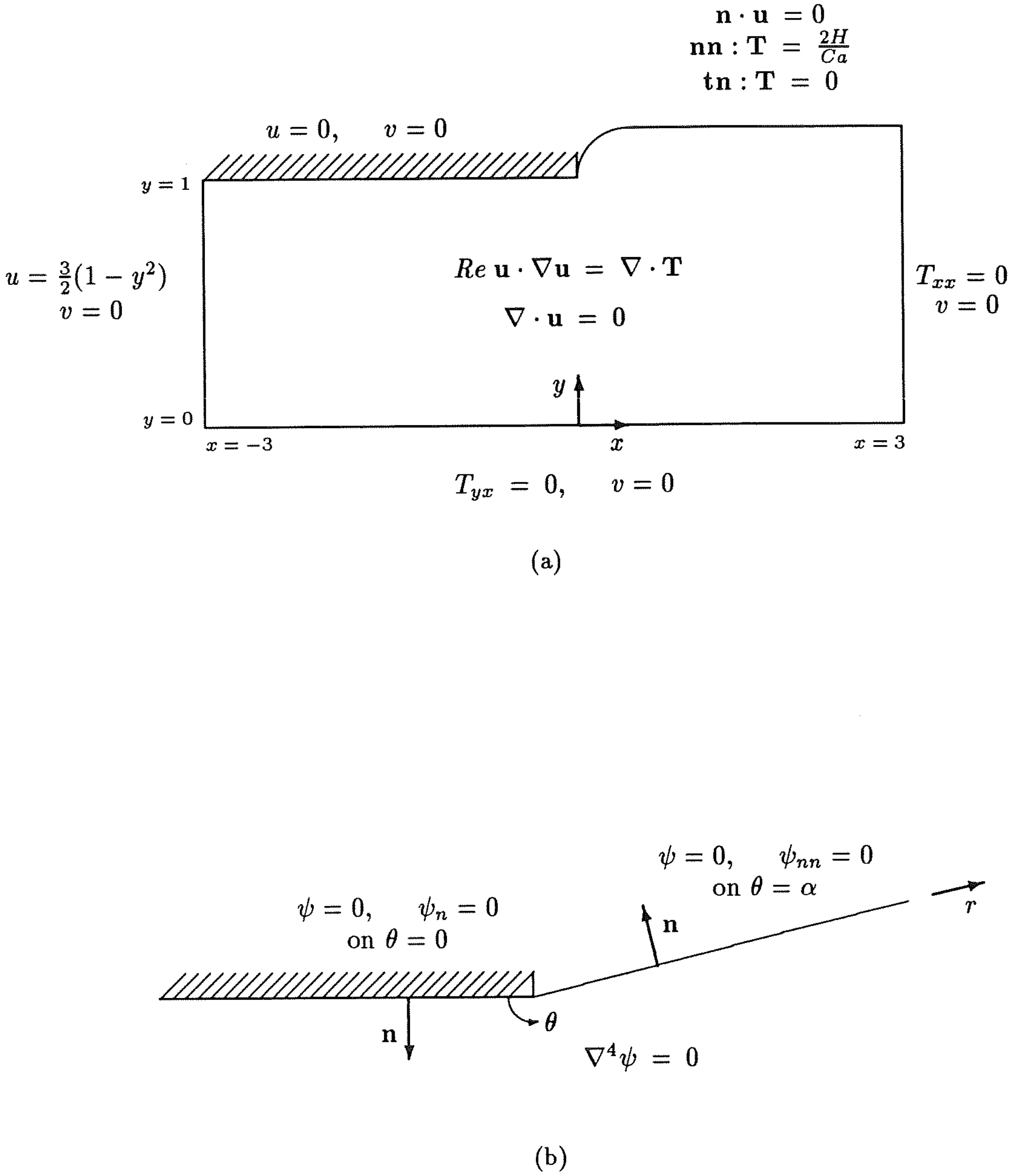

Figure 4.2: (a) Die-swell problem. (b) Local analysis of the singularity.

condition that the free surface remain a material surface provides the additional equation needed:

$$\mathbf{n} \cdot \mathbf{u} = 0\,, \tag{4.4}$$

where $\mathbf{n}$ is the unit normal vector pointing outwards from the free surface.

The remaining two conditions on the free surface serve as the boundary conditions in our formulation. A momentum balance on the free surface requires the shear stress to vanish and the normal stress in the liquid to balance any capillary pressure, or

$$\mathbf{nn} : \mathbf{T} \;=\; \frac{2H}{Ca}\,, \tag{4.5}$$

where Ca is the capillary number,

$$Ca \equiv \frac{\mu U}{\sigma}\,, \tag{4.6}$$

σ is the surface tension, and $2H$ is the mean curvature of the free surface, given by

$$2H = \frac{h_{xx}}{[1 + h_x^2]^{3/2}}\,. \tag{4.7}$$

Local Analysis of the Singularity

For the local analysis of the singularity we follow Michael [100] and Moffatt [104] and switch to planar polar coordinates (r,θ) (see Figures 4.1b and 4.2b). Using a streamfunction representation, the Stokes equation admits separated solutions of the form

$$\psi \;=\; r^{\lambda} f_{\lambda}(\theta)\,, \tag{4.8}$$

where ψ is the streamfunction, λ are the eigenvalues of the resulting eigenproblem, and $f_{\lambda}(\theta)$ is given by the general expression

$$f_{\lambda}(\theta) \;=\; A\cos\lambda\theta + B\sin\lambda\theta + C\cos{(\lambda-2)\theta} + D\sin{(\lambda-2)\theta}\,. \tag{4.9}$$

A, B, C and D are arbitrary constants determined from the boundary conditions. We require that $Re(\lambda) > 1$ to ensure that the velocity goes to zero at the singular point. For flow between two rigid walls meeting at a sharp corner, as in Figure 4.1b, we have two sets of solutions that correspond to the *antisymmetrical* and the *symmetrical* flows. For the antisymmetrical flow,

$$\psi \;=\; a_\lambda\, r^\lambda \left[\cos{(\lambda-2)\alpha}\, \cos{\lambda\theta} \;-\; \cos{\lambda\alpha} \cos{(\lambda-2)\theta}\right], \tag{4.10}$$

where α is the angle defined in Figure 4.1b, a_λ is a constant and λ satisfies the equation

$$\sin 2\mu\alpha \;=\; -\mu \sin 2\alpha \quad \text{with} \quad \mu = \lambda - 1\,. \tag{4.11}$$

For the symmetric case,

$$\psi \;=\; b_\lambda\, r^\lambda \left[\sin{(\lambda-2)\alpha}\, \sin{\lambda\theta} \;-\; \sin{\lambda\alpha} \sin{(\lambda-2)\theta}\right], \tag{4.12}$$

where b_λ is a constant and λ satisfies

$$\sin 2\mu\alpha \;=\; \mu \sin 2\alpha \quad \text{with} \quad \mu = \lambda - 1\,. \tag{4.13}$$

For the sudden expansion problem, α is $3\pi/4$; the first eigenvalues from equations (4.11) and (4.13), ordered in increasing real part, are listed in Table 4.1. It is worthwhile to note the following: (a) Although $\mu = 1$ is a solution to (4.11), it is not an eigenvalue for this problem [143]. (b) There is an infinite number of eigenvalues for both sets of solutions. (c) There is only one real eigenvalue for each set of solutions and it is less than 1. (d) The real part of the complex eigenvalues is always greater than 1. Holstein and Paddon [74] pointed out that the above solution is the zero-order approximation to inertial corner flow and that the Stokesian and inertial corner flows share the first three expansion terms.

An interesting characteristic of the local asymptotic solution of the sudden-expansion problem is that both the antisymmetrical and the symmetrical solutions contribute one

Table 4.1: Leading eigenvalues $\mu = \lambda - 1$ of the two asymptotic solution tests (sudden expansion).

No	Antisymmetrical	Symmetrical
1	0.54448	0.90853
2	$1.62926 \pm 0.23125i$	$2.30133 \pm 0.31584i$
3	$2.97184 \pm 0.37393i$	$3.64142 \pm 0.41879i$
4	$4.31038 \pm 0.45549i$	$4.97890 \pm 0.48663i$
5	$5.64711 \pm 0.51368i$	$6.31508 \pm 0.53763i$
6	$6.98287 \pm 0.55911i$	$7.65051 \pm 0.57859i$
7	$8.31803 \pm 0.59642i$	$8.98546 \pm 0.61285i$

singular term and the stresses vary as

$$T_N \sim c_1 r^{-0.456} + c_2 r^{-0.091} . \tag{4.14}$$

Unlike the stick-slip problem [121], the normal stresses along the walls are singular. Along the bisector ($\theta = 0$), the leading order symmetrical contributions to the radial velocity component and the pressure vanish; the antisymmetrical contributions to the circumferential velocity component also vanish. Therefore, at $\theta = 0$ and close to the singular point, the radial velocity component is proportional to $r^{0.544}$, and the circumferential velocity to $r^{0.909}$. The antisymmetrical contribution to the stress also vanishes at $\theta = 0$, and the stress is determined by the less singular symmetrical contribution.

For the die-swell problem, we consider the flow between a rigid boundary and a free surface as in Figure 4.2b. Michael [100] showed that for zero surface tension on a planar free surface, the angle α must be equal to π. Sturges [143] noted that this result does not apply to the die-swell problem because the free surface is not planar. Schultz and Gervasio [131] suggested that either the slope is zero or the mean curvature is infinite. The resulting eigenvalue problem for the geometry in Figure 4.2b is identical to equation (4.13); the first two roots for various angles up to $3\pi/2$ are listed in [143]. However, in the present work we assume that the radial form of the local solution is not very different from the solution for $\alpha = \pi$; therefore, the local solution is the same as that of the stick-slip problem:

$$\psi = r^{\lambda+1}a_\lambda[\cos(\lambda+1)\theta - \cos(\lambda-1)\theta], \qquad \text{for } \lambda = \frac{1}{2}, \frac{3}{2}, \frac{5}{2} \cdots, \tag{4.15}$$

and

$$\psi = r^{\lambda+1}b_\lambda[(\lambda-1)\sin(\lambda+1)\theta - (\lambda+1)\sin(\lambda-1)\theta], \quad \text{for } \lambda = 2,3,4,\cdots. \tag{4.16}$$

Using the same local solution, we avoid using different singular functions at different (apparent) angles of separation and finding the angle of separation itself. Note that the singular elements require only the knowledge of the radial form of the local solution. The validity of the above assumption is tested by studying the sensitivity of the results to variations of the singularity powers used in the construction of the basis functions.

4.3 Finite Element Formulation

The domain is discretized using triangular singular elements around the singular point and rectangular ordinary elements elsewhere, as illustrated in Figures 4.3 and 4.4. For the ordinary elements we use biquadratic basis functions for the velocities and bilinear for the pressure. These elements are mapped onto a 2x2 master element in (ξ,η) coordinates by means of biquadratic shape functions. As in Chapter III, the singular elements are collapsed quadrilaterals with 13 velocity and 8 pressure nodes mapped onto a 2x2 15-node element in the computational domain (ξ,η) by means of ordinary fourth-order polynomial shape functions in the ξ and second-order in the η direction. It is important to stress the following :

(a) the singular elements are compatible with the adjacent ordinary elements at $\xi = 1$,

(b) there is no pressure node at the singular point, and

(c) the three velocity nodes of the singular master element collapse to a single node with two degrees of freedom at the singular point in the physical domain.

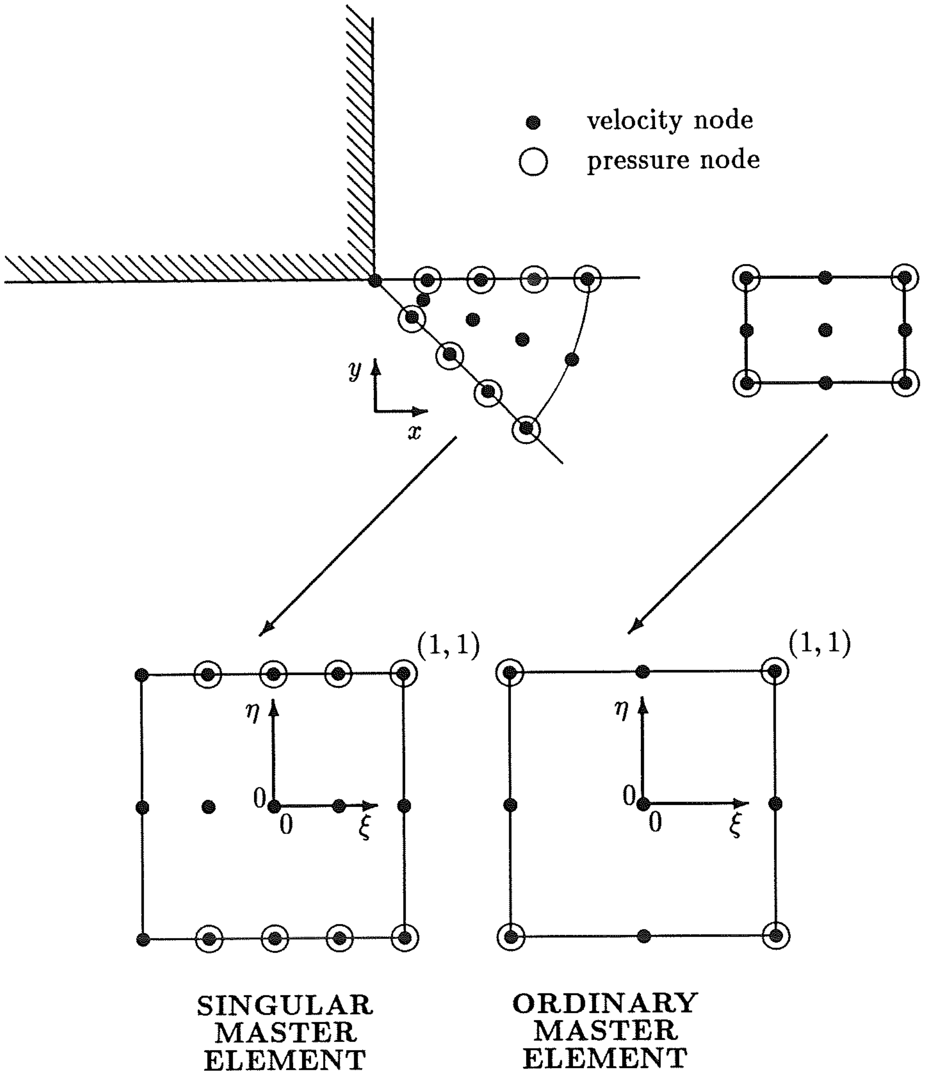

Figure 4.3: Ordinary and singular elements.

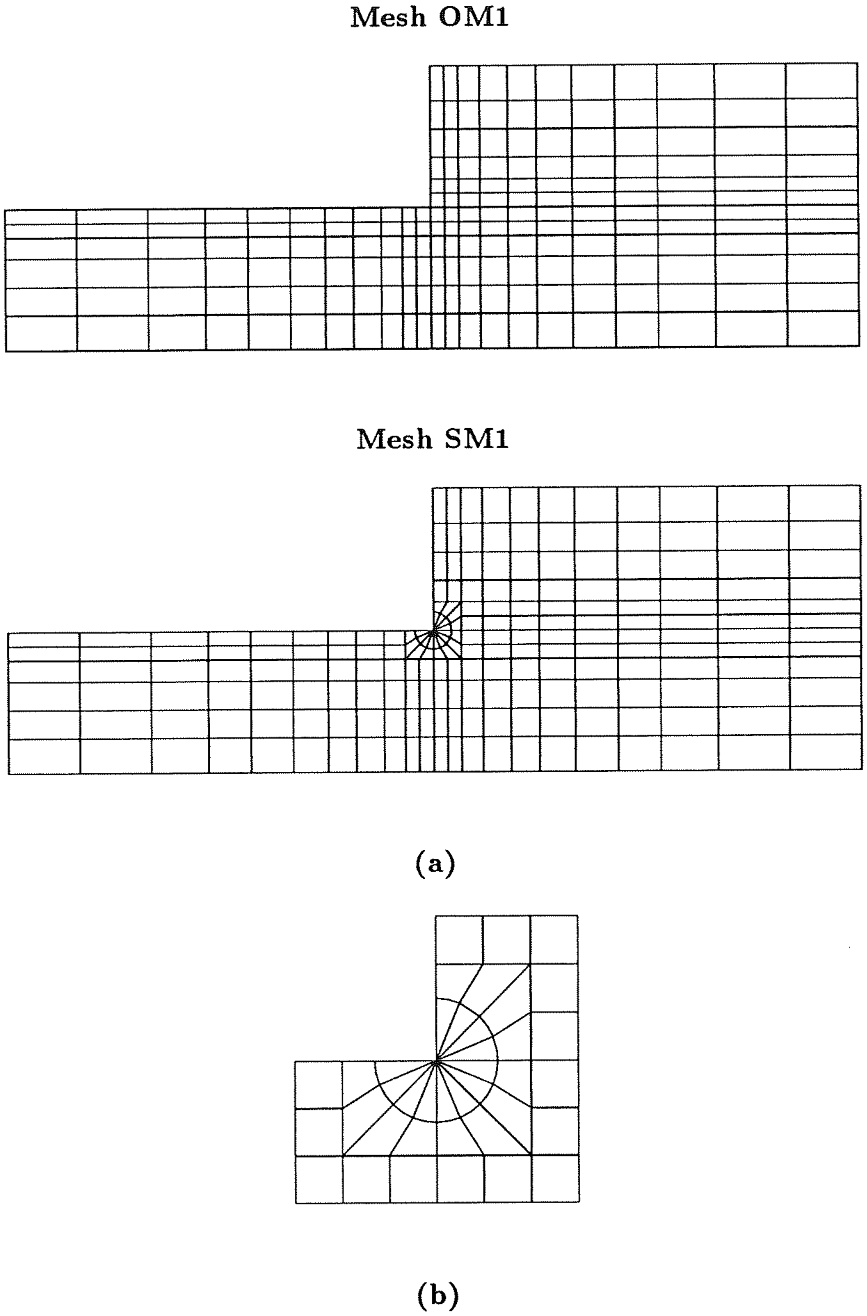

Figure 4.4: (a) Parts of the coarsest ordinary and singular meshes for the sudden-expansion problem.
(b) Structure of singular meshes near the corner.

The trial functions for the velocities are of the general form

$$\Phi^i = N^i(\xi)\, P^i(\eta)\,, \tag{4.17}$$

with P varying quadratically with η to maintain compatibility with the adjoining elements. With five nodes in the radial direction ξ, N is given by

$$N = A_0 + A_1\, \xi^{n_1} + A_2\, \xi^{n_2} + A_3\, \xi^{n_3} + A_4\, \xi^{n_4}\,. \tag{4.18}$$

The constants A_i are determined by requiring that $N^i(\xi_j) = \delta_{ij}$, where ξ_j are the equally spaced positions of the velocity nodes. An alternate way to generate the functions N^i is given by Hughes and Akin [78], but it is too tedious for the 13-node elements used here. The pressure basis functions are given by a lower-order interpolation:

$$\Psi^i = M^i(\xi)\, Q^i(\eta)\,, \tag{4.19}$$

with Q varying linearly with η (two pressure nodes in η direction) and M having the same form as $dN/d\xi$:

$$M = B_1\, \xi^{n_1-1} + B_2\, \xi^{n_2-1} + B_3\, \xi^{n_3-1} + B_4\, \xi^{n_4-1}\,. \tag{4.20}$$

Again, the constants B_i are determined by requiring that $\Psi^i(\xi_j) = \delta_{ij}$, where now ξ_j are the positions of the pressure nodes.

For the sudden expansion problem, we require that two terms of the velocity trial functions match the two leading expansion terms, and the other two are linear and quadratic. In other words, we choose $n_1 = 0.544$, $n_2 = 0.909$, $n_3 = 1$ and $n_4 = 2$. Similarly, for the die-swell problem we take $n_1 = 0.5$, $n_2 = 1$, $n_3 = 1.5$ and $n_4 = 2$. Note that for this special case the basis functions are easily obtained using Lagrange interpolation [55].

Applying Galerkin's principle, we weight the momentum equation by the velocity basis functions Φ^i and apply the divergence theorem,

$$\int_S \frac{2H}{Ca} \mathbf{n}\, \Phi^i\, dS - \int_V \{\, \nabla\mathbf{T} \cdot \nabla\Phi^i + Re\, \mathbf{u} \cdot \nabla\mathbf{u}\, \Phi^i \,\}\, dV = 0\,, \quad i = 1, 2, \cdots, N_u\,, \tag{4.21}$$

and we weight continuity by the pressure basis functions Ψ^i,

$$\int_V \nabla \cdot \mathbf{u} \, \Psi^i \, dV = 0 \, , \qquad i = 1, 2, \cdots, N_p \, . \quad (4.22)$$

Here V is the domain, S is the free surface boundary (for the die-swell problem), and N_u and N_p are the numbers of velocity and pressure nodes, respectively. In the case of the die-swell problem, we also weight the kinematic equation by the free surface quadratic basis functions W^i:

$$\int_S \mathbf{n} \cdot \mathbf{u} \, W^i \, dS = 0 \, , \qquad i = 1, 2, \cdots, N_h \, , \qquad (4.23)$$

where N_h is the number of free surface nodes. Equations (4.21), (4.22) and (4.23) constitute a nonlinear system of equations efficiently solved by the Newton method and standard subroutines, e.g., frontal methods [75].

The mesh is updated at each iteration by the newly found free-surface location values h_i, which are determined simultaneously with the primary unknowns u_i, v_i and p_i. Note that the nodes of the singular elements are at a constant distance from the singular point, rotating around the singular point according to the shape and the position of the free surface. The nodes of the ordinary elements are fixed at the x coordinate and move with the free surface in the y direction, so that the relative elevation is constant. The mid-nodes of the transition elements move in both x and y directions so that they are always at the middle of the elements' sides.

Standard 3x3 Gaussian quadrature is sufficient for the integration over the ordinary elements. However, the integration over the singular elements requires special or higher-order quadrature rules [139,55]. The simple quadrature used in Chapter III for the stick-slip problem is employed for the die-swell problem since the same singular elements are used. Nevertheless, it is tedious to develop a special quadrature for the sudden-expansion problem due to the many incommensurable powers of the radial coordinate that appear

Table 4.2: Data for sudden-expansion meshes ($L_2 = 10$).

Mesh	Number of elements	Number of nodes	Degrees of freedom	Size of corner elements
OM1	294	1261	2859	0.100
OM2	364	1549	3509	0.050
OM3	440	1861	4213	0.020
OM4	522	2197	4971	0.010
SM1	306	1347	3075	0.130
SM2	376	1635	3725	0.065
SM3	452	1947	4429	0.026
SM4	534	2283	5187	0.013

in the residual integrands. A higher-order (10x10) Gauss-Legendre integration was used instead.

4.4 Results and discussion

4.4.1 The sudden-expansion problem

The 2:1 sudden expansion problem was solved with both ordinary and singular finite elements for comparison. Results were obtained for various Reynolds numbers, ranging from 0 to 100. For our computations we constructed four ordinary (OM1, OM2, OM3, and OM4) and four singular meshes (SM1, SM2, SM3 and SM4). OM2 was obtained from OM1 by refining the columns and rows of elements near the corner. OM3 and OM4 were obtained in a similar manner. Information about the meshes is listed in Table 4.2. The singular meshes were generated from the corresponding ordinary meshes by replacing the 12 rectangular ordinary elements around the singular point with 12 triangular singular elements and 12 quadrilateral transition elements in the circular pattern shown in Figure 4.4. The radius of the singular elements was taken to be 1.2 times the size of the original ordinary square element (as in Chapter III).

The meshes were extended to a distance $L_1 = 3$ upstream, a length found adequate to approximate the inlet boundary conditions. As noted in [133], the outlet length L_2 should be greater than the maximum expected reattachment length plus a section sufficiently long to achieve fully developed flow beyond the point of reattachment. We took $L_2=10$ for *Re* up to 30, $L_2=15$ for $Re=50$, and $L_2=25$ for $Re=100$, in accordance with the reattachment length estimates in [45] and the outlet lengths used in [133]. No upwinding schemes were used [59]. We should note here that some of the meshes are very fine for Newtonian flow for two reasons: (a) to compare results from relatively coarse singular meshes with those from fine ordinary element meshes and (b) to check whether or not very small singular elements are required, provided that the form of the singularity is only valid very close to the wall at nonzero *Re*.

In general, the results from both the ordinary and the singular finite elements are in good agreement except in the vicinity of the singular point. In Figure 4.5, we plot the velocity, pressure and streamline contours at zero Reynolds number predicted with the singular finite elements (mesh SM1).

As expected, the results close to the singular point differ greatly from the ordinary finite element predictions. To illustrate this, we computed the normal stresses along the two walls forming the corner. In Figure 4.6 we compare the normal stresses along the horizontal wall ($y=1$) and in Figure 4.7 the normal stresses along the vertical wall ($x=0$) from meshes OM2, OM4 and SM1. The ordinary element results are characterized by spurious oscillations. The SFEM stresses are smooth and become infinite at the singular point, as they should. Figures 4.6 and 4.7 suggest that the singular elements give more accurate results, with no oscillations for relatively coarse meshes.

One of the goals in this investigation was to study the sensitivity of the results to the powers n_i of the basis functions. In Figure 4.8, we plot the normal stresses along the horizontal wall predicted with $n_1=0.544$, 0.2 and 0.8. We kept the values of the

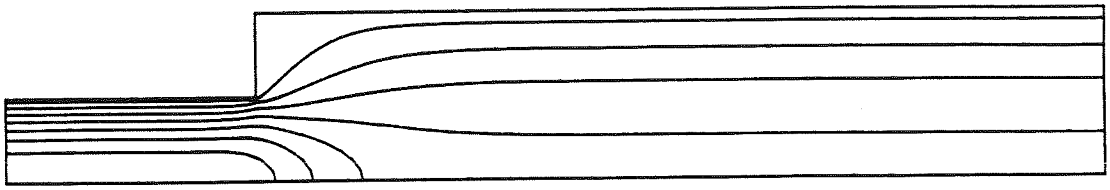

(a) U VELOCITY CONTOURS

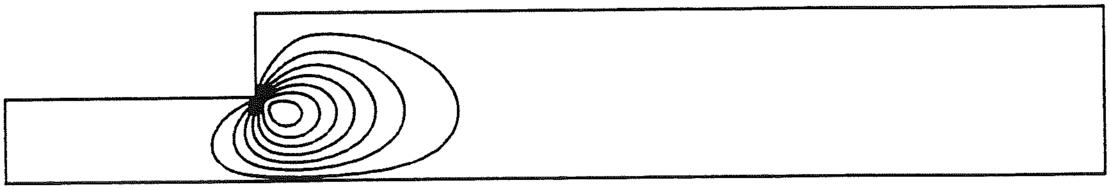

(b) V VELOCITY CONTOURS

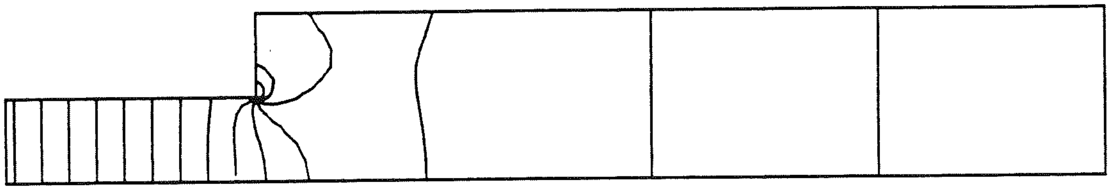

(c) PRESSURE CONTOURS

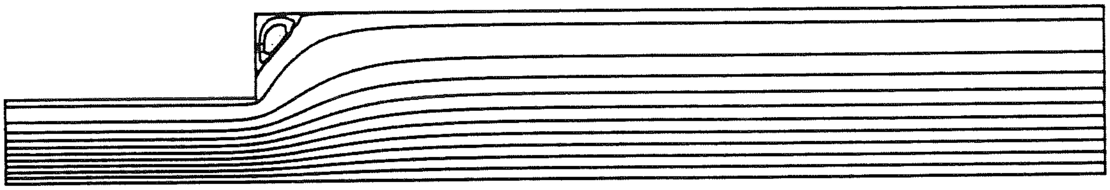

(d) STREAMLINES

Figure 4.5: Results at $Re = 0$: (a) x-velocity u, (b) y-velocity v, (c) pressure p, (d) streamlines.

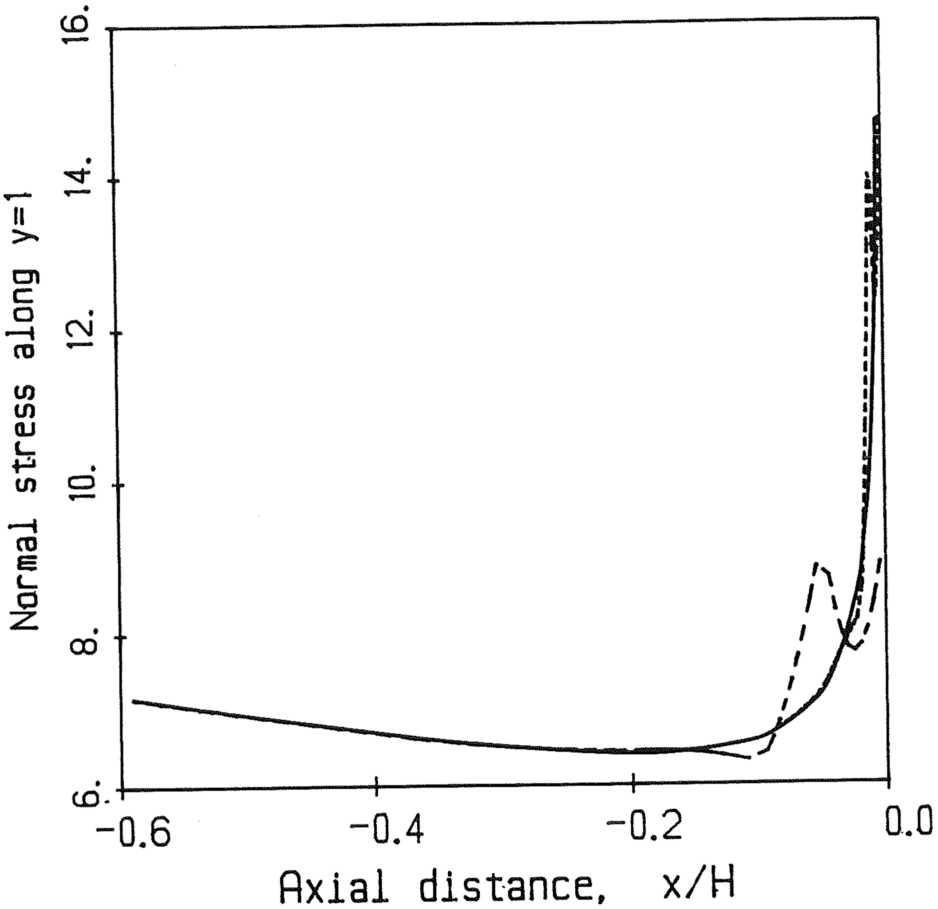

Figure 4.6: Normal stresses along the horizontal wall ($y = 1$) at $Re = 0$. Results with OM2 (- - -), OM4 (- - - -) and SM1 (———).

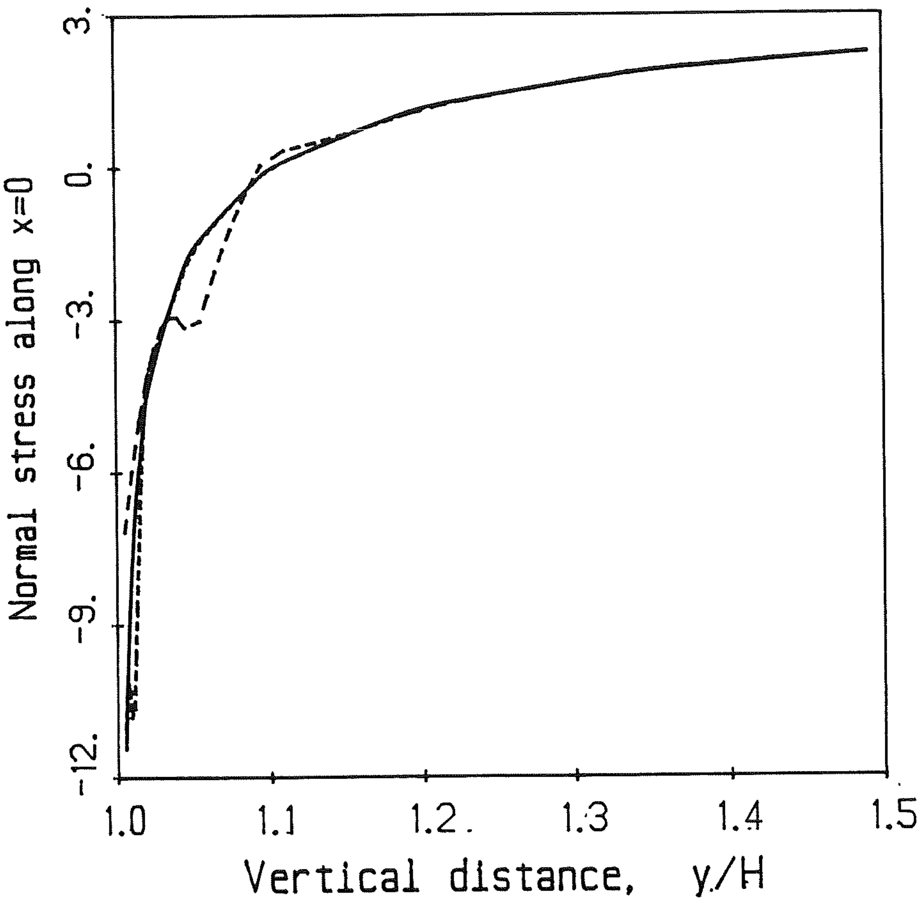

Figure 4.7: Normal stresses along the vertical wall ($x = 0$) at $Re = 0$. Results with OM2 (- - -), OM4 (- - - -) and SM1 (——).

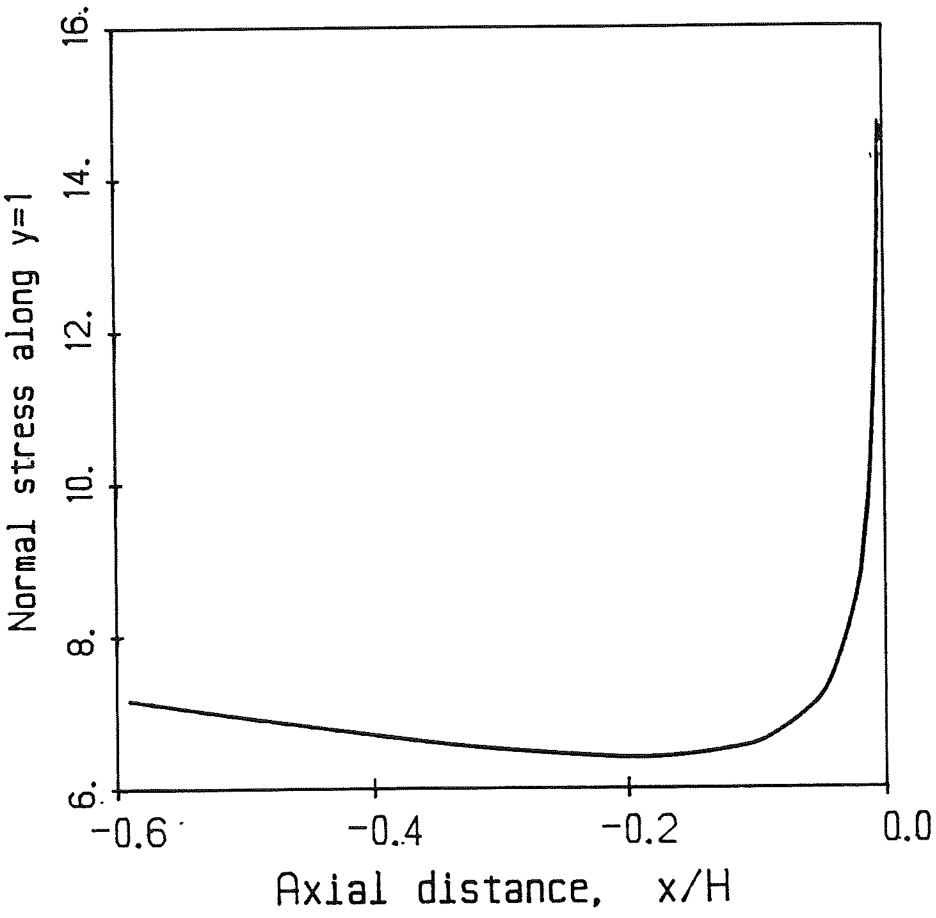

Figure 4.8: Normal stresses along the horizontal wall ($y = 1$) at $Re = 0$.
Results with SM1 and $n_1 = 0.2$ (- - -), 0.8 (- - - -) and 0.544 (——).

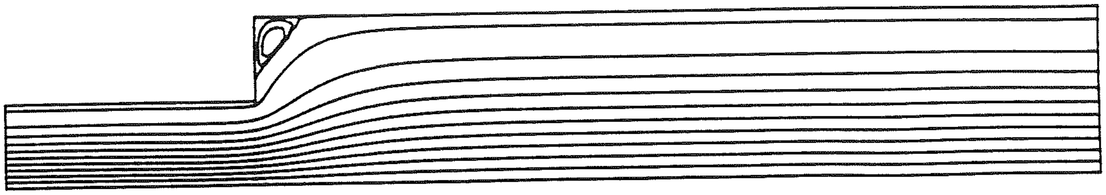

(a) Re = 0

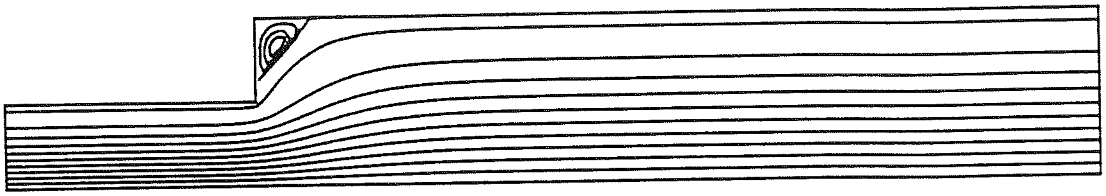

(b) Re = 1

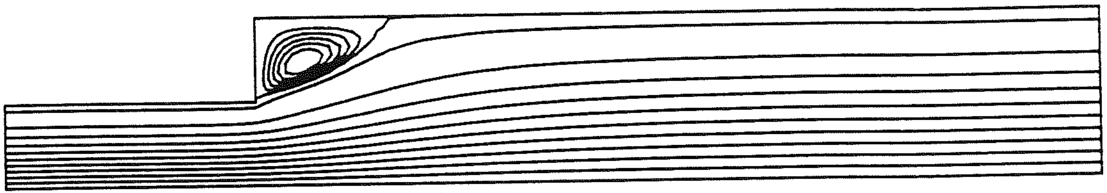

(c) Re = 10

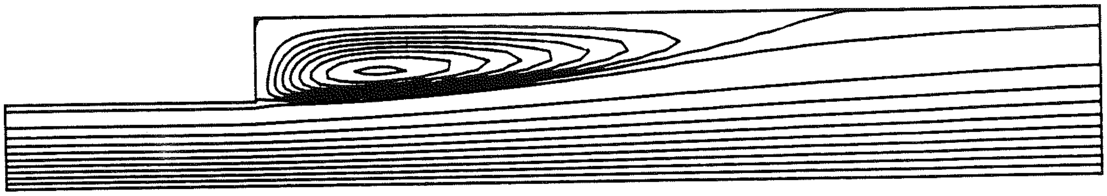

(d) Re = 50

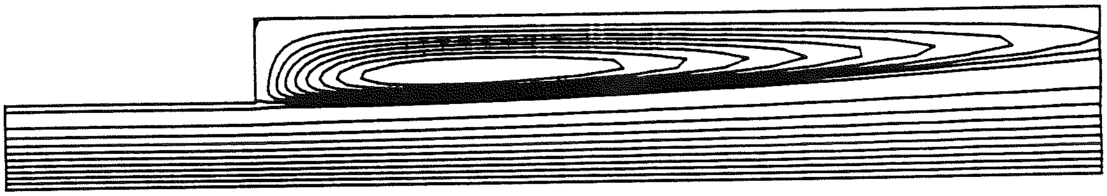

(e) Re = 100

Figure 4.9: Streamlines at different Re (with mesh SM1): (a) $Re = 0$, (b) $Re = 1$, (c) $Re = 10$, (d) $Re = 50$, (e) $Re = 100$.
The maximum values of the streamfunction in the vortex are 1.0006, 1.0010, 1.0124, 1.0412, and 1.0476, respectively.

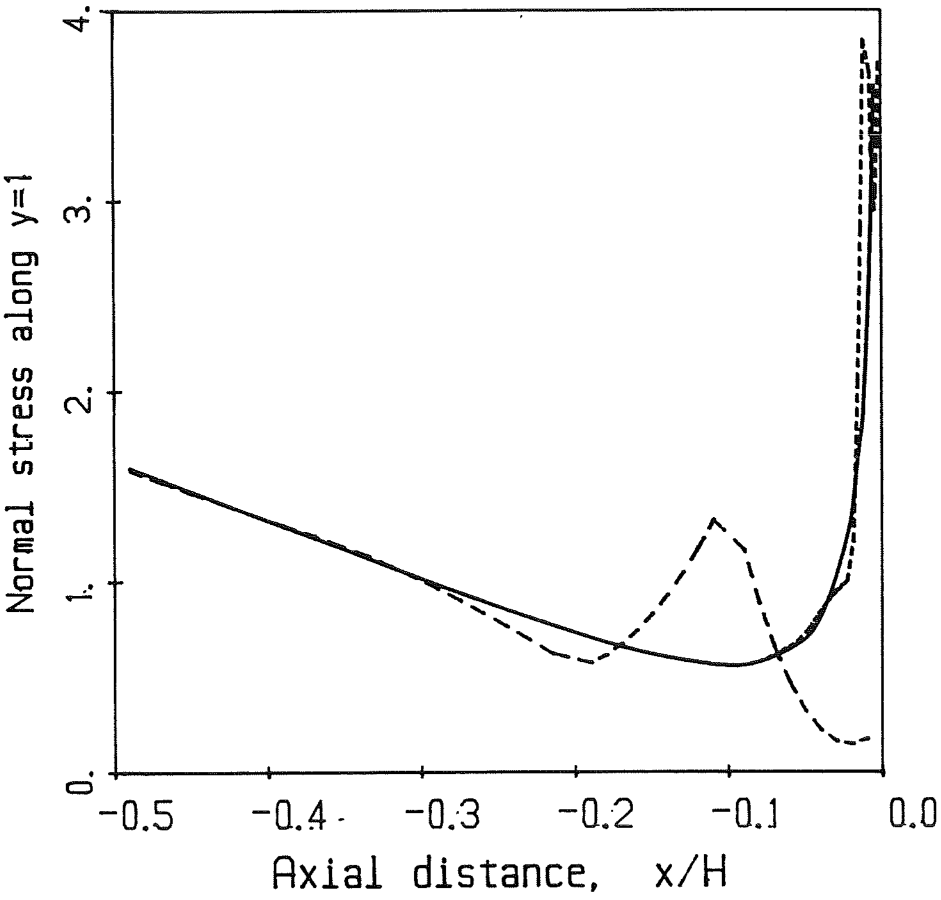

Figure 4.10: Normal stresses along the horizontal wall ($y = 1$) at $Re = 10$. Results with OM2 (- - -), OM4 (- - - -) and SM1 (———).

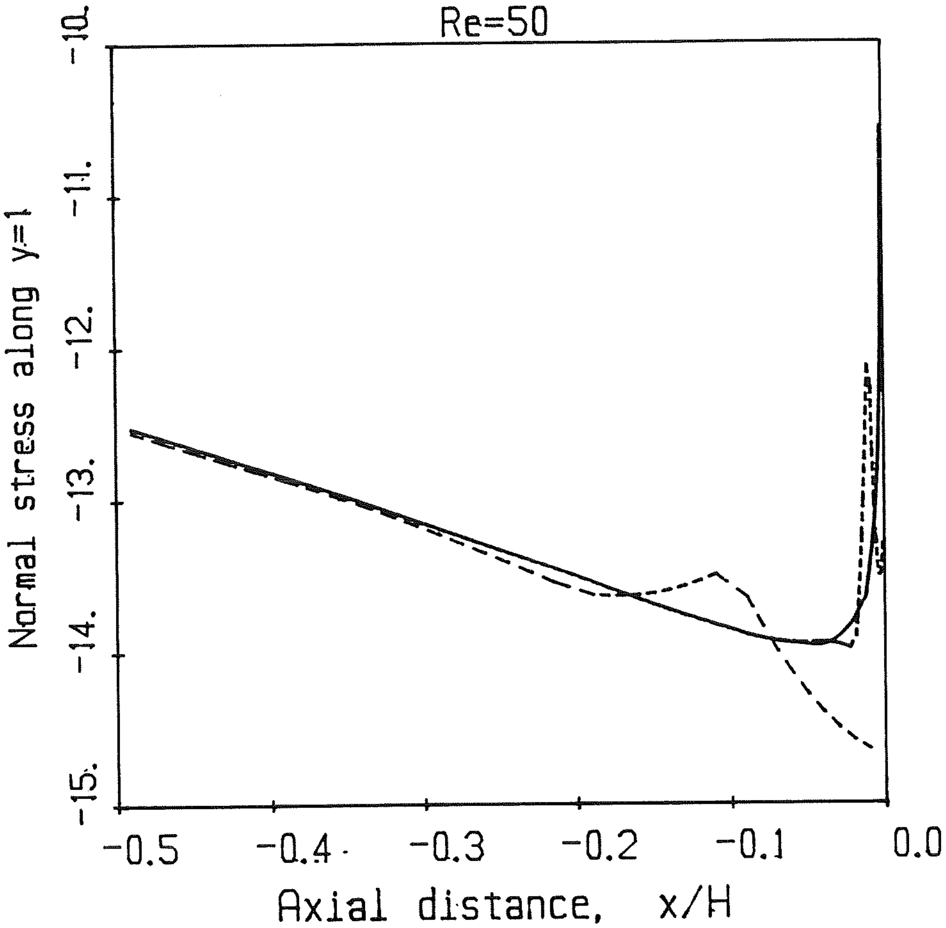

Figure 4.11: Normal stresses along the horizontal wall ($y = 1$) at $Re = 50$.
Results with OM2 (- - -), OM4 (- - - -) and SM1 (———).

other powers constant. The results agree well, indicating that the normal stresses are rather insensitive to the powers n_i. Changing the value of the second exponent n_2 from 0.909 to 0.5 and 1.5 reaffirmed this conclusion. It seems that the removal of the pressure node from the singular point plays a more crucial role in improving the solution than the accuracy of n_i.

Next, we applied singular finite elements at nonzero Reynolds numbers, $Re=0$, 1, 10, 50, and 100. Again the singular finite elements give the same solution far from the corner as the ordinary finite elements. The streamlines predicted with mesh SM1 are shown in Figure 4.9; the reattachment lengths are in good agreement with the results in [133]. The line of separation on the vertical wall moves towards the corner as Re is increased.

Once again, a more severe test is to compare the normal stress results. In Figures 4.10 and 4.11 the predicted normal stresses along the horizontal wall from meshes OM2, OM4 and SM1 have been plotted for $Re = 10$ and 50. The singular finite elements give more accurate results for relatively coarse meshes. Similar results were obtained for the normal stresses along the vertical wall $x=0$. All singular meshes give essentially the same results indicating that smaller singular elements are not necessary for the nonzero Reynolds number flow. This, in conjunction with the previous observation that the normal stresses are rather insensitive to the powers n_i, gave us confidence to proceed to the solution of the die-swell problem using the SFEM.

4.4.2 The die-swell problem

For the die-swell computations we constructed three ordinary (OM1, OM2, OM3) and three singular meshes (SM1, SM2, SM3). The singular meshes, shown in Figure 4.12, were again obtained by modifying the corresponding ordinary meshes. Data about all meshes are given in Table 4.3. The meshes extend up to four channel half-widths upstream and downstream. Again, as Reynolds number increases we must increase the downstream

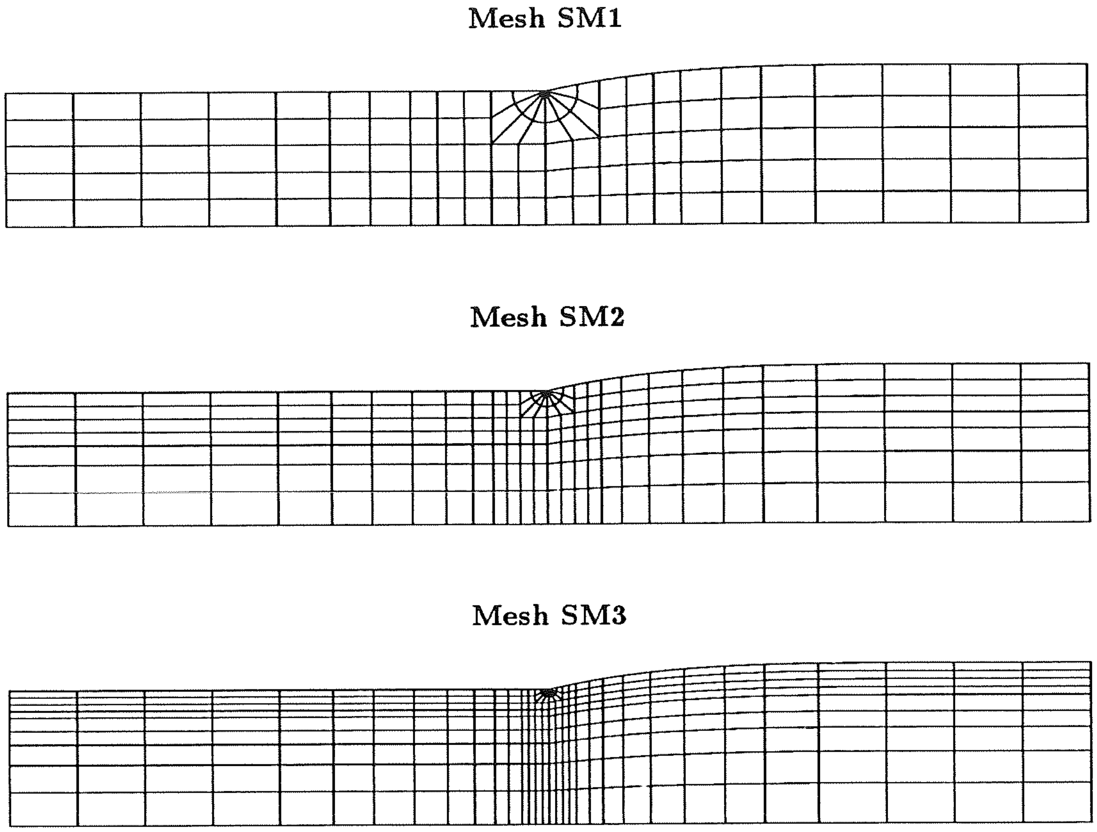

Mesh SM1

Mesh SM2

Mesh SM3

Figure 4.12: Singular meshes for the die-swell problem.

length L_2. As we previously mentioned, full-Newton iteration is used to solve this free-surface problem. The free-surface profile is computed simultaneously with the velocity and pressure fields, and the mesh is updated according to the position and the shape of the free surface. A zero-order continuation is used for both parameters involved, Re and Ca, to proceed to higher Re and lower Ca.

The obvious choice for comparisons between ordinary and singular finite elements is the free surface profile. In Figure 4.13, we plot the predicted free-surface profiles for all the ordinary meshes and SM1. All the singular meshes gave practically the same results and predicted the same die-swell ratio (1.186). As we see in Figure 4.13, the ordinary elements converge slowly to the solution obtained by a relatively coarse singular mesh. The singular elements speed up the convergence of the free surface considerably.

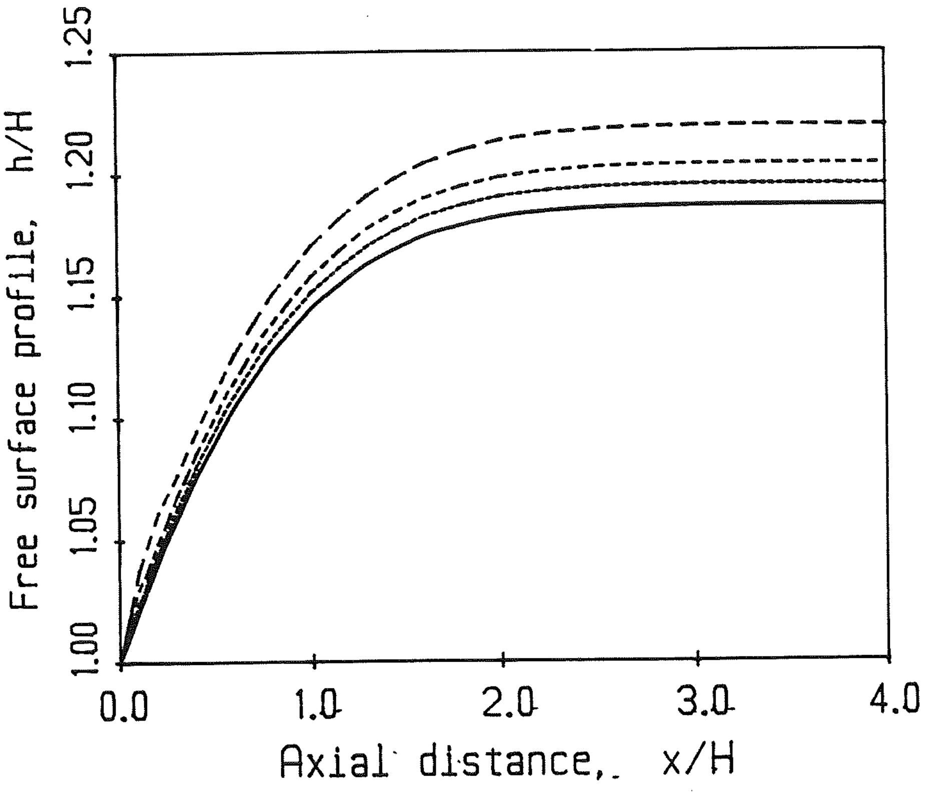

Figure 4.13: Computed free surface profiles at zero *Re* and zero surface tension. Results with OM1 (- - -), OM2 (- - -), OM3 (- - - -) and SM1 (——).

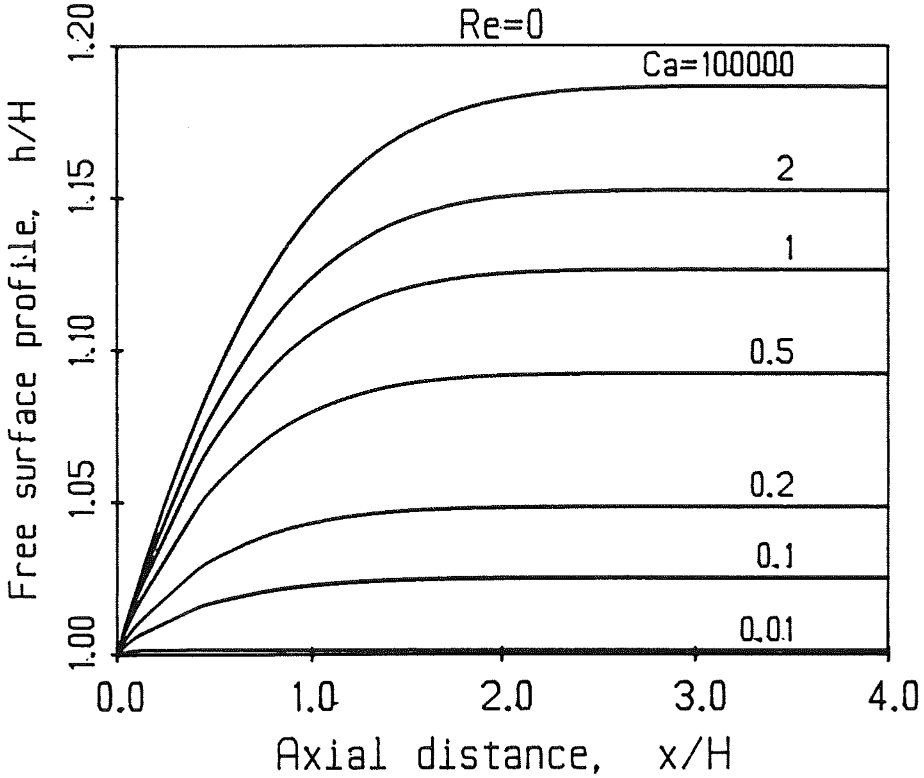

Figure 4.14: Free surface profiles at various Ca and zero Re.

Table 4.3: Data for die-swell meshes ($L_2=4$).

Mesh	Number of elements	Number of nodes	Degrees of freedom	Size of corner elements
OM1	120	539	1253	0.20
OM2	196	855	1971	0.10
OM3	288	1235	2833	0.05
SM1	128	597	1401	0.24
SM2	204	913	2119	0.12
SM3	296	1293	2981	0.06

Results have been obtained for various Re and Ca. The SFEM solution in the neighborhood of the singularity proved to be insensitive to variations of the powers n_i supporting the use of the same singular elements at any apparent angle of separation or at different capillary numbers. The free surface profiles for various capillary numbers at Re=0, obtained with mesh SM1, are plotted in Figure 4.14.

In closing, we should note that the SFEM is not free of shortcomings or limitations. The radial form of the singularity must be known (to a certain accuracy) and additional programming is required. The method also leads to stiffness matrices with bigger semibandwidths or frontwidths than those from the generating ordinary element meshes. Nevertheless, this is the price one must pay for the improved accuracy and the faster rate of convergence.

4.5 Concluding remarks

Singular finite elements have been used to solve the 2:1 sudden-expansion and the die-swell problems at various Reynolds numbers, ranging from 0 to 100. The singular elements surround the singular point and have no pressure node there. The corresponding basis functions embody the form of the singularity for each case. The elements used for creeping flow were used to solve the problem for nonzero Reynolds numbers, because the form of the local solution remains unchanged very close to the singular point. The method gives more accurate results than those from more refined ordinary finite element meshes; in addition, no oscillations are observed. The normal stress results were found to be rather insensitive to the singularity powers used in the construction of the singular basis functions.

For the die-swell problem, the singular elements developed for the stick-slip problem have been used. The singular elements speed up the convergence of the free surface considerably.

CHAPTER V

THE SINGULAR BASIS FUNCTION APPROACH

> "But there is one realization all men of good will share: in the end our works make us feel ashamed, we have to start out again, and each time the sacrifice has to be made anew."
>
> Hermann Hesse, *Narcissus and Goldmund.*

In Chapters III and IV we developed *singular finite elements* to solve the stick-slip, the sudden-expansion and the die-swell problems. These elements proved to be very successful in improving the accuracy in the vicinity of the singular point, in eliminating the normal stress oscillations and in improving the rate of convergence, especially that of the free surface in the die-swell problem. Nevertheless, as pointed out in the aforementioned chapters, the singular elements have a fundamental limitation: the region around the singular point cannot be refined extensively. By refining the mesh, the size of singular elements over which the singularity is given special attention is reduced.

The objective of this chapter is to employ the alternative *singular basis function approach* in order to avoid this difficulty. Two different methods are examined:

(1) The *blended singular basis function method* (BSBFM), and

(2) The *integrated singular basis function method* (ISBFM).

Before proceeding to fluid mechanics problems in Chapter VI, we will solve Laplace's equation here in order to test and evaluate the two methods[1].

5.1 Introduction

Singularities often occur in models of engineering problems due to discontinuities in the boundary conditions or abrupt changes in the boundary shape (e.g., corners). Two well-known examples are the crack-tip problem in fracture mechanics [141] and the sudden-expansion problem in fluid mechanics [57].

When using numerical methods to solve problems with singularities, one must pay special attention to the singular regions. In both the finite difference and the finite element methods, local refinement is often employed near the singularity in order to achieve reasonable accuracy. However, the accuracy achieved and the rate of convergence are generally not uniform nor satisfactory [141].

Incorporating the form of the singularity in the numerical solution improves the accuracy in the neighborhood of the singularity and increases the convergence rate. A local analysis produces the general form of the singularity:

$$u(r,\theta) = \sum_{i=1}^{\infty} \alpha_i \, r^{\lambda_i} \, f_i(\theta) \,, \tag{5.1}$$

where (r,θ) are the cylindrical coordinates centered at the singular point, u is the dependent variable, α_i are the singular coefficients, λ_i are the singularity exponents, and $f_i(\theta)$ represent the θ dependence of the solution. The local (or asymptotic) solution satisfies the governing equation in the domain and the boundary conditions along the boundary segments adjacent to the singular point (it does not identically satisfy the boundary conditions along the rest of the boundary). The idea of building the leading terms of the local expansion into the numerical solution has been successfully adopted in a variety

---

[1] The material of this chapter is to appear in [112].

of methods such as relaxation techniques [107], finite differences [164], finite elements [141,106,158,159,149,55,43,42], global elements [86,68], and boundary elements [82].

In this work, we focus on the finite element method, which has been very effective in solving complex problems in many different engineering fields. (For an in-depth review of singular finite element techniques, see Fix [42] and Gallagher [48].) The local solution can be incorporated in two basic ways:

1. Singular Finite Element Approach. Special elements are used in a small region around the singularity, while standard elements are used in the rest of the domain. The shape functions defined on the special elements take into account the known form of the singularity. This approach has one fundamental drawback: the polynomial (regular) portion of the mesh cannot be refined independently of the singular elements.

2. Singular Basis Function Approach. A set of supplementary functions chosen to reproduce the leading terms of the singularity solution is added to the standard finite element solution expansion. In this approach the singular terms may be chosen independently of the mesh.

In this chapter, we follow the singular basis function approach, in which the supplementary basis functions W_i take the general form

$$W_i = Q\, r^{\lambda_i} f_i(\theta)\,, \tag{5.2}$$

where Q is an optional blending function. At least three kinds of singular basis functions appear in the literature:

1. Functions with *two-zone blending* [141,158]. In this case,

$$Q = \begin{cases} 1\,, & 0 \leq r \leq r_0 \\ P_i(r)\,, & r_0 \leq r \leq r_1 \\ 0\,, & r \geq r_1 \end{cases} \tag{5.3}$$

   where r_0 and r_1 may be chosen independently of the mesh size, and the polynomial P_i smoothly forces the singular functions to zero at $r{=}r_1$. The functional form near the singular point is not affected by the blending, and no extra boundary terms appear in the finite element formulation.

2. Functions with *one-zone blending* [106,44]. Here, Q modifies the singular terms even near the singular point. One choice is simply to let r_0 go to 0 in equation (5.3). Another choice is to conform the blending to the underlying mesh, e.g.,

$$Q = \begin{cases} (1-x^2)(1-y^2)\,, & x^2 \leq 1,\ y^2 \leq 1 \\ 0\,, & \text{otherwise} \end{cases} \tag{5.4}$$

   for a rectangular grid with the singularity at x=0, y=0. Again, no extra boundary terms appear in the formulation, since the singular contributions are zero along the boundaries.

3. Exact functions (no blending) [106]. In this case, $Q = 1$. Additional boundary terms appear in the finite element formulation, since the singular functions are not zero along parts of the boundary. Also, the essential (Dirichlet) boundary conditions must be enforced separately.

Many researchers have successfully used the singular basis function approach to solve a variety of problems such as the Motz problem and the cracked-beam problem (described below), the L-shaped membrane vibration problem, problems with reentrant corners, and, of course, problems in fracture mechanics. The two-zone and one-zone blending methods have two main advantages over other singular treatments: they are easy to program and easily extended to nonlinear problems. However, the blending function introduces additional arbitrary parameters, contaminates the singular functions, and reduces the accuracy; in addition, a high-accuracy quadrature rule must be used to integrate the blended singular functions in the neighborhood of the singular point [141]. The unblended method avoids the singular function contamination problem, but it requires separate enforcement of the essential boundary conditions and accurate quadrature rules to evaluate the integrals.

In this chapter we present a new method with no blending functions, the integrated singular basis function method (ISBFM). In the ISBFM, the exact asymptotic terms are used as the singular functions, and the volume integrals with singular contributions are reduced to boundary integrals by means of the divergence theorem. This method avoids the reduced accuracy associated with the blending function and eliminates the need to evaluate singular integrands. The method is described in detail in section 5.2.

We demonstrate the ISBFM on two problems that have been extensively studied by other researchers: the Motz problem [107] and the cracked-beam problem [44]. To make comparisons, we also use one-zone blending functions, i.e., equation (5.4). We will refer to this method as the blended singular basis function method (BSBFM)[2].

The Motz problem

Figure 5.1 illustrates the Motz problem[3], which has been a benchmark problem in testing the various singular approaches proposed in the literature. Whiteman [164] employed special finite difference methods to solve the problem, while Hendry and Delves [68] and Kermode *et al.* [86] used the global element method to determine the singular coefficients[4].

---

[2] In Appendix C, we show that the one-zone blending functions give better results than the two-zone singular functions.

[3] The Motz problem is a transformation of the original problem defined by Motz in [107].

[4] The reader can find a comprehensive review for the Motz problem in [86].

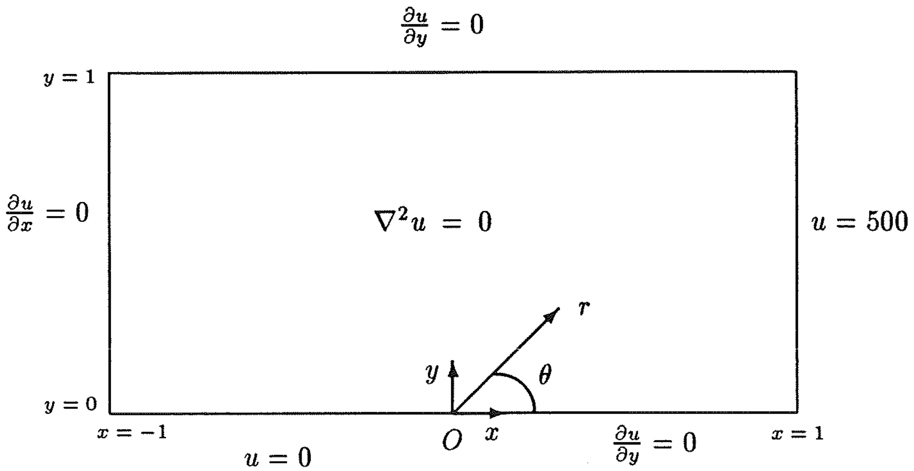

Figure 5.1: The Motz problem.

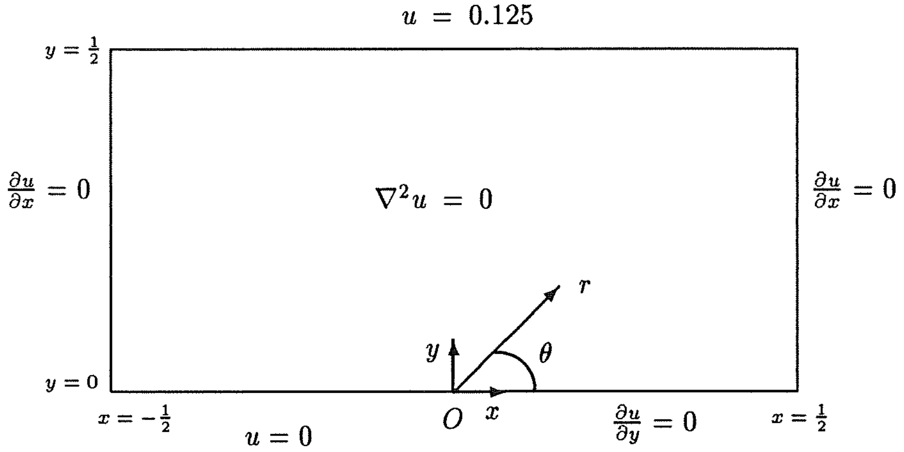

Figure 5.2: The cracked-beam problem.

Wait and Mitchell [159] used a two-zone blended singular basis function approach with disappointing results. The zones they employed were very small, and some of the singular functions were inappropriate for the Motz problem. Morley [106] applied both one-zone blending and no blending functions. While the solution was improved by the singular treatments, the actual values of the singular coefficients were not satisfactorily accurate. Wigley [165] obtained very accurate estimates for the leading singular coefficients with an inherently iterative approach. He first generated an approximate numerical solution using standard finite element or finite difference methods and then estimated the first singular coefficient from this solution. Next, he modified the original problem by subtracting out the first singular term and again generated an approximate numerical solution to this modified problem, which he used to estimate the second singular coefficient, and so on. Because it is iterative, his technique is applicable to finite element as well as finite difference methods. He obtained excellent results for the first several singular coefficients in the Motz problem as well as the cracked-beam problem.

The cracked-beam problem

The second problem we solved is the cracked-beam problem [42,165], illustrated in Figure 5.2. Fix, Gulati, and Wakoff [44] used blended singular basis function approaches for this problem. They found that their method was efficient and moderately accurate. In [44], Fix reviewed singular basis function approaches and discussed the cracked-beam problem. As mentioned above, Wigley [165] obtained very accurate coefficients for the cracked-beam using his iterative method [165].

In section 5.2, we present the finite element formulations with the standard finite element method, the BSBFM and the ISBFM. The results for the Motz problem, in section 5.3, indicate that the ISBFM yields an algebraic rate of convergence with respect to mesh refinement, and a rapid rate of convergence with the number of singular functions, which appears to be exponential[5]. The accuracy of both the ISBFM and the BSBFM is substantially better than that of the ordinary finite element method. Furthermore, the estimates of the leading coefficients with the ISBFM are more accurate than those with the BSBFM. In section 5.4 we solve the cracked-beam problem and confirm the accuracy and rate of convergence of the ISBFM. In section 5.5 we summarize our conclusions.

5.2 Finite Element Methods

Mathematically, we state the general problem as

$$\nabla^2 u = 0 \qquad \text{in } \Omega \tag{5.5}$$

$$u = g \qquad \text{on } \Gamma_1 \tag{5.6}$$

$$\frac{\partial u}{\partial n} = q \qquad \text{on } \Gamma_2 \tag{5.7}$$

where u is the unknown variable, Ω is the physical domain, Γ is the boundary of the domain ($\Gamma = \Gamma_1 + \Gamma_2$), and q and g are externally imposed values.

The weak form for Laplace's equation is given by

$$\int \nabla u \cdot \nabla \overline{u} \, d\Omega = \int q \overline{u} \, d\Gamma \,. \tag{5.8}$$

Here $\overline{u}$ is the virtual variable (or weight function), which is zero on boundary Γ_1. We use standard nine-node isoparametric finite elements to create a banded linear system of equations, which is solved using standard subroutines.

In our convergence studies, we will calculate the *variational indicator*[6], Π. For Laplace's equation, Π may be written as

$$\Pi = \frac{1}{2} \int \nabla u \cdot \nabla u \, d\Omega - \int q \, u \, d\Gamma \,. \tag{5.9}$$

---

[5] As discussed later in this chapter, the treatment of the singular terms is closely related to the spectral tau method [23].

[6] For more information about the variational indicator see [14,27,50].

Because there is no analytical expression for Π available (for the problems we chose), we use the estimate from a very fine mesh as the 'exact' value of Π (Π_{exact}).

5.2.1 The Blended Singular Basis Function Method (BSBFM)

In the BSBFM, we substitute the sum of regular (u^r) and singular (u^s) basis functions into the weak form (5.8), which becomes

$$\int \nabla(u^r + u^s) \cdot \nabla\overline{u}^r \, d\Omega = \int q\,\overline{u}^r \, d\Gamma \; , \tag{5.10}$$

for the regular functions and

$$\int \nabla(u^r + u^s) \cdot \nabla\overline{u}^s \, d\Omega = \int q\,\overline{u}^s \, d\Gamma \; , \tag{5.11}$$

for the singular functions. We use ordinary nine-node isoparametric basis functions for u^r and $\overline{u}^r$. However, as discussed in the introduction, rather than using the exact singular basis functions for u^s and $\overline{u}^s$ we multiply them by a polynomial blending function that decays to zero away from the singular point. Here, we use one-zone blending:

$$Q = (1 - x^2)(1 - y^2) \, . \tag{5.12}$$

Therefore, we write

$$u^s = \sum \alpha_i (1 - x^2)(1 - y^2)\, r^{\lambda_i} f_i(\theta) \; , \tag{5.13}$$

and

$$\overline{u}^s = \sum \overline{\alpha}_i (1 - x^2)(1 - y^2)\, r^{\lambda_i} f_i(\theta) \tag{5.14}$$

for the singular terms. The unknowns are the singular coefficients α_i, which are not associated with any specific physical location; λ_i and $f_i(\theta)$ are known for each specific singularity from the local analysis. We include only the first few terms of the local solution in (5.13) and (5.14). Inserting the expressions for u^r and u^s into (5.10) and (5.11) yields a matrix equation of the form:

$$\begin{bmatrix} \mathbf{K}_{rr} & \mathbf{K}_{rs} \\ \mathbf{K}_{rs}^T & \mathbf{K}_{ss} \end{bmatrix} \begin{bmatrix} \mathbf{u}^r \\ \underline{\alpha} \end{bmatrix} = \begin{bmatrix} \mathbf{F} \\ \mathbf{0} \end{bmatrix} \tag{5.15}$$

where $\mathbf{K}_{rr}$ represents the ordinary element stiffness, $\mathbf{K}_{ss}$ represents the stiffness due to the singular functions, and $\mathbf{K}_{rs}$ couples the ordinary and singular terms[7]. We must use a high-order numerical quadrature to evaluate $\mathbf{K}_{ss}$ and $\mathbf{K}_{rs}$ near the singularity[8]. However, no special boundary condition treatments are required since the singular functions are zero on the domain boundary Γ.

5.2.2 The Integrated Singular Basis Function Method (ISBFM)

In the ISBFM, we again use standard nine-node isoparametric basis functions for u^r and $\overline{u}^r$, but for the singular functions we use the exact asymptotic terms:

$$u^s = \sum \alpha_i \, r^{\lambda_i} f_i(\theta) \, , \tag{5.16}$$

and

$$\overline{u}^s = \sum \overline{\alpha}_i \, r^{\lambda_i} f_i(\theta) \, . \tag{5.17}$$

Because u^s and $\overline{u}^s$ satisfy the Laplace equation, it is possible to reduce equations (5.10) and (5.11) to

$$\int \nabla u^r \cdot \nabla \overline{u}^r d\Omega + \int \overline{u}^r \frac{\partial u^s}{\partial n} d\Gamma = \int q \, \overline{u}^r d\Gamma \, , \tag{5.18}$$

---

[7] Notice that the use of the singular functions destroys the banded structure of the stiffness matrix. The additional equations attach additional full rows and columns to the matrix that is otherwise banded about the main diagonal, resulting in an "arrow-shaped" matrix structure. Matrices of this structure are very often encountered in engineering problems when a basic boundary value problem is augmented with scalar constraints or is solved simultaneously with densely coupled algebraic equations. Extensions of the standard algorithms are used in inverting the stiffness matrix to avoid extra operations in elimination as well extra storage requirements. Strang and Fix [141] proposed a modified Choleski's factorization algorithm; Thomas and Brown [146] developed an LU-decomposition subroutine for arrow-shaped matrices.
We should notice that modifications are not required if a ***skyline*** solver is used [14].

[8] For the effect of the order of integration on the calculated values of the singular coefficients, see Appendix C.

and

$$\int u^r \frac{\partial \overline{u}^s}{\partial n}\, d\Gamma + \int \frac{1}{2}\left(\overline{u}^s \frac{\partial u^s}{\partial n} + u^s \frac{\partial \overline{u}^s}{\partial n}\right) d\Gamma = \int q\, \overline{u}^s \, d\Gamma \, . \tag{5.19}$$

Notice that the divergence theorem has been applied to equation (5.11) in order to reduce the volume integral to a boundary integral in equation 5.19.

The essential boundary conditions are weakly enforced on Γ_1 with Lagrange multipliers[9], λ_u. Equations (5.18) and (5.19) become

$$\int \nabla u^r \cdot \nabla \overline{u}^r d\Omega + \int \overline{u}^r \frac{\partial u^s}{\partial n}\, d\Gamma_2 + \int \lambda_u \, \overline{u}^r d\Gamma_1 = \int q\, \overline{u}^r d\Gamma_2 \, , \tag{5.20}$$

$$\int u^r \frac{\partial \overline{u}^s}{\partial n}\, d\Gamma_2 + \int \frac{1}{2}\left(\overline{u}^s \frac{\partial u^s}{\partial n} + u^s \frac{\partial \overline{u}^s}{\partial n}\right) d\Gamma_2 \, -$$

$$\int \frac{1}{2}\left(\overline{u}^s \frac{\partial u^s}{\partial n} + u^s \frac{\partial \overline{u}^s}{\partial n}\right) d\Gamma_1 + \int \lambda_u \, \overline{u}^s \, d\Gamma_1 = -\int g\, \frac{\partial \overline{u}^s}{\partial n}\, d\Gamma_1 + \int q\, \overline{u}^s \, d\Gamma_2 \tag{5.21}$$

$$\int (u^r + u^s)\, \overline{\lambda_u}\, d\Gamma_1 = \int g\, \overline{\lambda_u}\, d\Gamma_1 \, . \tag{5.22}$$

The Lagrange multipliers appear only on the boundary Γ_1. To interpolate λ_u, we use standard quadratic isoparametric shape functions M^i,

$$\lambda_u = \sum_{i=1}^{3} \lambda_u^i M^i \, . \tag{5.23}$$

Inserting these interpolations into (5.20), (5.21), and (5.22), and assembling contributions from all elements yield a matrix equation of the form

$$\begin{bmatrix} \mathbf{K}_{rr} & \mathbf{K}_{rs} & \mathbf{K}_{r\lambda} \\ \mathbf{K}_{rs}^T & \mathbf{K}_{ss} & \mathbf{K}_{s\lambda} \\ \mathbf{K}_{r\lambda}^T & \mathbf{K}_{s\lambda}^T & \mathbf{0} \end{bmatrix} \begin{bmatrix} \mathbf{u}^r \\ \underline{\alpha} \\ \underline{\lambda_u} \end{bmatrix} = \begin{bmatrix} \mathbf{F}_r \\ \mathbf{F}_s \\ \mathbf{F}_{\lambda_u} \end{bmatrix} . \tag{5.24}$$

---

[9] For the use of Lagrange multipliers with constrained optimization problems, see [15]. For the use of Lagrange multipliers with finite elements, see [10,25,77,88,109].

Table 5.1: Computed values of α_1 for the Motz problem with various uniform meshes (2N×N elements; 1 singular function; the exact value of α_1 is 401.1625).

N	ISBFM	BSBFM
1	399.0450	349.9189
2	400.9539	396.5159
4	401.1377	401.9309
8	401.1594	402.2152
10	401.1609	402.1885
20	401.1623	402.1159

Table 5.2: Effect of increasing the number of singular basis functions for the Motz problem with the ISBFM (2x1 uniform mesh).

N_{SBF}	α_1	α_2	α_3	α_4	α_5
1	399.0450				
2	399.1915	74.1222			
3	399.2029	82.7775	13.5579		
4	400.5984	82.8772	13.5196	-7.6573	
5	400.7623	82.7665	13.5727	-7.3083	1.0838
Exact	401.1625	87.6559	17.2379	-8.0712	

This matrix system is again solved using standard subroutines.

Two important points should be noted. First, since the terms involving u^s and $\overline{u}^s$ satisfy the boundary conditions near the singular point, all of the surface integrands are non-singular and are evaluated with an ordinary Gauss quadrature. Second, this approach is completely equivalent to subtracting the singular terms from the original problem (see Appendix C).

5.3 Results for the Motz Problem

Figure 5.1 shows the geometry, governing equations, and boundary conditions for the Motz problem. A non-removable singularity arises at x=y=0, where the boundary

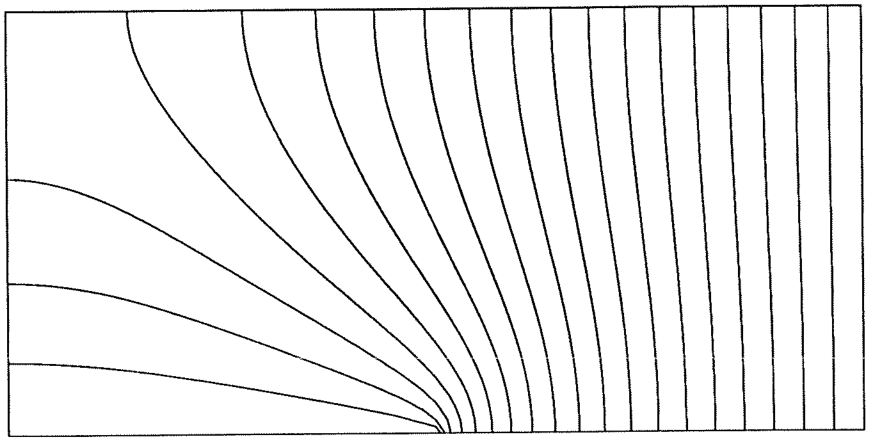

Figure 5.3: Contours for the Motz problem (contour lines at u=25, 50,..., 500).

Table 5.3: Effect of increasing the number of singular basis functions for the Motz problem with the BSBFM (2x1 uniform mesh).

N_{SBF}	α_1	α_2	α_3	α_4	α_5
1	349.9189				
2	349.9123	0.7500			
3	349.9102	-7.7960	8.0203		
4	342.0774	-7.9401	8.0938	-20.0383	
5	344.3108	-7.9247	8.0947	-19.5238	2.0777
Exact	401.1625	87.6559	17.2379	-8.0712	

condition suddenly changes from $u=0$ to $\partial u/\partial y=0$. The local solution [165] is given by

$$u(r,\theta) \;=\; \sum_{i=1}^{\infty} \alpha_i \, r^{(2i-1)/2} \cos\left[\left(\frac{2i-1}{2}\right)\theta\right] \tag{5.25}$$

where r, θ are shown in Figure 5.1. Figure 5.3 shows the contours of u for a typical solution.

First, we examine the effect of mesh refinement. Each mesh consists of 2N×N square nine-node elements. Table 5.1 displays the convergence of the first singular coefficient α_1 as the underlying mesh is refined, when only one singular function is used. Clearly, the ISBFM gives superior results compared to the BSBFM, converging rapidly to the exact value. Figure 5.4 shows the algebraic rate of convergence of Π as the mesh is refined. When no singular functions are used, the rate is only linear. Adding one singular function improves the convergence to slightly better than cubic (3.1), and a second singular function increases the rate to nearly quartic (3.9). Perhaps most significant, however, is the substantial increase in accuracy for Π when the first singular basis function is added. Figure 5.5 shows the rate of convergence of the singular coefficients α_i as the mesh is refined. With one singular basis function, α_1 converges essentially cubically. When two singular basis functions are used, the rate of convergence of α_2 is approximately linear, while the rate of convergence of α_1 is essentially unchanged.

Next, we study the effect of increasing the number of singular functions with a coarse 2×1 element mesh. As shown in Tables 5.2 and 5.3, increasing the number of functions for the ISBFM substantially improves the accuracy of the leading coefficients[10]. With the BSBFM, the leading coefficients are only slightly improved by the addition of more singular terms (due to the contamination of the singular functions by the blending); Whiteman [163], Morley [106], and Wait and Mitchell [159] also noted this effect. Figure 5.6 shows the rapid (roughly exponential) convergence of Π versus the number of

---

[10] N_{SBF} is the number of supplementary basis functions.

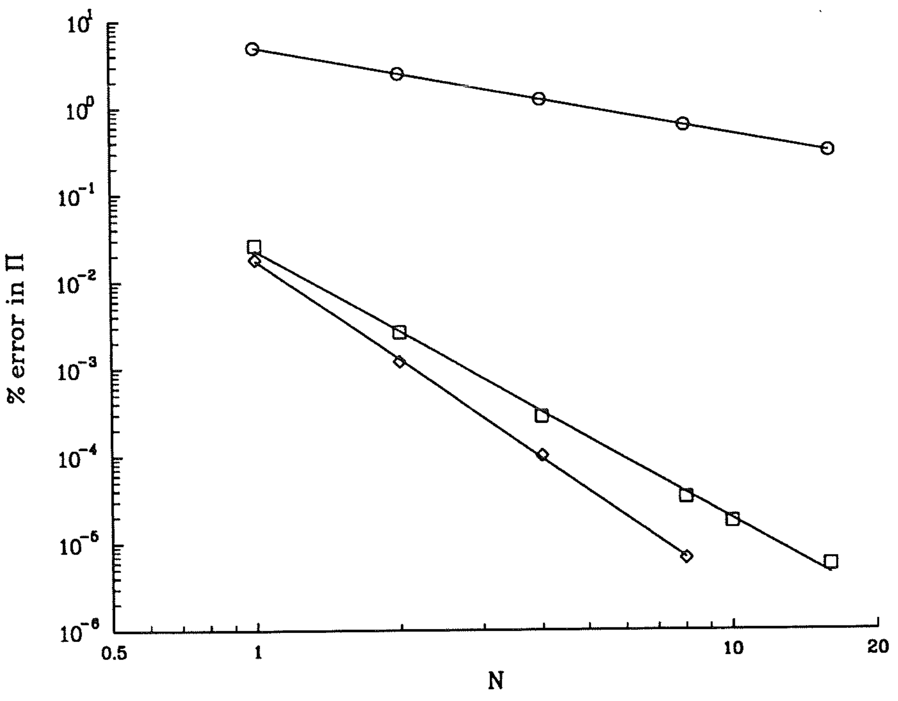

Figure 5.4: Convergence of Π with mesh refinement for the Motz problem (○: no singular functions, □: 1 singular function, ◇: 2 singular functions; Π_{exact} from 32×16 mesh with 20 singular functions).

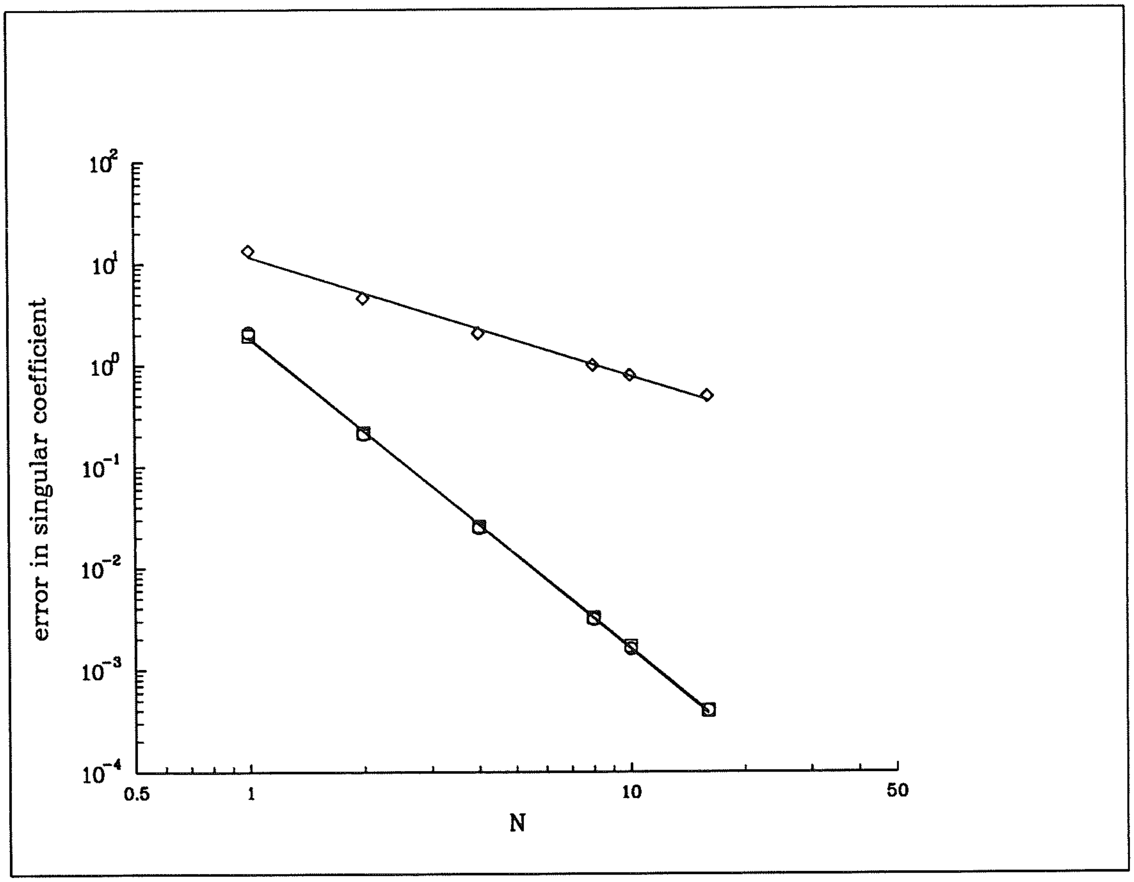

Figure 5.5: Convergence of singular coefficients with mesh refinement for the Motz problem (o: α_1 with 1 singular function, □: α_1 with 2 singular functions, ◇: α_2 with 2 singular functions).

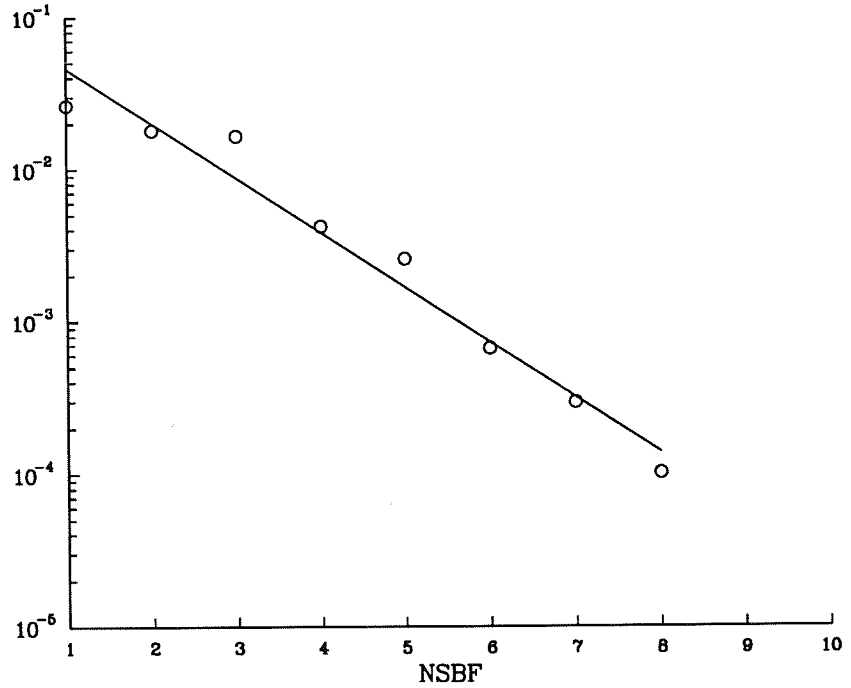

Figure 5.6: Convergence of Π with the number of singular functions for the Motz problem (2×1 Mesh; Π_{exact} from 32×16 mesh with 20 singular functions).

singular terms for the ISBFM. Note that we have only treated the strongest singularity in this problem, ignoring the corner singularities that would eventually be expected to reduce the convergence rate to algebraic.

Exponential convergence is typical of spectral techniques, and in fact, the ISBFM is closely related to the spectral tau methods[11] (see, e.g., Canuto [23]). The ISBFM differs from the spectral tau methods in three ways:

1. Some of the ISBFM basis functions are ordinary polynomials (u^r).
2. The ISBFM basis functions $r^{\lambda_i} f_i(\theta)$ are solutions to a regular Sturm-Liouville problem.
3. The volume integrals involving u^s and $\overline{u}^s$ are reduced to boundary integrals, since u^s and $\overline{u}^s$ satisfy the governing equation.

In spectral tau methods, the functions are Chebyshev polynomials and solutions to a singular Sturm-Liouville problem; the integration is carried out over the domain. However, the ISBFM and the spectral tau methods are closely related and the rapid convergence of the ISBFM with the number of singular basis functions is not surprising.

In Table 5.4 we compare the singular coefficients from the ISBFM with the values given in [165]. Here we use 20 singular functions with a very coarse 2×1 element mesh and a finer 16×8 mesh. The coarse mesh gives good results, and the finer mesh yields results in close agreement with the analytical values available and with Wigley's results for the higher coefficients.

At some point, we expect that the condition number of the matrices will become too large to permit an accurate solution of the equations. Table 5.5 shows the condition

---

[11] Spectral tau methods are members of the family of weighted residual methods in which the basis functions (u) and the weight functions ($\overline{u}$) are of the same form, but neither u nor $\overline{u}$ satisfies the boundary conditions. The boundary conditions are imposed separately through additional equations. Exponential convergence is ensured by taking the functions u to be tensor products of eigenfunctions associated with singular Sturm-Liouville problems.

Table 5.4: Leading coefficients for the Motz problem with the ISBFM compared with Wigley's results ($N_{SBF}=20$).

Coefficient i	2×1 mesh	16×8 mesh	Wigley [165]	Exact [126]
1	401.1624	401.1625	401.163	401.1625
2	87.6562	87.6559	87.655	87.65592
3	17.2380	17.2379	17.238	17.23792
4	-8.0712	-8.0712	-8.071	-8.0712
5	1.4403	1.4403	1.440	
6	0.3310	0.3310	0.331	
7	0.2754	0.2754	0.275	
8	-0.0869	-0.0869	-0.087	
9	0.0336	0.0336	0.0336	
10	0.0154	0.0154	0.0154	
11	0.0073	0.0073	0.0073	
12	-0.0032	-0.0032	-0.0032	
13	0.0012	0.0012	0.0012	
14	0.0005	0.0005	0.0005	

Table 5.5: Condition numbers for the Motz problem (ISBFM, 2x1 mesh).

N_{SBF}	$1/\kappa$
5	0.40×10^{-5}
10	0.60×10^{-7}
15	0.11×10^{-8}
20	0.47×10^{-10}
25	0.21×10^{-11}
30	0.44×10^{-13}
35	0.12×10^{-14}
40	0.48×10^{-16}

Table 5.6: Solution of the Motz problem at various points compared with the analytical solution and the values of Wigley (1988). 16x8 mesh; $N_{SBF}=1$.

(x_i, y_i)	OFE	BSBFM	ISBFM	Exact	Wigley
(−6/7, 6/7)	90.964	91.342	91.341	91.34	91.343
(−2/7, 2/7)	78.053	78.560	78.559	78.56	78.559
(0, 2/7)	140.477	141.562	141.560	141.6	141.560
(2/7, 2/7)	242.783	243.814	243.812	243.8	243.812
(0, 1/7)	102.056	103.772	103.768	103.77	103.768
(−1/28, 1/28)	31.770	33.594	33.590	33.59	33.592
(0, 1/28)	50.261	53.197	53.190	53.19	53.186
(1/28, 1/28)	79.286	83.682	83.672	83.67	83.671
(1/28, 0)	72.264	76.412	76.403	76.41	76.408
(3/28, 0)	131.740	134.452	134.447		134.447
(1/7, 0)	154.096	156.487	156.483	156.48	156.483

number estimates, κ, for a 2×1 mesh with various numbers of singular functions[12]. With 35 coefficients, the condition number is quite poor and the numerical results begin to diverge. It is interesting to note that, when we use 30 singular functions, the regular solution is zero to four decimal places.

In all the above tests, we used Lagrange multipliers to weakly enforce the essential boundary conditions. For this problem, the condition numbers of the matrices produced from strong enforcement are the same order of magnitude as those produced using the Lagrange multiplier approach. However, the solutions for large numbers of singular terms are not as accurate with strong enforcement, since aliasing occurs when the mesh is coarse and the singular functions vary rapidly.

Finally, the values of u obtained with (a) the ordinary finite element method (OFE), (b) the BSBFM, and (c) the ISBFM are compared with results from the literature in Table 5.6. We observe that both the BSBFM and the ISBFM yield improved (and essentially the same) results.

---

[12] Condition numbers were estimated with the LINPACK subroutine DGBCO.

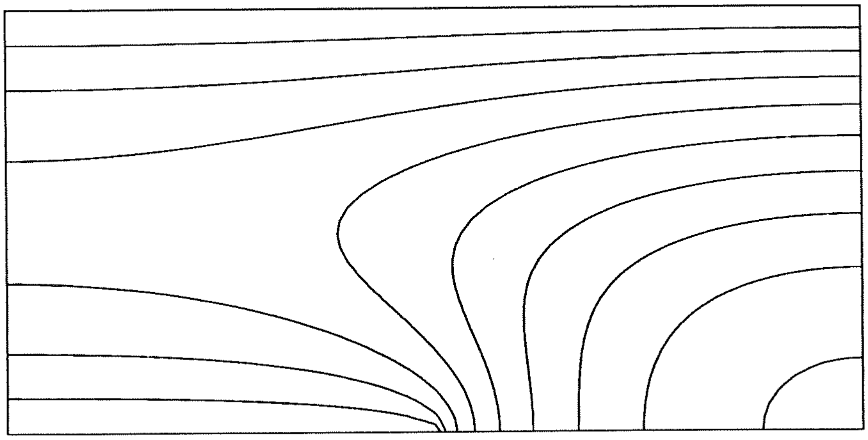

Figure 5.7: Contours for the cracked-beam problem (contours at u=0.01, 0.02,..., 0.09).

Table 5.7: Computed values of α_1 for the cracked-beam problem with various uniform meshes (2N×N elements; $N_{SBF}=1$).

N	ISBFM	BSBFM
1	0.19116	0.16486
2	0.19114	0.18843
4	0.19112	0.19123
8	0.19112	0.19140
10	0.19112	0.19139
20	0.19112	0.19135

5.4 Results for the cracked-beam problem

Figure 5.2 shows the geometry, governing equations, and boundary conditions for the torsion of a cracked beam[13] [42,165]. Once again, a non-removable singularity arises at x=y=0, where the boundary condition suddenly changes from u=0 to $\partial u/\partial y$=0. Clearly, the local solution is the same as that of the Motz problem, equation (5.25). Figure 5.7 shows the contours of u for a refined solution.

As for the Motz problem, the regular finite element mesh consists of 2N×N square nine-node elements. Table 5.7 compares the calculated values of α_1 from the ISBFM and

---

[13] In the original cracked-beam problem $\nabla^2 v = -1$ and $v = 0$ along the $y = 1/2$ boundary. Using the transformation $u = v + y^2/2$ leads to the problem we consider here.

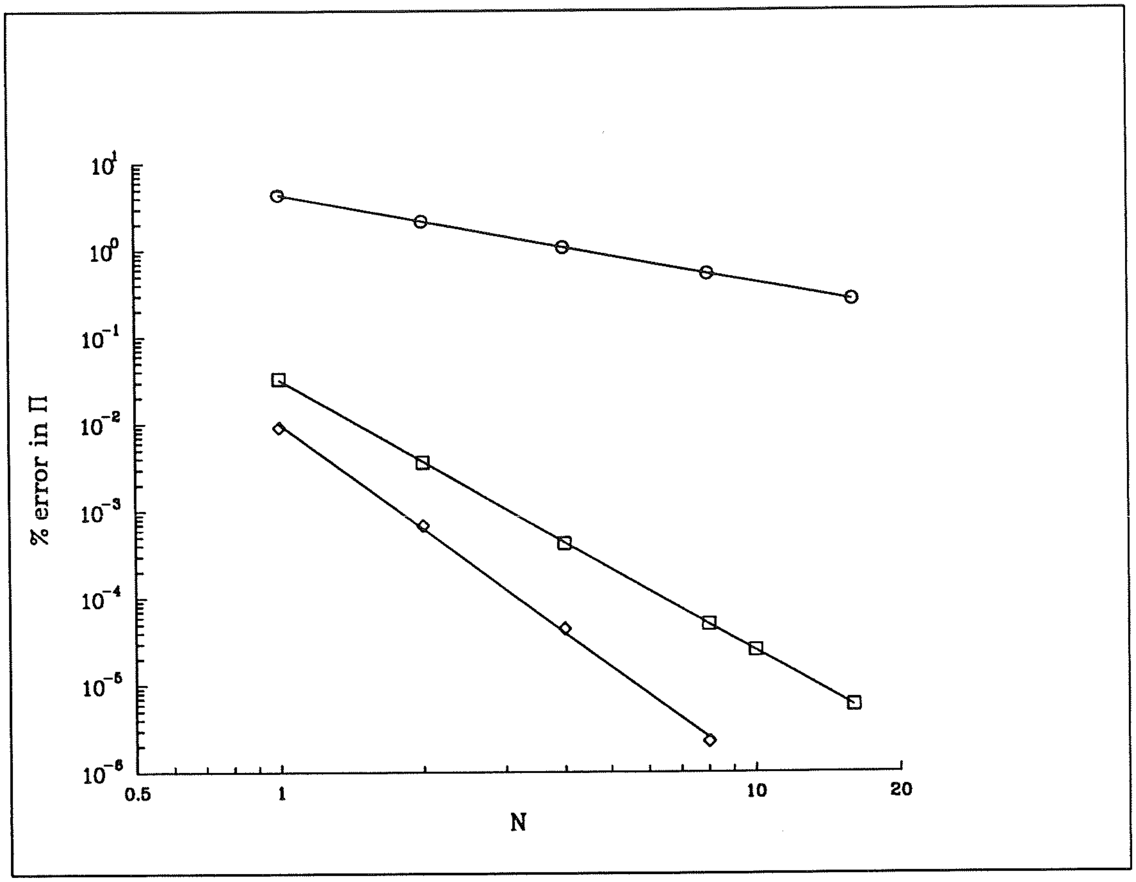

Figure 5.8: Convergence of Π with mesh refinement for the cracked-beam problem (○: no singular functions, □: 1 singular function, ◇: 2 singular functions; Π_{exact} from 32×16 mesh with 20 singular functions).

Table 5.8: Leading coefficients for the cracked-beam problem with the ISBFM compared with Wigley's results ($N_{SBF} = 20$).

Coefficient i	2×1 mesh	16×8 mesh	Wigley [165]
1	0.191119	0.191119	0.19112
2	-0.118116	-0.118116	-0.11811
3	-0.000000	-0.000000	0.00000
4	-0.000000	-0.000000	0.00000
5	-0.012547	-0.012547	-0.01256
6	-0.019033	-0.019033	-0.01905
7	-0.000000	0.000000	

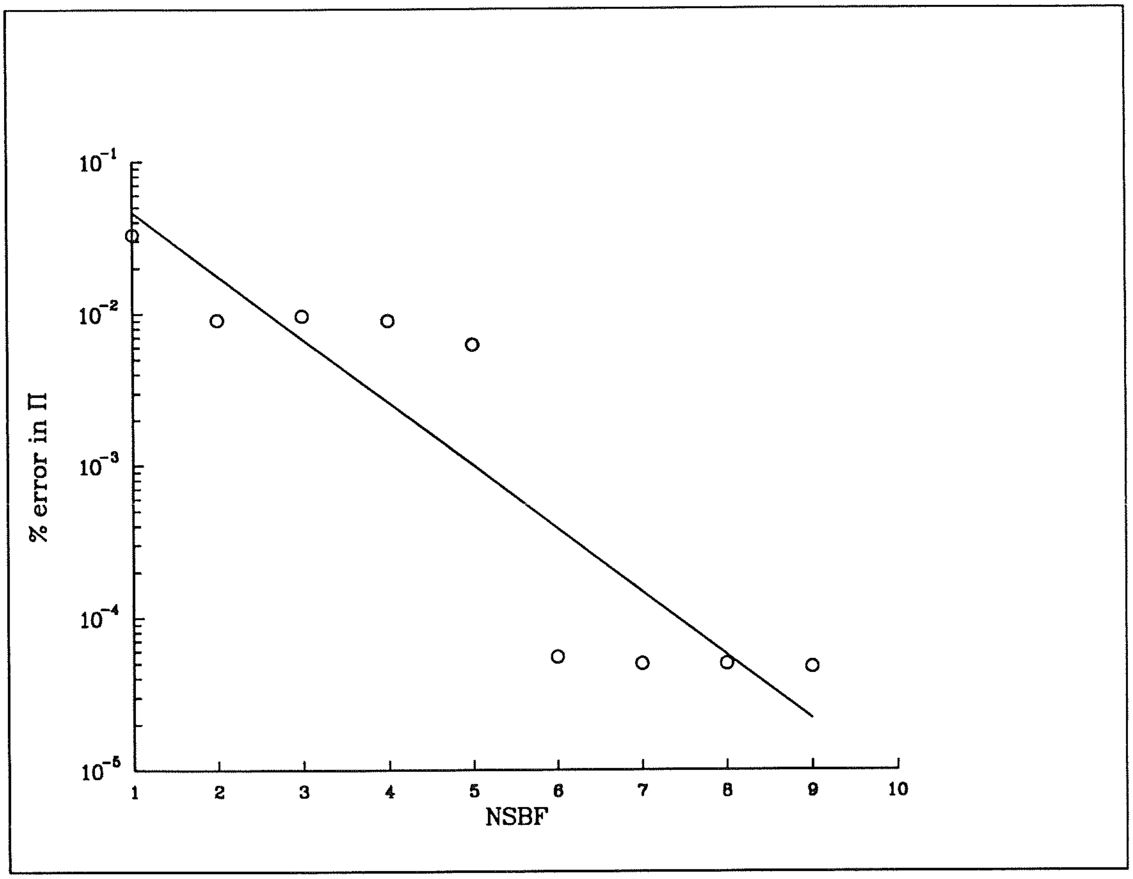

Figure 5.9: Convergence of Π with the number of singular functions for the cracked-beam problem (2×1 mesh; Π_{exact} from 32×16 mesh with 20 singular functions).

Table 5.9: Condition numbers for the cracked-beam problem (ISBFM, 2x1 mesh).

N_{SBF}	$1/\kappa$
5	0.43×10^{-5}
10	0.22×10^{-5}
15	0.61×10^{-7}
20	0.38×10^{-8}
25	0.10×10^{-11}
30	0.12×10^{-12}
35	0.27×10^{-19}
40	0.32×10^{-18}

Table 5.10: Solution of the cracked-beam problem at various points compared with results from the literature (16x8 mesh; $N_{SBF}=1$).

(x_i, y_i)	OFE	BSBFM	ISBFM	Fix *et al.*	Wigley
$(0, 1/24)$	0.026192	0.027431	0.027429	0.027425	0.027428
$(-11/24, 1/4)$	0.032847	0.032878	0.032879	0.032877	0.032878
$(11/24, 1/4)$	0.070657	0.070844	0.070844	0.070844	0.070844

the BSBFM as the underlying mesh is refined. The ISBFM again converges significantly faster than the BSBFM. Figure 5.8 shows the improvement in convergence rate with the addition of one or two singular functions. Again we see a substantial increase in accuracy from the addition of one singular term. Figure 5.9 demonstrates the roughly exponential convergence of the method as the number of singular functions increases. Notice that some of the singular functions produce almost no change in Π. Table 5.8 shows the first seven singular coefficients which agree well with Wigley's iterative results. In Table 5.9 we see that the condition number of these new matrices becomes poor somewhat more rapidly than in the Motz problem, and we observe that the results diverge when the condition number becomes poor. Finally, the values of u obtained with (a) the ordinary finite element method (OFE), (b) the BSBFM, and (c) the ISBFM are compared with results from the literature in Table 5.10. As in the Motz problem, both the BSBFM and the ISBFM yield improved (and essentially the same) results.

5.5 Concluding remarks

The Integrated Singular Basis Function Method (ISBFM) demonstrates significantly better convergence and accuracy than the more conventional Blended Singular Basis Function Method (BSBFM). The addition of one singular function increases the rate of convergence with mesh refinement from linear to cubic and dramatically improves the overall solution accuracy. For a fixed mesh, convergence with the number of singular functions is very rapid (roughly exponential). Although we have demonstrated the method only on examples involving singularities in the 2-D Laplace's equation, the approach is quite general and can be applied to a wide range of problems. The solution of the stick-slip problem with the ISBFM is the subject of Chapter VI.

CHAPTER VI

SINGULAR BASIS FUNCTION APPROACH: THE STICK-SLIP PROBLEM

6.1 Introduction

In this chapter we use the integrated singular basis function method (ISBFM) to solve the stick-slip problem[1]. The integrated singular basis function method was adequately discussed in Chapter V. It was shown that the ISBFM is superior to the blended singular basis function method (BSBFM) for two reasons:

1. It does not require the use of higher order integration since the volume integrals with singular contributions are reduced to boundary integrals far from the singular point.
2. It gives better estimates for the leading coefficients whereas the BSBFM gives good results only for the first coefficient.

---

[1] Preliminary results of the material presented in this chapter appear in [56] (see also Appendix D).

However, we should also notice that the BSBFM is easier to formulate and to program than the ISBFM. Apart from the singular coefficients, the global solution is essentially the same in both methods. The stick-slip problem has been also introduced and discussed in Chapters II and III. We will therefore focus on the finite element formulation in section 6.2, and on the results in section 6.3.

6.2 Finite element formulation

Before proceeding to the finite element formulation, we shall subtract the first few asymptotic terms from the solution. In other words, we shall transform the mathematical problem. The governing equations and the boundary conditions of the stick-slip problem are shown in Figure 6.1. Now if (u, v, p) is the solution and (u^s, v^s, p^s) the singular contributions, we can write

$$\begin{aligned} u^* &= u - u^s \\ v^* &= v - v^s \\ p^* &= p - p^s \end{aligned} \tag{6.1}$$

where (u^*, v^*, p^*) are the new unknowns. For the singular contributions we have

$$u^s = \sum_{j=1}^{N_{SBF}} \alpha_j \, W_u^j \tag{6.2}$$

$$v^s = \sum_{j=1}^{N_{SBF}} \alpha_j \, W_v^j \tag{6.3}$$

$$p^s = \sum_{j=1}^{N_{SBF}} \alpha_j \, W_p^j \tag{6.4}$$

In the above equations, N_{SBF} is the number of singular terms subtracted from the solution, α_j are the unknown singular coefficients, and W_u^j, W_v^j, W_p^j are the singular basis functions taken to be equal to the exact terms of the *even* solution set[2].

---

[2] The even solution set is responsible for the strongest singularity. The two solution sets for the stick-slip problem are given in Appendix B. Notice that we work in the cartesian coordinate system and the local solution must be expressed in this system.

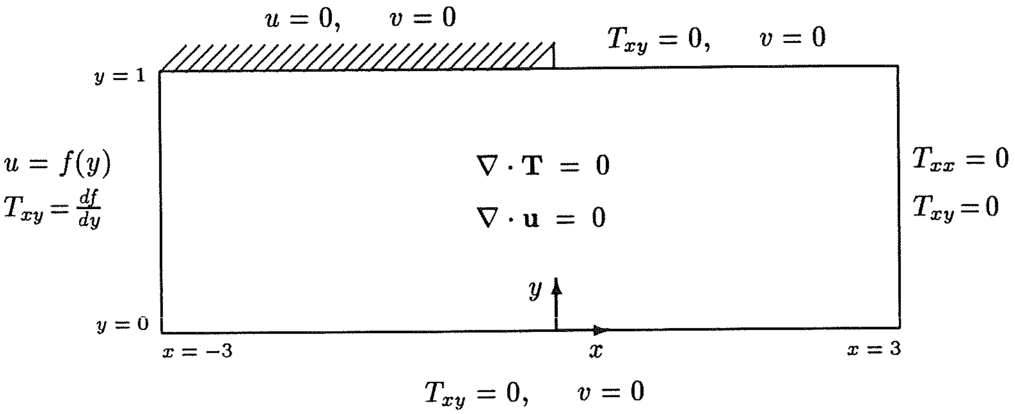

Figure 6.1: The stick-slip problem.

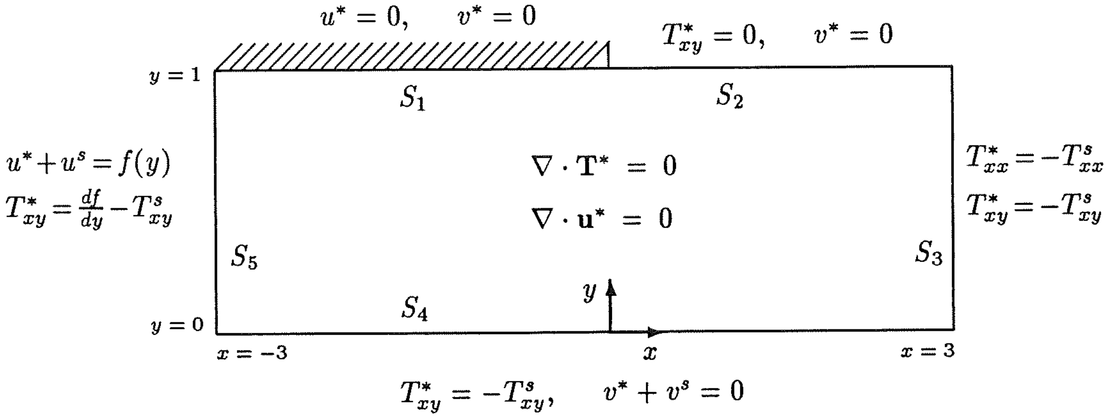

Figure 6.2: The modified stick-slip problem. The stars denote the new unknown variables and s denotes the singular contributions.

By substituting equations (6.1) into the governing equations, the mathematical problem is transformed to that shown in Figure 6.2. We should stress here that (u^s, v^s, p^s) satisfy the original governing equations and the boundary conditions along the wall and the slip surface. We should also point out that instead of using essential boundary conditions for v at the inlet and at the outlet, we use natural boundary conditions. The natural boundary conditions are weaker and do not require the use of Lagrange multipliers.

Now the unknown 'velocities' $\mathbf{u}^* = (u^*, v^*)$ are expanded in terms of biquadratic basis functions (Φ^j), and the unknown 'pressure' p^* is expanded in terms of bilinear basis functions (Ψ^j):

$$\mathbf{u}^* = \sum_{j=1}^{N_u} \mathbf{u}_\mathbf{j}^* \, \Phi^j \tag{6.5}$$

$$p^* = \sum_{j=1}^{N_p} p_j^* \, \Psi^j \tag{6.6}$$

where N_u and N_p are the numbers of the velocity and pressure nodes respectively.

By applying Galerkin's principle, we weight the continuity equation by Ψ^i, and the momentum equation by Φ^i:

$$\int_V \nabla \cdot \mathbf{u}^* \, \Psi^i \, dV = 0 \,, \qquad i = 1, 2, \cdots, N_p \,, \tag{6.7}$$

$$\int_V \nabla \cdot \mathbf{T}^* \, \Phi^i \, dV = 0 \,, \qquad i = 1, 2, \cdots, N_u \,, \tag{6.8}$$

where V is the physical domain.

To account for the additional unknown coefficients α_i, N_{SBF} residual equations are still required. For this purpose we add the x-momentum equation weighted by W_u^i and the y-momentum equation weighted by W_v^i to the continuity equation weighted by W_p^i. If we let

$$\mathbf{W}_\mathbf{u}^\mathbf{i} = (W_u^i, W_v^i) \,, \tag{6.9}$$

then we can write

$$\int_V \left[(\nabla\cdot\mathbf{T}^*)\cdot\mathbf{W}_\mathbf{u}^\mathbf{i} + \nabla\cdot\mathbf{u}^*\,W_p^i\right] dV = 0\,, \qquad i=1,2,\cdots,N_{SBF}\,. \qquad (6.10)$$

After applying the divergence theorem, the residual equations (6.8) and (6.10) become:

$$\int_S \mathbf{n}\cdot\mathbf{T}^*\,\Phi^i\,dS - \int_V \mathbf{T}^*\cdot\nabla\Phi^i\,dV = 0\,, \qquad i=1,2,\cdots,N_u\,. \qquad (6.11)$$

and

$$\int_S (\mathbf{n}\cdot\mathbf{T}^*)\cdot\mathbf{W}_\mathbf{u}^\mathbf{i}\,dS - \int_V \left[\mathbf{T}^* : \nabla\mathbf{W}_\mathbf{u}^\mathbf{i} - \nabla\cdot\mathbf{u}^*\,W_p^i\right] dV = 0, \quad i=1,2,\cdots,N_{SBF}, \quad (6.12)$$

where S is the boundary of V. Equation (6.12) can be simplified further if we apply the divergence theorem once again:

$$\int_S (\mathbf{n}\cdot\mathbf{T}^*)\cdot\mathbf{W}_\mathbf{u}^\mathbf{i}\,dS - \int_S (\mathbf{n}\cdot\mathbf{T}^{\mathrm{Si}})\cdot\mathbf{u}^*\,dS + \int_V \left[\mathbf{u}^*\cdot(\nabla\cdot\mathbf{T}^{\mathrm{Si}}) + p^*\,\nabla\cdot\mathbf{W}_\mathbf{u}^\mathbf{i}\right] dV = 0,$$

$$i=1,2,\cdots,N_{SBF}\,. \qquad (6.13)$$

$\mathbf{T}^{\mathrm{Si}}$ is the contribution of the ith singular functions to the stress tensor (e.g., $T_{xx}^{Si} = -W_p^i + 2\frac{\partial W_u^i}{\partial x}$ etc.). The volume integral of equation (6.13) is zero because the singular functions satisfy the original governing equations. Therefore, the residual equation is reduced from a volume to a surface integral:

$$\int_S \left[(\mathbf{n}\cdot\mathbf{T}^*)\cdot\mathbf{W}_\mathbf{u}^\mathbf{i} - (\mathbf{n}\cdot\mathbf{T}^{\mathrm{Si}})\cdot\mathbf{u}^*\right] dS = 0\,, \qquad i=1,2,\cdots,N_{SBF}\,. \qquad (6.14)$$

As discussed in Chapter V, the reduction of the volume integrals involving singular terms to boundary integrals eliminates the need to use high order integration in the vicinity of the singular point. Notice that there is no boundary contribution on either the wall or the slip surface since the singular functions satisfy the conditions along these boundaries.

Let us now examine the boundary terms in more detail. As illustrated in Figure 6.2 the boundary S consists of five parts: (a) the wall S_1, (b) the slip surface S_2, (c) the outlet

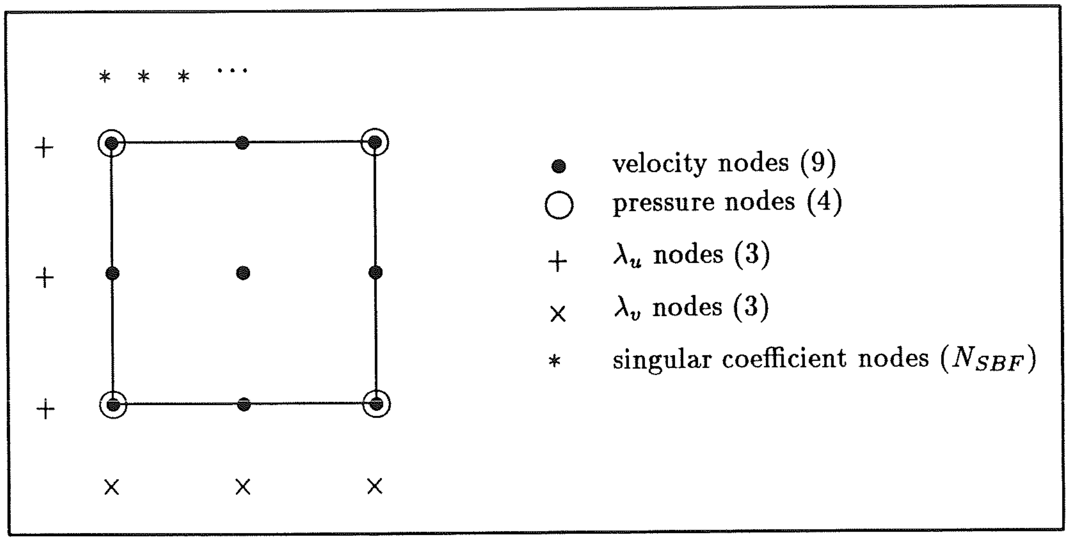

Figure 6.3: Nodes and pseudonodes in the first element. The number of degrees of freedom is $28+N_{SBF}$.

plane S_3, (d) the midplane S_4, and (e) the inlet plane S_5. The boundary terms along the wall (S_1) are ignored because essential boundary conditions for u^* and v^* are to be used. Along the slip surface (S_2) the **i**-components of the boundary terms are neglected since $T^*_{xy} = T^S_{xy} = 0$. The **j**-components are also ignored because of the essential boundary condition for v^*.

To impose the conditions $v^* + v^s = 0$ along S_4 and $u^* + u^s = f(y)$ along S_5, we use the Lagrange multiplier functions λ_v and λ_u respectively[3]. The Lagrange multipliers are expanded in terms of quadratic basis functions M^j:

$$\lambda_u = \sum_{j=1}^{N_y} \lambda_u^j \, M^j \tag{6.15}$$

$$\lambda_v = \sum_{j=1}^{N_x} \lambda_v^j \, M^j \tag{6.16}$$

where N_x and N_y are the numbers of nodes along S_4 and S_5 respectively.

---

[3] For the use of Lagrange multipliers with finite elements, see [10,25,77,88,109].

Using Lagrange multipliers introduces N_y+N_x new unknowns (λ_u^j and λ_v^j) into the system. These unknowns along with the singular coefficients are introduced by means of $N_x+N_y+N_{SBF}$ pseudonodes with one degree of freedom[4]. The nodes and pseudonodes for the first element (lower left of the domain) are shown in Figure 6.3.

The boundary term of equation (6.11) becomes:

$$\int_S \mathbf{n}\cdot\mathbf{T}^*\,\Phi^i\,dS \;=\; \mathbf{i}\left[-\int_{S_3} T^S_{xx}\,\Phi^i\,dy + \int_{S_4} T^S_{xy}\,\Phi^i\,dx - \int_{S_5} \lambda_u\,\Phi^i\,dy\right] + \\ \mathbf{j}\left[-\int_{S_3} T^S_{xy}\,\Phi^i\,dy - \int_{S_4} \lambda_v\,\Phi^i\,dx + \int_{S_5}\left(T^S_{xy} - \frac{df}{dy}\right)\Phi^i\,dy\right] . \tag{6.17}$$

Similarly for the two terms of equation (6.14) we have

$$\int_S (\mathbf{n}\cdot\mathbf{T}^*)\cdot\mathbf{W}^i_{\mathbf{u}}\,dS \;=\; -\int_{S_3} T^S_{xx}\,W^i_u\,dy + \int_{S_4} T^S_{xy}\,W^i_u\,dx - \int_{S_5}\lambda_u\,W^i_u\,dy \\ -\int_{S_3} T^S_{xy}\,W^i_v\,dy - \int_{S_4}\lambda_v\,W^i_v\,dx + \int_{S_5}\left(T^S_{xy} - \frac{df}{dy}\right) W^i_v\,dy\,, \tag{6.18}$$

$$\int_S (\mathbf{n}\cdot\mathbf{T}^{\mathrm{Si}})\cdot\mathbf{u}^*\,dS \;=\; \int_{S_3}\left[u^*\,T^{Si}_{xx} \,+\, v^*\,T^{Si}_{xy}\right]\,dy \;-\; \int_{S_4}\left[u^*\,T^{Si}_{xy} \,+\, v^*\,T^{Si}_{yy}\right]\,dx \;- \\ \int_{S_5}\left[u^*\,T^{Si}_{xx} \,+\, v^*\,T^{Si}_{xy}\right]\,dy\,. \tag{6.19}$$

The final forms of the residual equations are listed below:

1. Continuity equations

$$\int_V \left(\frac{\partial u^*}{\partial x} + \frac{\partial v^*}{\partial y}\right)\Psi^i\,dxdy \;=\; 0\,, \qquad\qquad i = 1,2,\cdots,N_p \tag{6.20}$$

2. Momentum equations

$$-\int_V \left(T^*_{xx}\,\frac{\partial\Phi^i}{\partial x} \,+\, T^*_{xy}\,\frac{\partial\Phi^i}{\partial y}\right)\,dxdy \;- \\ \int_{S_3} T^S_{xx}\,\Phi^i\,dy + \int_{S_4} T^S_{xy}\,\Phi^i\,dx - \int_{S_5}\lambda_u\,\Phi^i\,dy \;=\; 0\,, \qquad i = 1,2,\cdots,N_u \tag{6.21}$$

---

[4] For the singular coefficients one could alternatively use only one pseudonode with N_{SBF} degrees of freedom.

$$-\int_V \left(T^*_{xy} \frac{\partial \Phi^i}{\partial x} + T^*_{yy} \frac{\partial \Phi^i}{\partial y} \right) dxdy - \int_{S_3} T^S_{xy} \Phi^i \, dy -$$

$$\int_{S_4} \lambda_v \Phi^i \, dx + \int_{S_5} T^S_{xy} \Phi^i \, dy = \int_{S_5} \frac{df}{dy} \Phi^i \, dy \,, \qquad i = 1, 2, \cdots, N_u \tag{6.22}$$

3. Singular-coefficient equations

$$- \int_{S_3} T^S_{xx} W^i_u \, dy + \int_{S_4} T^S_{xy} W^i_u \, dx - \int_{S_5} \lambda_u W^i_u \, dy -$$

$$\int_{S_3} T^S_{xy} W^i_v dy - \int_{S_4} \lambda_v W^i_v dx + \int_{S_5} T^S_{xy} W^i_v dy - \int_{S_3} \left[u^* \, T^{Si}_{xx} + v^* \, T^{Si}_{xy} \right] dy +$$

$$\int_{S_4} \left[u^* \, T^{Si}_{xy} - v^s \, T^{Si}_{yy} \right] \, dx + \int_{S_5} \left[-u^s \, T^{Si}_{xx} + v^* \, T^{Si}_{xy} \right] \, dy = - \int_{S_5} \left(f \, T^{Si}_{xx} - \frac{df}{dy} W^i_v \right) \, dy \,,$$

$$i = 1, 2, \cdots, N_{SBF} \tag{6.23}$$

4. Lagrange-multiplier equations

$$- \int_{S_4} \left(v^* + v^S \right) \, M^i \, dx = 0 \,, \qquad i = 1, 2, \cdots, N_x \tag{6.24}$$

$$- \int_{S_5} \left(u^* + u^S \right) \, M^i \, dy = - \int_{S_5} f \, M^i \, dy \,, \qquad i = 1, 2, \cdots, N_y \tag{6.25}$$

Notice that use of the essential boundary conditions along S_4 and S_5 was made in the substitution in order to preserve the symmetry of the stiffness matrix. Equations (6.20)-(6.25) constitute a symmetric system of linear equations which may be solved by a frontal solver [75,160]. The total number of unknowns N is

$$N = N_p + 2N_u + N_{SBF} + N_x + N_y \,. \tag{6.26}$$

6.3 Results and discussion

In order to make comparisons with the ordinary and singular element results of Chapter III, the same uniform meshes were again used: mesh I with 12x2 elements, mesh II with 24x4 elements, and mesh III with 48x8 elements. The meshes are extended upstream and downstream to a distance equal to three channel halfwidths to ensure the validity

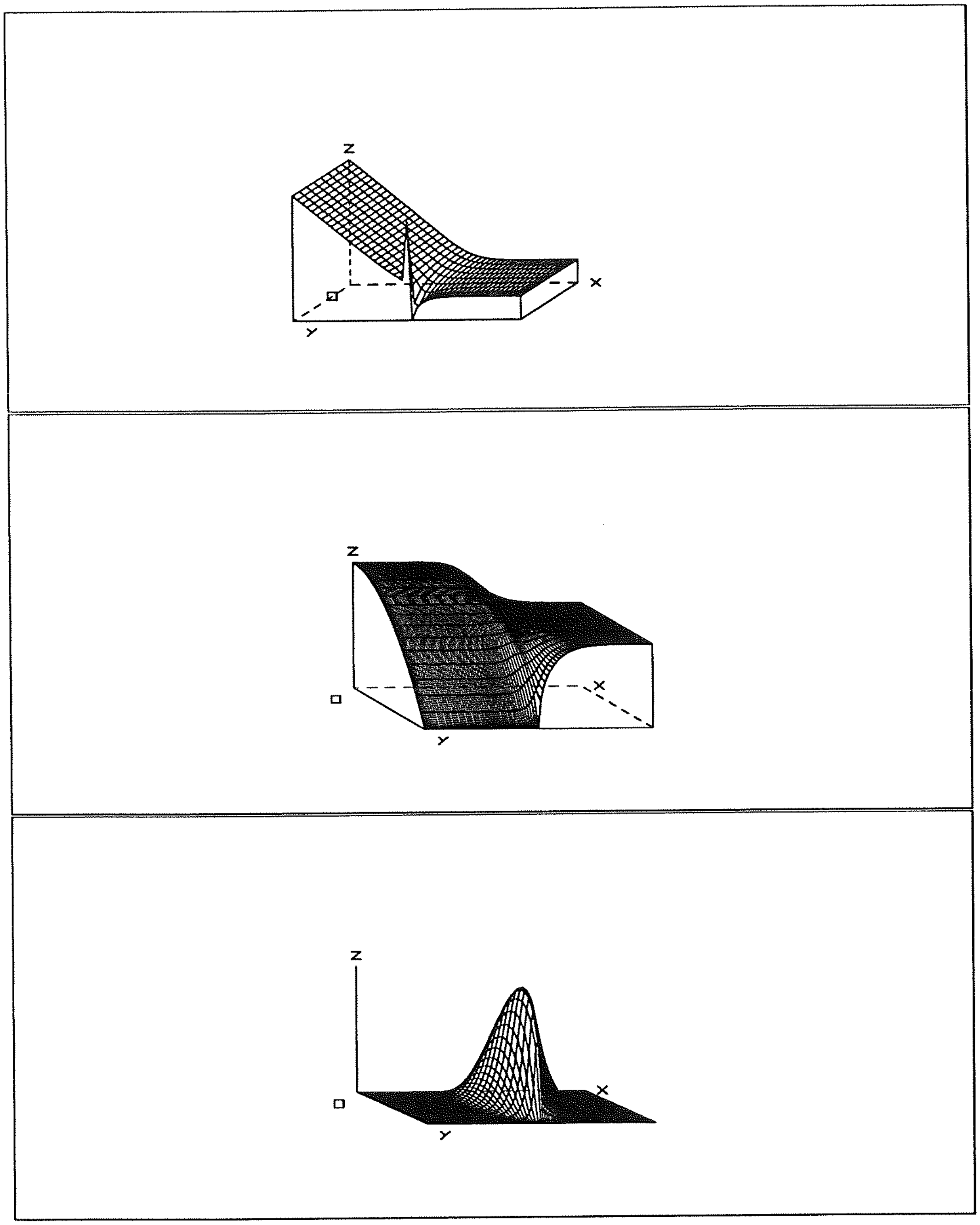

Figure 6.4: 3-D view of the solution of the stick-slip problem: p (top), u (middle), v (bottom). Note that the pressure is, in fact, infinite at the singular point.

Table 6.1: Computed leading coefficients for the stick-slip problem with the ISBFM. The analytical value for α_1 is 0.69099.

Mesh	N_{SBF}	α_1	α_2	α_3	α_4	α_5
12X2	1	0.72445				
	2	0.68718	0.29322			
	3	0.68504	0.30989	-0.00534		
	4	0.70774	0.12913	-0.01916	0.00264	
	5	0.69303	0.24604	-0.00992	0.00057	0.00004
	10	0.69329	0.24373	-0.00953	0.00047	-0.00002
	20	0.69303	0.24389	-0.00909	-0.00007	-0.00014
24X4	1	0.70762				
	2	0.68979	0.28263			
	3	0.68944	0.28790	-0.00452		
	4	0.68820	0.30816	0.00171	-0.00090	
	5	0.69151	0.25432	-0.01388	0.00061	0.00008
	10	0.69143	0.25562	-0.01248	0.00045	0.00002
	20	0.69138	0.25604	-0.01173	0.00001	-0.00009
48X8	1	0.69929				
	2	0.69064	0.27457			
	3	0.69058	0.27659	-0.00400		
	4	0.69048	0.27984	-0.00140	-0.00035	
	5	0.69112	0.25884	-0.01662	0.00064	0.00012
	10	0.69105	0.26096	-0.01365	0.00041	0.00003
	20	0.69104	0.26139	-0.01263	0.00001	-0.00008

of the imposed boundary conditions. Three dimensional plots of the solution (u, v, p) are shown in Figure 6.4. The ISBFM gives essentially the same results as the ordinary elements (and the singular elements as well) far from the singular point.

Results have been obtained for various values of N_{SBF} with the three meshes. The estimates for the first five coefficients are listed in Table 6.1. The results obtained with the BSBFM are shown in Table 6.2. Table 6.3 compares the first three coefficients from ISBFM and BSBFM with the values obtained in Chapter III using the singular finite elements[5], and the values given by Ingham and Kelmanson[6] [82]. We observe that the

---

[5] The singular coefficients are not directly calculated with the singular finite element method (nor with the ordinary elements). A least-squares fit of the slip surface velocity was used for this purpose (see Chapter III).

[6] Ingham and Kelmanson used a singular boundary element method [82].

Table 6.2: Computed leading coefficients for the stick-slip problem with the BSBFM. The analytical value for α_1 is 0.69099.

Mesh	N_{SBF}	α_1	α_2	α_3	α_4	α_5
12X2	1	0.67399				
	2	0.67494	0.02117			
	3	0.67677	0.02386	0.01254		
	4	0.67727	0.03052	0.01317	0.00275	
	5	0.67750	0.03101	0.01505	0.00265	0.00109
	10	0.67783	0.02990	0.01702	0.00213	0.00231
	20	0.67858	0.03218	0.01870	0.00324	0.00393
24X4	1	0.68684				
	2	0.68737	0.03655			
	3	0.68770	0.03879	0.01209		
	4	0.68786	0.04760	0.01287	0.00341	
	5	0.68789	0.04787	0.01407	0.00335	0.00057
	10	0.68791	0.04752	0.01497	0.00317	0.00124
	20	0.68792	0.04767	0.01559	0.00322	0.00176
48X8	1	0.69004				
	2	0.69043	0.06239			
	3	0.69051	0.06439	0.01297		
	4	0.69060	0.07696	0.01408	0.00527	
	5	0.69060	0.07712	0.01498	0.00522	0.00041
	10	0.69061	0.07790	0.01535	0.00602	0.00081
	20	0.69061	0.07828	0.01587	0.00633	0.00121

Table 6.3: Estimates of the first 3 coefficients with mesh III and N_{SBF}=5 (only for ISBFM and BSBFM) compared with the values of Ingham and Kelmanson (1984) and the analytical value for α_1.

Method	α_1	α_2	α_3
Analytical solution [121]	0.69099	——	——
ISBFM	0.69112	0.25884	-0.01662
BSBFM	0.69060	0.07712	0.01498
Singular elements [55]	0.69173	0.27168	0.05013
Ordinary elements [55]	0.67170	0.19812	-0.02297
Boundary elements [82]	0.69108	0.26435	0.04962

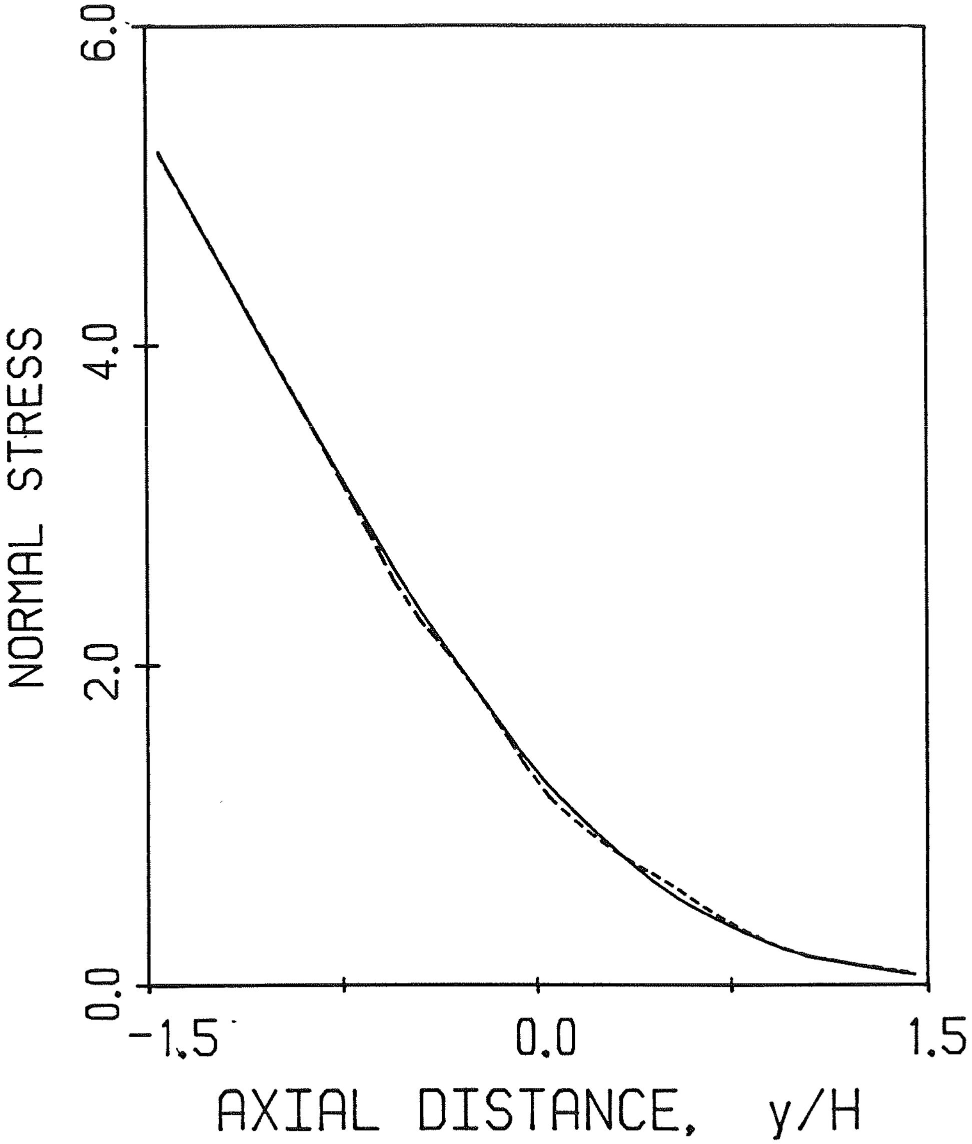

Figure 6.5: Normal stresses with mesh I (- - -: $N_{SBF} = 1$, —: $N_{SBF} = 5$).

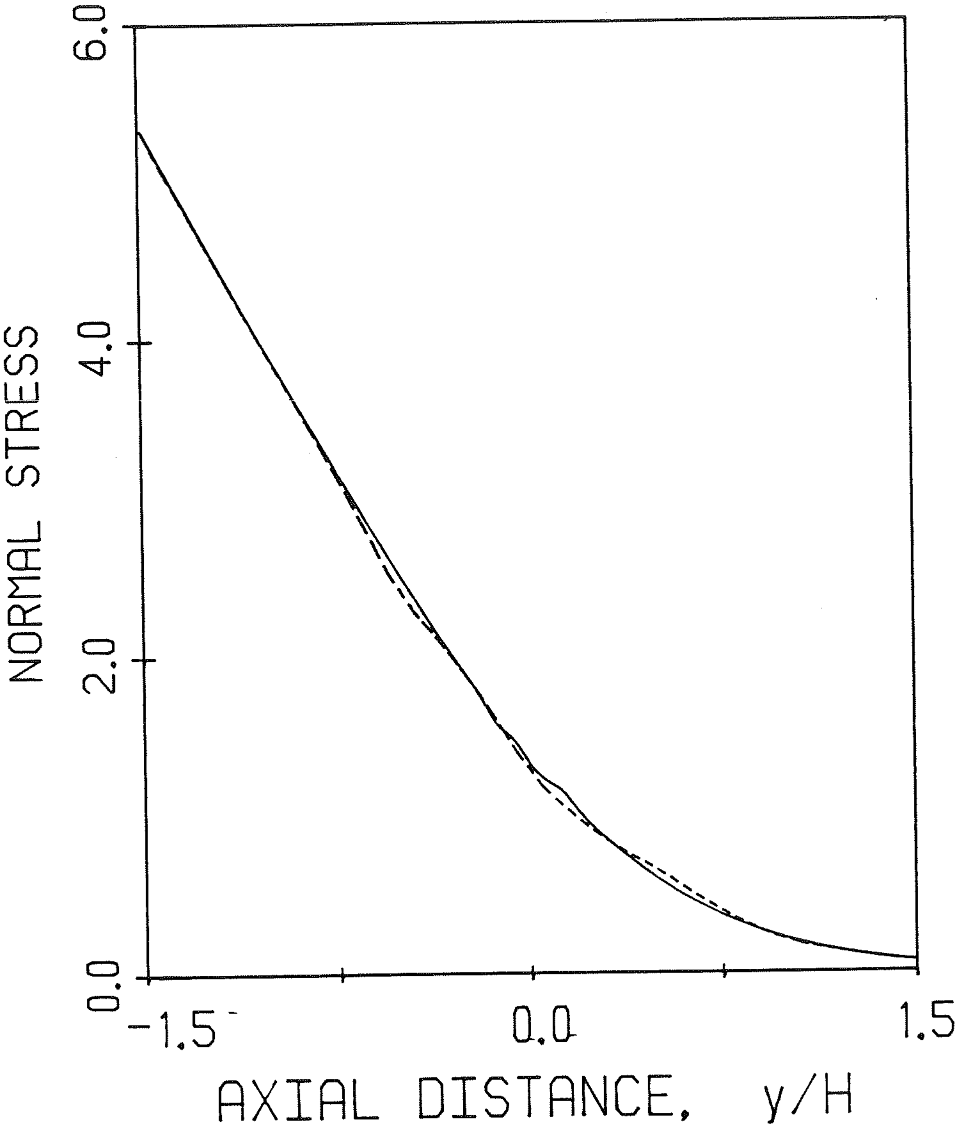

Figure 6.6: Normal stresses with $N_{SBF} = 1$ (- - -: mesh I, —: mesh III).

first coefficient α_1 appears to converge to the analytical value 0.69099 as the mesh is refined or as N_{SBF} increases. A similar trend is also observed for the other leading coefficients. The second coefficient from the ISBFM compares well with the value found by Ingham and Kelmanson [82]. Notice that with the BSBFM a satisfactory estimate is obtained only for the first coefficient (see Chapter V and [163,158]).

As in Chapters III and IV, the normal stress along the wall and the slip surface was used as a test for the numerical calculations. The normal stresses with mesh I and $N_{SBF} = 1$ and 5 are plotted in Figure 6.5. Unlike the ordinary element solution, the oscillations have been essentially eliminated. As N_{SBF} increases the normal stress becomes smoother.

The normal stresses with meshes I and III, and $N_{SBF} = 1$ are plotted in Figure 6.6. In contrast to the singular elements no spurious small amplitude oscillations appear in the normal stress as the mesh is refined. However, the singular elements give more accurate results with coarse meshes (see Chapter III and [56]).

6.4 Concluding remarks

The integrated singular basis function approach was used to solve the stick-slip problem. Compared to the ordinary finite elements, the method eliminates the oscillations that characterize the normal stress along the wall and the slip surface.

Compared to the singular elements, the method gives smoother results as the mesh is refined. The singular elements give slightly better results for coarse meshes but small amplitude oscillations appear with mesh refinement. Another advantage of the singular basis function approach is the direct calculation of the singular coefficients.

Compared to the blended singular basis function approach, the ISBFM gives more accurate estimates for the singular coefficients and does not require high order numerical integration.

CHAPTER VII

THESIS SUMMARY AND RECOMMENDATIONS

> "When the sea increases
> the ink ceases."
>
> George Seferis.

The primary goal of this work was to develop singular finite elements for Newtonian flow problems with stress singularities in order to improve the accuracy and the convergence rate of the solution especially near the singular point. This goal was accomplished using two different approaches:

1. Singular element approach
2. Singular basis function approach

In the singular finite element approach, special elements, with the basis functions constructed to describe the radial form of the local similarity solution, are used around the singular point. Three Newtonian problems have been solved with this approach:

1. The stick-slip problem
2. The 2:1 sudden-expansion problem

3. The planar die-swell problem

The method gives accurate results with coarse meshes and eliminates the spurious stress oscillations which contaminate the standard finite element solution. In the case of the die-swell problem, the convergence rate of the free surface has been considerably accelerated.

In the singular basis function approach, the first few terms of the local similarity solution are directly subtracted from the governing equations. A novel method has been developed; it uses double integration by parts which reduces the volume integrals with singular contributions to boundary integrals and thus eliminates numerical integration inaccuracies and the need to use high-order integration. The method has been applied to two standard Laplace-equation problems:

1. The Motz problem
2. The cracked-beam problem

and has improved the solution accuracy compared to that achieved using the standard finite element method. It also directly gives more accurate estimates for the singular coefficients than those obtained with other singular techniques.

The singular basis function approach was also extended to solve the stick-slip problem, and more accurate results have been obtained than those from the standard finite element method. Compared to the singular element approach, the method gives more accurate results as the underlying mesh is refined. Also, the singular coefficients are directly calculated. The singular finite element method gives better results with coarse meshes. With this method, however, the mesh around the singularity cannot be refined extensively because the size of the singular elements over which the singularity is given special attention is reduced.

Before extending the singular methods developed in this thesis to non-Newtonian problems, some additional tests with Newtonian problems are recommended. The solution of the backward facing step problem[1] with singular elements can be easily obtained with minor modifications to the existing sudden-expansion code (the form of the singularity and the geometry are the same in both problems). A more severe test would be the solution of the driven-cavity problem in which the singularity is non-integrable ($\mathbf{T} \sim r^{-1}$).

As for the singular basis function approach, the solution of the the Newtonian die-swell problem is recommended. Improving the accuracy in the neighborhood of the exit will allow precise calculation of the angle of separation and of the mean curvature at the exit.

A natural extension of this thesis would be the development of singular finite elements for viscoelastic flows. As indicated in [87,2,95,31], this will greatly facilitate further understanding of the high Weissenberg number problem. However, complete non-Newtonian local analyses are available only for power-law and second-order fluids. Local analyses for other viscoelastic models would be desirable. Some recent works appear to be promising. Davies (1988) used biorthogonal series expansions to obtain the local solution near a sharp corner for a corotational Maxwell model. Apelian *et al.* (1988), in solving the stick-slip problem for a modified upper convected Maxwell model, assumed that the leading order behavior is Newtonian and properly scaled the contribution of the upper-convected derivative to obtain an estimate for the elastic contribution to the radial form of the singularity. Such treatment is possible for other viscoelastic models as well [4]. Notice that knowledge of the exact radial form of the singularity is more than adequate for the development of singular finite elements[2]. With the present singular basis function approach, however, the complete form (both the radial and angular dependence) is required.

---

[1] This problem was suggested by Gresho [60].

[2] The results in Chapters III and IV indicate that the numerical solution is not very sensitive to the values of the singularity exponents.

APPENDICES

APPENDIX A

MODELLING OF A LOW PRESSURE CVD REACTOR. FLOW AND ENERGY ANALYSIS

A.1 Introduction

Chemical vapor deposition (CVD) is a very important process in the semiconductor industry for growing the thin solid films required for device fabrication. The deposition occurs on a hot substrate via chemical reactions involving vapor-phase species. CVD must produce thin, non-defective, uniform films with reproducible and controllable properties such as composition, adhesion, crystal structure, and surface morphology. More detailed discussions about the various categories of CVD processes can be found in [71,85,155].

CVD is a very complex process involving fluid flow, energy and mass transfer and chemical reactions. The success and control of the process depends critically on the reactor configuration and the operating conditions. The two most common reactor configurations are the *horizontal* and the *vertical* reactors. In the past few years, numerical methods (both finite differences and finite elements) have been used in order to solve the governing differential equations in two and three dimensions [46,85,156]. Fotiadis *et al.* [46,47] investigated two- and three-dimensional flows in both vertical and horizontal reactors using the finite element method. They also illustrated the importance of the thermal boundary conditions and of the shape of the reactor.

Assuming negligible volume changes due to the reaction and negligible heat of reaction, one can decouple the flow and energy solution from the mass transfer and reaction analysis. These assumptions are not always justified, but when possible (e.g., when the concentration of the reactants in the carrier gas is low) they simplify the modelling of the CVD reactors considerably, reduce memory and computational requirements and allow the study of different reactions for the same flow and thermal conditions.

The long term objective of this study is to model the low-temperature CVD of AlN, Al_2O_3, and $Al_xO_yN_z$ thin films as dielectrics for devices fabricated on III-V compound semiconductors such as $GaAs$ and InP. This process is being investigated experimentally with a vertical reactor [36].

This appendix concerns the solution of the fluid mechanics and heat transfer problem with this particular reactor and the conditions used in the experiments. The effects of Reynolds number, gravity, and thermal conditions are considered in detail, in order to obtain more insight into the transport phenomena and to better organize the experiments. Interesting flow patterns are obtained when gravity is taken into account. The character of the flow changes drastically when the feed is introduced at the bottom of the reactor (opposite to the direction of gravity).

The geometry of the reactor and the operating conditions presently used in the experiments are presented in section A.2. The governing equations and the finite element formulation are presented in sections A.3 and A.4 respectively. Finally, the results are discussed in section A.5.

A.2 Reactor geometry

The calculations were performed with a geometry close to that of the reactor used in the experiments[1]. A schematic of the reactor illustrating all the characteristic lengths

---

[1] The real reactor is not perfectly axisymmetric.

Table A.1: Dimensions of the CVD reactor.

Symbol	Description	Length (inches)
H_i	length of inlet nozzle	10.0
H	height of the reactor	13.1
H_o	length of outlet nozzle	13.0
R	radius of reactor	2.917
R_o	radius of inlet/outlet nozzles	0.75
R_s	radius of susceptor	1.25
H_s	height of susceptor	0.75
Z	axial plate separation	6.175
w	wall thickness	0.0415

Table A.2: Composition of the feed to the CVD reactor.

Gas	Fraction
NH_3	0.2 - 0.7
$HMDA$	0.001 - 0.04
Ar or H_2	0.3 - 0.8

is shown in Figure A.1. The lengths are tabulated in Table A.1. The reaction gases are fed vertically from the bottom through a nozzle onto the wafer of 2.4 inches diameter. The feed consists of NH_3 and H_2 (or Ar) as the carrier gases and hexamethyldialuminum (HMDA). The composition of the feed is shown in Table A.2. The wafer is clamped to the susceptor which is heated by two resistance heaters[2]. The temperature of the susceptor, T_{susc}, varies from 700-1000 K. The pressure in the reactor varies from 0.1 up to 10 Torr. The volumetric flow rate at the inlet varies from 50-250 sccm.

A.3 Governing Equations

The basic assumptions for the flow in the reactor are: (a) the Mach number is small and compressibility effects are neglected (notice that density variations with

---

[2] For more information about the reactor and the operating conditions, see [36].

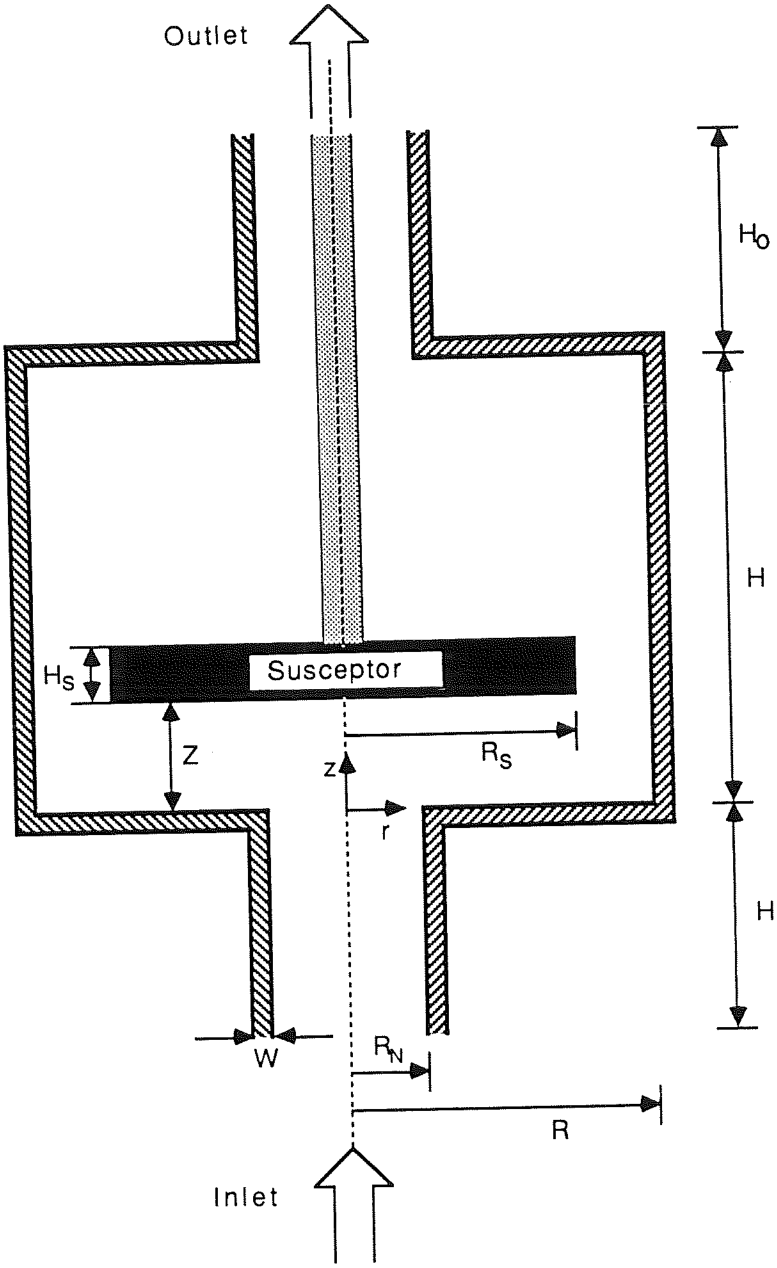

Figure A.1: Schematic of the CVD reactor.

Table A.3: Mean inlet velocity, Reynolds and Stokes numbers over the range of pressures and flow rates used in the experiments. It is assumed that the feed is 100% NH_3. Temperature at inlet, 300 K (Pr=0.9).

P Torr	Q sccm	U_o m/s	Re	St
0.10	50	5.55	0.94	0.0056
	130	14.40	2.44	0.0022
	250	27.80	4.70	0.0011
5.	50	0.111	0.94	14.20
	130	0.289	2.44	5.47
	250	0.555	4.70	2.84
10.	50	0.056	0.94	56.9
	130	0.144	2.44	21.9
	250	0.278	4.70	11.4

temperature are important), (b) The flow is laminar and in quasi-steady state relative to the film growth dynamics (speed of film growth negligible), (c) The flow is axisymmetric ($\frac{\partial\cdot}{\partial\theta} = 0$), (d) The susceptor is not rotated ($u_\theta = 0$), and (e) Gravity is in the z direction. The momentum equation for the carrier gas takes the form

$$\rho\, \mathbf{u} \cdot \nabla \mathbf{u} \;=\; \nabla \cdot \mathbf{T} \;+\; \rho\, g\, \mathbf{e_z}\,, \tag{A.1}$$

where $\mathbf{u}$ is the velocity vector (only the axial and radial components are considered here), ρ is the density, g is the gravitational acceleration, and $\mathbf{T}$ is the stress tensor given by

$$\mathbf{T} \;=\; -(p + \frac{2}{3}\,\mu\, \nabla \cdot \mathbf{u})\, \mathbf{I} \;+\; \mu\, [\nabla \mathbf{u} \;+\; (\nabla \mathbf{u})^T]\,. \tag{A.2}$$

Here μ is the viscosity and $\mathbf{I}$ is the unit tensor.

The continuity equation with variable density is given by

$$\nabla \cdot (\rho\, \mathbf{u}) \;=\; 0\,. \tag{A.3}$$

The density is calculated using the ideal gas law as the equation of state:

$$\rho \;=\; \frac{P^o M}{R\, T}\,, \tag{A.4}$$

where P^o is the operating pressure of the reactor, M is the molecular weight, R is the ideal gas constant, and T is the temperature. Notice that variations of the pressure due to fluid mechanical forces are negligible (due to the low Mach numbers).

The basic assumptions for the energy equation are: (a) viscous dissipation is neglected, (b) pressure changes and Duffour effects are neglected (this assumption is justified only if the gases involved in the process have similar molecular weights), (c) heats of reaction are also neglected (limit of dilute reactants), and (d) steady state is assumed. The energy equation becomes:

$$\rho C_p \, \mathbf{u} \cdot \nabla T \; = \; \nabla \cdot \kappa \nabla T \, , \tag{A.5}$$

where C_p is the heat capacity, and κ is the thermal conductivity of the gas.

It is more convenient to nondimensionalize equations (A.1), (A.3), (A.4) and (A.5). Quantities and properties at the inlet of the reactor are used as scales; the mean velocity U_o is used as the velocity scale, the radius R_o as the length scale, and the inlet temperature T_o as the temperature scale; the density, the viscosity, the thermal conductivity κ, and the heat capacity C_p are scaled with the corresponding properties at the inlet ρ_o, μ_o κ_o, and C_{po}; the pressure and the stresses are measured in $\mu_o U_o / R_o$. Three dimensionless numbers are introduced: the Reynolds number,

$$Re \; \equiv \; \frac{\rho_o \, U_o R_o}{\mu_o} \, , \tag{A.6}$$

the Stokes number,

$$St \; \equiv \; \frac{\rho_o \, g R_o^2}{\mu_o U_o} \, , \tag{A.7}$$

and the Prandtl number,

$$Pr \; \equiv \; \frac{C_{po} \, \mu_o}{\kappa_o} \, . \tag{A.8}$$

The ideal gas law is now

$$\rho \; = \; \frac{1}{T} \, , \tag{A.9}$$

and the dimensionless forms of the momentum, the continuity, and the energy equations become:

$$\frac{Re}{T}\,\mathbf{u}\cdot\nabla\mathbf{u} = \nabla\cdot\mathbf{T} + \frac{St}{T}\,\mathbf{e_z}\,, \tag{A.10}$$

$$\nabla\cdot\left(\frac{\mathbf{u}}{T}\right) = 0\,, \tag{A.11}$$

and

$$Re\;Pr\,\frac{C_p}{T}\,\mathbf{u}\cdot\nabla T = \nabla\cdot\kappa\nabla T\,. \tag{A.12}$$

Notice that κ, μ, and C_p are temperature dependent. A power law dependence is assumed for the thermal conductivity and the viscosity. The powers involved are calculated from experimental data (see section A.6). The heat capacity is assumed constant in this work.

Boundary conditions for the momentum and energy equations must also be specified. A parabolic flow profile is assumed at the inlet, symmetry boundary conditions are taken at the axis of symmetry, zero velocity is assumed at the solid surfaces and zero stresses are assumed at the exit. The temperature is specified at the inlet, and is assumed to be uniform at the susceptor. A symmetry boundary condition is used for the temperature along the axis of symmetry, and a natural boundary condition is applied at the exit. It is also assumed that both the wall and the susceptor support are cooled to the inlet temperature. However, the effects of insulating either the wall or the support are also examined.

In addition to the primitive variables u, v, p, and T, the streamfunction Ψ is of interest since it facilitates visualization of the results. For a compressible fluid in cylindrical coordinates, Ψ is defined by

$$\rho\,u = \frac{1}{r}\frac{\partial\Psi}{\partial r}\,, \tag{A.13}$$

and

$$\rho\,v = -\frac{1}{r}\frac{\partial\Psi}{\partial z}\,, \tag{A.14}$$

where u and v are the axial and the radial velocity components respectively. The stream-function is computed solving the Poisson equation:

$$\nabla^2 \Psi = 2\rho\, u + r\left(u\frac{\partial \rho}{\partial r} - v\frac{\partial \rho}{\partial z}\right) + \rho\, r\left(\frac{\partial u}{\partial r} - \frac{\partial v}{\partial z}\right) . \qquad \text{(A.15)}$$

A.4 Finite element formulation

The Galerkin finite element method is used to discretize the governing equations. Biquadratic basis functions, N^i, are used to expand the velocity components (u and v) and the temperature (T), and to weight the momentum and the energy equations. Bilinear basis functions, M^i, are used to expand the pressure (p), and to weight the continuity equation. The resulting residual equations are:

$$R_c^i = \int_V \left[v + r\left(\frac{\partial v}{\partial r} + \frac{\partial u}{\partial z}\right) - \frac{r}{T}\left(v\frac{\partial T}{\partial r} + u\frac{\partial T}{\partial z}\right)\right] M^i\, dr\, dz\,, \qquad \text{(A.16)}$$

$$R_u^i = \int_V \left[T^{zz}N_z^i + T^{rz}N_r^i + \frac{Re}{T}N^i\left(v\frac{\partial u}{\partial r} + u\frac{\partial u}{\partial z}\right) + \frac{St}{T}N^i\right] r\, dr\, dz\,, \qquad \text{(A.17)}$$

$$R_v^i = \int_V \left[T^{rz}N_z^i + T^{rr}N_r^i + \frac{T^{\theta\theta}}{r}N^i + \frac{Re}{T}N^i\left(v\frac{\partial v}{\partial r} + u\frac{\partial v}{\partial z}\right) + \frac{St}{T}N^i\right] r\, dr\, dz\,, \qquad \text{(A.18)}$$

$$R_E^i = \int_V \left[\frac{Re\,Pr}{T}\,C_p\,N^i\left(v\frac{\partial T}{\partial r} + u\frac{\partial T}{\partial z}\right) + \kappa\left(\frac{\partial T}{\partial r}\,N_r^i + \frac{\partial T}{\partial z}\,N_z^i\right)\right] r\, dr\, dz\,, \qquad \text{(A.19)}$$

Here R_c^i, R_u^i, R_v^i, and R_E^i are the continuity, z-momentum, r-momentum, and energy residual equations respectively; V is the computational domain[3]. The two-letter superscripts denote the stress tensor components and the subscripts denote differentiation. Equations (A.16), (A.17), (A.18), and (A.19) constitute a system of nonlinear equations which is solved by Newton iteration and frontal solvers [75].

---

[3] Notice that the standard finite element method is used here without any special elements.

Mesh I – 15240 unknowns

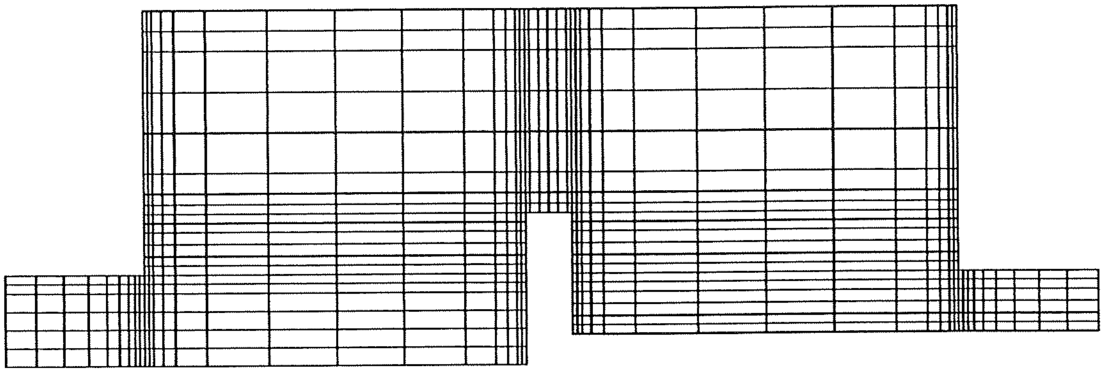

Figure A.2: Mesh used for all the computations (scaled 1:2 in the r direction).

A.5 Results and discussion

Calculations were carried out for various *Re* (ranging from 0 to 100), *St* (from −30 to 30), T_{susc} (from 300 to 1,050K) and different thermal boundary conditions. The inlet temperature was 300 K and the Prandtl number equal to unity in all cases. It was also assumed that the feed was 100% NH_3. The finite element mesh used for all the results is shown in Figure A.2. It consisted of 1116 elements (15240 unknowns). The inlet and outlet nozzles are cut at distances equal to 3 times the radius, a length adequate to approximate the inlet and outlet boundary conditions (the actual lengths are given in Table A.1).

The effect of the *Re* for zero gravity and isothermal conditions was studied first. The results are illustrated in Figure A.3. Note that all graphs are scaled 1:2 in the r direction to more clearly show the results. An interesting characteristic of the flow for this geometry is the appearance of a vortex around the periphery of the susceptor, in addition to the one formed behind it. These two vortices increase in size and strength, as *Re* increases, and finally merge to form a large vortex. As *Re* increases, the flow close to the susceptor approaches a uniform thickness boundary layer flow which in general favors film thickness uniformity. The recirculation cell at the inlet is caused by the sudden expansion in flow

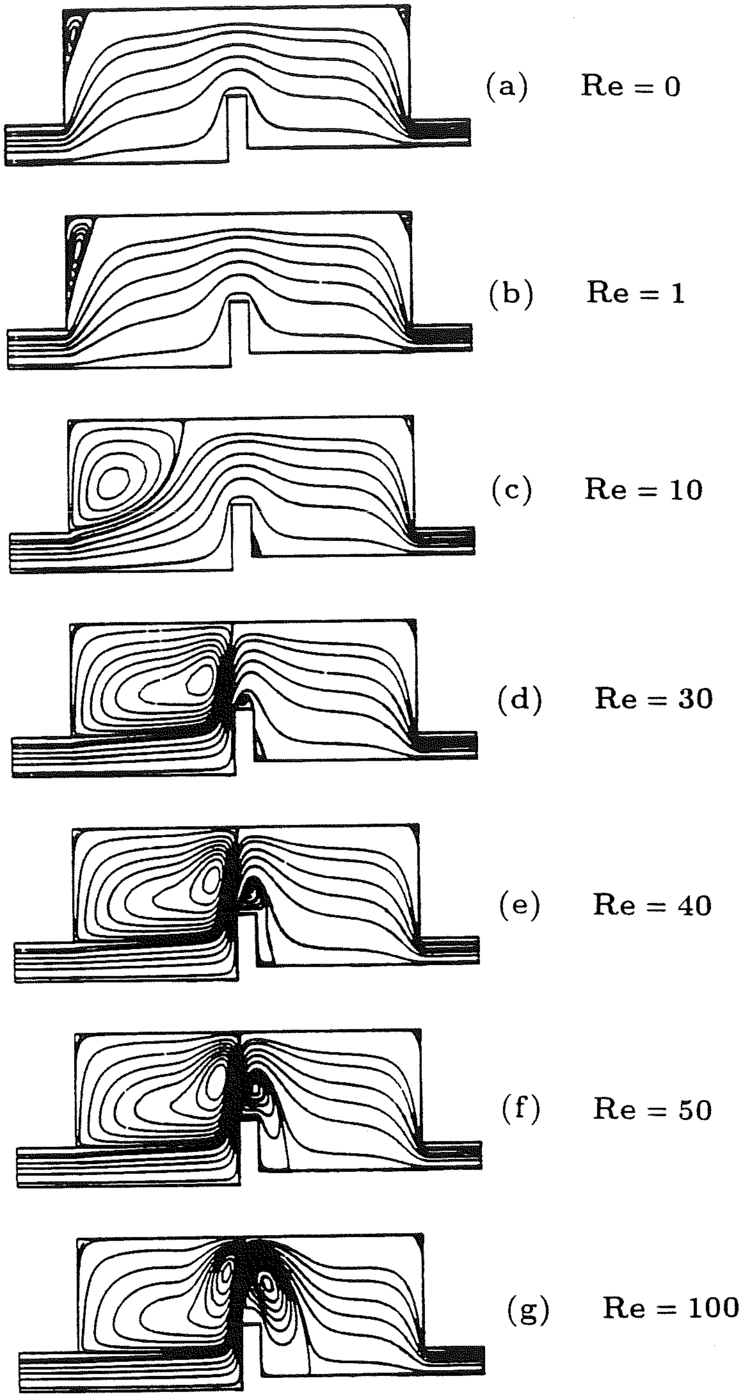

Figure A.3: Streamlines at different *Re*, zero gravity, and isothermal conditions.

cross-sectional area at the inlet and increases in size as Re increases. It can be eliminated by reshaping the reactor inlet [46].

It is well known that the thermal boundary conditions play an important role in the solution of CVD flow. As pointed out by Fotiadis *et al.* [47], inclusion of radiation effects is important. To illustrate the effect of the thermal boundary conditions, we obtained results for three different cases:

1. Cooled reactor walls and insulated susceptor support.
2. Insulated reactor walls and cooled susceptor support.
3. Cooled reactor walls and susceptor support.

The computed streamlines and isotherms for $Re=1$, $St=0$, and $T_{susc}=750K$ are shown in Figure A.4. More drastic changes in the flow field and the temperature solution may occur at different conditions, especially when gravity is taken into account. The changes in the flow field and the temperature distribution as Reynolds number increases are shown in Figures A.5, A.6, and A.7 for the three cases examined. In all the subsequent results we assume that both the reactor wall and the susceptor support are cooled.

The gravity effect (i.e., the influence of the Stokes number) is very important if there are density variations in the gas (nonisothermal case). In our experiments [36], we observed that in some instances when the feed is introduced from the top of the reactor (flow in the same direction with gravity) the film quality is unsatisfactory; furthermore, particle formation from the susceptor is observed. When the feed is introduced from the bottom this undesired phenomenon disappears, and the film quality and thickness uniformity are improved. The computational results show significant changes in the flow field as the Stokes number increases (equivalent to increasing the operating pressure of the reactor). The results for Re=2, T_{susc}=750 K and flow opposite to the direction of gravity

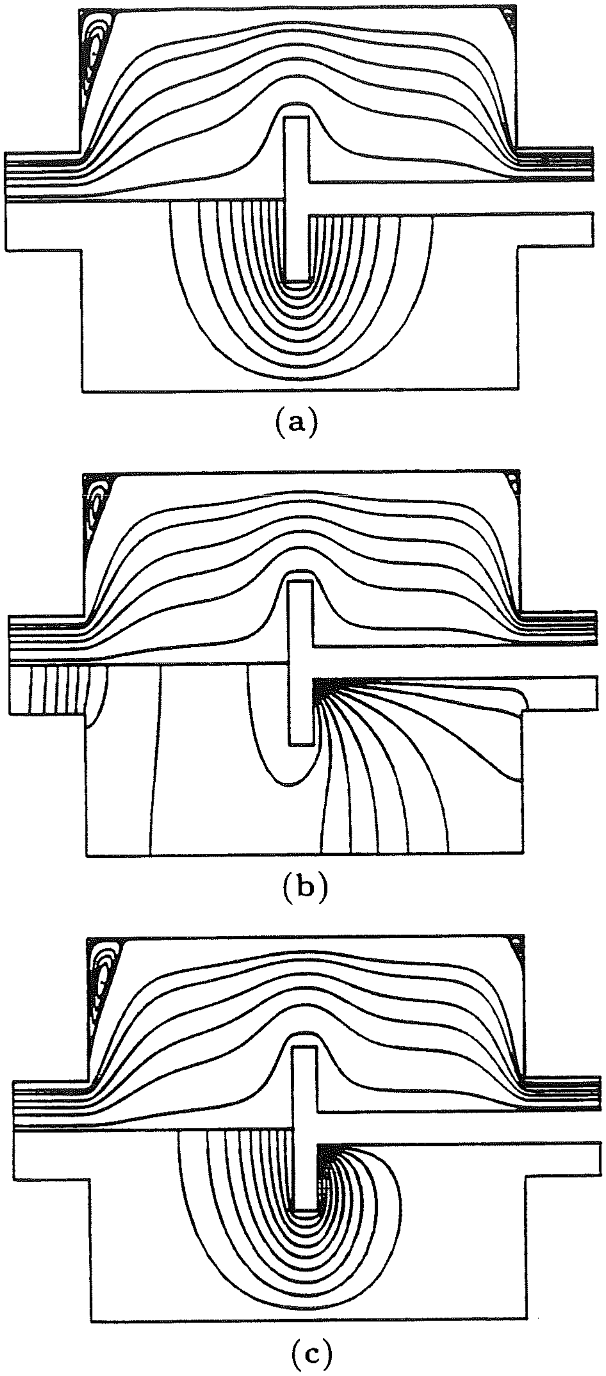

Figure A.4: Streamlines (top) and isotherms (bottom) at *Re*= 1, T_{susc}= 750 K, and zero gravity.
(a) Cooled reactor walls and insulated susceptor support.
(b) Insulated reactor walls and cooled susceptor support.
(c) Cooled reactor walls and susceptor support.

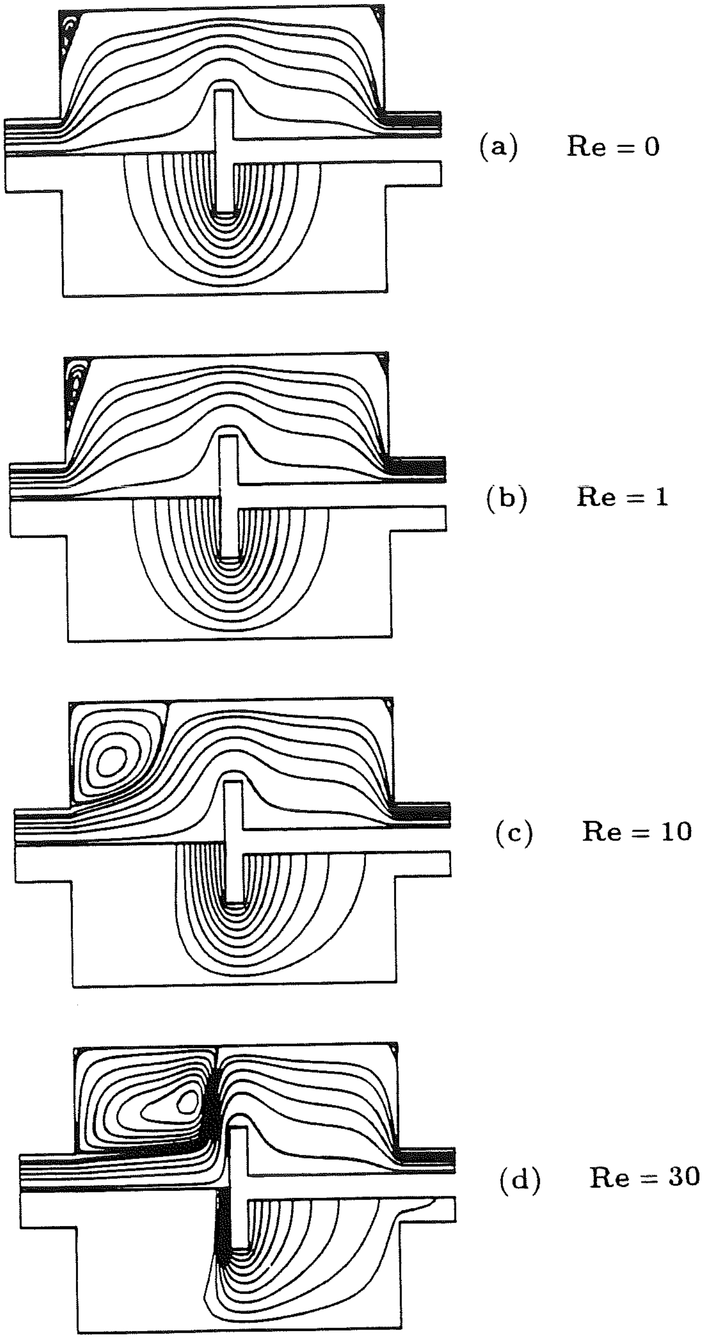

(a) Re = 0

(b) Re = 1

(c) Re = 10

(d) Re = 30

Figure A.5: Streamlines (top) and isotherms (bottom) at T_{susc}= 750 K, zero gravity and different Reynolds numbers.
Reactor walls are cooled and susceptor support is insulated.

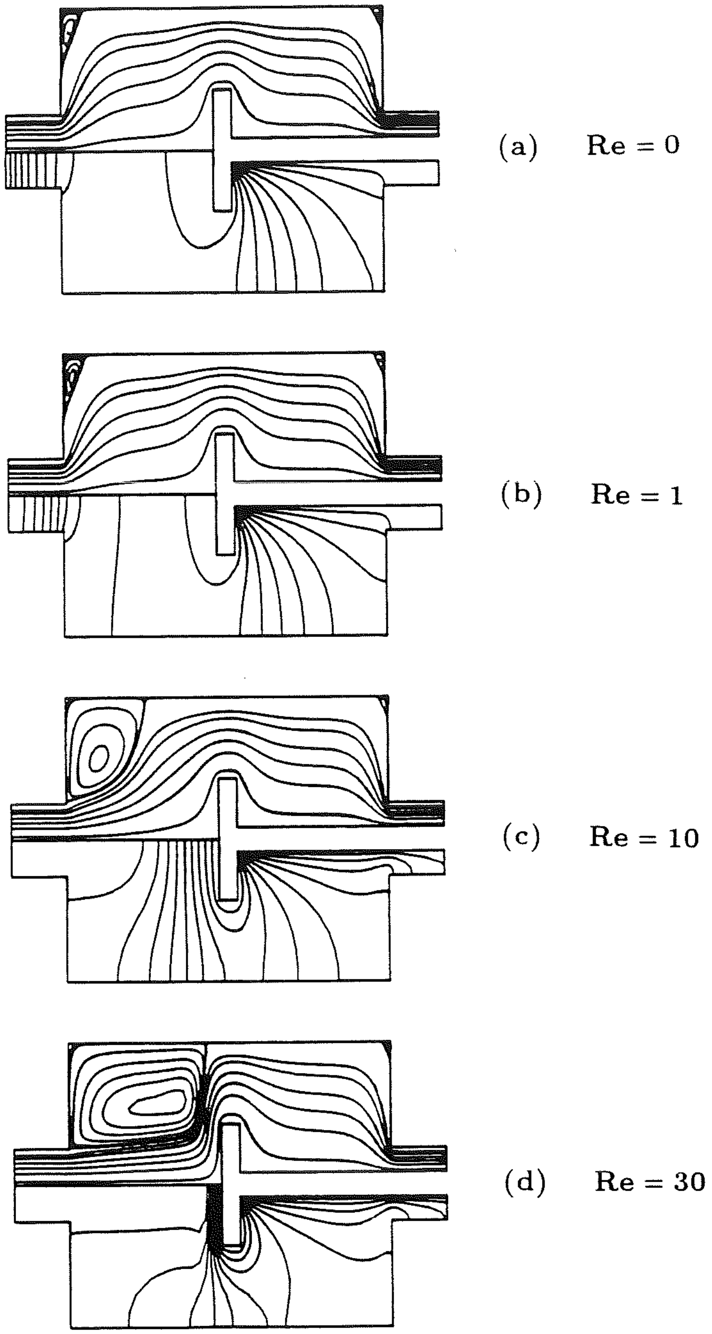

(a) Re = 0

(b) Re = 1

(c) Re = 10

(d) Re = 30

Figure A.6: Streamlines (top) and isotherms (bottom) at T_{susc}= 750 K, zero gravity and different Reynolds numbers.
Reactor walls are insulated and susceptor support is cooled.

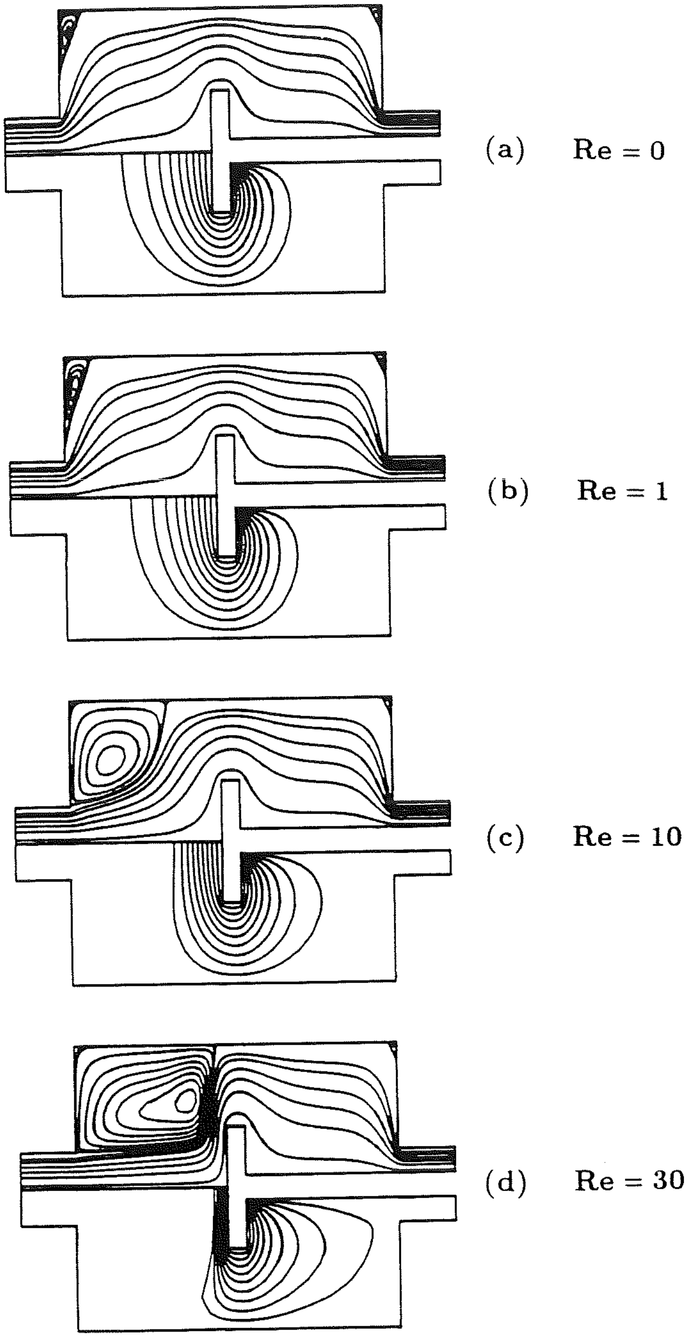

(a) Re = 0

(b) Re = 1

(c) Re = 10

(d) Re = 30

Figure A.7: Streamlines (top) and isotherms (bottom) at T_{susc}= 750 K, zero gravity and different Reynolds numbers.
Reactor walls and susceptor support are cooled.

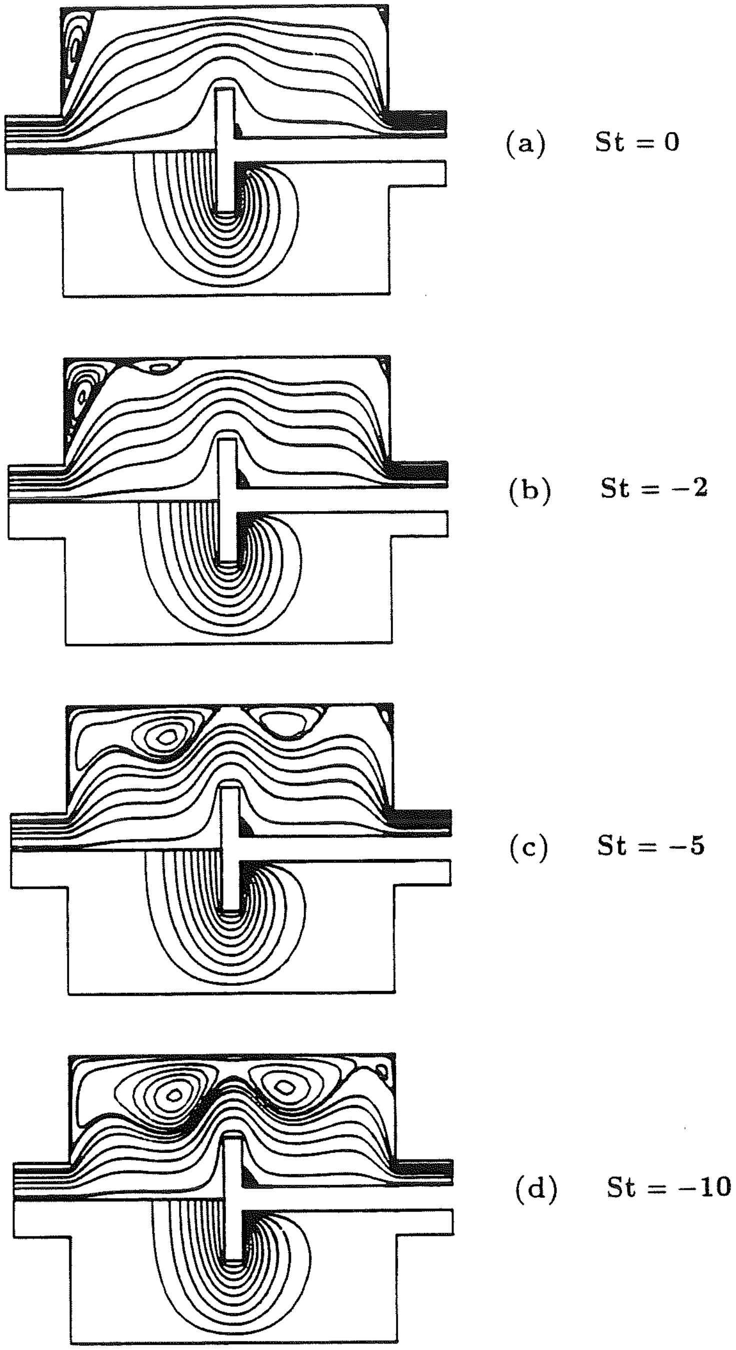

Figure A.8: Streamlines (top) and isotherms (bottom) at $Re = 2$, T_{susc}= 750 K, and different Stokes numbers. The flow is opposite to the direction of gravity. Reactor walls and susceptor support are cooled.

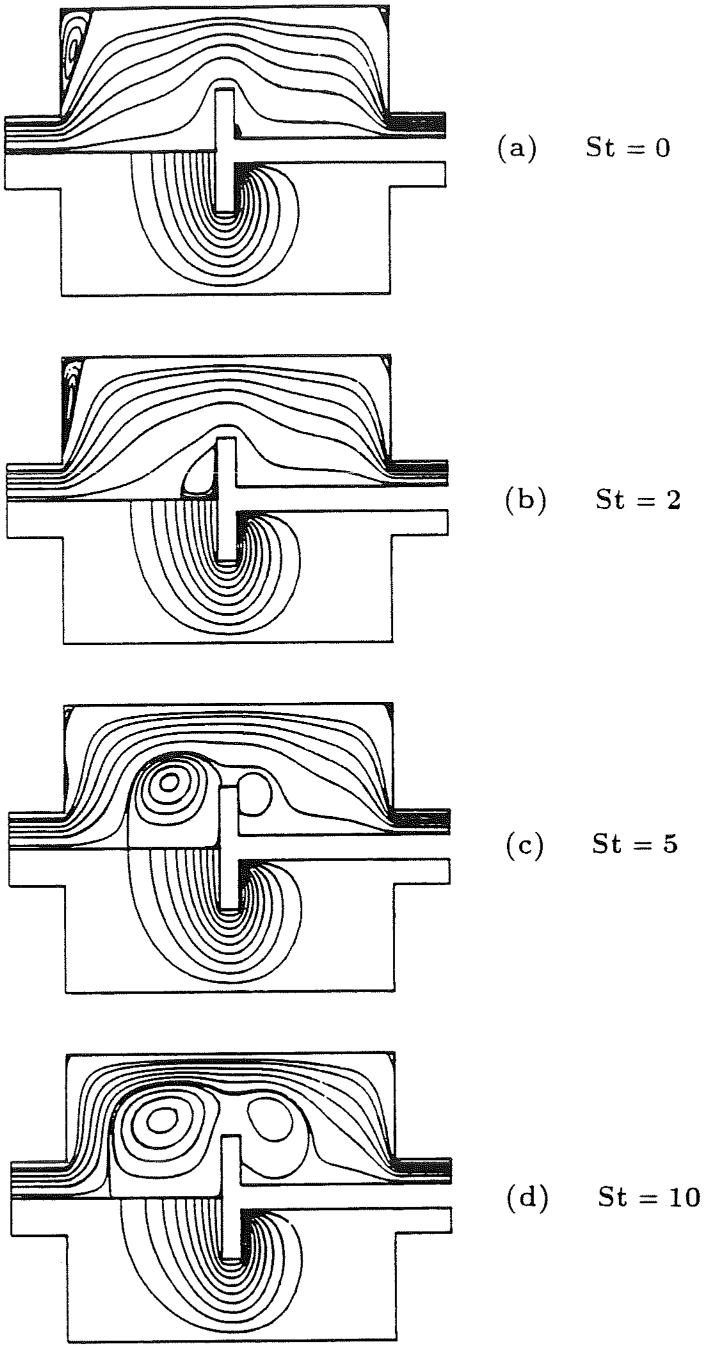

Figure A.9: Streamlines (top) and isotherms (bottom) at $Re = 2$, T_{susc}= 750 K, and different Stokes numbers. The flow is in the same direction as gravity. Reactor walls and susceptor support are cooled.

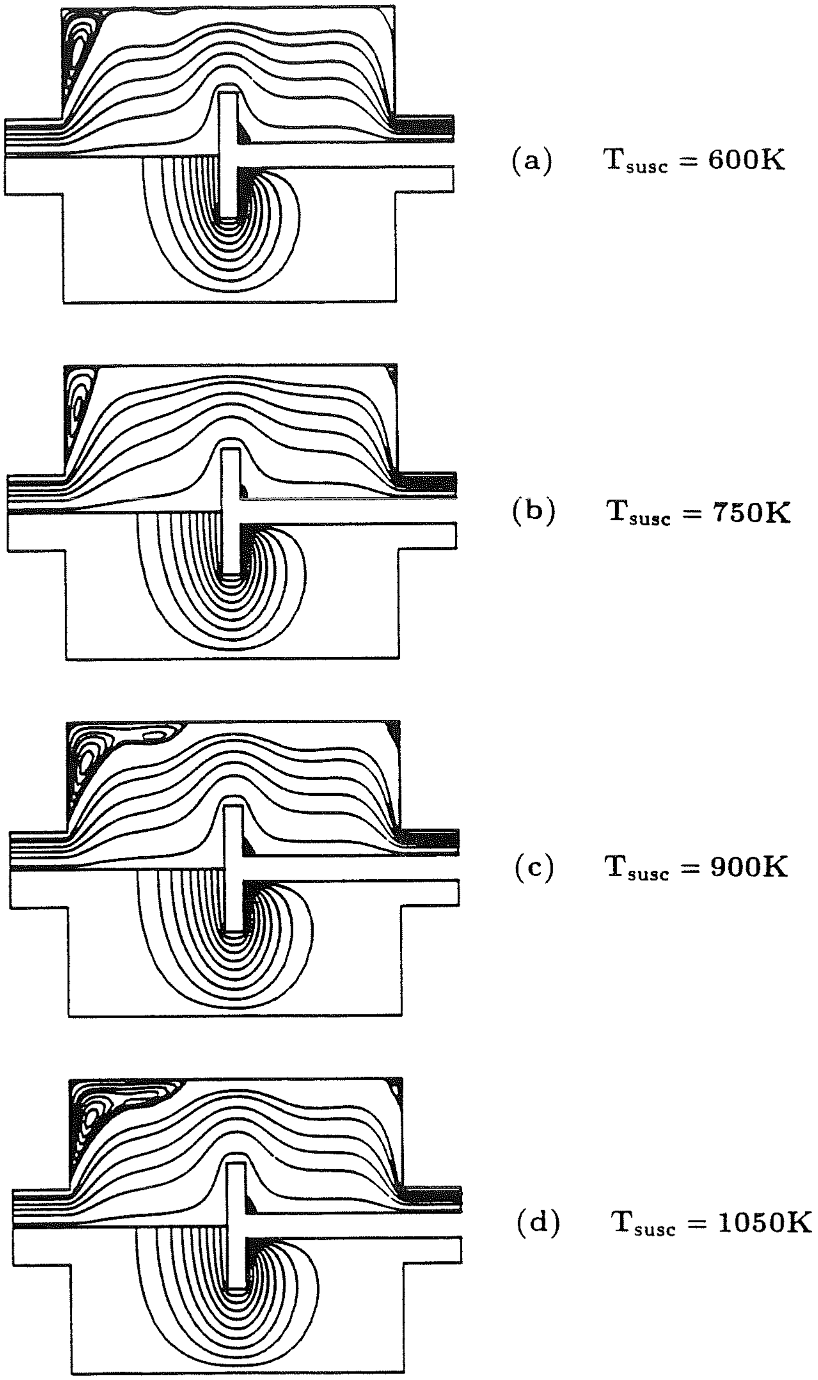

Figure A.10: Streamlines (top) and isotherms (bottom) at $Re = 2$, $St = -2$, and different susceptor temperatures T_{susc}. The flow is opposite to the direction of gravity. Reactor walls and susceptor support are cooled.

are shown in Figure A.8. As St increases, new vortices are formed near the wall and finally merge to a large recirculation region. However, the flow pattern around the susceptor remains basically the same in agreement with Wahl's results [156]. Quite different patterns are obtained, however, when the flow is in the direction of gravity (Figure A.9). Large buoyancy driven recirculation cells, due to the density gradient close to the susceptor, are formed above and below the susceptor, whereas the recirculation caused by the expansion of the flow cross-section at the inlet decreases in size. This flow behavior is in agreement with the results in [46,47]. Recirculation cells around the susceptor are undesirable. As indicated by Fotiadis *et al.* [46], these cells can be removed by increasing the inlet flow (which also improves film thickness uniformity). From the results in Figure A.8, we conclude that having the flow from the bottom to the top is an alternative way to eliminate these cells.

The effect of the temperature of the susceptor on the flow is shown in Figure A.10, where we plotted the results for Re=2, St=2 and T_{susc}=600, 750, 900 and 1,050K.

A.6 Concluding remarks

The fluid mechanics and heat transfer in a vertical CVD reactor have been studied using finite elements. We illustrated the importance of the thermal boundary conditions. Gravity and its direction are also important and cause the formation of interesting flow patterns. Undesirable recirculation cells around the susceptor can be removed by having the flow opposite to the gravity direction.

A.7 Temperature dependence of the physical properties

In this section, we calculate the powers describing the temperature dependence of the thermal conductivity and the viscosity of the four gases of interest: NH_3, Ar, H_2, and

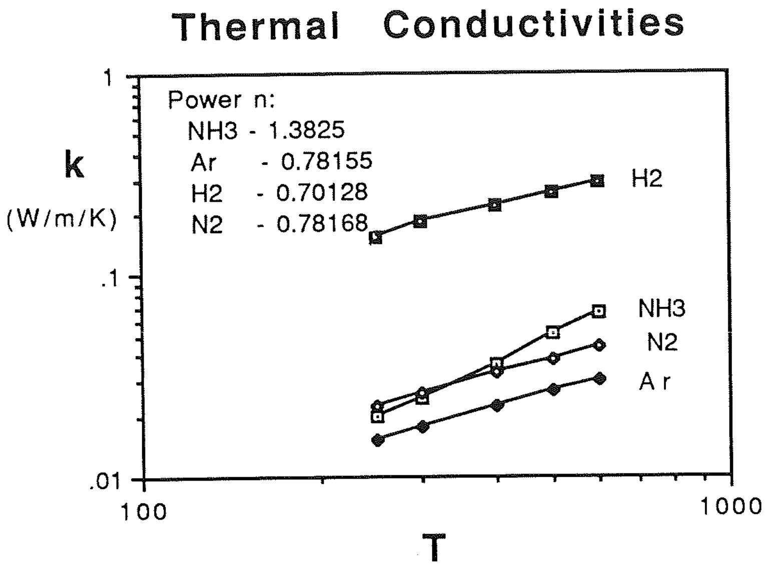

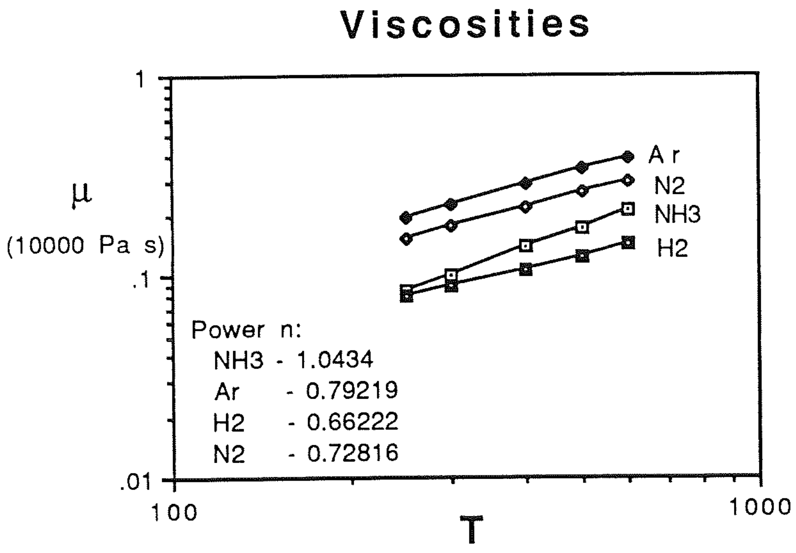

Figure A.11: Temperature dependence of κ and μ for NH_3, Ar, H_2, and N_2.

N_2. It is assumed that

$$\frac{\kappa(T_2)}{\kappa(T_1)} = \left(\frac{T_2}{T_1}\right)^{n_\kappa},$$

and

$$\frac{\mu(T_2)}{\mu(T_1)} = \left(\frac{T_2}{T_1}\right)^{n_\mu}.$$

To calculate n_κ and n_μ we use the data given in [116]. The data along with the computed values of the powers are shown in Figure A.11.

APPENDIX B

LOCAL SIMILARITY SOLUTIONS

Two-dimensional corner flows have been extensively investigated by different researchers [32,63,84,100,101,104,105]. In this appendix we summarize the two cases that are of primary interest in this thesis:

1. Flow near a sharp corner
2. Flow between a wall and a free surface (at a 180° angle)

These two flows were first examined by Moffatt[1] [104].

For steady, incompressible flow with negligible inertia forces[2], the stream function $\Psi(r,\theta)$ satisfies the Stokes equation

$$\nabla^4 \Psi = 0 ; \tag{B.1}$$

here (r,θ) are the plane polar coordinates centered at the singular point.

As has been demonstrated by Lugt and Schwiderski [96], equation (B.1) admits separated solutions of the form

$$\Psi = r^{(\lambda+1)} f_\lambda(\theta) , \tag{B.2}$$

---

[1] For local analyses concerning non-Newtonian flows see [4,31,66,81,142].

[2] The inertia forces are negligible close to the wall.

where λ is the exponent (or the eigenvalue) of the corresponding solution which may be real or complex. The function $f_\lambda(\theta)$ is of the general form

$$f_\lambda(\theta) \;=\; A\,\cos(\lambda+1)\theta \,+\, B\,\sin(\lambda+1)\theta \,+\, C\,\cos(\lambda-1)\theta \,+\, D\,\sin(\lambda-1)\theta \qquad \text{(B.3)}$$

where A, B, C, D are arbitrary constants. In the particular cases when $\lambda = -1$, 0 or 1 the function $f_\lambda(\theta)$ degenerates to the forms[3]:

$$f_{-1}(\theta) \;=\; A\,\cos 2\theta \,+\, B\,\sin 2\theta \,+\, C\,\theta \,+\, D \qquad \text{(B.4)}$$

$$f_{0}(\theta) \;=\; A\,\cos\theta \,+\, B\,\sin\theta \,+\, C\,\theta\,\cos\theta \,+\, D\,\theta\,\sin\theta \qquad \text{(B.5)}$$

$$f_{1}(\theta) \;=\; A\,\cos 2\theta \,+\, B\,\sin 2\theta \,+\, C\,\theta \,+\, D \qquad \text{(B.6)}$$

The radial and transverse velocity components u_r, u_θ respectively are given by

$$u_r \;\equiv\; \frac{1}{r}\frac{\partial\psi}{\partial\theta} \;=\; r^{\lambda}\, f_\lambda^{(1)}(\theta)\,, \qquad \text{(B.7)}$$

and

$$u_\theta \;\equiv\; -\frac{\partial\psi}{\partial r} \;=\; -(\lambda+1)\, r^{\lambda}\, f_\lambda(\theta)\,, \qquad \text{(B.8)}$$

where $f_\lambda^{(1)}(\theta)$ is the first derivative of $f_\lambda(\theta)$[4]:

$$\begin{aligned} f_\lambda^{(1)}(\theta) \;=\; & [-(\lambda+1)\,A\,\sin(\lambda+1)\theta \,+\, (\lambda+1)\,B\,\cos(\lambda+1)\theta \,- \\ & (\lambda-1)\,C\,\sin(\lambda-1)\theta \,+\, (\lambda-1)\,D\,\cos(\lambda-1)\theta]\,. \end{aligned} \qquad \text{(B.9)}$$

From the above two equations one finds for the stress components:

$$\tau^{rr} \;=\; 2\,\mu\,\frac{\partial u_r}{\partial r} \;=\; 2\,\mu\,\lambda\, r^{(\lambda-1)}\, f_\lambda^{(1)}(\theta) \qquad \text{(B.10)}$$

---

[3] Notice that the equation given by Moffatt [104] for the case $\lambda = -1$ is wrong. There is also a particular solution independent of θ [84]:

$$\Psi \;=\; A\,r^2\,\log r \,+\, B\,\log r \,+\, C\,r^2 \,+\, D\,.$$

In this case, the pressure is given by:

$$p \;=\; -4\,\mu\,A\,\theta\,.$$

[4] Similar notation is followed for all the higher derivatives of $f_\lambda(\theta)$.

$$\tau^{\theta\theta} \;=\; 2\,\mu\left[\frac{1}{r}\,\frac{\partial u_\theta}{\partial \theta} \,+\, \frac{u_r}{r}\right] \;=\; -2\,\mu\,\lambda\,r^{(\lambda-1)}\,f_\lambda^{(1)}(\theta) \tag{B.11}$$

$$\tau^{r\theta} \;=\; \mu\left[r\,\frac{\partial}{\partial r}\left(\frac{\partial u_\theta}{\partial r}\right) \,+\, \frac{1}{r}\,\frac{\partial u_r}{\partial \theta}\right] \;=\; \mu\,r^{(\lambda-1)}\,\left[-(\lambda^2-1)\,f_\lambda(\theta) \,+\, f_\lambda^{(2)}(\theta)\right] \tag{B.12}$$

Here, μ is the viscosity.

Finally the pressure is found by solving the r-momentum equation[5]

$$p \;=\; \mu\frac{r^{(\lambda-1)}}{(\lambda-1)}\,\left[(\lambda+1)^2\,f_\lambda^{(1)}(\theta) \,+\, f_\lambda^{(3)}(\theta)\right]\;, \tag{B.13}$$

or

$$p \;=\; -4\,\mu\,\lambda\,r^{(\lambda-1)}\,[C\,\sin{(\lambda-1)\theta} \;-\; D\,\cos{(\lambda-1)\theta}]\,. \tag{B.14}$$

B.1 Flow near a sharp corner

Consider the flow between two rigid boundaries fixed at an angle 2α (Figure B.1). The solution of this problem was determined in [32] and [104]. It is assumed that the stream function can be expanded in a series of the form

$$\Psi \;=\; \sum_{n=1}^{\infty} A_n\,r^{(\lambda_n+1)}\,f_{\lambda_n}(\theta)\,,$$

where the exponents λ_n are suitably ordered so that

$$0 < Re(\lambda_1) < Re(\lambda_2) < \cdots\,.$$

The first of the inequalities ensures that the velocity vanishes at the corner. As indicated by Moffatt [104], a disturbance far from the corner can generate either an *antisymmetrical* or a *symmetrical* flow pattern near the corner, and the corresponding stream function $\Psi(r,\theta)$ is an even or odd function of θ respectively. By taking advantage of the linearity of the Stokes equation, we may consider the two types of flow separately.

---

[5] The pressures for the special cases of $\lambda = -1, 0$ and 1 are given in [84].

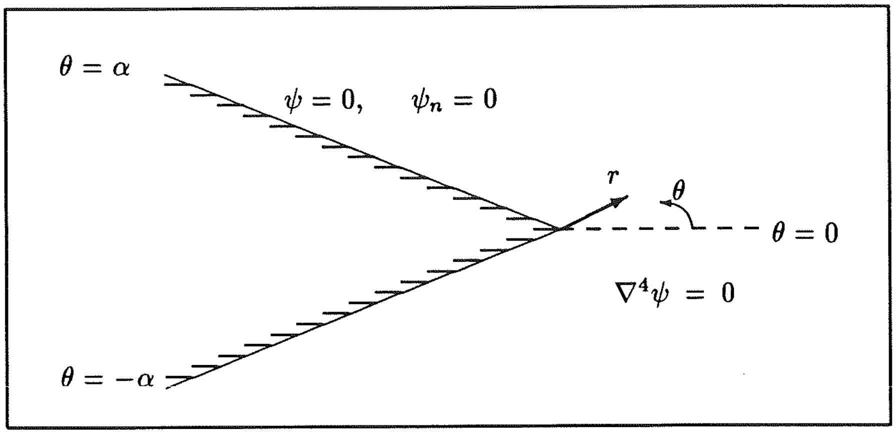

Figure B.1: Geometry of flow at a corner.

Table B.1: Real and imaginary parts of the leading exponent $\lambda_1 = p_1 + iq_1$ in the axisymmetric flow at a corner.

$2\alpha^o$	p_1	q_1
30.0	8.0630	4.2029
60.0	4.0593	1.9520
90.0	2.7396	1.1190
120.0	2.0941	0.6046
146.4	1.7892	0.0000
150.0	1.9130	
180.0	1.0000	
210.0	0.7520	
240.0	0.6157	
270.0	0.5445	
300.0	0.5122	
330.0	0.5015	
360.0	0.5000	

Table B.2: Real and imaginary parts of the leading exponent $\lambda_1 = p_1 + iq_1$ in the symmetric flow at a corner.

$2\alpha^o$	p_1	q_1
30.0	14.3303	5.1964
60.0	7.1820	2.4557
90.0	4.8083	1.4639
120.0	3.6307	0.8812
150.0	2.9367	0.3637
159.2	2.8144	0.0000
180.0	2.0000	
210.0	1.4858	
240.0	1.0000	
270.0	0.9085	
300.0	0.7309	
330.0	0.5982	
360.0	0.5000	

Antisymmetric flow between rigid boundaries

For this type of flow $f_\lambda(\theta)$ is even ($B = D = 0$) and

$$f_\lambda(\theta) \;=\; A\,\cos(\lambda+1)\theta \;+\; C\,\cos(\lambda-1)\theta\,. \tag{B.15}$$

For a nontrivial solution λ satisfies the equation

$$\sin 2\lambda\alpha \;=\; -\lambda \sin 2\alpha\,. \tag{B.16}$$

The leading exponents (λ_1) of equation (B.16) for various angles 2α are listed in Table B.1[6]. For $2\alpha \geq 146.4^o$ equation (B.16) has one real solution which decreases as the angle 2α increases. For $2\alpha < 146.4^o$ equation (B.16) admits no real solutions[7].

Symmetric flow between rigid boundaries

For this type of flow $f_\lambda(\theta)$ is odd ($A = C = 0$) and

$$f_\lambda(\theta) \;=\; B\,\sin(\lambda+1)\theta \;+\; D\,\sin(\lambda-1)\theta\,. \tag{B.17}$$

---

[6] The values given in [104] are slightly different.

[7] As indicated by Moffatt [104], complex exponents imply the existence of an infinite sequence of eddies near the corner.

For a nontrivial solution λ satisfies the equation

$$\sin 2\lambda\alpha = \lambda \sin 2\alpha . \tag{B.18}$$

The solutions of equation (B.18) with the smallest real part are listed in Table B.2. For $2\alpha \geq 159.2^o$ equation (B.18) has one real solution which decreases as the angle 2α increases. For $2\alpha < 159.2^o$ equation (B.18) admits no real solutions.

We should notice that equations (B.17) and (B.18) hold also for the flow between a rigid boundary and a free surface positioned at $\theta = 0$. Based on physical arguments, Michael [100] showed that the angle of separation, α, can not take arbitrary values[8]. He showed that for zero surface tension it must be $\alpha = \pi$, which is exactly the case of the stick-slip problem.

B.2 Local solution for the stick-slip problem

The two solution sets for the flow between a wall and a free surface at an angle $\alpha = \pi$ are given below.

Odd set of solutions

$$\begin{aligned}
\psi &= r^{\lambda+1}\left[\cos(\lambda+1)\theta - \cos(\lambda-1)\theta\right] \\
u_r &= r^{\lambda}\left[-(\lambda+1)\,\sin(\lambda+1)\theta + (\lambda-1)\,\sin(\lambda-1)\theta\right] \\
u_\theta &= -(\lambda+1)\,r^{\lambda}\,\left[\cos(\lambda+1)\theta - \cos(\lambda-1)\theta\right] \\
p &= 4\,\mu\,\lambda\,r^{\lambda-1}\,\sin(\lambda-1)\theta
\end{aligned}$$

$$\lambda = \frac{1}{2}, \frac{3}{2}, \frac{5}{2} \cdots$$

The graphs of the first three solutions are plotted in Figures B.2-B.4.

Even set of solutions

$$\psi = r^{\lambda+1}\left[(\lambda-1)\sin(\lambda+1)\theta - (\lambda+1)\sin(\lambda-1)\theta\right]$$

---

[8] For a thorough discussion on the separation of Stokes flow see [101].

$$
\begin{aligned}
u_r &= (\lambda^2 - 1)\, r^\lambda \left[\cos(\lambda+1)\theta - \cos(\lambda-1)\theta\right] \\
u_\theta &= -(\lambda+1)\, r^\lambda \left[(\lambda-1)\sin(\lambda+1)\theta - (\lambda+1)\sin(\lambda-1)\theta\right] \\
p &= -4\,\mu\,\lambda\,(\lambda+1)\, r^{\lambda-1}\, \cos(\lambda-1)\theta
\end{aligned}
$$

$$\lambda = 2, 3, 4, \cdots$$

The x- and y- velocity components are obtained by invoking the identities:

$$u = -u_r \cos\theta + u_\theta \sin\theta \tag{B.19}$$

$$v = -u_r \sin\theta - u_\theta \cos\theta \tag{B.20}$$

with

$$r = \sqrt{x^2 + y^2} \tag{B.21}$$

and

$$\theta = \begin{cases} \tan^{-1}\left(-\frac{y}{x}\right), & x \le 0 \\ \pi + \tan^{-1}\left(-\frac{y}{x}\right), & x > 0 \end{cases} \tag{B.22}$$

The first few terms for u, v, and p are given below:

$\underline{\lambda = 1/2}$

$$
\begin{aligned}
u &= 2\, r^{1/2} \sin\frac{\theta}{2} \left(1 + \cos^2\frac{\theta}{2}\right) \\
v &= r^{1/2} \sin\frac{\theta}{2} \sin\theta \\
p &= -2\, r^{-1/2} \sin\frac{\theta}{2}
\end{aligned}
$$

$\underline{\lambda = 3/2}$

$$
\begin{aligned}
u &= 2\, r^{3/2} \sin\frac{\theta}{2} \left(7\cos^2\frac{\theta}{2} - 1\right) \\
v &= -3\, r^{3/2} \sin\frac{\theta}{2} \sin\theta \\
p &= 6\, r^{1/2} \sin\frac{\theta}{2}
\end{aligned}
$$

$\underline{\lambda = 2}$

$$\begin{aligned} u &= 12\, r^2\, \sin^2\theta \\ v &= 0 \\ p &= -24\, r\, \cos\theta \end{aligned}$$

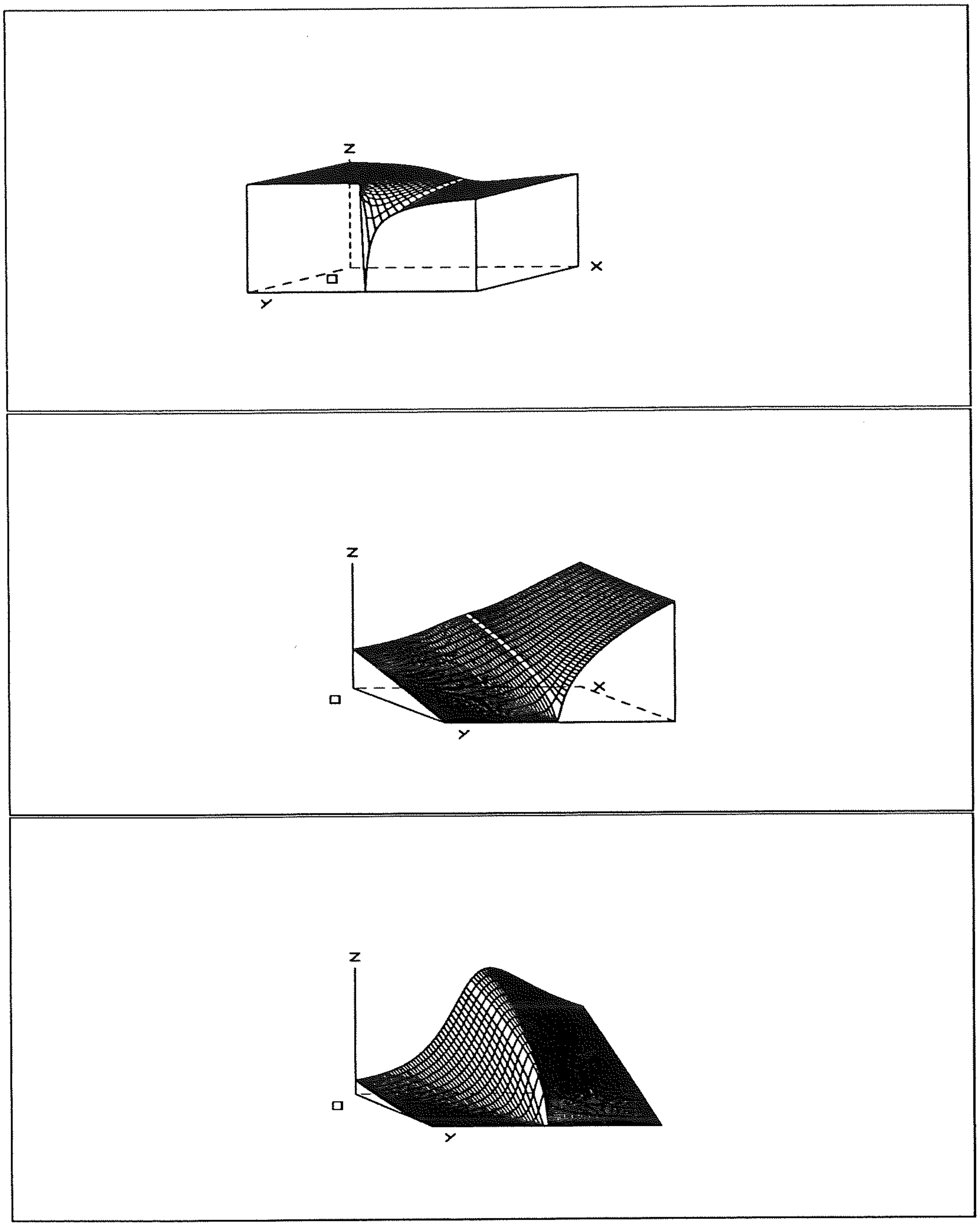

Figure B.2: 3-D view of the local solution for $\lambda = 1/2$: p (top), u (middle), v (bottom). The pressure is, in fact, infinite at the singular point.

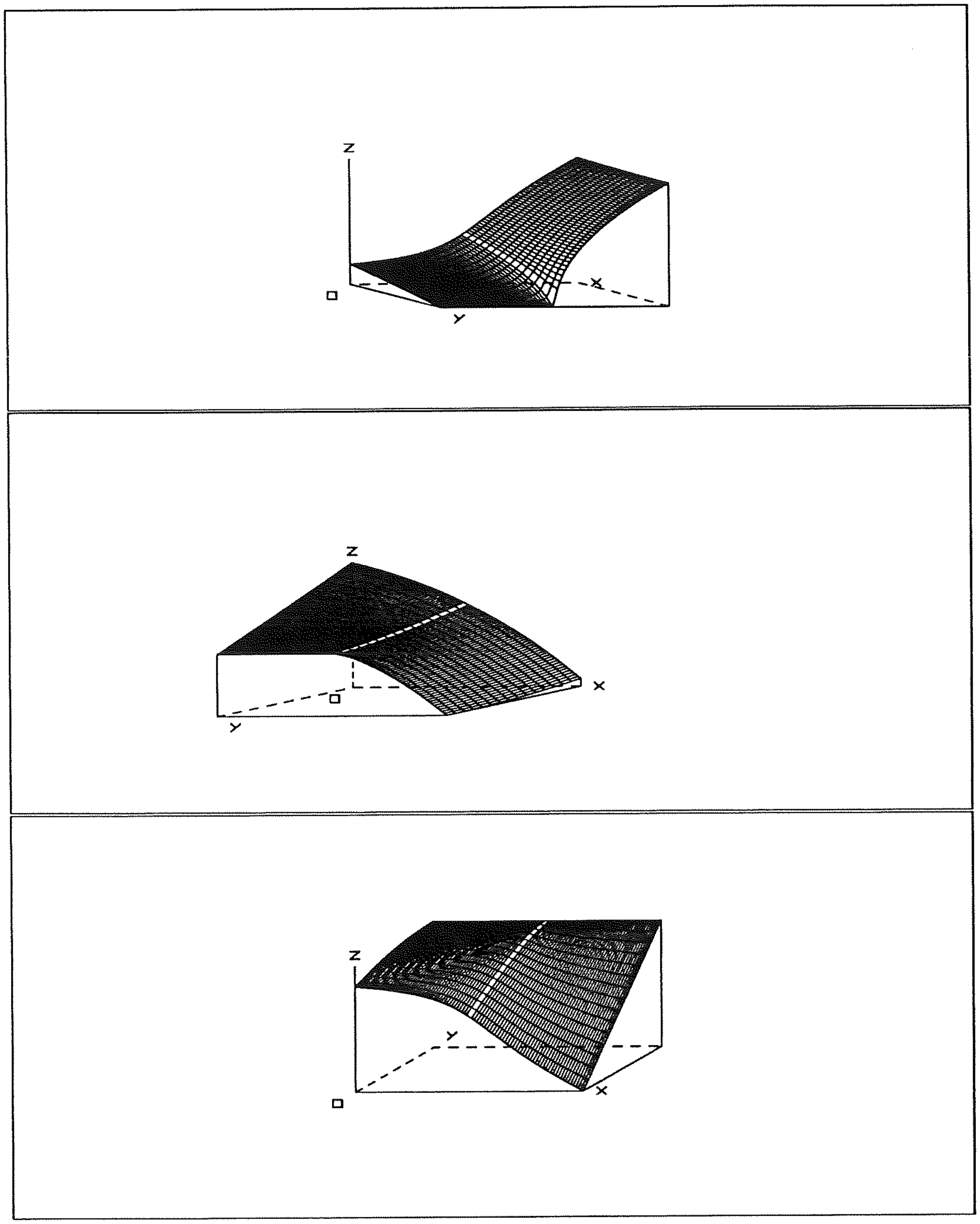

Figure B.3: 3-D view of the local solution for $\lambda = 3/2$: p (top), u (middle), v (bottom).

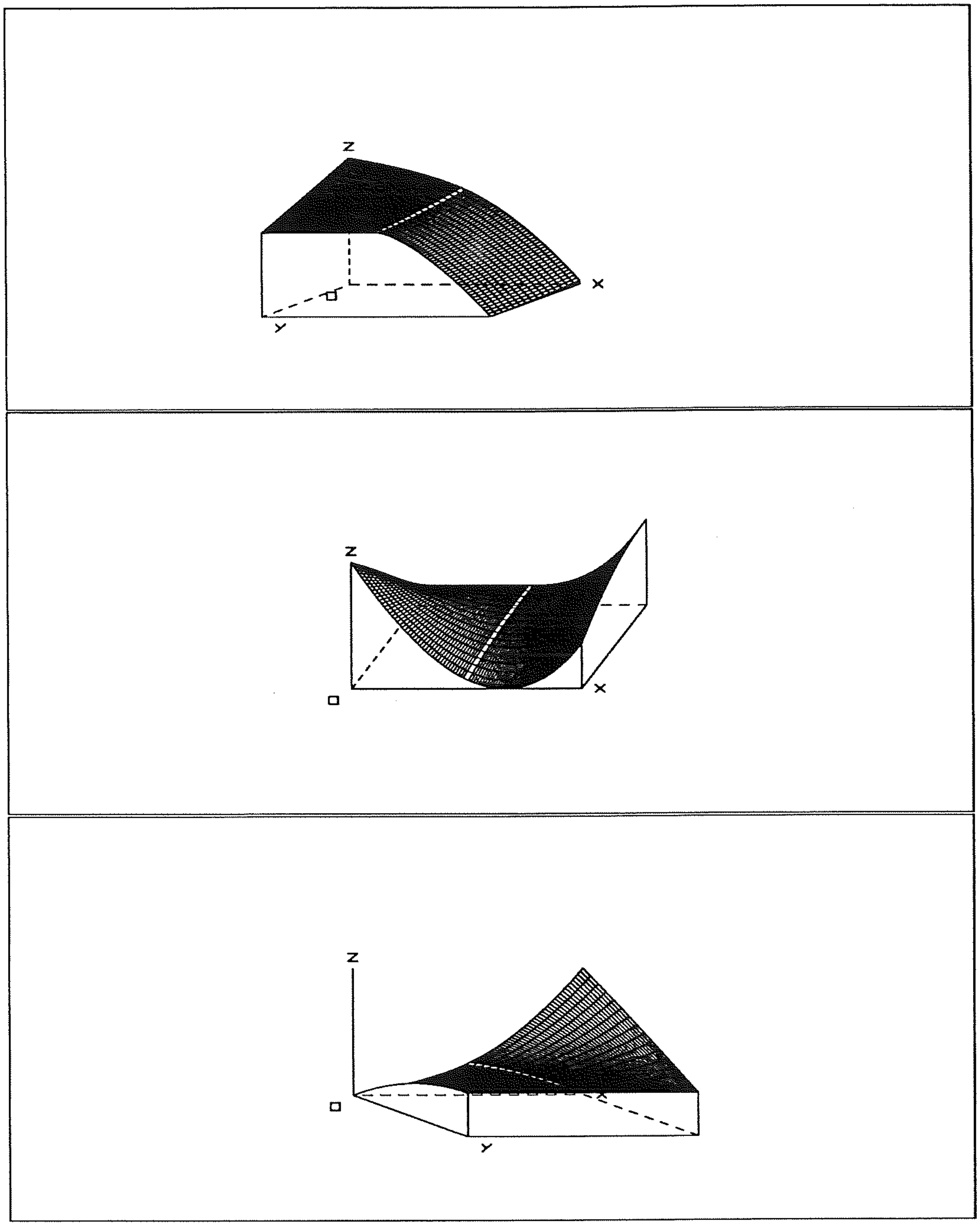

Figure B.4: 3-D view of the local solution for $\lambda = 5/2$: p (top), u (middle), v (bottom).

APPENDIX C

THE MOTZ PROBLEM – ADDITIONAL RESULTS

In this appendix we present more details about the finite element formulations for the Motz problem introduced and discussed in Chapter V. The three methods considered in Chapter V are:

1. The standard finite element method,
2. The blended singular basis function method (BSBFM), and
3. The integrated singular basis function method (ISBFM).

Three different blendings are examined with the BSBFM in an attempt to improve the estimates for the singular coefficients and to understand the limitations of the method.

In addition to the formulation, some results for the Motz problem are given at the end of the appendix.

C.1 Finite Element Formulation

The governing equations and the geometry of the Motz problem are depicted in Figure 5.1. The local solution is of the form:

$$u = \sum_{i=1}^{\infty} \alpha_i \, r^{\frac{2i-1}{2}} \cos \frac{2i-1}{2}\theta \,, \tag{C.1}$$

Table C.1: Values of the singular coefficients α_i for the Motz problem.

Method	Reference	α_1	α_2	α_3	α_4
Singular functions	[106]	401.41	88.61	-20.07	-26.78
Singular elements	[157]	393.6 398.0	-18.3 -80.8		
Global elements	[68]	401.162	87.6558	17.2381	-8.0705
Conformal transformation (exact)	[126]	401.1625	87.65592	17.23792	-8.0712
Global elements	[86]	401.1625	87.6553	17.2435	-8.0981
Iterative method	[165]	401.163	87.655	17.238	-8.071

where $(r,\ \theta)$ are the radial coordinates centered on the singular point, and α_i are the unknown singular coefficients. The first term of equation (C.1) is the most singular term causing an inverse square root singularity for the derivatives.

A summary of the various estimates of the first singular coefficients α_i is given in Table C.1.

C.1.1 Ordinary Finite Elements

The unknown u is expanded in terms of biquadratic basis functions Φ^i:

$$u = \sum_{i=1}^{N_u} u_i \, \Phi^i \,, \tag{C.2}$$

where N_u is the number of unknowns, and u_i are the nodal values.

We apply Galerkin's principle by weighting the governing equation with the basis functions Φ^i, and then we use the divergence theorem:

$$\int_S \frac{\partial u}{\partial n} \Phi^i \, dS - \int_V \nabla u \cdot \nabla \Phi^i \, dV = 0 \,, \qquad i = 1, 2, \ldots, N_u \,. \tag{C.3}$$

Here, V is the physical domain, S denotes its boundary, n is the normal direction to S, and N_u the number of unknowns. The boundary terms can be omitted because we have only essential and homogeneous natural boundary conditions, and equation (C.3) is simplified to

$$-\int_V \nabla u \cdot \nabla \Phi^i \, dV = 0\,, \qquad\qquad i = 1, 2, \ldots, N_u\,. \tag{C.4}$$

Equations (C.4) constitute a symmetric and banded linear system of equations.

C.1.2 The Blended Singular Basis Function Method

To the ordinary finite element expansion we add the singular basis functions W^i:

$$u = \sum_{i=1}^{N_u} u_i\, \Phi^i + \sum_{i=1}^{N_{SBF}} \alpha_i\, W^i\,, \tag{C.5}$$

where N_{SBF} is the number of singular functions, and α_i are the unknown coefficients.

For comparisons, we constructed 3 different sets of singular functions:

$$\text{BSBF1}: \quad W^i = \begin{cases} r^{\frac{(2i-1)}{2}} \cos\frac{2i-1}{2}\theta\,, & 0 \le r \le R/2 \\ \frac{1}{R^2}(r-R)^2\,(ar-b)\,\cos\frac{2i-1}{2}\theta\,, & R/2 \le r \le R \\ 0\,, & r \ge R \end{cases}$$

$$\text{BSBF2}: \quad W^i = \begin{cases} \frac{1}{R^3} r^{\frac{(2i-1)}{2}}(r-R)^2\,(2r+R)\,\cos\frac{2i-1}{2}\theta\,, & 0 \le r \le R \\ 0\,, & r \ge R \end{cases}$$

$$\text{BSBF3}: \quad W^i = \begin{cases} r^{\frac{(2i-1)}{2}}(1-\frac{x^2}{H^2})(1-\frac{y^2}{H^2})\,\cos\frac{2i-1}{2}\theta\,, & 0 \le |x|, |y| \le H \\ 0\,, & \text{elsewhere} \end{cases}$$

BSBF1 are functions with two-zone blending as suggested by Strang and Fix [141]. They are identical to the asymptotic expansion terms in a semicircular area of radius $R/2$. For greater values of r they are given by a polynomial in r which merges smoothly to zero at R. The coefficients a and b are determined by demanding continuity of W^i and its first derivative at $r = R/2$.

BSBF2 and BSBF3 are functions with one-zone blending. BSBF2 are defined again over a semicircular area of radius R and obtained as the product of the asymptotic expansion terms times a polynomial in r which is equal to 1 at $r = 0$, and merges smoothly to zero at R. As r goes to zero, W^i converges to the exact solution. Finally, BSBF3 are defined over a rectangular area and merge smoothly to zero at its boundaries. Again as r goes to zero, W^i converges to the asymptotic solution.

Applying Galerkin's principle, we weight the governing equation by Φ^i and W^i. After using the divergence theorem we get:

$$\int_S \frac{\partial u}{\partial n} \Phi^i \, dS - \int_V \nabla u \cdot \nabla \Phi^i \, dV = 0 , \qquad i = 1, 2, \ldots, N_u , \tag{C.6}$$

and

$$\int_S \frac{\partial u}{\partial n} W^i \, dS - \int_V \nabla u \cdot \nabla W^i \, dV = 0 , \qquad i = 1, 2, \ldots, N_{SBF} , \tag{C.7}$$

Note that the total number of unknowns is now $N_u + N_{SBF}$. The boundary terms in equations (C.6) and (C.7) can be omitted on those parts of the boundary where a homogeneous natural boundary condition is applied. The boundary terms on S_1 are also ignored; in equation (C.6) because we have essential conditions for u_i, and in equation (C.7) because W^i are zero. Therefore,

$$- \int_V \nabla u \cdot \nabla \Phi^i \, dV = 0 , \qquad i = 1, 2, \ldots, N_u , \tag{C.8}$$

and

$$- \int_V \nabla u \cdot \nabla W^i \, dV = 0 , \qquad i = 1, 2, \ldots, N_{SBF} . \tag{C.9}$$

Equations (C.8), (C.9) constitute a symmetric linear system of equations whose banded structure has been destroyed due to equation (C.9).

C.1.3 The Integrated Singular Basis Function Method

In the ISBFM we subtract the asymptotic terms directly from the governing equation. The singular functions are now identical to the corresponding asymptotic expansion terms:

$$W^i = r^{\frac{2i-1}{2}} \cos\left[\left(\frac{2i-1}{2}\theta\right)\right] . \tag{C.10}$$

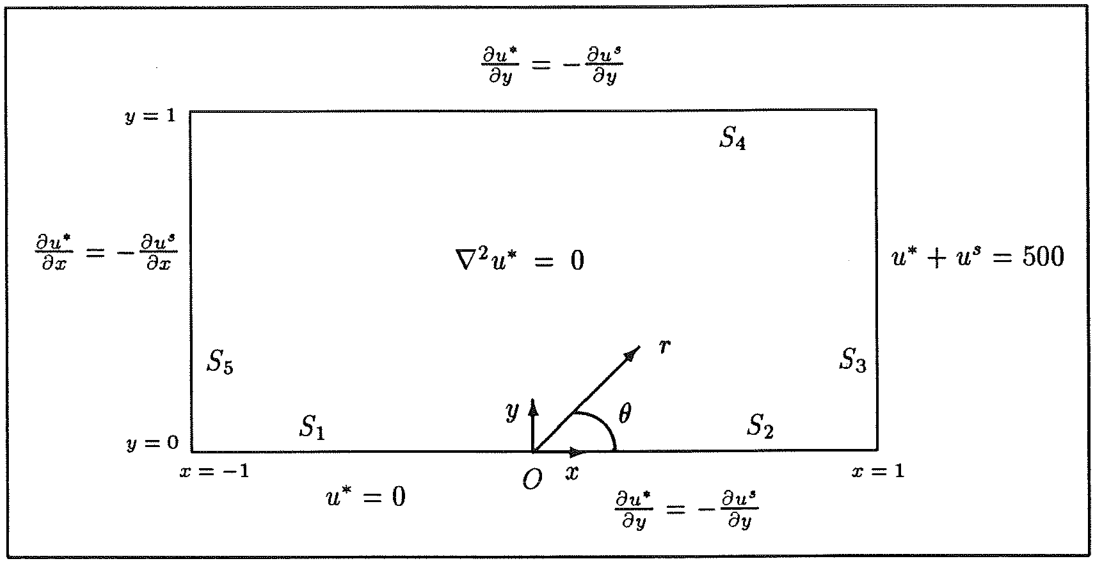

Figure C.1: The modified Motz problem.

Let u^s be the singular part of u,

$$u^s = \sum_{i=1}^{N_{SBF}} \alpha_i W^i , \qquad \text{(C.11)}$$

and u^* be the part of the solution approximated by the standard finite element expansion,

$$u^* = u - u^s . \qquad \text{(C.12)}$$

Notice that u^s satisfies the governing equation and the boundary conditions along $y = 0$, and the original problem is transformed to the one shown in Figure C.1.

Again we use the Galerkin method (and the divergence theorem) to obtain:

$$\int_S \frac{\partial u^*}{\partial n} \Phi^i \, dS - \int_V \nabla u^* \cdot \nabla \Phi^i \, dV = 0 , \qquad i = 1, 2, \ldots, N_u , \qquad \text{(C.13)}$$

and

$$\int_S \frac{\partial u^*}{\partial n} W^i \, dS - \int_V \nabla u^* \cdot \nabla W^i \, dV = 0 , \qquad i = 1, 2, \ldots, N_{SBF} . \qquad \text{(C.14)}$$

To reduce the singular volume integrals of equation (C.14) to boundary integrals, we apply the divergence theorem once more:

$$\int_V \nabla u^* \cdot \nabla W^i \, dV = \int_S u^* \frac{\partial W^i}{\partial n} \, dS - \int_V u^* \nabla^2 W^i \, dV . \qquad \text{(C.15)}$$

But the volume integral in equation (C.15) is zero, since W^i satisfy Laplace's equation. Therefore equation (C.14) becomes:

$$\int_S \left(\frac{\partial u^*}{\partial n} W^i - u^* \frac{\partial W^i}{\partial n} \right) dS = 0 , \qquad i = 1, 2, \ldots, N_{SBF} . \qquad \text{(C.16)}$$

Notice that the boundary terms are not ignored now since $\frac{\partial u^*}{\partial n} = -\frac{\partial u^s}{\partial n}$. Furthermore, to impose the essential condition on S_3 we employ Lagrange multipliers λ_u^i expanded in terms of quadratic basis functions M^i:

$$\lambda_u = \frac{\partial u^*}{\partial x} = \sum_{i=1}^{N_y} \lambda_u^i M^i . \qquad \text{(C.17)}$$

N_y is the number of nodes on S_3. The final equations are:

$$\int_{S_3} \lambda_u M^i dy + \int_{S_4} \frac{\partial u^s}{\partial y} \Phi^i dx + \int_{S_5} \frac{\partial u^s}{\partial x} \Phi^i dy - \int_V \nabla u^* \cdot \nabla \Phi^i dV = 0, \qquad i = 1, 2, \ldots, N_u, \qquad \text{(C.18)}$$

$$\int_{S_3} (\lambda_u W^i - u^* \frac{\partial W^i}{\partial x}) dy + \int_{S_4} (\frac{\partial u^s}{\partial y} W^i + u^* \frac{\partial W^i}{\partial y}) dx + \int_{S_5} (\frac{\partial u^s}{\partial x} W^i + u^* \frac{\partial W^i}{\partial x}) dy = 0 , \qquad i = 1, 2, \ldots, N_{SBF}. \qquad \text{(C.19)}$$

and

$$\int_{S_3} (u^* + u^s) M^i dy = 500 \int_{S_3} M^i dy , \qquad i = 1, 2, \ldots, N_y . \qquad \text{(C.20)}$$

The total number of unknowns is now $N_u + N_{SBF} + N_y$. Notice that the linear system of equations defined by equations (C.17)-(C.19) becomes symmetric after substituting $u^* = 500 - u^s$ to the first integral of equation (C.19).

C.2 Results and Discussion

To make comparisons, we first used a uniform mesh with 16x8 elements (element size = 1/8). Both R and H were taken equal to the meshsize. We first studied the effect of the order of the Gauss-Legendre quadrature with N_{SBF}=1.

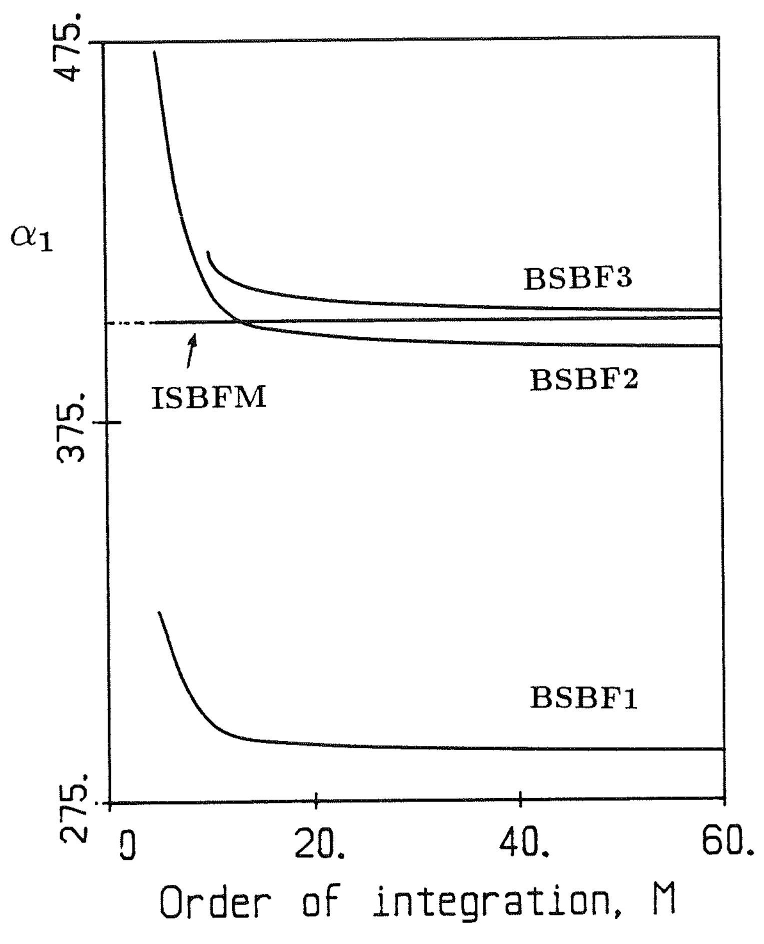

Figure C.2: The coefficient α_1 as a function of the order of integration m (16x8 uniform mesh; R and H equal to meshsize; - - - -: analytical value).

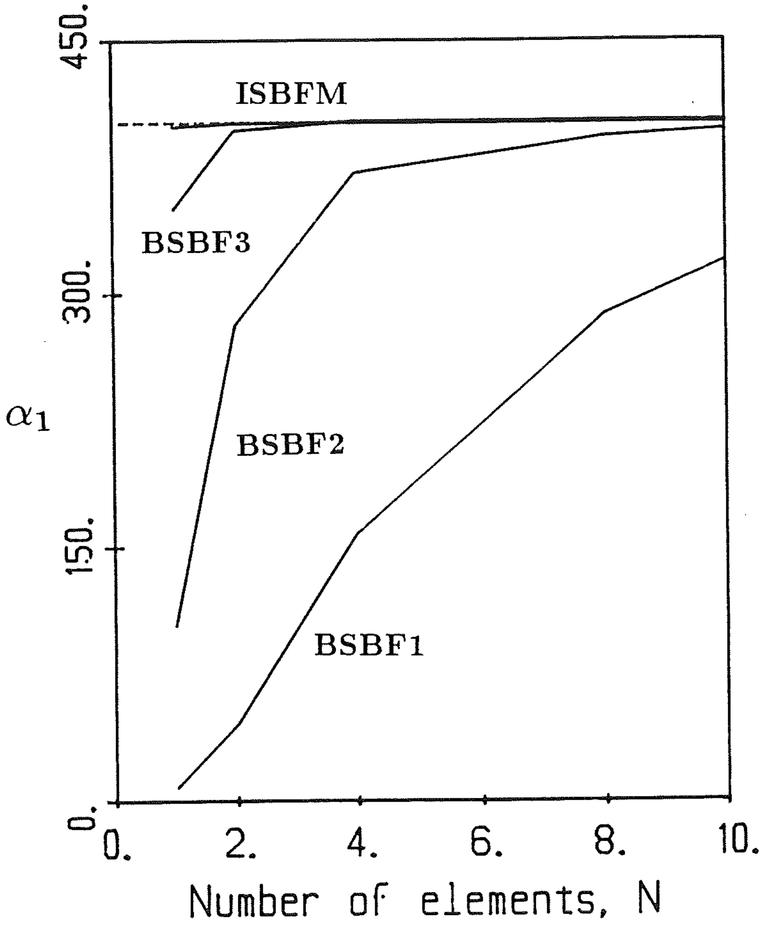

Figure C.3: Effect of mesh refinement on α_1 (N is the number of elements in the y-direction; R or H are equal to the meshsize; - - - -: analytical value).

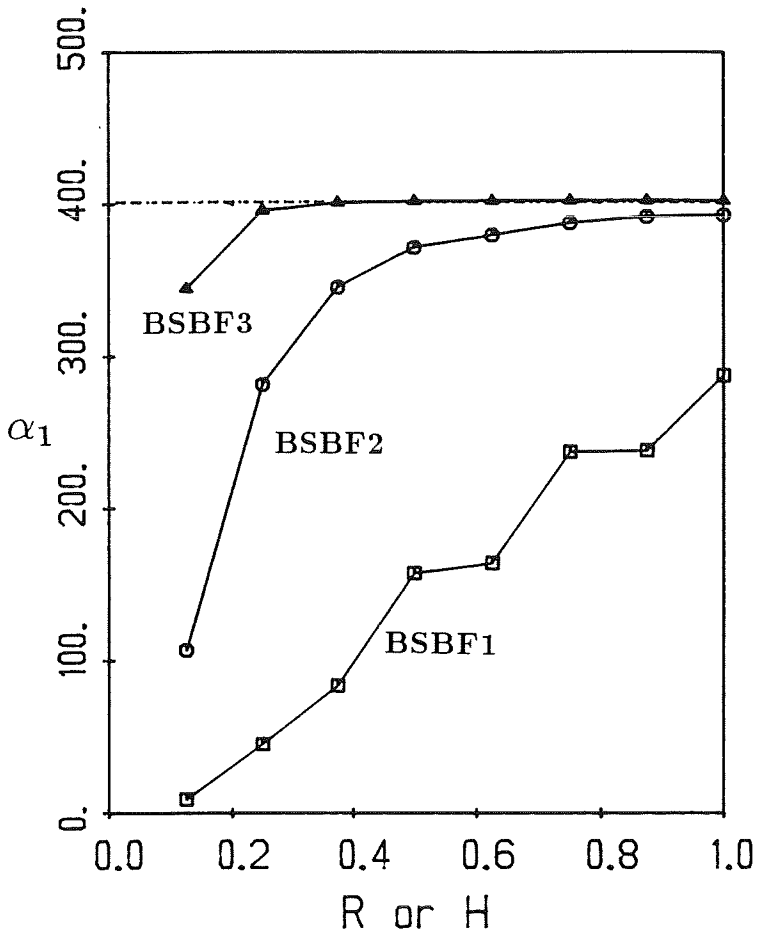

Figure C.4: Effect of R (or H) on the first coefficient α_1 (16x8 uniform mesh).

The computed values of α_1 are plotted in Figure C.2. We observe that the BSBFM requires a high order integration if converged results are to be obtained. BSBF1 and BSBF2 give poor estimates for α_1, whereas BSBF3 appears to converge to the exact value as the order of integration increases. For all the BSBFM results hereafter, a high order integration is employed only for the two elements sharing the singular point; each element is divided into 64 rectangles over which a 15x15 Gauss quadrature is used.

To study the effect of the mesh refinement on the first coefficient, we obtained results with different uniform meshes keeping R (or H) equal to the meshsize. In Figure C.3, the calculated coefficients α_i are plotted versus the number of elements in the y-direction. The results appear to approach the analytical value with mesh refinement in all cases. However, again the ISBFM gives much more accurate values than the BSBFM. Among the singular functions used with the BSBFM, BSBF3 appears to give the best results.

Let us point out that the *singular domain*[1] in the BSBFM included only the two elements sharing the singular point or parts of them. Therefore, only a few nodal values could change, conforming to the addition of the singular function. Apparently, bigger values of R (or H) are required to allow the ordinary finite element expansion coefficients to adjust themselves to the presence of one or more singular terms. To verify the above argument we ran the programs with the 16x8 element mesh and varying R from 1/8 up to 1. The computed coefficients are plotted in Figure C.4. We observe that the results with BSBF2 and BSBF3 converge very close to the exact value. The results with BSBF1 exhibit analogous behavior but higher values of R (in other words, more elements within the singular domain) are required to reach a plateau. It appears that BSBF3 constitutes a much better choice than BSBF2 or BSBF1 and this is due to the fact that the singular domain boundary does not pass through the interior of any elements. In

---

[1] *Singular domain* is the region over which the singular functions are defined. In the ISBFM, the singular domain coincides with the physical domain.

Table C.2: Values of the leading coefficients with BSBF3 (16x8 uniform mesh).

N_{SBF}	α_1	α_2	α_3	α_4	α_5
1	402.21518				
2	402.21517	10.867980			
3	402.21516	15.206817	-3.563013		
4	402.21590	15.206704	-3.562949	-5.609400	
5	402.21758	15.206599	-3.562890	-6.309102	-2.677194
Exact	401.1625	87.65592	17.23792	-8.0712	

Table C.3: Values of the leading coefficients with the ISBFM (16x8 uniform mesh).

N_{SBF}	α_1	α_2	α_3	α_4	α_5
1	401.15943				
2	401.15932	86.663115			
3	401.15932	87.620929	14.601808		
4	401.16197	87.621421	14.599367	-7.474597	
5	401.16224	87.620709	14.602983	-7.469682	1.225553
Exact	401.1625	87.65592	17.23792	-8.0712	

BSBF1 and BSBF2, the ordinary finite element expansion coefficients are not flexible enough to adjust themselves to the subtraction of the singular basis functions, resulting in a lower estimate of the first expansion coefficient. This argument explains the poor results obtained in [158] where R was taken equal to the meshsize.

We concluded that BSBF3 is the best of the blended singular basis functions examined, and that care must be taken so that an adequate number of elements is included in the singular domain. The latter can be achieved either by increasing H or by refining the mesh within the singular domain. Because a fine mesh will be costly we take H equal to to the size of the domain. All the results with the BSBFM hereafter were obtained with BSBF3.

The next step was to calculate more singular coefficients. The coefficients with N_{SBF}=1 up to 5 are listed in Tables C.2 (BSBFM) and C.3 (ISBFM). With the BSBFM the first coefficient remains essentially the same as we increase the number of singular functions. The estimates of the higher coefficients are poor. On the other hand, in the ISBFM the coefficients appear to converge to the analytical values as we increase N_{SBF}.

The disappointing results with the BSBFM for the higher coefficients may be due to contamination from the blending; extra higher order terms not satisfying the asymptotic solution are introduced with every W^i. For example with the BSBF3,

$$W^1 = r^{\frac{1}{2}}\,(1-x^2)\,(1-y^2)\,\cos\frac{\theta}{2} \qquad \Longrightarrow$$

$$W^1 = r^{\frac{1}{2}}\,\cos\frac{\theta}{2} - r^{\frac{5}{2}}\,\cos\frac{\theta}{2} + r^{\frac{7}{2}}\,\cos\frac{\theta}{2}\,\sin^2\theta\,\cos^2\theta\,.$$

Therefore, one can expect a good estimate only for the first expansion coefficient.

APPENDIX D

TWO FINITE ELEMENT METHODS FOR SINGULARITIES IN STOKES FLOW: THE STICK-SLIP PROBLEM

Abrupt changes in boundary conditions give rise to singularities in Stokes flow[1]. We compare two methods for improving the finite element solution in the neighborhood of the singularity – singular finite elements and supplementary singular trial functions. In our primitive variable formulation of the problem, the pressure (a nodal quantity) is singular which guides our approach. Both methods give significantly better results than ordinary uniform finite element meshes. Singular elements improve the solution significantly, with little computational effort. However, as the mesh is refined and the singular element radius decreases the solution develops mild oscillations. Supplementary singular trial functions also improve the solution, which converges smoothly with mesh refinement.

D.1 Introduction

As in fracture mechanics problems, abrupt changes in boundary conditions for Stokes flow give rise to singularities in the solution. One particularly important application with a singularity is in man-made textile manufacturing processes where an extremely viscous fluid is drawn through a die and then cooled to form a solid fiber. An unrestrained fiber

---

[1] The material of this appendix appears in [56].

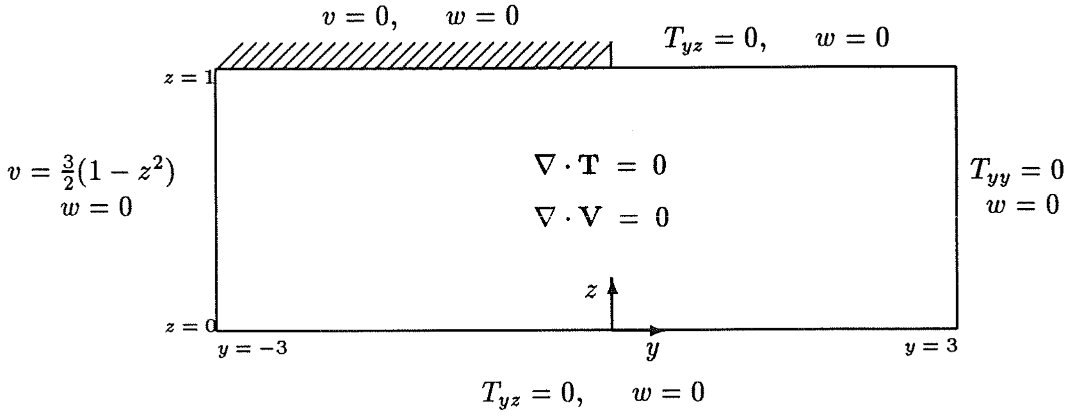

Figure D.1: The stick-slip problem.

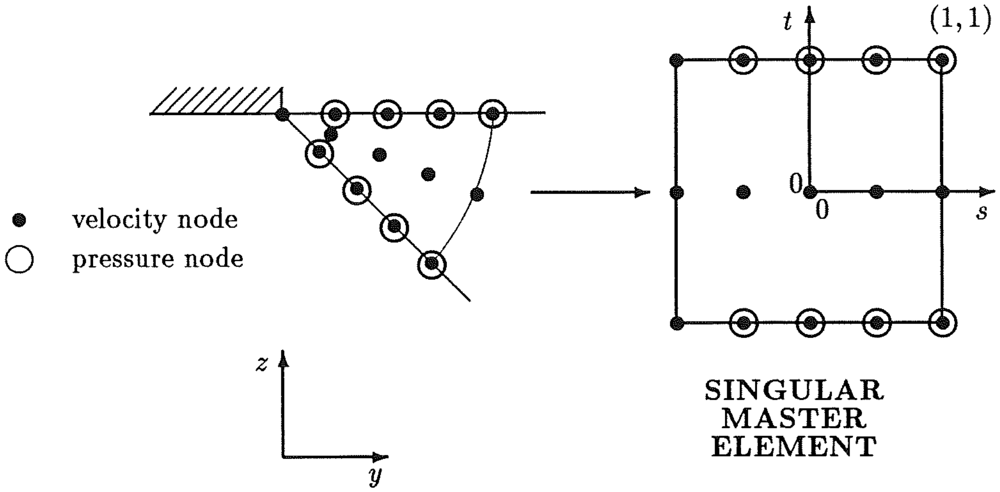

Figure D.2: Mapping of the singular elements.

expands as it exits the die and the problem of determining the amount of expansion is known as the "die-swell problem". In this study, we consider a special case which involves a fluid with infinite surface tension so that the surface does not expand (the *stick-slip problem*, see Figure D.1).

Methods for improving the finite element representation of the singularity generally require a knowledge of the nature of the singularity. Michael [100] and Moffatt [104] showed that the form of the stream function near the singularity in the stick-slip problem is:

$$\psi = r^{\lambda+1}\alpha_\lambda \left[\cos(\lambda+1)\theta - \cos(\lambda-1)\theta\right] \qquad \text{for} \quad \lambda = \frac{1}{2}, \frac{3}{2}, \frac{5}{2}, \ldots$$

$$\psi = r^{\lambda+1}\beta_\lambda \left[(\lambda-1)\sin(\lambda+1)\theta - (\lambda+1)\sin(\lambda-1)\theta\right] \quad \text{for} \quad \lambda = 2, 3, 4, \ldots$$

where α_λ and β_λ are constants determined by the global solution and r and θ are polar coordinates originating at the singular point. The velocities therefore have an $r^{\frac{1}{2}}$ leading term, and the stresses (including pressure) have an $r^{-\frac{1}{2}}$ behavior.

As other researchers have done in solving solid mechanics problems involving singularities, we have used two basic finite element approaches to solve this singular fluid flow problem. In the first approach (similar to the fracture mechanics work of Tracey [149]), we develop special elements for use near the singularity. The interpolation functions for these elements have the form of the singular functions. In the second approach (used by Fix [43] and Morley [106] in solving Laplace's equation) we add an extra set of trial functions. The trial functions are taken to be "blended" singular functions which decay to zero far from the singular point. Because pressure (a singular quantity) is a nodal variable in our primitive variable formulation, implementing these two basic approaches poses new problems.

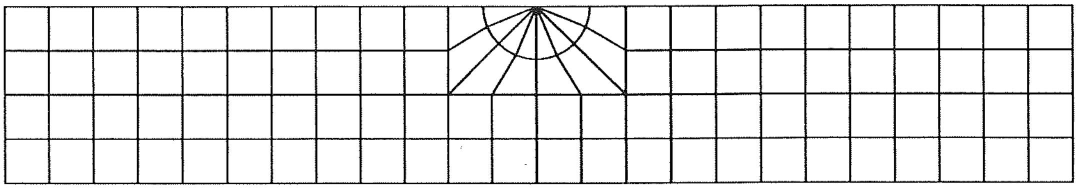

Figure D.3: A typical singular element mesh.

D.2 Finite Element Techniques

We employ standard finite element methods to produce the stress-divergence weak form of the Stokes flow equations in primitive variables [14,11]. For our regular finite elements, we use nine node elements which are biquadratic in velocity and bilinear in pressure. We use three uniform meshes for comparison purposes in our study: 2 × 12 square elements, 4 × 24 square elements, and 8 × 48 square elements.

D.2.1 Singular Element Approach

Figure D.2 shows the master element and its intended wedge-shaped physical geometry. In the t direction we use standard polynomial interpolations – quadratic in velocity and linear in pressure. As a result the element is compatible with ordinary finite elements. In the s direction we use interpolations which mimic the radial form of the singularity:

$$v, w \sim a + b\sqrt{1+s} + c(1+s) + d\sqrt{(1+s)^3} + e(1+s)^2 ,$$

$$p \sim f\frac{1}{\sqrt{1+s}} + g + h\sqrt{1+s} + i(1+s) .$$

Notice that there is no pressure node at the singular point. To integrate the stiffness matrix numerically, we modify the standard Gauss weights and locations to exactly evaluate polynomials in $\sqrt{(1+s)}$ over a wedge with a small subtended angle. Details of the formulation are given in [55].

For this study we replace the eight finite elements nearest to the singular point with eight singular elements and eight regular elements. Figure D.3 shows a typical mesh.

D.2.2 Supplementary Singular Trial Function Approach

Here we use an ordinary finite element mesh, but add an extra set of trial functions to the finite element expansion of the form $(1-y^2)(1-z^2)$ multiplied by the exact singular functions. The blending function $(1-y^2)(1-z^2)$ causes these extra trial functions to vanish far from the singularity. However, we must now evaluate the singular terms using a very high numerical integration order near the singularity. We divided each of the two elements closest to the singularity into 64 subdomains and used 15-point Gauss quadrature in each subdomain. In the remaining elements we used ordinary 4-point quadrature.

D.3 Results and Discussion

Each approach produces good results far from the singularity (e.g., for the centerline pressure).

A more meaningful performance measure is the normal stress at z=1 (the stick and slip surfaces). Figure D.4 shows the normal stress for the ordinary meshes, the ordinary meshes modified to include singular elements, and the ordinary meshes supplemented by singular trial functions. Both singular techniques generate significantly smoother results than the ordinary mesh. The singular element method appears to give slightly more accurate results for the coarsest mesh. However, the singular trial function approach in general gives superior results which become smoother as the regular mesh is refined while the singular element results exhibit some small-amplitude oscillations. (This appears to be due to the fact that the singular elements become smaller as the regular mesh becomes finer [55].)

Often, we wish to know the coefficients α_λ for the singular functions (analogous to the stress intensity factor in fracture mechanics). Richardson [121] analytically derived the first coefficient for the stick-slip problem which should be (as noted by Ingham and

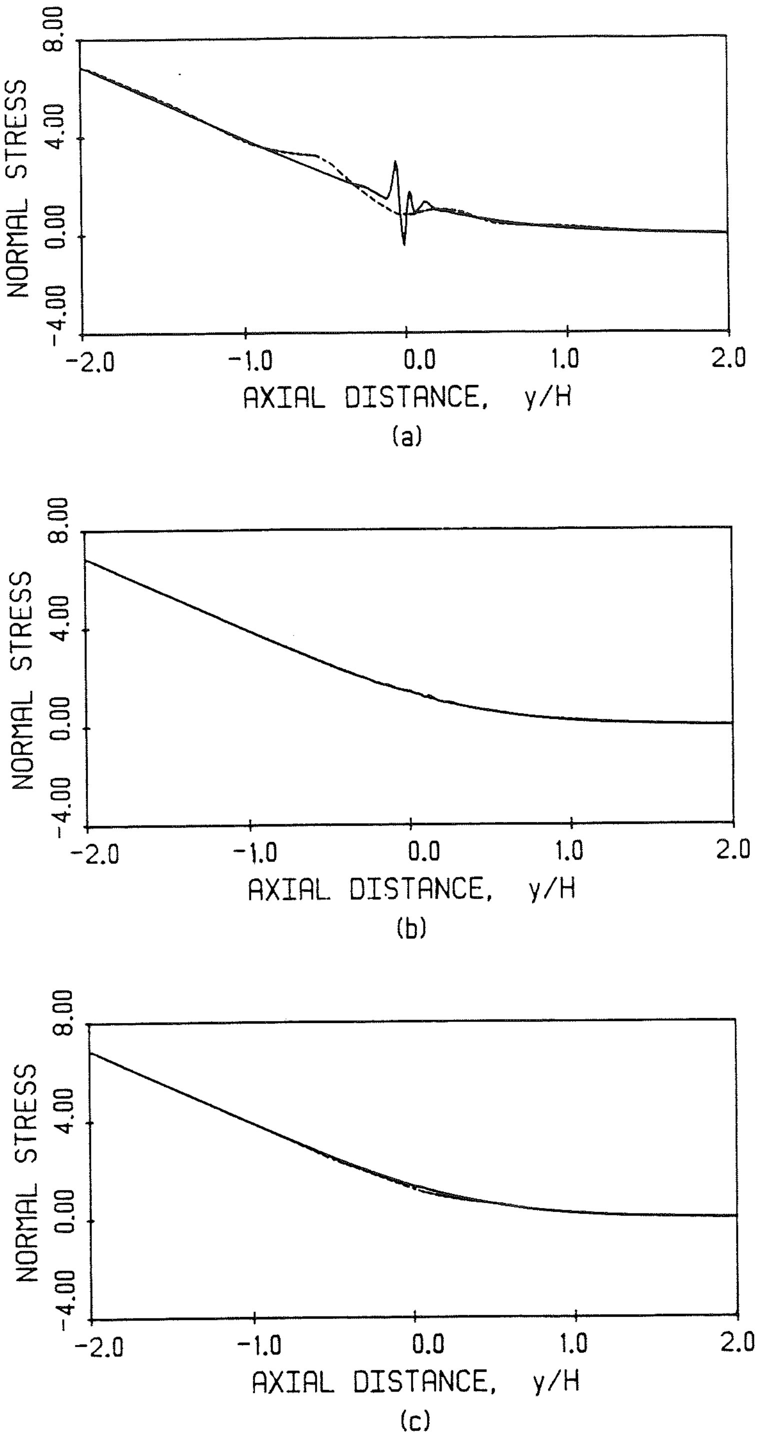

Figure D.4: Normal stresses along $z = 1$ with (a) ordinary elements, (b) singular elements and (c) singular functions (- - - -: mesh I, 12x2 elements, ——-: mesh III, 48x8 elements).

Table D.1: Singular coefficient estimates from finest ordinary and singular element meshes.

Method	$\alpha_{1/2}$	$\alpha_{3/2}$
Ordinary Finite Elements	0.67170	0.19812
Singular Finite Elements	0.69173	0.27168
Ingham & Kelmanson	0.69108	0.26435
Analytical Solution	0.69099	—

Table D.2: Singular coefficients from singular trial function approach.

N_{SBF}	Mesh I		Mesh II		Mesh III	
	$\alpha_{1/2}$	$\alpha_{3/2}$	$\alpha_{1/2}$	$\alpha_{3/2}$	$\alpha_{1/2}$	$\alpha_{3/2}$
1	0.673988	-	0.686836	-	0.690038	-
2	0.674944	0.021165	0.687367	0.036553	0.690429	0.062385
3	0.676769	0.023857	0.687695	0.038791	0.690507	0.064387
4	0.677274	0.030522	0.687862	0.047595	0.690595	0.076963

Kelmanson [82]) $\sqrt{3/2\pi} = 0.69099$. Ingham and Kelmanson found the first several coefficients by a boundary integral technique. For the refined regular and singular element meshes we can estimate the coefficients by using a least squares fit on the nodal velocities. Table D.1 compares the values obtained from the eight slip-surface nodal velocities closest to the singularity.

For the singular trial function approach we directly identify the singular coefficients as solution variables. Table D.2 shows the various values. The singular trial function approach converges smoothly as the underlying mesh is refined. The first singular coefficient is quite accurate even for coarse meshes, while the higher coefficients are unacceptable. However, adding additional singular trial functions does not significantly improve the results. (Whiteman [163] and Wait and Mitchel [158] also noted that additional trial functions produced little improvement.)

D.4 Conclusions

Both the singular element and singular trial function approaches significantly improved the ability to model the stick-slip problem accurately with coarse finite element meshes. The singular element approach gave slightly better results than the singular trial function method for coarse meshes, but produced some small amplitude spurious oscillations for fine meshes with small singular elements. The singular trial function method converged smoothly as the underlying mesh was refined. Adding more than one singular trial function did not improve the solution significantly.

BIBLIOGRAPHY

BIBLIOGRAPHY

[1] Adachi, A. and N. Yoshioka (1984), "Tube exit flows and laminar Newtonian jets in the atmosphere," *Advances in rheology*, B. Mena, A. Garcia-Rejon and C. Rangel-Najaile (eds.), Universidad Nacional Autonoma de Mexico, Vol. 2, 329.

[2] André, P. and J-R Clermont (1987), "Numerical simulation of the die swell problem of a Newtonian fluid by using the concept of stream function and a local analysis of the singularity at the corner," *J. Non-Newt. Fluid Mech.* **23**, 335.

[3] Akin, J. E. (1976), "The generation of elements with singularities," *Int. j. numer. methods eng.* **10**, 1249.

[4] Apelian, M. R., R. C. Armstrong and R. A. Brown (1988), "Impact of the constitutive equation and singularity on the calculation of stick-slip flow: the modified upper-convected Maxwell model (MUCM)," *J. Non-Newt. Fluid Mech.* **27**, 299.

[5] Askar, H. G. (1987), "Special elements for point singularities," *Comp. Meth. Appl. Mech. Eng.* **63**, 271.

[6] Atluri, S. N. (1988) "Remarks on mixed and singular finite elements and on the field boundary element method," Chapter 9 in *Finite elements. Theory and application*, D. L. Dwoyer, M. Y. Hussaini and R. G. Voigt (eds.), Springer-Verlag, New York.

[7] Atluri, S. N. (1980) "Higher-order, special, and singular-finite elements," Chapter 4 in *Survey of finite element methods*, A. K. Noor and W. Pilkey (eds.), ASME.

[8] Babuška, I. (1970), "The finite element method for elliptic equations with discontinuous coefficients," *Computing* **5**, 207.

[9] Babuška, I. (1971), "The rate of convergence for the finite element method," *SIAM J. Numer. Anal.* **8**, 304.

[10] Babuška, I. (1973), "The finite element method with Lagrangian multipliers," *Numer. Math.* **20**, 179.

[11] Baker, A. J. (1983), *Finite element computational fluid mechanics*, McGraw-Hill, New York.

[12] Barsoum, R. S. (1977), "Triangular quarter-point elements as elastic and perfectly-plastic crack-tip elements," *Int. j. numer. methods eng.* **11**, 85.

[13] Batchelor, J., J. P. Berry and F. Horsfall (1973), "Die swell in elastic and viscous fluids," *Polymer* **14**, 297.

[14] Bathe, K. J. (1982), *Finite element procedures in engineering analysis*, Prentice-Hall, Englewood Cliffs, New Jersey.

[15] Bertsekas, D. P. (1982), *Constrained optimization and Lagrange multiplier methods*, Academic Press, New York.

[16] Bird, R. B., W. E. Stewart and E. N. Lightfoot (1967), *Transport phenomena*, Wiley, New York.

[17] Bixler, N. E. (1982), *Stability of coating flows*, Ph.D. Thesis, University of Minnesota.

[18] Boudouvis, A. G. and L. E. Scriven (1984), "Explicitly vectorized frontal routine for hydrodynamic stability and bifurcation analysis by Galerkin/finite element methods," *Proc. Supercomp. Appl. Symp.*, Oct. 31-Nov. 1.

[19] Brebbia, C. A. (ed.) (1981), *Boundary element methods*, C.M.L. Publications, Springer-Verlag.

[20] Brodkey, R. S. (1967), *The phenomena of fluid motions*, Addison-Wesley Series in Chemical Engineering.

[21] Brown, R. A., L. E. Scriven and W. J. Silliman (1980), "Computer-aided analysis of nonlinear problems in transport phenomena," in *New approaches to nonlinear problems in dynamics*, P. J. Holmes (ed.), Soc. Ind. Appl. Math., Philadelphia, 289.

[22] Brown, R. A., R. C. Armstrong, A. N. Beris and P.-W. Yeh (1986), "Galerkin finite element analysis of complex viscoelastic flows," *Comp. Meth. Appl. Mech. Eng.* **58**, 201.

[23] Canuto, C., M. Y. Hussaini, A. Quarteroni and T. A. Zang (1986), *Spectral Methods in Fluid Dynamics*, Springer-Verlag, New York.

[24] Carnahan, B., H. A. Luther and J. O. Wilkes (1969), *Applied numerical methods*, John Wiley & Sons, Inc., New York.

[25] Carey, G. F. and J. T. Oden (1983), *Finite elements. A second course*, Vol. II, Prentice-Hall, Inc., Englewood Cliffs, New Jersey.

[26] Chandrasekhar, S. (1961), *Hydrodynamic and hydromagnetic stability*, Oxford Glarendon Press.

[27] Courant, R. and D. Hilbert (1989), *Methods of mathematical physics*, Vol. I, John Wiley & Sons, New York.

[28] Coyle, D. (1984), *The fluid mechanics of roll coating. Steady flows, stability and rheology*, Ph.D. Thesis, University of Minnesota.

[29] Crochet, M. J. (1987), "Numerical simulation of flow processes," *Chem. Eng. Sci.* **42**, 979.

[30] Dandapat, B. S. and A. S. Gupta (1978), "Notes on the flow near a wall and dividing streamline intersection," *AIAA J.* **16**, 849.

[31] Davies, A. R. (1988), "Re-entrant corner singularities in non-Newtonian flow. Part I: Theory," *J. Non-Newt. Fluid Mech.* **29**, 269.

[32] Dean, W. R. and P. E. Montagnon (1949), *Proc. Camb. Phil. Soc.* **45**, 389.

[33] Delves, L. M. and C. A. Hall (1979), "An implicit matching principle for global element calculations," *J. Inst. Math. Appl.* **23**, 223.

[34] Delves, L. M. and C. Phillips (1980), "A fast implementation of the global element method," *J. Inst. Math. Appl.* **26**, 177.

[35] Drazin, P. G. and W. H. Reid (1981), *Hydrodynamic stability*, Cambridge University Press.

[36] Dupuie, J. L. (1990), Ph.D. Thesis, University of Michigan, in preparation.

[37] Dussan, E. B. V. and S. H. Davis (1974), "On the motion of a fluid-fluid interface along a solid surface," *J. Fluid Mech.* **65**, 71.

[38] Dussan, E. B. V. (1976), "The moving contact line: the slip boundary condition," *J. Fluid Mech.* **77**, 665.

[39] Dutta, A. and M. E. Ryan (1982), "Dynamics of a creeping Newtonian jet with gravity and surface tension: a finite difference technique for solving steady free-surface flows using orthogonal curvilinear coordinates," *AIChE J.* **28**, 220.

[40] Dutta, A. (1983), "An alternative analysis of the plane stick-slip problem," *J. Appl. Mech.* **50**, 863.

[41] Ellwood, K., G. C. Georgiou, T. C. Papanastasiou and J. O. Wilkes (1989), "Laminar Jets of Bingham Plastic Liquids," *J. Fluid Mech.*, submitted (1989).

[42] Fix, G. J. (1988) "Singular finite element methods," Chapter 3 in *Finite elements. Theory and application*, D. L. Dwoyer, M. Y. Hussaini and R. G. Voigt (eds.), Springer-Verlag, New York.

[43] Fix, G. (1969), "Higher-order Rayleigh-Ritz approximations," *J. Math. Mech.* **18**, No. 7, 645.

[44] Fix, G. J., S. Gulati and G. I. Wakoff (1973), "On the use of singular functions with finite element approximations," *J. Comp. Phys.* **13**, 209.

[45] Fletcher, D. F., S. J. Maskell and M. A. Patrick (1985), "Heat and mass transfer computations for laminar flow in an axisymmetric sudden expansion," *Computers & Fluids* **13**, 207.

[46] Fotiadis, D. I., A. M. Kremer, D. R. McKenna and K. F. Jensen (1987), "Complex flow phenomena in vertical MOCVD reactors: Effects on deposition uniformity and interface abruptness," *J. Crystal Growth* **85**, 154.

[47] Fotiadis, D. I., E. O. Einset, H. K. Moffat and K. F. Jensen (1989), "Finite element analysis of chemical vapor deposition reactor flows," in *Finite Element Analysis in Fluids*, T. J. Chung and G. R. Karr (eds.), UAH Press, 428.

[48] Gallagher, H. (1982), "Finite element analysis for crack tip problems," in *Proceedings of Symposium on Finite Element Method*, Science Press, Beijing, China, 102.

[49] Gear, R. L., M. Keentok, J. F. Milthorpe and R. I. Tanner (1983), "The shape of low Reynolds number jets," *Phys. Fluids* **26**, 7.

[50] Gelfand, I. M. and S. V. Fomin (1963), *Calculus of variations*, Prentice-Hall, Englewood Cliffs, New Jersey.

[51] Georgiou, G. C., T. C. Papanastasiou and J. O. Wilkes (1988), "Laminar Newtonian jets at high Reynolds and high surface tension," *AIChE J.* **34**, 1559.

[52] Georgiou, G. C., T. C. Papanastasiou and J. O. Wilkes (1987), "Laminar jets at high Reynolds numbers," Annual Meeting of AIChE, New York, Nov. 1987.

[53] Georgiou, G. C., T. C. Papanastasiou and J. O. Wilkes (1988), "Coating via atomization: stability of Newtonian and Bingham liquid jets," Annual Spring National Meeting of AIChE, New Orleans, March 1988.

[54] Georgiou, G. C., W. W. Schultz and L. Olson (1988), "Singular finite elements for fluid flow problems," *APS Division of Fluid Mechanics 41st Annual Meeting*, Buffalo, New York.

[55] Georgiou, G. C., L. G. Olson, W. W. Schultz and S. Sagan (1989), "A singular finite element for Stokes flow: the stick-slip problem," *Int. j. numer. methods fluids*, in press.

[56] Georgiou, G. C., L. G. Olson and W. W. Schultz (1989), "Two finite element methods for singularities in Stokes flow: The stick-slip problem," in *Finite Element Analysis in Fluids*, T. J. Chung and G. R. Karr (eds.), UAH Press, 992.

[57] Georgiou, G. C., L. G. Olson and W. W. Schultz (1989), "Singular finite elements for the sudden-expansion and the die-swell problems," *Int. j. numer. methods fluids*, accepted (1989).

[58] Goren, S. L. and S. Wronski (1966), "The shape of low-speed capillary jets of Newtonian liquids," *J. Fluid Mech.* **25**, 185.

[59] Gresho, P. M. and R. L. Lee (1981), "Don't suppress the wiggles — They're telling you something," *Computers & Fluids* **9**, 223.

[60] Gresho, P. M. (1989), *Personal Communication.*

[61] Grisvald, P. (1985), *Elliptic problems in nonsmooth domains*, Pitman, London.

[62] Grisvald, P., W. Wendland and J. R. Whiteman (1985), *Singularities and constructive methods for their treatment*, Springer-Verlag, Berlin.

[63] Gupta, M. M., R. P. Manohar and B. Noble (1981), "Nature of viscous flows near sharp corners," *Computers & Fluids* **9**, 379.

[64] Hancock, C. (1984), "The angle of separation in Stokes flow near a sharp corner," *Quart. J. Mech. Appl. Math.* **37**, 1.

[65] Harmon, D. B. (1955), "Drop sizes from low speed jets," *J. Franklin Inst.* **259**, 519.

[66] Hassager, O. (1988), "Singular behavior of power-law fluids in Hele Shaw flow," *J. Non-Newt. Fluid Mech.* **29**, 337.

[67] Hassager, O. (1988), *Personal Communication.*

[68] Hendry, J. A. and L. M. Delves (1979), "The global element method applied to a singular harmonic boundary value problem," *J. Comp. Phys.* **33**, 33.

[69] Henriksen, P. and O. Hassager (1988), "Corner flow of power law fluids," *10th International Congress on Rheology*, Sydney.

[70] Henshell, R. D. and K. G. Shaw (1975), "Crack tip elements are unnecessary," *Int. j. numer. methods eng.* **9**, 495.

[71] Hess, D. W., K. F. Jensen and T. J. Anderson (1985), "Chemical vapor deposition: A chemical engineering perspective," *Rev. Chem. Eng.* **3**, 97.

[72] Hocking, L. M. (1975), "A moving fluid interface on a rough surface," *J. Fluid Mech.* **76**, 801.

[73] Hocking, L. M. (1977), "A moving fluid interface. Part 2. The removal of the force singularity by a slip flow," *J. Fluid Mech.* **79**, 209.

[74] Holstein, H. and D. J. Paddon (1981), "A singular finite difference treatment of re-entrant corner flow," *J. Non-Newt. Fluid Mech.* **8**, 81.

[75] Hood, P. (1976), "Frontal solution program for unsymmetric matrices," *Int. j. numer. methods eng.* **10**, 379.

[76] Houtman, C., D. B. Graves and K. F. Jensen (1986), "CVD in stagnation point flow," *J. Electrochem. Soc.* **85**, 961.

[77] Huebner, K. H. and E. A. Thornton (1982), *The finite element method for engineers*, John Wiley & Sons.

[78] Hughes, T. J. R. and J. E. Akin (1980), "Techniques for developing 'special' finite element shape functions with particular reference to singularities," *Int. j. numer. methods eng.* **15**, 733.

[79] Huh, C. and L. E. Scriven (1971), "Hydrodynamic model of steady movement of a solid/liquid/fluid contact line," *J. Colloid Interface Sci.* **35**, 85.

[80] Huh, C. and S. G. Mason (1977), "The steady movement of a liquid meniscus in a capillary tube," *J. Fluid Mech.* **81**, 401.

[81] Huilgol, R. R. and R. I. Tanner, "The separation of a second-order fluid at a straight edge," *J. Non-Newt. Fluid Mech.* **2**, 89.

[82] Ingham, D. B. and M. A. Kelmanson (1984), *Boundary integral equation analyses of singular, potential and biharmonic problems*, Springer-Verlag, Berlin, 21.

[83] Irons, B. M. (1970), "A frontal solution program for finite element analysis," *Int. j. numer. methods eng.* **2**, 5.

[84] Jeffrey, D. J. and J. D. Sherwood (1980), "Streamline patterns and eddies in low-Reynolds-number flow," *J. Fluid Mech.* **96**, 315.

[85] Jensen, K. F. (1989), "Chemical Vapor Deposition," to appear in Advances in Chemistry Series No. 221, *Chemical Engineering Materials Processing*, D. W. Hess and K. F. Jensen (eds.).

[86] Kermode, M., A. McKerrell and L. M. Delves (1985), "The calculation of singular coefficients," *Comp. Meth. Appl. Mech. Eng.* **50**, 205.

[87] Keunings, R. (1986), "On the high Weissenberg number problem," *J. Non-Newt. Fluid Mech.* **20**, 209.

[88] Kikuchi, N. (1986), *Finite element methods in mechanics*, Cambridge University Press, Cambridge.

[89] Kistler, S. F. and L. E. Scriven (1984), "Coating flow theory by finite element and asymptotic analysis of the Navier-Stokes system," *Int. j. numer. methods fluids* **4**, 207.

[90] Lau, H. C. and W. R. Schowalter (1986), "A model for adhesive failure of viscoelastic fluids during flow," *J. Rheol.* **30**, 193.

[91] Lee, N. Y., W. W. Schultz and J. P. Boyd (1987), "Spectral solutions for flows with corner singularities," *APS Division of Fluid Mechanics 40th Annual Meeting*, Eugene, Oregon.

[92] Lee, N. Y., W. W. Schultz and J. P. Boyd (1989), "Stability of fluid in a rectangular enclosure by spectral method," *Int. J. Heat Mass Transfer* **32**, 513.

[93] Lefeber, D. (ed.) (1988), *Solving problems with singularities using boundary elements*, Computational Mechanics Publications, Southampton and Boston.

[94] Lehman, R. S. (1959), "Developments at an analytic corner of solutions of elliptic partial differential equations," *J. Math. Mech.* **8**, 727.

[95] Lipscomb, G. G., R. Keunings and M. M. Denn (1987), "Implications of boundary singularities in complex geometries," *J. Non-Newt. Fluid Mech.* **24**, 85.

[96] Lugt, H. J. and E. W. Schwiderski (1965), "Flows around dihedral angles, I. Eigenmotion analysis," *Proc. Roy. Soc. Lond.* **A285**, 382.

[97] Marchal, J. M. and M. J. Crochet (1987), "A new mixed finite element for calculating viscoelastic flow," *J. Non-Newt. Fluid Mech.* **26**, 77.

[98] McKerrell, A. (1988), "The global element method applied to fluid flow problems," *Computers & Fluids* **16**, 41.

[99] McKerrell, A., C. Phillips and L. M. Delves (1981), "Chebyshev expansion methods for the solution of elliptic partial differential equations," *J. Comp. Phys.* **40**, 444.

[100] Michael, D. H. (1958), "The separation of a viscous liquid at a straight edge," *Mathematica* **5**, 82.

[101] Michael, D. H. and M. E. O'Neill (1977), "The separation of Stokes flows," *J. Fluid Mech.* **80**, 785.

[102] Middleman, S. and J. Gavis (1961), "Expansion and contraction of capillary jets of viscoelastic liquids," *Phys. Fluids* **4**, 355.

[103] Miller, A. D. and R. L. Dewar (1986), "Galerkin method for differential equations with regular singular points," *J. Comp. Phys.* **66**, 356.

[104] Moffatt, H. K. (1964), "Viscous and resistive eddies near a sharp corner," *J. Fluid Mech.* **18**, 1.

[105] Moffatt, H. K. and B. R. Duffy (1980), "Local similarity solutions and their limitations," *J. Fluid Mech.* **96**, 299.

[106] Morley L. S. D. (1973), "Finite element solution of boundary-value problems with non-removable singularities," *Phil. Trans. Roy. Soc. Lond.* **A275**, 463.

[107] Motz, H. (1946), "The treatment of singularities in relaxation methods," *Quart. Appl. Math.* **4**, 371.

[108] Nickell, R. E., R. I. Tanner and B. Caswell (1974), "The solution of viscous incompressible jet and free-surface flows using finite element methods," *J. Fluid Mech.* **65**, 189.

[109] Oden, J. T. and G. F. Carey (1983), *Finite elements. Mathematical aspects*, Vol. IV, Prentice-Hall, Inc., Englewood Cliffs, New Jersey.

[110] Okabe, M. (1981), "Fundamental theory of the semi-radial singularity mapping with applications to fracture mechanics," *Comp. Meth. Appl. Mech. Eng.* **26**, 53.

[111] Okabe, M. and N. Kikuchi (1981), "Some general Lagrange interpolations over simplex finite elements with reference to derivative singularities," *Comp. Meth. Appl. Mech. Eng.* **28**, 1.

[112] Olson, L. G., G. C. Georgiou and W. W. Schultz (1989), "An efficient finite element method for subtracting off singularities at corners for Laplace's equation – The Motz problem," *J. Comp. Phys.*, submitted.

[113] Omodei, B. J. (1979), "Computer solutions of a plane Newtonian jet with surface tension," *Computers & Fluids* **7**, 79.

[114] Omodei, B. J. (1980), "On the die-swell of an axisymmetric Newtonian jet," *Computers & Fluids* **8**, 275.

[115] Orr, F. M. and L. E. Scriven (1978), "Rimming flow: numerical simulation of steady, viscous, free-surface flow with surface tension," *J. Fluid Mech.* **84**, 145.

[116] Perry, R. H., D. W. Green and J. O. Maloney (1984), *Perry's Chemical Engineers' Handbook*, McGraw-Hill, New York.

[117] Pina, H. L. G., J. L. M. Fernandes and C. A. Brebbia (1981), "The effect of mesh refinement in the boundary element solution of Laplace's equation with singularities," in *Boundary Element Methods*, C.A. Brebbia (ed.), Springer-Verlag.

[118] Ramamurthy, A. V. (1986), "Wall slip in viscous fluids and influence of materials of construction," *J. Rheol.* **30**, 337.

[119] Reddy, K. R. and R. I. Tanner (1978), "Finite element solution of viscous jet flows with surface tension," *Computers & Fluids* **6**, 83.

[120] Reid, R. C., J. M. Prausnitz and T. K. Sherwood (1977), *The Properties of Gases and Liquids*, McGraw-Hill, New York.

[121] Richardson, S. (1970), "A 'stick-slip' problem related to the motion of a free jet at low Reynolds numbers," *Proc. Cambridge Phil. Soc.* **67**, 477.

[122] Richardson, S. (1970), "The die-swell phenomenon," *Rheol. Acta* **9**, 193.

[123] Richardson, S. (1973), "On the no-slip boundary condition," *J. Fluid Mech.* **59**, 707.

[124] Roenigk, K. F. and K. F. Jensen (1985), "Analysis of multicomponent LPCVD processes," *J. Electrochem. Soc.* **134**, 448.

[125] Rosenberg, J. R. and R. Keunings (1988), "Further results on the flow of a Maxwell fluid through an abrupt contraction," *J. Non-Newt. Fluid Mech.* **29**, 295.

[126] Rosser, J. B. and N. Papamichael (1975), "A power series solution of a harmonic mixed boundary value problem," *MRC Technical Summary, Rept. 1405*, University of Wisconsin.

[127] Ruschak, K. J. (1980), "A method for incorporating free boundaries with surface tension in finite element fluid-flow simulators," *Int. j. numer. methods eng.* **15**, 639.

[128] Saito, H. and L. E. Scriven (1981), "Study of coating flow by finite element method," *J. Comp. Phys.* **42**, 53.

[129] Schiff, B. (1988), "Finite element eigenvalues for the Laplacian over an L-shaped domain," *J. Comp. Phys.* **76**, 233.

[130] Schubert, G. (1967), "Viscous flow near a cusped corner," *J. Fluid Mech.* **27**, 647.

[131] Schultz, W. W. and C. Gervasio (1989), "A study of the singularity in the die swell problem," *Quart. J. Appl. Math. Mech.*, in press.

[132] Schultz, W. W., N. Y. Lee and J. P. Boyd (1989), "Chebyshev pseudospectral method of viscous flows with corner singularities," *J. Sci. Comp.*, in press.

[133] Scott, P. S., F. A. Mirza and J. Vlachopoulos (1986), "A finite element analysis of laminar flows through planar and axisymmetric abrupt expansions," *Computers & Fluids* **14**, 423.

[134] Sih, G. C. (ed.) (1973), *Methods of fracture I. Methods of analysis and solutions of crack problems*, Noordhoff International Publishing, Leyden.

[135] Silliman, W. J. and L. E. Scriven (1980), "Separating flow near a static contact line: Slip at a wall and shape of a free surface," *J. Comp. Phys.* **34**, 287.

[136] Silliman, W. J. (1979), *Viscous film flows with contact lines: Finite element simulation, a basis for stability and design optimization*, Ph.D. Thesis, University of Minnesota.

[137] Silliman, W. J. and L. E. Scriven (1978), "Slip of liquid inside a channel exit," *Phys. Fluids* **21**, 2115.

[138] Slobodeckiĭ, N. (1966), "Generalized Sobolev spaces and their application to boundary problems for partial differential equations," *Amer. Math. Soc. Transl.* **57**, 207.

[139] Solecki, J. S. and J. L. Swedlow (1984), "On quadrature and singular finite elements," *Int. j. numer. methods eng.* **20**, 395.

[140] Stern, M. (1979), "Families of consistent conforming elements with singular derivative fields," *Int. j. numer. methods eng.* **14**, 409.

[141] Strang, G. and G. J. Fix (1973), *An analysis of the finite element method*, Prentice-Hall, Englewood Cliffs, New Jersey.

[142] Sturges, L. D. (1977), *Ph.D. Thesis*, University of Minnesota.

[143] Sturges, L. D. (1979), "Die swell: The separation of the free surface," *J. Non-Newt. Fluid Mech.* **6**, 155.

[144] Tanner, R. I. (1985), *Engineering rheology*, Oxford University Press.

[145] Thatcher, R. W. (1975), "Singularities in the solution of Laplace's equation in two dimensions," *J. Inst. Math. Appl.* **16**, 303.

[146] Thomas, P. D. and R. A. Brown (1987), "LU decomposition of matrices with augmented dense constraints," *Int. j. numer. methods eng.* **24**, 1451.

[147] Tillet, J. P. K. (1968), "On the laminar flow of a free jet of liquid at high Reynolds numbers," *J. Fluid Mech.* **32**, 273.

[148] Ting, K. and W.-H. Chen (1988), "Hybrid finite-element analysis of Laplace's equation with singularities," *AIAA J.* **26**, 119.

[149] Tracey, D. M. (1971), "Finite elements for determination of crack tip elastic stress intensity factors," *Eng. Fracture Mech.* **3**, 255.

[150] Tracey, D. M. and T. S. Cook (1977), "Analysis of power type singularities using finite elements," *Int. j. numer. methods eng.* **11**, 1225.

[151] Trang, C. T. and Y. L. Yeow (1986), "Extrudate-swell of Newtonian and non-Newtonian fluids — The effect of gravitational body force," *J. Non-Newt. Fluid Mech.* **20**, 103.

[152] Trogdon, S. A. and D. D. Joseph (1980), "The stick-slip problem for a round jet I. Large surface tension," *Rheol. Acta* **19**, 404.

[153] Tsamasphyros, G. (1987), "Singular element construction using a mapping technique," *Int. j. numer. methods eng.* **24**, 1305.

[154] Voigt, R. G., D. Gottlieb and M. Y. Hussaini (1982), *Spectral methods for partial differential equations*, SIAM.

[155] Vossen, J. L. and W. Kern (1978), *Thin Film Processes*, Academic Press.

[156] Wahl, G. (1977), "Hydrodynamic description of CVD processes," *Thin Solid Films* **40**, 13.

[157] Wait, R. (1977), "Singular isoparametric finite elements," *J. Inst. Math. Appl.* **20**, 133.

[158] Wait, R. and A. R. Mitchell (1971), "Corner singularities in elliptic problems by finite element methods," *J. Comp. Phys.* **8**, 45.

[159] Wait, R. (1978), "Finite element methods for elliptic problems with singularities," *Comp. Meth. Appl. Mech. Eng.* **13**, 141.

[160] Walters, R. A. (1980), "The frontal method in hydrodynamics simulations," *Computers & Fluids* **8**, 265.

[161] Wasow, W. (1957), "Asymptotic development of the solution of Dirichlet's problem at analytic corners," *Duke Math. J.* **24**, 47.

[162] White, S. A., A. D. Gotsis and D. G. Baird (1987), "Review of the entry flow problem: experimental and numerical," *J. Non-Newt. Fluid Mech.* **24**, 121.

[163] Whiteman, J. R. (1985), "Numerical solution of steady state diffusion problems containing singularities," Chapter 6 in *Finite Elements in Fluids*, Vol. 2, R. H. Gallagher, J. T. Oden, C. Taylor and O. C. Zienkiewicz (eds.), John Wiley & Sons.

[164] Whiteman, J. R. (1971), "Finite-difference techniques for a harmonic mixed-boundary problem having a reentrant boundary," *Proc. Roy. Soc. Lond.* **A323**, 271.

[165] Wigley, N. M. (1988), "An efficient method for subtracting off singularities at corners for Laplace's equation," *J. Comp. Phys.* **78**, 369.

[166] Wigley, N. M. (1969), "On a method to subtract off a singularity at a corner for the Dirichlet or Neumann problem," *Math. Comp.* **23**, 395.

[167] Woods, L. C. (1953), "Points in Poisson's equation," *Quart. J. Mech. Appl. Math.* **6**, 163.

[168] Yih, C.-S. (1979), *Fluid Mechanics*, West River Press, Ann Arbor, Michigan.

[169] Ying, L.-A. (1982), "Some 'special' interpolation formulae for triangular and quadrilateral elements," *Int. j. numer. methods eng.* **18**, 959.

[170] Zienkiewicz, O. C. (1977), *The finite element method*, McGraw-Hill, London.

[171] Zienkiewicz, O. C., S. Qu, R. L. Taylor and S. Nakazawa (1986), "The patch test for mixed formulations," *Int. j. numer. methods eng.* **23**, 1873.

“The most beautiful sea
is the one we have not sailed yet.”

Nazim Hikmet.